SISSA

Dynamics of full counting statistics, thermalization, and deconfinement transition in long range Ising model.

Candidate:

Nishan Ranabhat

Supervisor:

Prof. Mario Collura

Theory and Numerical Simulation of Condensed Matter
Scuola Internazionale Superiore Studi di Avanzati

Trieste, Italy

Contents

1 Introduction **2**

- 1.1 Quantum quench and thermalization . . . 3
  - 1.1.1 Local relaxation . . . 4
  - 1.1.2 Thermalization of closed quantum systems . . . 6
- 1.2 Spin model with long range interaction . . . 8

2 Simulation of $1\mathcal{D}$ quantum systems **15**

- 2.1 Tensor network and tensor operations . . . 16
  - 2.1.1 Tensor basics . . . 16
  - 2.1.2 Contraction cost . . . 18
  - 2.1.3 Tensor decomposition . . . 19
- 2.2 A need to restructure the manybody wavefunction . . . 21
- 2.3 Matrix product state (MPS) . . . 24
  - 2.3.1 Matrix product state for $1\mathcal{D}$ system . . . 28
- 2.4 Matrix product operator . . . 29
  - 2.4.1 Hamiltonians as MPO . . . 31
- 2.5 Matrix product density operator . . . 35
- 2.6 Density Matrix Renormalization Group . . . 37
- 2.7 Time Dependent Variational Principle . . . 40
- 2.8 Lanczos solvers . . . 45
- 2.9 Codes availability . . . 48

3 Dynamics of order parameter statistics **49**

- 3.1 Full counting statistics . . . 50
- 3.2 Quench dynamics . . . 52
  - 3.2.1 Quench of the transverse field . . . 55
  - 3.2.2 Quench of the interaction range . . . 63
- 3.3 Conclusion . . . 64
- 3.A Calculating full counting statistics with MPS . . . 65
- 3.B Integrable limits . . . 66

3.B.1 Nearest neighbor limit 66
3.B.2 Fully connected limit 68
3.C Convergence with bond dimension 71

4 Thermalization : a full counting statistics approach 74
4.1 Numerical extraction of effective temperature 77
4.2 Results 78
4.2.1 Quench to dynamical ferromagnetic regime 79
4.2.2 Quench to dynamical paramagnetic regime 80
4.3 Signatures in domain wall kink 81
4.4 Conclusions 82
4.A Exact time evolution 83
4.B Simulations details 84
4.B.1 Simulation of finite temperature density operator 85
4.B.2 Errors and data convergence 88
4.C Thermal phase transition in long range Ising model 89
4.D Confinement dynamics in different regimes 90

5 Dynamical deconfinement transition 93
5.1 Introduction 93
5.2 Confinement in LRIM 95
5.3 Quench Dynamics 98
5.3.1 Signatures in average domain wall kinks 100
5.3.2 Signatures in kink fluctuation 101
5.4 Conclusions 105
5.A Two kink model 106
5.B Single kink model and localization length 107
5.C Simulation details 109
5.D Full counting statistics of domain wall kinks 112

6 Summary and Outlook 114

List of Publications

This thesis includes materials from following articles:

1. **N. Ranabhat** and M. Collura, “Dynamics of the order parameter statistics in the long range Ising model,” *SciPost Phys.*, vol. 12, p. 126, 2022. Available: `https://scipost.org/10.21468/SciPostPhys.12.4.126`
2. **N. Ranabhat** and M. Collura, ”Thermalization of long range Ising model in different dynamical regimes: a full counting statistics approach”, arXiv:2212.00533v3. Available: `https://arxiv.org/abs/2212.00533v3` (to appear in SciPost)
3. **N. Ranabhat**, A. Santini, E. Tirrito, M. Collura,”Dynamical deconfinement transition driven by density of excitations”, arXiv:2310.02320v2. Available: `https://arxiv.org/abs/2310.02320` (under review in Physical Review Letters)

Chapter 1

Introduction

The primary justification for studying manybody physics is succinctly captured in the phrase '*More is different*,' which is the title of a 1972 paper by Phil Anderson[1]. Anderson argued that the collective behavior of a manybody system exhibits a fundamentally distinct emergent behavior that cannot be built from the mere summation of its individual components. Over the past 50 years since the publication of this work, significant achievements have been made in addressing inquiries related to the equilibrium behavior of both classical and quantum many-body systems [2]. However, a general understanding of the nonequilibrium dynamics of many-body systems, particularly in the quantum regime, remains largely unclear[3, 4]. Historical investigations of quantum manybody physics have relied on effective models to describe the behavior of experimentally observed complex condensed matter systems. However, in the past two decades, significant advancements have been made in the realm of synthetic quantum simulators across various Atomic, Molecular, and Optical (AMO) platforms. These simulators enable the direct realization of effective models in a near isolated environment thus allowing the simulation of unitary dynamics of a closed quantum system.

The theoretical interest in nonequilibrium manybody dynamics has been largely driven by the success of these AMO platforms in simulating the physics of interacting manybody systems. One notable pioneering experiment was Quantum Newton's cradle, which studied the nonequilibrium dynamics of trapped one dimensional Bose gases composed of 40 to 250 ^{87}Rb atoms [5]. This experiment revealed that the system failed to reach thermal equilibrium, even after thousands of collisions. Subsequent advancements have since been made in diverse platforms such as trapped ions [6], quantum gases in optical lattices [7, 8], Rydberg atoms [9], dipolar quantum gases [10], and polar molecules [11]. These platforms offer precise control over the Hamiltonian parameters and accurate measurement of the order parameters, in addition to facilitating various nonequilibrium protocols, including sudden quenches of global and local parameters, adiabatic variations of parameters (annealing), and periodic driving fields. The simulation of effective manybody models addresses fundamental questions in nonequilibrium dynamics, such as the thermalization of closed quantum systems perturbed out of equilibrium, the relevant time scales, the existence of dynamical phases, and the corresponding universality classes for dynamical criticality. Concurrently, the development of controllable and noise-free quantum simulators is pivotal for advancing future quantum technologies.

In this thesis, we investigate the nonequilibrium quench dynamics of a one dimensional spin model featuring a two-body spin-spin interaction decaying as a power-law of spatial separation $\sim 1/r^{\alpha}$. The inherent long range interaction allows for stable long range correlated states that are robust against thermal fluctuations. The interaction strength α is highly tunable in current AMO platforms which makes it a paradigmatic model to study nonequilibrium dynamics. Additional insights into global quantum quench and relaxation dynamics are provided in Section 1.1 of this chapter. Section 1.2 of this chapter provides further details of the specific model and a succinct review of its properties.

Rest of the thesis is organized as follows: Chapter 2 provides an in-depth exploration of tensor network formalism, with a specific focus on matrix product states (MPS) and their significance in simulating one-dimensional many-body systems. Additionally, it discusses Density Matrix Renormalization Group (DMRG) and Time Dependent Variational Principle (TDVP) algorithms. Chapter 3 explores the relaxation dynamics of the probability distribution function (PDF) of subsystem magnetization in the long range Ising model (LRIM) following a global quantum quench. The content in this chapter is adapted from ([12]). Chapter 4 builds on Chapter 3 and examines the thermalization of LRIM in various dynamical regimes based on the relaxation dynamics of the PDF. The content in this chapter is adapted from ([13]). Finally Chapter 5 investigates dynamical deconfinement transition with thermally tuned density of excitations. This chapter is adapted from [14].

1.1 Quantum quench and thermalization

A commonly employed protocol for driving a system away from equilibrium is global quantum quench. A quantum quench involves the sudden alteration of a parameter in the Hamiltonian, followed by the subsequent unitary time evolution of the system with the new Hamiltonian. If this change encompasses the entire system, it is called a global quench. Conversely, modifying the parameters associated solely with local degrees of freedom constitutes a local quench. Throughout this thesis, we have exclusively employed the global quench protocol. Consider a system described by Hamiltonian $\hat{H}(h)$, where h is a tunable parameter. We initialize the system in the ground state of Hamiltonian $\hat{H}(h_i)$. At time $t = 0$, the Hamiltonian changes abruptly from $\hat{H}(h_i)$ to $\hat{H}(h_f)$ and unitarily evolves the initial state with the new Hamiltonian, which is generally not an eigenstate of the system. The temporal evolution of the state for $t > 0$ is governed by the Schrödinger equation,

$$|\psi_t\rangle = e^{-it\hat{H}(h_f)} |\psi_i\rangle . \tag{1.1}$$

The unitary evolution conserves the total energy of the system at all $t > 0$ and the post quench energy density is larger than the ground state energy density of the post-quench Hamiltonian,

$$\lim_{N\to\infty} \frac{1}{N} \langle\psi_i|\hat{H}|\psi_i\rangle = \lim_{N\to\infty} \frac{1}{N} \langle\psi_t|\hat{H}|\psi_t\rangle > \lim_{N\to\infty} \frac{E_{\text{final}}}{N}, \tag{1.2}$$

where E_{final} is the ground state energy of the post-quench Hamiltonian. Owing to the extensive energy above the ground state induced by the quench, the system remains in a region of the Hilbert space, which is macroscopically distinct from the ground state. This significant departure is the primary driver of the nontrivial dynamics observed in the quantum system post-quench. It is noteworthy that the initial state need not be a pure state; rather, we can commence the evolution from any generic mixed state $\hat{\rho}_i$ [15]. The subsequent behavior of the system following the quench is assessed by computing the expectation value of relevant order parameter,

$$\begin{aligned} \mathrm{Tr}[\hat{O}\hat{\rho}_t] &= \mathrm{Tr}[\hat{O}e^{-it\hat{H}}\hat{\rho}_i e^{-it\hat{H}}] && \text{(1.3a)} \\ &= \sum_{m,n} C_{m,n} \langle m|\hat{O}|n\rangle e^{-i[E_n - E_m]t}, && \text{(1.3b)} \end{aligned}$$

where $\hat{\rho}_t = e^{-it\hat{H}}\hat{\rho}_i e^{-it\hat{H}}$ and $\hat{\rho}_i = \sum_{m,n} C_{m,n} |m\rangle \langle n|$ is the expansion of the initial density matrix $\hat{\rho}_i$ in the eigenbasis of final Hamiltonian. Intriguing physics stems from the oscillatory factor in Equation 1.3, which gives rise to interference effects [16]. The widespread use of the global quench protocol is attributed to its effectiveness in exploring various exotic nonequilibrium phenomena, such as dynamical quantum phase transitions [17, 18, 19], many-body localization [20, 21, 22], dynamical confinement [23], and others.

1.1.1 Local relaxation

A critical inquiry regarding quantum quench pertains to the destiny of isolated systems at late times. The emergence of a late-time stationary state is not guaranteed after a quantum quench. For example, consider a quantum quench protocol involving a pure state, as described in Equation 1.1, and an order parameter defined by the Hermitian operator $\hat{O}m, n = |m\rangle \langle n| + |n\rangle \langle m|$, where $|m\rangle$ and $|n\rangle$ represent the eigenkets of the post-quench Hamiltonian. The post-quench evolution of $\hat{O}_{m,n}$ is expressed as follows,

$$\mathrm{Tr}[\hat{O}_{m,n}\rho_t] = e^{-i[E_n - E_m]t}\langle\psi_i|m\rangle\langle n|\psi_i\rangle + h.c. \tag{1.4}$$

The expectation value of $\hat{O}_{m,n}$ exhibits persistent oscillations with no indication of a stationary state at later times. The absence of a stationary state can be attributed to the non-local nature of the operator $\hat{O}_{m,n}$. Although the system as a whole may not relax, local relaxation in spatial regions is evident [24, 25, 26, 27]. In lattice models, a local operator acts on a finite number of lattice sites within a finite distance in the thermodynamic limit. These include operators acting on single sites, multiple sites separated by finite distances, or over a finite compact subsystem within the entire system. Throughout this thesis, we focus on the local operators defined over finite subsystems.

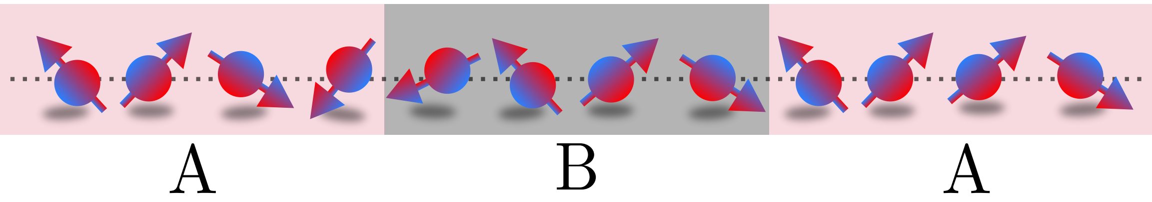

Figure 1.1: Partitioning a full system into two spatial Sections: a finite subsystem B and its complement A. In thermodynamic limit the finite subsystem B can be thought of as a system immersed withing a large bath A.

Consider a quantum system defined over N lattice sites divided into two disjoint Sections: a finite subsystem B and its compliment A, as shown in figure 1.1. The post-quench reduced density matrices corresponding to B and A are $\hat{\rho}_t^B = \mathrm{Tr}_A[\hat{\rho}_t^{A\cup B}]$ and $\hat{\rho}_t^A = \mathrm{Tr}_B[\hat{\rho}_t^{A\cup B}]$ respectively. The system is said to relax locally if the following limit exist,

$$\lim_{t\to\infty}\lim_{N\to\infty}\hat{\rho}_t^B = \hat{\rho}_\infty^B \tag{1.5}$$

for a finite subsystem B. Assuming local relaxation the stationary state $\hat{\rho}^{\mathrm{SS}}$ is defined for the full system such that,

$$\lim_{N\to\infty}\mathrm{Tr}_A[\hat{\rho}^{\mathrm{SS}}] = \hat{\rho}_\infty^B. \tag{1.6}$$

$\hat{\rho}^{\mathrm{SS}}$ is time independent. It should be noted that this doesn't imply $\hat{\rho}_{t\to\infty}^{A\cup B} = \hat{\rho}^{\mathrm{SS}}$. Finally, consider two density matrices $\hat{\rho}$ and $\hat{\rho}'$. The ensembles corresponding to these two density matrices are called locally equivalent if for a finite subsystem B the following equation holds true,

$$\lim_{N\to\infty} \mathrm{Tr}_A[\hat{\rho}] = \lim_{N\to\infty} \mathrm{Tr}_A[\hat{\rho}']. \tag{1.7}$$

Local equivalence is denoted by $\hat{\rho} =_{\mathrm{loc}} \hat{\rho}'$. It should be noted that local equivalence does not imply equality of $\hat{\rho}$ and $\hat{\rho}'$. The existence of a time-independent stationary state that corresponds to a nonequilibrium quantum system remains a key area of investigation.

1.1.2 Thermalization of closed quantum systems

The concept of thermalization in a quantum system stems from classical thermalization. In classical thermalization, a perturbed closed system ergodically explores a constant energy manifold, leading to the characterization of macroscopic quantities through a microcanonical ensemble corresponding to the conserved energy [28]. In a closed quantum system, where energy is the sole conserved quantity, thermalization is defined by the presence of local equivalence between the stationary state and a thermal ensemble that is dependent on the conserved energy. In our framework, this equivalence is established with the canonical Gibbs ensemble (CGE),

$$\hat{\rho}^{\mathrm{SS}} =_{\mathrm{loc}} \hat{\rho}^{\mathrm{CGE}} = \frac{e^{\beta_{\mathrm{eff}}\hat{H}}}{\mathrm{Tr}[e^{\beta_{\mathrm{eff}}\hat{H}}]}, \tag{1.8}$$

where the parameter β_{eff} is the effective inverse temperature that is fixed by the initial energy density of the system,

$$\lim_{N\to\infty} \frac{1}{N}\mathrm{Tr}[\hat{\rho}_i\hat{H}] = \lim_{N\to\infty} \frac{1}{N}\mathrm{Tr}[\hat{\rho}^{\mathrm{CGE}}\hat{H}]. \tag{1.9}$$

Practically local equivalence mentioned in equation 1.8 implies that the expectation value of a local operator $\hat{O}_{\mathrm{loc}}$ over the stationary state $\hat{\rho}^{\mathrm{SS}}$ is equal to the expectation value defined over $\hat{\rho}^{\mathrm{CGE}}$,

$$\lim_{N\to\infty} \frac{1}{N}\mathrm{Tr}[\hat{\rho}^{\mathrm{SS}}\hat{O}_{\mathrm{loc}}] = \lim_{N\to\infty} \frac{1}{N}\mathrm{Tr}[\hat{\rho}^{\mathrm{CGE}}\hat{O}_{\mathrm{loc}}]. \tag{1.10}$$

An alternative perspective to understanding thermalization in a closed quantum system arises from the equivalence between the canonical Gibbs ensemble and the microcanonical ensemble in the thermodynamic limit. We commence with the time-dependent expectation of a generic operator, as given by Equation 1.3: $\mathrm{Tr}[\hat{O}\hat{\rho}_t] = \sum_{m,n} C_{m,n}\langle m|\hat{O}|n\rangle e^{-i[E_n-E_m]t}$. While this expectation value possesses a time independent diagonal term, the off-diagonal term consists of oscillating phases that are dependent on the energy difference of the corresponding energy eigenstates. If we assume non-degenerate energy spectrum, then in the long-time limit, each off-diagonal contributes a random phase that gets cancelled out. Consequently, in the long time limit the expectation value of a generic operator consists only of the diagonal elements,

$$\lim_{t\to\infty} \mathrm{Tr}[\hat{O}\hat{\rho}_t] = \sum_m C_{m,m}\langle m|\hat{O}|m\rangle. \tag{1.11}$$

We can define an equivalent time-independent ensemble based on this argument known as the diagonal ensemble[29, 30],

$$\hat{\rho}^{\mathrm{diag}} = \sum_m C_{m,m}|m\rangle\langle m|. \tag{1.12}$$

If the system equilibrates, the stationary state should necessarily be described by a diagonal ensemble, that is, $\hat{\rho}^{\mathrm{SS}} = \hat{\rho}^{\mathrm{diag}}$. The corresponding stationary state expectation value is given by equation 1.11. In thermodynamic limit the canonical Gibbs ensemble defined in equation 1.8 is equivalent to a microcanonical ensemble,

$$\hat{\rho}^{\mathrm{MC}} = \frac{1}{N_{E_0,\Delta}} \sum_{|E_m - E_0| < \Delta} |m\rangle\langle m|, \tag{1.13}$$

where E_0 is the energy of the initial state, E_m is the energy corresponding to the energy eigenket $|m\rangle$, Δ is the sufficiently narrow energy shell [30], and $N_{E_0,\Delta}$ is the normalization term, which is the total number of eigenkets within the energy shell 2Δ. Thermalization in this perspective means the local equivalence of the diagonal ensemble and the microcanonical ensemble, $\hat{\rho}^{\mathrm{diag}} =_{\mathrm{loc}} \hat{\rho}^{\mathrm{MC}}$, or at the level of observables,

$$\sum_m C_{m,m}\langle m|\hat{O}|m\rangle = \frac{1}{N_{E_0,\Delta}} \sum_{|E_m - E_0| < \Delta} \langle m|\hat{O}|m\rangle. \tag{1.14}$$

The left-hand side explicitly depends on the information of the initial state through coefficients $C_{m,m}$ whereas the right-hand side depends only on a single parameter E_0, which may be the same for different initial states. This apparent incongruity was independently addressed by J. M. Deutsch [29] and M. Srednicki [31] through the Eigenstate Thermalization Hypothesis (ETH). According to ETH, for a local operator $\hat{O}_{\mathrm{loc}}$ in a non-integrable system, the expectation value $\langle m|\hat{O}_{\mathrm{loc}}|m\rangle$ is smooth and does not fluctuate significantly between eigenkets that are close in energy. Consequently, for any initial state with a narrow energy distribution (sharp distribution of $C_{m,m}$ vs. E_m), Equation 1.14 holds. It is crucial to note that ETH is a hypothesis and there is no general proof for it. Nevertheless, ETH has been verified for a family of non-integrable systems [32, 33, 30, 34, 35, 36, 37, 38]. Many-body localized systems are special cases that do not satisfy ETH, even if they are non-integrable [39].

1.2 Spin model with long range interaction

The study of models with long range interactions is of significant interest owing to the profound impact of the range of interactions between the constituents on the phase diagram and critical behaviors of systems. long range interactions introduce nonlocal behaviors, which lead to the emergence of several exotic phenomena that are absent in their short range counterparts [40, 41]. Recent advances in experimental capabilities for controlling and manipulating atomic, molecular, and optical (AMO) systems have fueled interest in the physics of models featuring long range interactions. Specifically, the incorporation of two-body long range interactions has become feasible across various AMO platforms including Rydberg atoms, dipolar gases, polar molecules, atoms in optical cavities and trapped ions [40, 41]. Beyond the fascinating emergent physics, the study of long range interacting systems is crucial for the development of future quantum technologies. These systems offer the potential to overcome constraints on correlation spreading and lack long range order at finite temperatures, as observed in local systems [4, 40].

While any generic interaction beyond the nearest-neighbor interaction can be called long range, including finite-range interaction and exponentially decaying interaction, here we consider the power-law decaying interaction, where the interaction between two particles decays as the inverse power of the distance between them $\sim 1/r^{\alpha}$. An interesting feature of the power-law decaying interaction is that the effective interaction can be finely tuned with the parameter. This give rise to the idea of effective dimension; there is a correspondence between the universal behavior of long range interacting model with spatial dimension $\mathcal{D}$ and parameter α and the locally interacting system with dimension $\mathcal{D}_{\text{eff}} = 2(\mathcal{D} + z)/(\alpha - d)$, where z is the dynamical critical exponents [41, 42]. Consequently, this allows us to gauge the behavior of the system at higher spatial dimensions by studying the corresponding long range system in one dimension. Furthermore, long range models exhibit diverse universality behavior as a function of α: for $\alpha < \frac{5}{3}\mathcal{D}$ the system exhibits a mean field universality class; for $\frac{5}{3}\mathcal{D} < \alpha < \alpha^*$, it exhibits unique long range critical behavior; and for $\alpha > \alpha^*$ it exhibits a short range universality class (akin to $\alpha \to \infty$) [42].

In this thesis we consider a spin one-half long range Ising model (LRIM) in one dimension that is described by the hamiltonian,

$$\hat{H}(J, \alpha, h) = -\frac{1}{\mathcal{K}(\alpha)} \sum_{i<j}^{N} \frac{|J|}{|i-j|^{\alpha}} \hat{s}_i^x \hat{s}_j^x - h \sum_{i=1}^{N} \hat{s}_i^z \tag{1.15}$$

where $\hat{s}_i^{\mu}, \mu = x, y, z$ are the spin one-half matrices at site i. We consider open boundary condition, that is relevant to existing experimental setups. For $\alpha \leq 1$, the inverse power-law interaction series diverges with the lattice size (represented by hatched region in Figure 1.3) and is normalized using the Kac normalization constant,

$$\mathcal{K}(\alpha) = \frac{1}{N-1} \sum_{i<j}^{N} \frac{1}{|i-j|^{\alpha}} = \frac{1}{N-1} \sum_{n=1}^{N} \frac{N-n}{n^{\alpha}}. \tag{1.16}$$

This normalization ensures the intensivity of the energy density in the regime $\alpha \leq 1$. LRIM has been experimentally realized in a system of trapped ions utilizing a linear radio frequency Paul trap, providing exceptional tunability of the interaction range, α [6]. Additionally, employing a single-shot spin detection method allows for precise measurement of the individual state of each ion spin with an impressive efficiency approaching 99 percent [45]. Figure 1.2 panel (a) shows linear chain of 51 ^{40}Ca^{+} ions trapped with linear Paul trap. Panel (b) shows the time evolution of

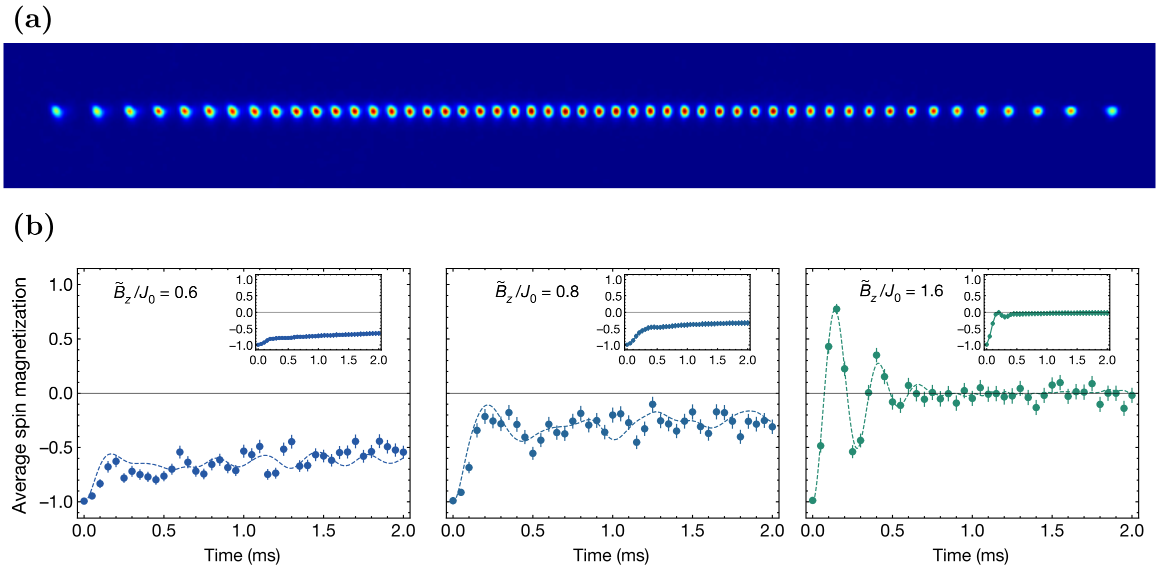

Figure 1.2: (a) A linear chain of 51 ^{40}Ca^{+} ions trapped with linear Paul trap. Picture adapted from `https://quantumoptics.at/en/`. (b) Evolution of average magnetization of 16 spin LRIM (dots) starting from a fully polarized symmetry broken phase to three different post quench transverse fields (Note: $\tilde{B}_z$ is equivalent to h and J_0 is equivalent to J in equation 1.15). The dashed lines are exact diagonalization results. Picture adapted from [18].

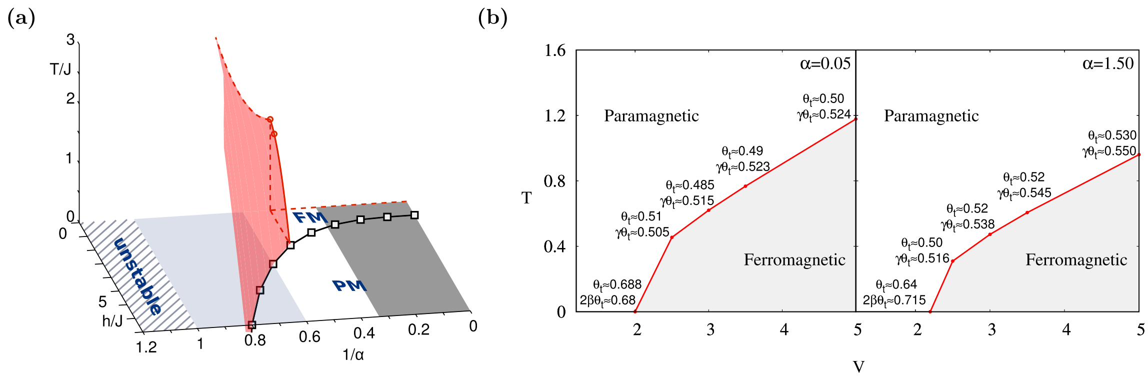

Figure 1.3: Equilibrium phase diagram of LRIM: (a) Solid black line separates ferromagnetic phase from paramagnetic phase. Light grey region $\alpha < \frac{5}{3}$ represents mean field universality class, dark grey region $\alpha > 3$ represents Ising universality class. At $\alpha = 2$ and $h = 0$ the model undergoes Berezinskii-Kosterlitz-Thouless (BKT) type thermal transition which also extends to finite h (represented by red dots). Figure adapted from [43]. (b) Thermal phase transition from ferromagnetic to paramagnetic phase at $\alpha = 0.05, 1.50$ with the corresponding critical exponents. Here, the parameter V is the spin-spin interaction in the unit of h (equivalent to J in equation 1.15). Figure adapted from [44].

average magnetization following the global quench of transverse field as realized in trapped ion experiment.

For a finite $|J|$ LRIM exhibits a quantum phase transition (QPT) from an ordered ferromagnetic phase to a paramagnetic phase induced by the transverse field. This transition is associated with the spontaneous breaking of $\mathbb{Z}_2$ symmetry along $x-$direction and is characterized by a zero average magnetization ($\langle \sum_i \hat{s}_i^x \rangle = 0$) in the paramagnetic phase transitioning into a finite average magnetization ($\langle \sum_i \hat{s}_i^x \rangle \neq 0$) with two degenerate ground states at the critical point h_c^α. At $\alpha = \infty$, the model reduces to the transverse field Ising model (TFIM) [46], which can be solved exactly by mapping it to a system of spinless fermions through Jordan-Wigner transformations [47]. TFIM exhibits a quantum phase transition at $h_c^\alpha = J/2$. As α decreases, this transition point shifts towards higher values of magnetic field h [48, 43] (see Figure 1.3 panel (a)). The universality class of this transition is identical to that of the (1+1)-dimensional classical Ising model [49]. Conversely, at the opposite extreme, with $\alpha = 0$, the model becomes fully connected and is equivalent to the Lipkin–Meshkov–Glick (LMG) model [50] with critical point at $h_c^\alpha = J$. This regime is analytically tractable using the Bethe ansatz [51]. However, for large N limit semiclassical solutions appear

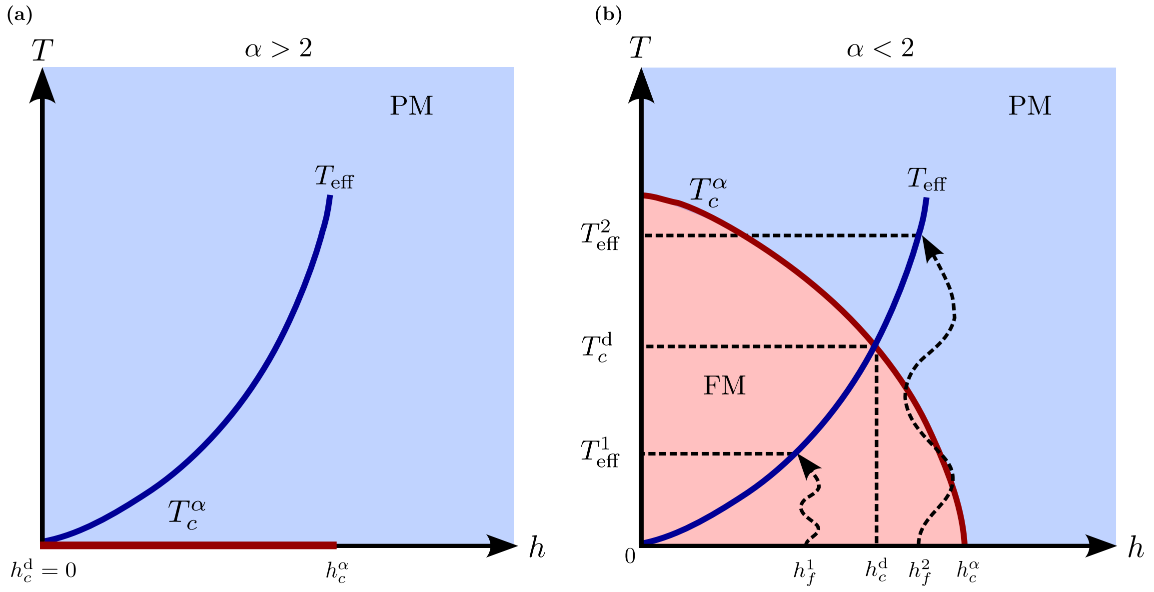

Figure 1.4: Cartoon phase diagram of LRIM: (a) for $\alpha > 2$ there is no thermal phase transition, ferromagnetic order is only present along the $T = 0$ line (horizontal red line) from $h = 0$ to $h = h_c^\alpha$. (b) for $\alpha < 2$ the model sustains long range ferromagnetic order at finite T. Solid red line T_c^α represents the thermal critical line, solid blue line T_{eff} represents the effective temperature corresponding to the global quantum quench, $h_i = 0 \rightarrow h_f$.

to be a more powerful approach providing an accurate description of the dynamical behavior [52, 41].

For systems featuring local interactions, the persistence of long range order remains viable at finite temperatures when $\mathcal{D} \geq 2$. Adjusting parameter α to a smaller value enhances the long-range interaction between spins, effectively mimicking a higher spatial dimension within $1\mathcal{D}$ LRIM. Consequently, the LRIM sustains long-range ferromagnetic order at a finite temperature for $\alpha < 2$. The thermal phase transition in LRIM has been investigated using large-scale path integral Monte Carlo simulations [44]. Figure 1.4, panel (b), illustrates the thermal phase transition from the ferromagnetic to paramagnetic phase for two values of α and varying interaction strengths. The critical exponents extracted from these simulations confirm that the transitions belong to the same universality class as the corresponding classical long-range Ising model.

The ability to sustain long range order at finite temperature leads to the emergence of dynamical phases in LRIM [48, 43]. This makes the LRIM an interesting paradigmatic model for studying nonequilibrium dynamics. Conventionally, the dynamical phase transition in LRIM is characterized by a sudden change in the initial magnetic order following a global quantum quench, and is captured by the time-averaged order parameter, $\bar{S} = \lim_{t\to\infty} \frac{1}{t}\int_0^t \langle \hat{S}^x(t) \rangle$, where $\hat{S}^x = \sum_i s_i^x/N$. In the thermodynamic limit, this transition is associated with $\mathbb{Z}_2$ symmetry breaking. One of the main subjects of this thesis is the investigation of dynamical phases in LRIM following a global quantum quench. Global quantum quench injects an extensive amount of energy into a closed quantum system. Consequently, the system relaxes in an energy space distinctly above the ground state of the post-quench Hamiltonian (see Section 1.1 for more details) [53]. This energy corresponds to the effective temperature, T_{eff} as defined in Equation 1.9. Figure 1.4 (b) shows the cartoon phase diagram of the LRIM for $\alpha < 2$. The solid blue line represents the effective temperature T_{eff} corresponding to the post-quench transverse field h_f corresponding to quench $h_i = 0 \to h_f$. The point at which T_{eff} intersects the equilibrium phase transition line T_c^α corresponds to the dynamical critical points h_c^d. If $h_f < h_c^d$ the system strongly retains the initial ferromagnetic order, whereas for $h_f > h_c^d$ the system loses the initial ferromagnetic order with the emergence of paramagnetic order. The range $h_c^d < h_f < h_c^\alpha$ is an interesting regime that is ferromagnetic for equilibrium transitions and paramagnetic for dynamical transitions. For $\alpha > 2$, there is no long-range ferromagnetic order for any $T \neq 0$, and the system is expected to be in the dynamical paramagnetic phase for all nontrivial quenches $h_f > 0$. Dynamical phase transition in LRIM has been realized in system of trapped ions [6] (see figure 1.2 panel (b)). Although the dynamical phases of LRIM have been qualitatively understood, the underlying critical behavior corresponding to the transition remains a challenging open question. In this thesis, we investigate the dynamical phases of LRIM by employing full counting statistics (FCS). In Chapter 3 we highlight FCS as a robust alternative to characterize dynamical phases compared to the expectation of the order parameter. We show that the FCS provides important qualitative signatures in the regime of slow relaxation, where the lower-order moments become inconclusive. In Chapter 4 we extend this idea to study the signatures of thermalization in LRIM.

The speed of correlation spreading in locally interacting quantum systems is limited by the Lieb-Robinson bound [54] which predicts a linear light-cone like spread of correlation. However, long range interacting systems circumvent this bound and allow for a super-ballistic spread of correlation [40, 41]. However LRIM exhibit some anomalous and completely counter-intuitive dynamics that further makes it an interesting model to study. For $\alpha < 1$, bipartite entanglement entropy demonstrates suppressed logarithmic growth following a quantum quench [55, 56, 57]. It has been demonstrated that in the strong long range regime, $\alpha < 1$, entanglement growth is dominated by collective spin squeezing, thus leading to logarithmic growth [58, 59]. This slow growth of bipartite entanglement following a quench makes matrix prod-

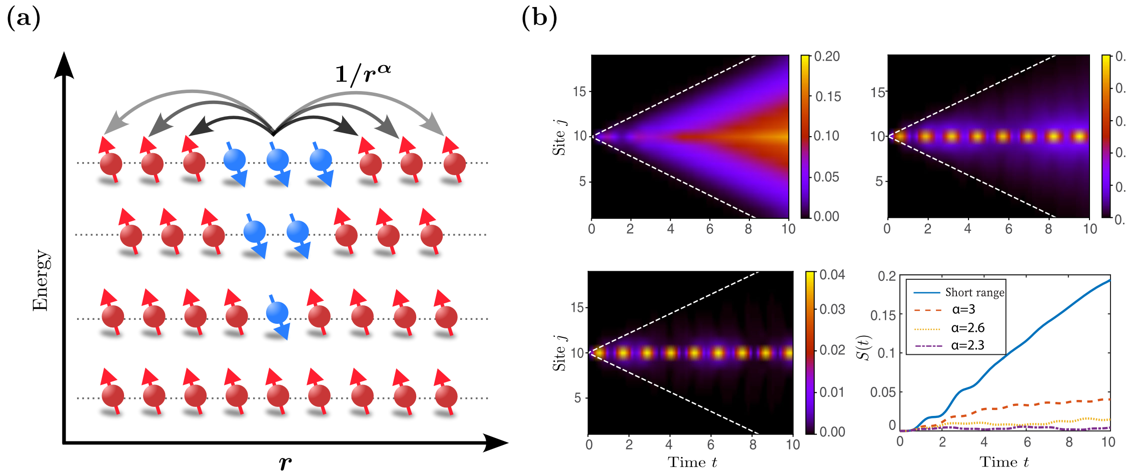

Figure 1.5: (a) Domain wall as excitations in LRIM. Fading arrows represents power law decaying interaction between spins. (b) Signature of domain wall confinement in LRIM: first three panels are the connected correlation spreading $\langle \hat{s}^x_j \hat{s}^x_k \rangle_c$ (k placed at the center of the chain) for $\alpha = \{\infty, 2.6, 2.3\}$ and $h = 0.27$. The last panel is the corresponding growth of entanglement entropy. Figure adapted from [61]

uct state (MPS)-based numerical studies very effective in this system (see Sections 2.2 and 2.3 in the next chapter for details of MPS and entanglement growth). This counter-intuitive behavior continues well into the weak long range regime $1 < \alpha < 2$ with strongly suppressed correlation spreading [60, 61]. The underlying mechanism behind these anomalous correlation dynamics in this regime is the phenomenon of confinement. The long range interaction of the model introduces an effective potential that constrains the spreading of the domain walls, consequently binding a pair of domain wall excitation (see Figure 1.5 panel (a)) into a stable quasiparticle called a meson (akin to the meson in quark confinement). The expression for the effective confining potential in a simple setting of two domain-wall kinks can be calculated easily. Consider an excited state with two domain-wall kinks separated by $2l$ located centrally in a chain of length $2N$. The excess potential of this excited state above the ground state is given by,

$$V_{\alpha,N}(l) = 4J \sum_{i=N-l}^{N+l} \sum_{j=N+l-i}^{2N-i} \frac{1}{j^\alpha} \qquad (1.17)$$

We don't include the Kac normalization term here to be consistent with Chapter 5. In the continuous space limit the sums in the potential can be approximated with integrals,

$$\begin{aligned} V_{\alpha,N}(l) &\rightarrow 4J \int_{N-l}^{N+l} dx \int_{N+l-x}^{2N-x} \frac{dy}{y^{\alpha}} &(1.18)\\ &= \frac{4J}{(1-\alpha)} \int_{N-l}^{N+l} [(2N-x)^{1-\alpha} - (N+l-x)^{1-\alpha}]dx &(1.19)\\ &= \frac{4J}{(1-\alpha)(2-\alpha)} [(N+l)^{2-\alpha} - (N-l)^{2-\alpha} - (2l)^{2-\alpha}] &(1.20) \end{aligned}$$

In the limit $N \gg l$ we can approximate potential by expanding the first two terms in l/N and only taking the linear term,

$$V_{\alpha,N}(l) = 4J \left[\frac{2l}{(1-\alpha)N^{\alpha-1}} - \frac{(2l)^{2-\alpha}}{(1-\alpha)(2-\alpha)} \right] + O[(l/N)^2] + \ldots \qquad (1.21)$$

In the thermodynamic limit $N \rightarrow \infty$, $V_{\alpha,N}(l)$ is finite for a finite domain wall size only for $\alpha > 1$. For $1 < \alpha < 2$ the potential diverges with the domain wall size, $V_{\alpha,N}(l) \sim l^{2-\alpha}$ therefore, creating a pair of domain walls is energetically unfavorable and strongly confined. This leads to the ability of the LRIM to strongly retain long range ferromagnetic order. By contrast, for $\alpha > 2$ the potential $V_{\alpha,N}(l)$ is bounded from above; however, the low excitations are still composed of bound states [60]. The confined system exhibits quasilocalized dynamics, including the oscillation of order parameters, slow correlation spreading, and entanglement growth [62, 61, 63]. Figure 1.5 panel (b) illustrates the correlation spreading and bi-partite entanglement entropy in LRIM for three different values of α. Although it is linear for the short-range limit for $\alpha = \{2.3, 2.6\}$ we observe severe suppression. In the short range model, quasilocalized dynamics due to confinement were observed to be destroyed by increasing the density of domain wall excitations [64]. In Chapter 5 we investigate the robustness of confinement in LRIM with thermally tuned density of excitations. We highlight that the fluctuation of domain wall kinks provides a stronger signature of the deconfinement transition than the average domain wall kinks.

Chapter 2

Simulation of $1\mathcal{D}$ quantum systems

The quantum many-body problem poses an inherent challenge because of the exponential growth of Hilbert space as the system size increases. Although certain class of problems admit analytically tractable solutions, a considerable number of intriguing problems are analytically intractable. Over the past few decades, the rapid advancement of computer hardware coupled with an exponential increase in computational capacity [65, 66] has transformed the numerical simulation of many-body physics using classical devices into a formidable field. The exact diagonalization technique, both full and iterative diagonalization, yields numerically precise results constrained only by the machine precision. Nevertheless, the exact diagonalization of many-body problems beyond a few tens encounters severe limitations even with state-of-the-art computational resources [67, 68]. Various alternative methods have been developed, each with its strengths and weaknesses, such as dynamical mean field theory [69], quantum Monte Carlo [70], series expansion techniques [71], and density functional theory [72].

The tensor network method represents a relatively recent addition to the field of numerical simulation of many-body physics, wherein entities such as wave functions, density matrices, and operators are decomposed into tensors, and quantum operations are formulated as tensor contractions. The techniques developed based on this formalism are guided by the entanglement content and its structure within many-body interacting systems. Tensor network gained prominence in many-body physics following its successful application in the already established density matrix renormalization group (DMRG) algorithm [73, 74, 75, 76]. Subsequently, a multitude of tensor network-based methods have emerged, namely, time-evolving block decimation (TEBD) [77, 78], time-dependent variational principle (TDVP) [79, 80], projected entangled pair states (PEPS) [81], multi-scale entanglement renormalization ansatz (MERA) [82], and tensor renormalization group (TRG) [83]. Notably, tensor network have transcended their origins in many-body physics and have found applications in diverse fields, such as machine learning, holography, and quantum computing, reflecting their versatility and impact across scientific disciplines.

This Section provides a comprehensive overview of tensor networks, with a primary emphasis on simulating one dimensional many-body spin systems using matrix product states (MPS). The discussion will delve into two specific algorithms in considerable detail: the Density Matrix Renormalization Group (DMRG) and Time-Dependent Variational Principle (TDVP). Most of the numerical results presented in this thesis are simulated using these two algorithms.

2.1 Tensor network and tensor operations

Tensor network is a method for structuring numerical data within multidimensional arrays [84, 85, 86, 87]. It enables the execution of intricate linear algebra operations in a concise manner, ideally suited for contemporary computational devices. In this Section, we provide a formal introduction to tensors, tensor network, and crucial tensor network operations. These will serve as the foundation for all the representations and algorithms discussed in this chapter.

2.1.1 Tensor basics

The tensor is a generalization of vectors and matrices. A generic rank-N tensor is described as a complex multidimensional array denoted by $T_{\gamma_1,\ldots,\gamma_i,\ldots,\gamma_N} \in \mathbb{C}^{D_1\times\ldots\times D_i\times\ldots\times D_N}$. Each index, informally referred to as the "leg" of the tensor, assumes values from set $\{1, 2, \ldots, d_i\} \in \mathbb{Z}+^{D_i}$. Here, D_i signifies the dimension associated with the index γ_i, and the overall dimension of the full tensor is given by the product $\prod_{i=1}^{N} D_i$. Consequently, every individual element within tensor T can be uniquely identified by a tuple comprising N independent integers, denoted as $(\gamma_1, \ldots, \gamma_i, \ldots, \gamma_N)$. This definition of words rank and dimension is specific to this thesis.

Scalar is a rank-0, vector is a rank-1, and matrix is a rank-2 tensor. In the case of higher-rank tensors that possess multiple legs, intricate operations can be effectively executed using tensor network diagrams. These diagrams provide a visual and intuitive means of representing and manipulating tensors, simplifying complex computations, and facilitating a deeper understanding of their behavior. In figure 2.1 we present the tensor network diagram for a scalar, a vector, a matrix, and a generic rank-N tensor.

Tensor network is a collection of tensors in which a subset of their total indices are contracted in some fashion. Contracting the indices of two tensors is the most fundamental operation in tensor network and is a generalization of matrix multiplication.

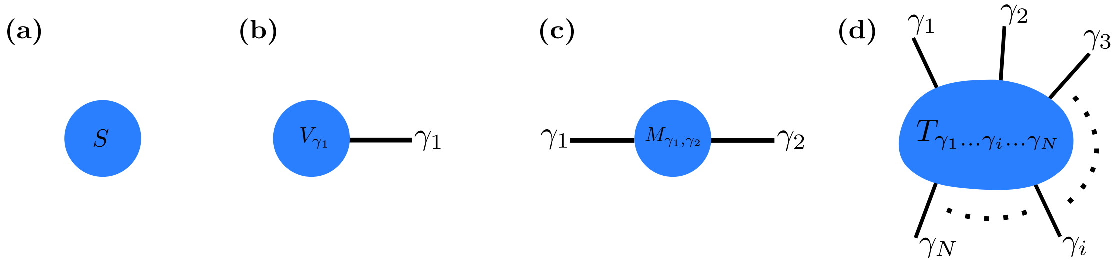

Figure 2.1: tensor network diagrams : (a) Scalar, (b) vector, (c) matrix, (d) a generic rank-N tensor.

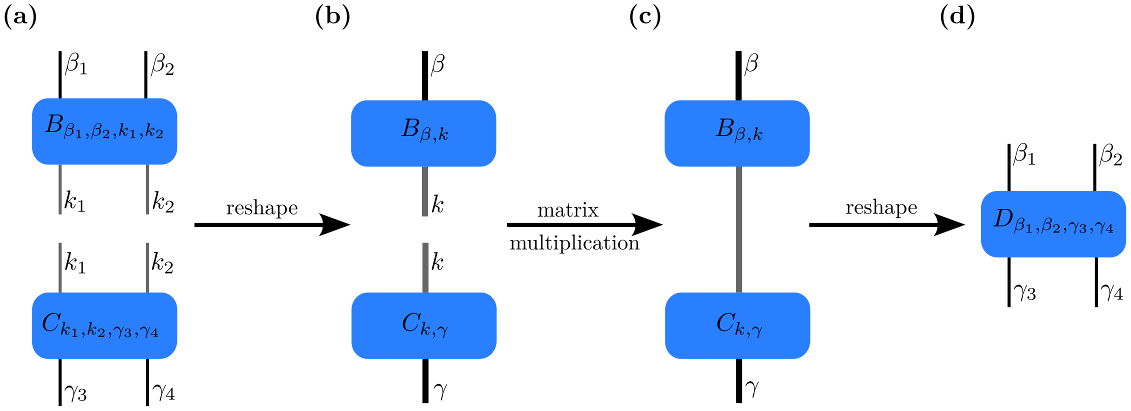

Figure 2.2: Contracting two tensors with four legs each. The grey legs are the contracted indices and the black legs are the free indices.(a) In each tensor the free indices and contracting indices are fused together into a single indices.(b) The resulting matrices are multiplied along the contracted indices.(c) Finally the free indices are split into original indices.

Two tensors B and C of ranks N and $\tilde{N}$, and dimensions $\prod_{i=1}^{N} D_i^B$ and $\prod_{j=1}^{\tilde{N}} D_j^C$ can be contracted along the l shared indices $(k_1, \ldots, k_l)$ by summing over the space of shared indices as shown in equation 2.1. The result is a rank-$N + \tilde{N} - 2l$ tensor with dimension $\prod_{i=1}^{N-l} D_i^B \times \prod_{j=l+1}^{\tilde{N}} D_j^C$.

$$\sum_{k_1,\ldots,k_l} B_{\beta_1,\ldots,\beta_{N-l},k_1,\ldots,k_l} C_{k_1,\ldots,k_l,\gamma_{l+1},\ldots,\gamma_{\tilde{N}}} = D_{\beta_1,\ldots,\beta_{N-l},\gamma_{l+1},\ldots,\gamma_{\tilde{N}}} \tag{2.1}$$

Alternatively, every tensor contraction of arbitrary ranks can be accomplished using matrix multiplication. This is achieved by first reshaping the tensors into matrices by fusing all free indices into one single index and all shared indices into another single index; $B_{(\beta_1,\ldots,\beta_{N-l}),(k_1,\ldots,k_l)} \to B_{\beta,k}$ and $C_{(k_1,\ldots,k_l),(\gamma_{l+1},\ldots,\gamma_{\tilde{N}})} \to C_{k,\gamma}$. For simplicity we have considered the special case where the last l indices of B and the first l indices of C are the shared indices. In general we can fuse any set of indices by permuting the indices in correct order before fusing them. This is followed by a matrix multiplication along the shared index, $\sum_k B_{\beta,k}C_{k,\gamma} = D_{\beta,\gamma}$. Finally, the free indices are reshaped back to the original indices $D_{\beta,\gamma} \to D_{\beta_1,\ldots,\beta_{N-l},\gamma_{l+1},\ldots,\gamma_{\tilde{N}}}$. Figure 2.2 shows the contraction of two rank-4 tensors via matrix multiplication. Modern scientific computing provides several options for performing highly sophisticated tensor network contractions. The tensor contraction operations at the backend of all results in this thesis has been performed using the TensorOperations.jl [88] library in Julia programming language [89].

2.1.2 Contraction cost

The speed of any tensor network algorithms fundamentally boils down to speed of the underlying tensor network contractions [84, 85]. The speed of contracting a pair of arbitrary tensors B and C as defined in 2.1 is parameterized by the total number of underlying scalar multiplications and is given by,

$$\text{cost}\left[\sum_{k_1,\ldots,k_l} B_{\beta_1,\ldots,\beta_{N-l},k_1,\ldots,k_l} C_{k_1,\ldots,k_l,\gamma_{l+1},\ldots,\gamma_{\tilde{N}}}\right] = \frac{\dim(B)\times\dim(C)}{\dim(B\cap C)} \tag{2.2}$$

where $\dim(B) = \prod_{i=1}^{N} D_i^B$, $\dim(C) = \prod_{j=1}^{\tilde{N}} D_j^C$, and $\dim(B\cap C) = \prod_{i=N-l+1}^{l} D_i^B$ (or $\prod_{j=1}^{l} D_j^C$). While the contraction cost for a pair of tensors remains constant, the contraction cost for a tensor network comprising more than two tensors with varying ranks and dimensions depends on the chosen order of contraction. Therefore, identifying the optimal contraction order for a given tensor network is crucial. In Figure 2.3, we show the contraction of three tensors with two different orders. The tensor T is of rank-2, and both B and C are of rank-3. For simplicity, we assume that all indices of these tensors have equal dimensions, D. According to Equation 2.2 the contraction cost in Figure 2.3(a) is $O(D^5)$ while the cost of contraction in Figure 2.3(b) is $O(D^4)$. For a large D this results in substantial speedup, highlighting the significance of determining the optimal contraction order for every tensor contraction within a tensor network algorithm.

The challenge of identifying the optimal order for contracting a tensor network consisting of an arbitrary number of tensors with different ranks and dimensions is

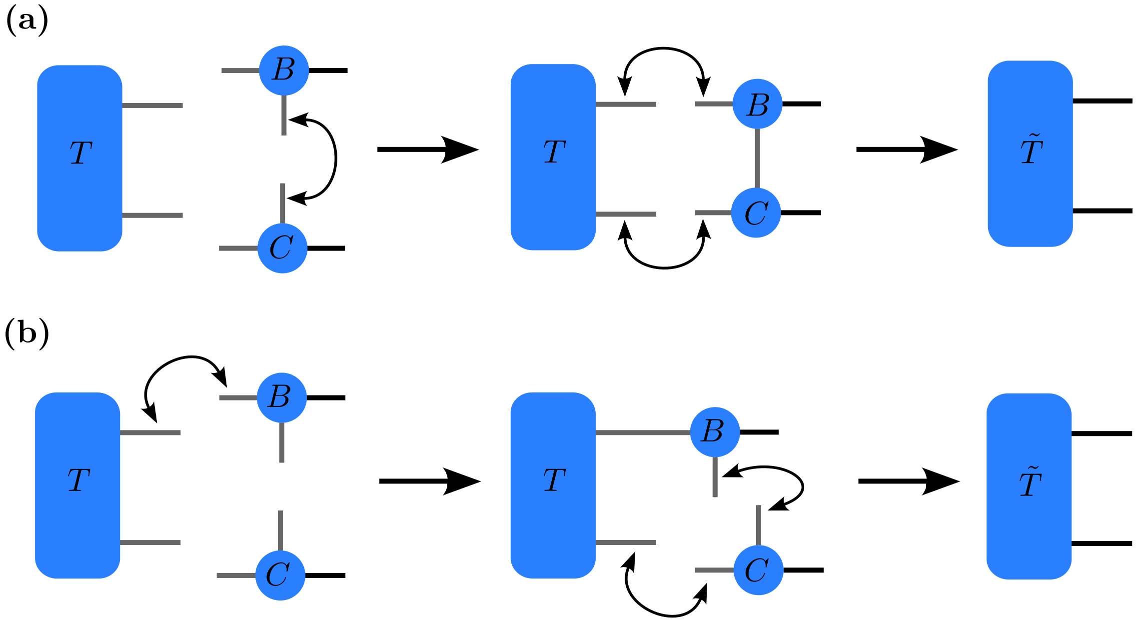

Figure 2.3: Two different orders of tensor contraction. (*a*) Expensive order with a cost of $O(D^5)$.(*b*) Cheaper order with a cost of $O(D^4)$.

NP-hard [90]. However, tensor network algorithms commonly encountered in solving many-body physics problems, particularly in low dimensions, often do not involve complex tensor contractions, and the optimal contraction order can be determined through simple observation. In recent years, multiple approaches have been proposed for identifying the optimal contraction order [90, 91, 92, 93].

2.1.3 Tensor decomposition

Tensor decomposition takes a single tensor and decomposes it into two or more constituent tensors. The indices of the original tensor are distributed among these constituent tensors, which are interconnected through the shared internal indices. In this light, tensor decomposition can be thought of as the reverse operation of tensor contraction. In this Section, we delve into two specific decompositions that play a crucial role in important tensor network algorithms for many-body physics: singular value decomposition (SVD) and QR decomposition.

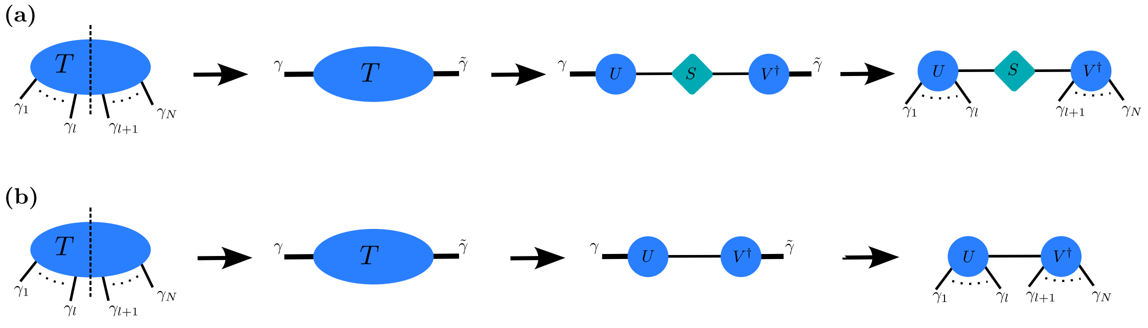

Figure 2.4: Singular value decomposition (a) and QR decomposition (b) of a tensor T.

Singular value decomposition (SVD)

Singular value decomposition is primarily a matrix decomposition that decomposes a matrix M of dimension $m \times n$ into three components,

$$M_{i,j} = \sum_{k=1}^{\min(m,n)} U_{i,k} S_{k,k} V^\dagger_{k,j} \tag{2.3}$$

where,

1. U is of dimension $m \times \min(m,n)$ and has orthonormal columns, $U^\dagger U = \mathbb{I}$ where $\mathbb{I}$ is an identity matrix.

2. S is a square diagonal matrix of dimension $\min(m,n) \times \min(m,n)$. The diagonal entries are called the singular values. The number of non-zero diagonal entries of S is called the Schmidt rank of M, not to be confused with the rank of a tensor as defined in Section 2.1.1. The diagonal entries $S_{k,k}$ are taken in descending order without any loss of generality.

3. $V^\dagger$ is of dimension $\min(m,n) \times n$ and has orthonormal rows, $VV^\dagger = \mathbb{I}$.

The cost of SVD is $O(mn^2)$ (assuming $m \geq n$) [94]. Any generic tensor can be decomposed by SVD. This is achieved by bipartitioning the tensor indices into two groups and fusing them to form a matrix, followed by a SVD, and finally splitting the original free indices,

$$T_{(\gamma_1,\ldots,\gamma_l),(\gamma_{l+1},\ldots,\gamma_N)} = \sum_{k=1}^{D} U_{\gamma_1,\ldots,\gamma_l,k} S_{k,k} V^\dagger_{k,\gamma_{l+1},\ldots,\gamma_N} \tag{2.4}$$

where, $D = \min\Big(\prod_{i=1}^{l} D_i^T, \prod_{i=l+1}^{N} D_i^T\Big)$ and the bipartition is made at site l. Figure 2.4 (a) shows the tensor network diagram of the SVD of a generic tensor.

QR decomposition

QR decomposition decomposes a matrix M of dimension $m \times n$ into two constituent components,

$$M_{i,j} = \sum_{k} Q_{i,k} R_{k,j} \tag{2.5}$$

where,

1. Q is a $m \times m$ unitary matrix (assuming $m \geq n$), $QQ^\dagger = Q^\dagger Q = \mathbb{I}$.
2. R is a $m \times n$ upper triangular matrix.

The lowest $(m - n)$ rows of matrix R are comprised of zeros, allowing for a more compact representation of the decomposition as follows: $M_{i,j} = \sum_k Q^1_{i,k} R^1_{k,j}$, where Q^1 denotes a rectangular matrix with dimensions $m \times n$ and features orthonormal columns ($QQ^\dagger$), while R^1 is an upper triangular square matrix sized at $n \times n$. This is commonly referred to as the thin QR decomposition [95, 94]. Although Q^1 shares the characteristic of right orthonormality with matrix U in the SVD, it is important to note that these matrices are not identical. Likewise, any arbitrary tensor can be decomposed using QR decomposition by partitioning its indices into two groups, much like the SVD decomposition,

$$T_{(\gamma_1,\ldots,\gamma_l),(\gamma_{l+1},\ldots,\gamma_N)} = \sum_{k=1}^{D} Q_{\gamma_1,\ldots,\gamma_l,k} R^\dagger k, \gamma_{l+1}, \ldots, \gamma_N \tag{2.6}$$

where, $D = \prod_{i=1}^{l} D_i^T$ (assuming $\prod_{i=1}^{l} D_i^T \geq \prod_{i=l+1}^{N} D_i^T$) and the bipartition is made at site l. Figure 2.4 (b) shows the tensor network diagram of the SVD of a generic tensor.

2.2 A need to restructure the manybody wavefunction

Lets consider a quantum manybody system of N interacting particles each with d local degrees of freedom. The generic state of such a system can be described by the wavefunction,

$$|\psi\rangle = \sum_{\sigma_1,\ldots\sigma_l\ldots,\sigma_N} C_{\sigma_1,\ldots\sigma_l\ldots,\sigma_N} |\sigma_1\rangle \otimes \ldots |\sigma_l\rangle \ldots \otimes |\sigma_N\rangle \tag{2.7}$$

where $|\sigma_l\rangle$ is the state representing the particle at site l. $C_{\sigma_1,\ldots\sigma_l\ldots,\sigma_N}$ are d^N complex numbers that contains full information of the manybody quantum system. A standard method of representing $C_{\sigma_1,\ldots\sigma_l\ldots,\sigma_N}$ is as a d^N dimension vector.

Alternatively, $C_{\sigma_1,\ldots\sigma_l\ldots,\sigma_N}$ can be understood as an element of a tensor with rank-N and dimension d^N. This exponential scaling of the dimension of tensor C with the system size N is what makes the study of manybody physics so challenging. To gauge the implications of exponential scaling, consider a quantum system of $N = 300$ spin-1/2 particles. The hilbert space dimension for this system is 2^{300}, which significantly surpasses the estimated total number of atoms in the observable universe [96]. Therefore, dealing with many-body problems within this representation becomes unattainable beyond a few tens given the current limitations of computational resources[67, 68]. Another notable constraint of this representation is its inability to access the entanglement properties of the system directly. Given that entanglement is a defining characteristic that separates a quantum system from a classical one [97, 98, 99] and is a quantifiable resource [100], it is reasonable to anticipate that a good representation of a quantum state should provide insights into entanglement features.

Although the dimension of the Hilbert space scales exponentially with the system size, it is imperative to recognize that many physically relevant states are situated within a small subset of this vast space. Notably, for short-range interacting systems with a gap in the energy spectrum, it has been observed that the ground state adheres to area laws [101, 102, 103, 104, 105, 106, 107, 108]. This suggests that the entanglement entropy of a spatial region within a system is proportional to its area rather than its volume [106]. Remarkably, the states that conform to these area laws constitute a minuscule fraction of the Hilbert space. Therefore, it is sufficient to focus our search on the ground state of gapped, short-range interacting quantum systems within this infinitesimal corner of the Hilbert space. Moreover, this corner of the Hilbert space is most appropriately parameterized by a family of tensor network states [109, 75, 76] which allows for smooth manipulation of the relevant degrees of freedom within renormalization group (RG) methods.

A primitive illustration of the utility of re-configuring the manybody wavefunction into a tensor network ansatz can be seen in the Schmidt decomposition of the state defined in Equation 2.7. We begin by bipartitioning the system into two two halves, A and B and do the SVD of the state,

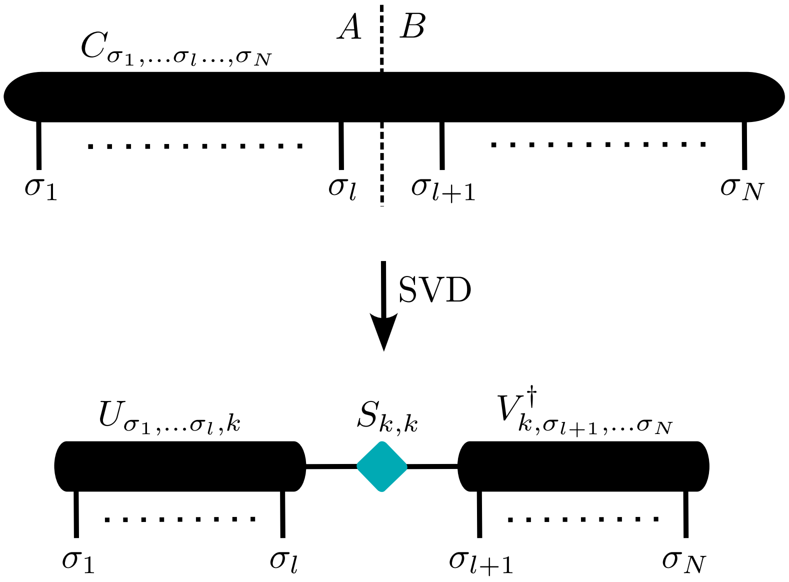

Figure 2.5: Singular value decomposition of a manybody state tensor C with bipartition at site l.

$$|\psi\rangle = \sum_{\sigma_l,\ldots\sigma_l,\sigma_{l+1}\ldots\sigma_N} C_{(\sigma_1,\ldots\sigma_l),(\sigma_{l+1}\ldots,\sigma_N)}(|\sigma_1\rangle \otimes \ldots |\sigma_l\rangle) \otimes (|\sigma_{l+1}\rangle \ldots \otimes |\sigma_N\rangle) \tag{2.8a}$$

$$= \sum_{\sigma,\tilde{\sigma}} C_{\sigma,\tilde{\sigma}} \left|\sigma\right\rangle_A \otimes \left|\tilde{\sigma}\right\rangle_B \tag{2.8b}$$

$$= \sum_{\sigma,\tilde{\sigma}} \sum_{k=1}^{D} U_{\sigma,k} S_{k,k} V^{\dagger}_{k,\tilde{\sigma}} \left|\sigma\right\rangle_A \otimes \left|\tilde{\sigma}\right\rangle_B \tag{2.8c}$$

$$= \sum_{k=1}^{D} \lambda_k \left|k\right\rangle_A \otimes \left|k\right\rangle_B \tag{2.8d}$$

where, $D = \min\Big(\prod_{i=1}^{l} D_i^C, \prod_{i=l+1}^{N} D_i^C\Big)$ and $\lambda_k = S_{k,k}$ are the singular values in descending order ($\lambda_k \leq \lambda_{k+1}, \forall k$). $\left|k\right\rangle_A = U_{\sigma,k} \left|\sigma\right\rangle_A$ and $\left|k\right\rangle_B = V^{\dagger}_{\tilde{\sigma},k} \left|\tilde{\sigma}\right\rangle_B$ are orthonormal bases of region A and B. The representation in equation 2.8 provides us information about the entanglement properties of the state ψ. If $k = 1$, the two bipartitions have no entanglement whereas $k > 1$ implies the two bipartitions are entangled. We can also calculate the reduced density matrices of each bipartitions,

$$\hat{\rho}_A = \mathrm{Tr}_B[|\psi\rangle\langle\psi|] = \sum_{k=1}^{D} \lambda_k^2 |k\rangle_{AA}\langle k| \qquad \hat{\rho}_B = \mathrm{Tr}_A[|\psi\rangle\langle\psi|] = \sum_{k=1}^{D} \lambda_k^2 |k\rangle_{BB}\langle k| \quad (2.9)$$

Furthermore, the state $|\psi\rangle$ is maximally entangled if the reduced density matrix of the bipartition $\hat{\rho}_A$ (or $\hat{\rho}_B$) is maximally mixed, that is, $\lambda_k^2 = 1/D$ [110]. We can also calculate the von Neumann entanglement entropy shared by the bipartitions

$$S_{A|B} = -\mathrm{Tr}[\tilde{\rho}_A \mathrm{log}_2 \tilde{\rho}_A] = -\mathrm{Tr}[\tilde{\rho}_B \mathrm{log}_2 \tilde{\rho}_B] = -\sum_k \lambda_k^2 \mathrm{log}_2 \lambda_k^2 \quad (2.10)$$

Consequently, $S_{A|B}$ is bounded from above and below, $0 \leq S_{A|B} \leq \log_2 D$. From equation 2.10 it is clear that the representation derived in equation 2.8 allows us to truncate the singular values based on the decay behavior of entanglement entropy by capping k by a finite constant value $\chi < D$. The corresponding truncated state,

$$|\psi\rangle \rightarrow |\tilde{\psi}\rangle = \sum_{\sigma,\tilde{\sigma}} \sum_{k=1}^{\chi} \tilde{U}_{\sigma,k} \tilde{S}_{k,k} \tilde{V}^{\dagger}_{k,\tilde{\sigma}} |\sigma\rangle_A \otimes |\tilde{\sigma}\rangle_B \quad (2.11)$$

is the optimal rank-χ approximation of $|\psi\rangle$ for the given bipartition $A|B$ [111].This observation suggests the feasibility of approximating the quantum many-body wavefunction as a network of tensors with an overall dimension that does not exhibit exponential scaling with the system size and where local entanglement properties are conveniently accessible.

2.3 Matrix product state (MPS)

Any arbitrary quantum manybody state of form 2.7 can be decomposed into one dimensional network of tensors called the matrix product state [112, 113, 75]. The procedure involves iteratively decomposing the state tensor C from one of the ends. The full procedure is shown in figure 2.6 a. We begin from the left edge by reshaping $C_{\sigma_1,\ldots\sigma_l\ldots,\sigma_N}$ into a $d \times d^{N-1}$ matrix $C_{\sigma_1,(\sigma_2,\ldots,\sigma_N)}$. This matrix is decomposed by SVD,

$$C_{\sigma_1,(\sigma_2,\ldots,\sigma_N)} = \sum_{c_1=1}^{d} U_{\sigma_1,c_1} S_{c_1,c_1} V^{\dagger}_{c_1,(\sigma_2,\ldots,\sigma_N)} = \sum_{c_1=1}^{d} A^{\sigma_1}_{c_0,c_1} C_{c_1,\sigma_2,\ldots,\sigma_N}. \quad (2.12)$$

In equation 2.12 U_{σ_1,c_1} is reshaped as rank-3 tensor $A^{\sigma_1}_{c_0,c_1}$ by introducing a fictitious index c_0 and S_{c_1,c_1} and $V^{\dagger}_{c_1,(\sigma_2,\ldots,\sigma_N)}$ are contracted into tensor $C_{c_1,\sigma_2,\ldots,\sigma_N}$. This

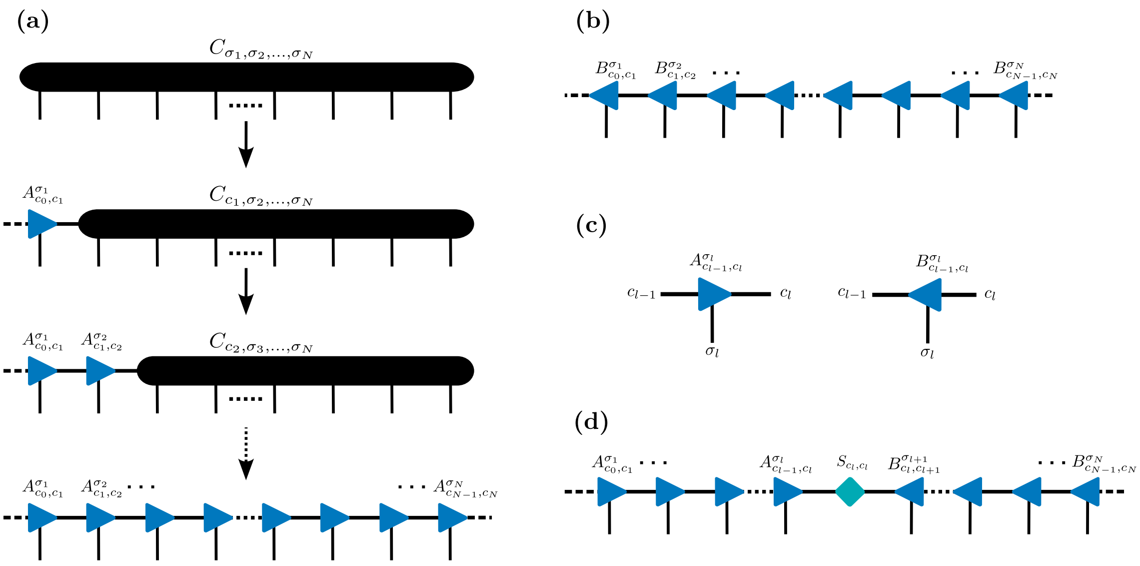

Figure 2.6: (a) Iterative decomposition of coefficient tensor C into left canonical MPS. **(b)** C decomposed as right canonical MPS. (c) Notation convention for tensors A and B. d C decomposed as mixed canonical MPS.

is followed by reshaping the tensor $C_{c_1,\sigma_2,\ldots,\sigma_N}$ into matrix $C_{(c_1,\sigma_2)(\sigma_3,\ldots,\sigma_N}$ and its subsequent SVD,

$$C_{(c_1,\sigma_2),(\sigma_3,\ldots,\sigma_N)} = \sum_{c_2=1}^{d^2} U_{c_1,\sigma_2,c_2} S_{c_2,c_2} V^{\dagger}_{c_2,(\sigma_3,\ldots,\sigma_N)} = \sum_{c_2=1}^{d^2} A^{\sigma_2}_{c_1,c_2} C_{c_2,\sigma_3,\ldots,\sigma_N}, \tag{2.13}$$

where $U_{c_1,\sigma_2,c_2} \rightarrow A^{\sigma_2}_{c_1,c_2}$ and $S_{c_2,c_2}V^{\dagger}_{c_2,(\sigma_3,\ldots,\sigma_N)} \rightarrow C_{c_2,\sigma_3,\ldots,\sigma_N}$. This procedure is iteratively repeated for all sites $l = 1, 2, \ldots, N$ to obtain the full decomposition of the state tensor of rank-N as a product of N rank-3 tensors,

$$C_{\sigma_1,\ldots\sigma_l\ldots,\sigma_N} = \sum_{c_1\ldots c_l\ldots c_N} A^{\sigma_1}_{c_0,c_1} \ldots A^{\sigma_l}_{c_{l-1},c_l} \ldots A^{\sigma_N}_{c_{N-1},c_N}. \tag{2.14}$$

In tensor $A^{\sigma_l}_{c_{l-1},c_l}$, the index σ_l is referred to as the physical index, representing the physical dimension of the Hilbert space of a single particle, whereas c_{l-1} and c_l are auxiliary indices that contain information regarding the entanglement content of the state. Unless otherwise specified, we adhere to the notation convention depicted in Figure 2.6(c) for the tensor network diagram of tensor A. In Equation 2.14, the constituent tensors have dimensions of $1 \times d \times d, \ldots, d^{N/2-1} \times d \times d^{N/2}, d^{N/2} \times d \times d^{N/2-1}, \ldots, d \times d \times 1$, respectively. This demonstrates exponential scaling with respect to the system size N. Each A tensor is constructed by reshaping the U matrices of the singular value decomposition (SVD), which satisfies $U^\dagger U = \mathbb{I}$. Consequently, it exhibits the following property,

$$\begin{align} U^\dagger U = \mathbb{I} \rightarrow \delta_{c_l', c_l} &= \sum_{c_{l-1},\sigma_l} \left(U_{(c_{l-1},\sigma_l),c_l}\right)^\dagger U_{(c_{l-1},\sigma_l),c_l} \tag{2.15a} \\ &= \sum_{c_{l-1},\sigma_l} U^\dagger_{c_l',(c_{l-1},\sigma_l)} U_{(c_{l-1},\sigma_l),c_l} \tag{2.15b} \\ &= \sum_{c_{l-1},\sigma_l} A^{\sigma_l \dagger}_{c_l', c_{l-1}} A^{\sigma_l}_{c_{l-1},c_l}. \tag{2.15c} \end{align}$$

The tensors A are called left normalized and the MPS representation in equation 2.14 is called left canonical. Figure 2.7 (a) shows the tensor diagram corresponding to the equation 2.15.

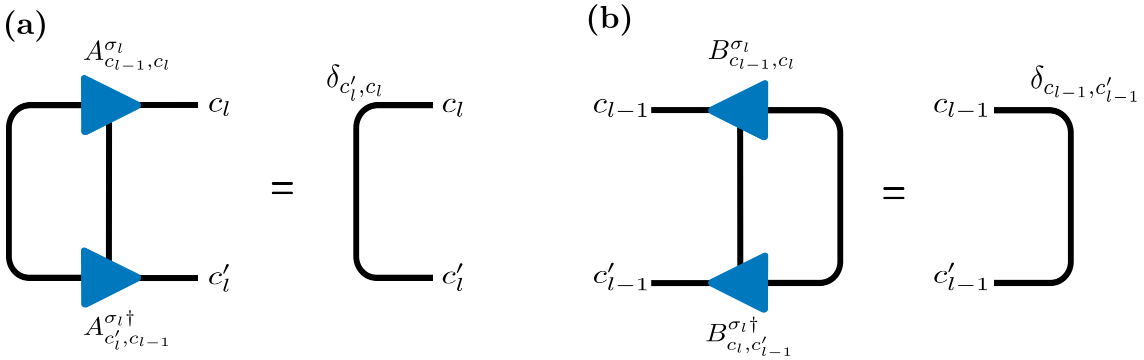

Figure 2.7: The left (a) and right canonical (b) conditions for MPS tensors A and B.

Alternatively, we can start the decomposition from the right edge and iteratively move towards the left as follows,

$$\begin{aligned}
C_{\sigma_1,\ldots,\sigma_N} &= C_{(\sigma_1,\ldots\sigma_l\ldots,\sigma_{N-1}),\sigma_N} && \text{(2.16a)}\\
&= \sum_{c_{N-1}=1}^{d} U_{(\sigma_1,\ldots,\sigma_{N-1}),c_{N-1}} S_{c_{N-1},c_{N-1}} V^{\dagger}_{c_{N-1},\sigma_N,c_N} && \text{(2.16b)}\\
&= \sum_{c_{N-1}=1}^{d} C_{(\sigma_1,\ldots,\sigma_{N-2}),(\sigma_{N-1},c_{N-1})} B^{\sigma_N}_{c_{N-1},c_N} && \text{(2.16c)}\\
&= \sum_{c_{N-1}=1}^{d} \sum_{c_{N-2}=1}^{d^2} U_{(\sigma_1,\ldots,\sigma_{N-2}),c_{N-2}} S_{c_{N-2},c_{N-2}} V^{\dagger}_{c_{N-2},\sigma_{N-1},c_{N-1}} B^{\sigma_N}_{c_{N-1},c_N} && \text{(2.16d)}\\
&= \sum_{c_{N-1}=1}^{d} \sum_{c_{N-2}=1}^{d^2} C_{(\sigma_1,\ldots,\sigma_{N-3}),(\sigma_{N-2},c_{N-2})} B^{\sigma_{N-1}}_{c_{N-2},c_{N-1}} B^{\sigma_N}_{c_{N-1},c_N} && \text{(2.16e)}\\
&\ldots && \text{(2.16f)}\\
&= \sum_{c_1,\ldots c_l\ldots,c_N} B^{\sigma_1}_{c_0,c_1} \ldots B^{\sigma_l}_{c_{l-1},c_l} \ldots B^{\sigma_N}_{c_{N-1},c_N} && \text{(2.16g)}
\end{aligned}$$

Since each B tensors are built by reshaping $V^\dagger$ matrices that satisfy $VV^\dagger = \mathbb{I}$, they are right-normalized,

$$\sum_{c_l,\sigma_l} B^{\sigma_l}_{c_{l-1},c_l} B^{\sigma_l\dagger}_{c_l,c'_{l-1}} = \delta_{c_{l-1},c'_{l-1}} \tag{2.17}$$

and the state represented as right-normalized MPS is called right canonical. Figure 2.6 (b) shows the tensor network diagram for right canonical MPS. We can also decompose the state tensor into a mixed canonical MPS,

$$C_{\sigma_1,\ldots\sigma_l\ldots,\sigma_N} = \sum_{c_1\ldots c_l\ldots c_N} A^{\sigma_1}_{c_0,c_1} \ldots A^{\sigma_l}_{c_{l-1},c_l} S_{c_l,c_l} B^{\sigma_{l+1}}_{c_l,c_{l+1}} \ldots B^{\sigma_N}_{c_{N-1},c_N}. \tag{2.18}$$

This is accomplished by initially left-normalizing the first l sites from the left, and subsequently right-normalizing the remaining sites from the right. The site l is known as the orthogonality center. The tensor diagram for the mixed canonical representation is shown in Figure 2.6 (d). This decomposition retains the state in the Schmidt decomposition,

$$|\psi\rangle = \sum_{c_l=1}^{D} \lambda_{c_l} \left|c_l\right\rangle_A \otimes \left|c_l\right\rangle_B, \tag{2.19}$$

where $D = \min(d^l, d^{N-l}) \sim O(d^N)$, $\lambda_{c_l} = S_{c_l,c_l}$ are the singular values in descending order and,

$$|c_l\rangle_A = \sum_{\sigma_1\ldots\sigma_l} \sum_{c_1\ldots c_{l-1}} A^{\sigma_1}_{c_0,c_1} \ldots A^{\sigma_l}_{c_{l-1},c_l} \qquad |c_l\rangle_B = \sum_{\sigma_{l+1}\ldots\sigma_N} \sum_{c_{l+1}\ldots c_N} B^{\sigma_{l+1}}_{c_l,c_{l+1}} \ldots B^{\sigma_N}_{c_{N-1},c_N}. \tag{2.20}$$

The bipartite states $|c_l\rangle_A$ and $|c_l\rangle_B$ are orthonormal by construction.

The decomposition of state tensor C into MPS is exact, and the constituent tensors exhibit exponential scaling with respect to the system size. However, when we represent the state in a mixed canonical form, as indicated in Equation 2.18, bipartite entanglement becomes readily accessible, as reflected in the singular values $\{\lambda_{c_l}\}$ (refer to equation 2.10). This enables us to employ approximate the state by truncating the spectrum by retaining only the χ largest values,

$$|\psi\rangle \to |\tilde{\psi}\rangle = \sum_{c_l=1}^{\chi} \lambda_{c_l} |c_l\rangle_A \otimes |c_l\rangle_B \,. \tag{2.21}$$

Consequently the error behind this truncation procedure is quantified by summing over all the discarded singular values,

$$\epsilon_l = \sum_{c_l=\chi+1}^{D} \lambda^2_{c_l}, \tag{2.22}$$

Here, we reject the exponential portion of the singular values. This truncation procedure is central to all renormalization group schemes and, consequently, underpins numerous tensor network based algorithms for simulating manybody systems.

2.3.1 Matrix product state for $1\mathcal{D}$ system

The matrix product state is inherently dense, implying that a typical quantum state, as described in Eq. 2.7, can be expressed as an MPS by sufficiently increasing the dimension of its constituent tensors. For a generic many-body state, we observed that the dimensions of these constituent tensors increase exponentially with the system size. Therefore, it is crucial to acknowledge that MPS serves as an effective representation exclusively for the states for which the approximation technique defined in Eq. 2.19 can be employed without incurring substantial errors, thereby capping the auxiliary index dimensions with a number that is independent of system size. This has been shown to be true for the ground states of short-range 1D Hamiltonians away from criticality [107, 114] and more recently extended to long-range interacting systems with locally bounded interactions [115].

The intuitive argument behind the efficiency of MPS ansatz to represent local gapped Hamiltonian follows from the area laws[101, 102, 103, 104, 105, 106, 107, 108] which state that the bipartite entanglement entropy of the locally interacting Hamiltonian away from criticality is proportional to its area, $S_{A|B} \propto N^{\mathcal{D}-1}$, where $\mathcal{D}$ is the geometric dimension of the system. This suggests $S_{A|B} \sim$ const in one dimension, whereas in higher dimensions, it diverges as a power law of N. In one dimensional critical systems, we observe logarithmic divergence, that is, $S_{A|B} \propto \log_2 N$ [107]. Considering the case of a maximally entangled state, the von Neumann bipartite entanglement entropy is $S^{\max}_{A|B} = \log_2 D$, where D is the dimension of the reduced density matrix $\hat{\rho}_A$ (or $\hat{\rho}_B$) defined in equation 2.9. In the language of mixed canonical MPS, encoding an entanglement $S^{\max}_{A|B}$ corresponding to bipartition $A|B$ at site l suffices to have an auxiliary index of dimension $2^{S^{\max}_{A|B}}$. Following area law $S_{A|B} \sim$ const for one dimensional therefore the auxiliary index dimension required to encode entanglement for such states is independent of the system size and capped from above. Alternatively, there exists an integer $\chi_{\max}$ which is independent of N such that the truncation procedure defined in equation 2.21 incur an error of the machine precision order. For a two-dimensional system following area laws, $S_{A|B} \sim N$. Consequently, the auxiliary index dimension necessary to encode the entanglement scales exponentially $\chi_{\max} \sim 2^N$. For critical systems, this scaling is polynomial $\chi_{\max} \sim N^{\text{const}}$. For this reason, MPS is a good ansatz in one dimension, but not in higher dimensions. For a mathematically rigorous approach refer to the following articles, [109, 114].

2.4 Matrix product operator

Now that the quantum manybody state is expressed as MPS we need to express the quantum operators in a compatible representation. Such a representation is called a matrix product operator (MPO) [116, 117, 118, 119, 120] and any arbitrary operator can be expressed expressed as an MPO,

$$\hat{O} = \sum_{\boldsymbol{\sigma}} \sum_{\boldsymbol{\sigma'}} C_{\boldsymbol{\sigma}\boldsymbol{\sigma'}} |\boldsymbol{\sigma}\rangle \langle\boldsymbol{\sigma'}| \tag{2.23a}$$

$$= \sum_{\boldsymbol{\sigma}} \sum_{\boldsymbol{\sigma'}} O^{\sigma'_1,\sigma_1} \ldots O^{\sigma'_l,\sigma_l} \ldots O^{\sigma'_N,\sigma_N} |\boldsymbol{\sigma}\rangle \langle\boldsymbol{\sigma'}| \tag{2.23b}$$

where, O^{σ_l,σ'_l} is a compact form for $O^{\sigma_l,\sigma'_l}_{n_{l-1},n_l}$ which is a rank-4 tensor. The σ_l and σ'_l are the physical indices whereas n_{l-1} and n_l are the auxiliary indices. Figure 2.8 (a) shows the tensor network diagram of a generic MPO. With operators represented as MPO, its application to state represented as MPS is straightforward,

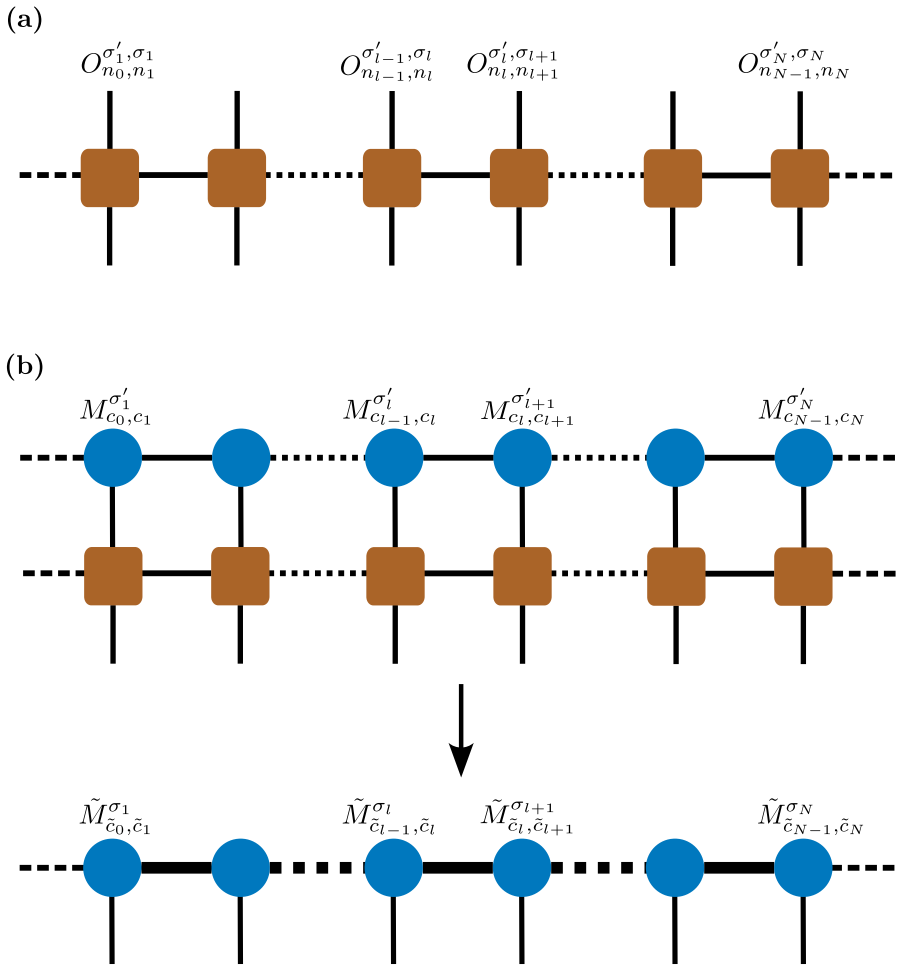

Figure 2.8: (a) representation of generic operator as MPO. (b) application of MPO on MPS, the output is a MPS with increased bond dimension.

$$\hat{O}\,|\psi\rangle = \sum_{\boldsymbol{\sigma},\boldsymbol{\sigma'}}\sum_{\boldsymbol{\sigma''}} O^{\sigma'_1,\sigma_1}\dots O^{\sigma'_l,\sigma_l}\dots O^{\sigma'_N,\sigma_N} M^{\sigma''_1}\dots M^{\sigma''_l}\dots M^{\sigma''_N}\,|\boldsymbol{\sigma}\rangle\,\langle\boldsymbol{\sigma'}|\boldsymbol{\sigma''}\rangle \tag{2.24a}$$

$$= \sum_{\boldsymbol{\sigma},\boldsymbol{\sigma'}} O^{\sigma'_1,\sigma_1}\dots O^{\sigma'_l,\sigma_l}\dots O^{\sigma'_N,\sigma_N} M^{\sigma'}\dots M^{\sigma'_l}\dots M^{\sigma'_N}\,|\boldsymbol{\sigma}\rangle \tag{2.24b}$$

$$= \sum_{\boldsymbol{\sigma},\boldsymbol{\sigma'}}\sum_{\boldsymbol{n},\boldsymbol{c}} O^{\sigma'_1,\sigma_1}_{n_0,n_1} M^{\sigma'_1}_{c_0,c_1}\dots O^{\sigma'_l,\sigma_l}_{n_{l-1},n_l} M^{\sigma'_l}_{c_{l-1},c_l}\dots O^{\sigma'_N,\sigma_N}_{n_{N-1},n_N} M^{\sigma'_N}_{c_{N-1},c_N}\,|\boldsymbol{\sigma}\rangle \tag{2.24c}$$

$$= \sum_{\boldsymbol{\sigma}}\sum_{\tilde{\boldsymbol{c}}} \tilde{M}^{\sigma_1}_{\tilde{c}_0,\tilde{c}_1}\dots \tilde{M}^{\sigma_l}_{\tilde{c}_{l-1},\tilde{c}_l}\dots \tilde{M}^{\sigma_N}_{\tilde{c}_{N-1},\tilde{c}_N}\,|\boldsymbol{\sigma}\rangle \tag{2.24d}$$

where, $\tilde{M}^{\sigma_l}_{\tilde{c}_{l-1},\tilde{c}_l}$ is a rank-3 tensor obtained by contracting $O^{\sigma_l',\sigma_l}_{n_{l-1},n_l}$ with $M^{\sigma_l'}_{c_{l-1},c_l}$ along their shared physical index σ_l. The resulting MPS has dimensions $\dim(M) = dD^2D_O^2$, where D is the dimension of the auxiliary indices of the input tensor M and D_O is the dimension of the auxiliary index of MPO. Figure 2.8 (b) illustrates the corresponding tensor network diagram for Equation 2.24, with a thicker horizontal link in the output MPS denoting an increased dimension of the auxiliary index.

2.4.1 Hamiltonians as MPO

The existence of a MPO representation of an arbitrary operator is guaranteed but searching for an exact decomposition of a complex operator such as a manybody Hamiltonian is exponentially complex [121] task. However, there exists a recipe based on weighted finite state automaton that lets us map a local manybody Hamiltonian into MPO [119, 122],

$$\hat{H} \to \hat{O}^1 \ldots \hat{O}^l \ldots \hat{O}^N \tag{2.25}$$

where, $\hat{O}^l = \sum_{\sigma_l,\sigma_l'} O^{\sigma_l',\sigma_l} \left|\sigma_l\right\rangle \left\langle\sigma_l'\right|$ is the operator valued matrix that acts on the local Hilbert space at site l. This approach runs in opposite direction, rather than decomposing $\hat{H}$ we find a finite state automaton that generates its correct factorization.

The finite state automaton corresponding to short range spin Hamiltonians are rather straight forward. Consider a magnetization operator along z direction expanded in full Hilbert space,

$$h\sum_{l=1}^{N} \hat{z}_l = \sum_{i+1+j=N} \mathbb{I}^{\otimes i} \otimes h\hat{z} \otimes \mathbb{I}^{\otimes j}, \quad \forall\, i,j \in [0,\mathbb{Z}^+], \tag{2.26}$$

where $\hat{z} = \hat{\sigma_z}/2$, and $\hat{\sigma_z}/2$ is the Pauli matrix along z-axis. Equation 2.26 is a sum of tensor product of strings of identity matrices at all but one site. Such strings can be constructed by moving from right to left putting $\mathbb{I}$ matrix in all but one specified site where we put $\hat{z}$. During this process we encounter two distinct conditions, **1**: where all the matrices on the right are $\mathbb{I}$, and **2**: where there is one $\hat{z}$ matrix on right and $\mathbb{I}$ matrix on all other sites. The transition from condition **1** to **2** takes place by putting $\hat{z}$ matrix at a specified site. The finite state automaton corresponding to this operator is shown in figure 2.9 a. We start from the rightmost edge by adding $\mathbb{I}$ on each site, this signifies the trivial transition **1** → **1**. Adding $\hat{z}$ on a specified site signifies the transition **1** → **2**. This is followed by adding $\mathbb{I}$ on remaining sites which signifies another trivial transition **2** → **2**. The bulk matrix corresponding to the given finite state automaton can be constructed in a straightforward manner,

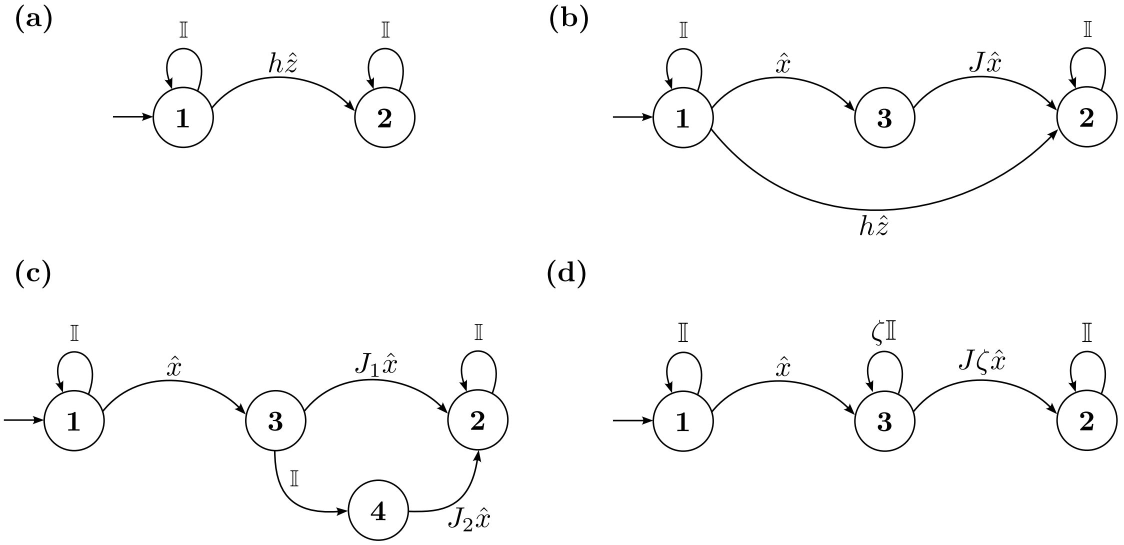

Figure 2.9: Finite state automaton representation, (a) magnetization operator along z axis, (b) transverse field Ising Hamiltonian, (c) Hamiltonian with both nearest and next nearest neighbor $\hat{x}\hat{x}$ interaction, (d) Hamiltonian with exponentially decaying $\hat{x}\hat{x}$ interaction.

$$\hat{O}^l = \begin{bmatrix} \mathbb{I} & 0 \\ h\hat{z} & \mathbb{I} \end{bmatrix}. \tag{2.27}$$

We put zero at all the forbidden transition, here **2** → **1** is a forbidden transition. For a finite system with open boundary condition we have a row and column vectors at the left and right edges respectively,

$$\hat{O}^1 = \begin{bmatrix} h\hat{z} & \mathbb{I} \end{bmatrix}, \qquad \hat{O}^N = \begin{bmatrix} \mathbb{I} \\ h\hat{z} \end{bmatrix}. \tag{2.28}$$

Hamiltonian with higher order interactions can be written by adding intermediate states in the finite state automaton. Figure 2.9 (b) shows the finite state automaton for nearest neighbor transverse field Ising Hamiltonian,

$$J\sum_{l=1}^{N-1} \hat{x}_l\hat{x}_{l+1} + h\sum_{l=1}^{N} \hat{z}_l = \sum_{i+2+j=N} \mathbb{I}^{\otimes i} \otimes \hat{x} \otimes J\hat{x} \otimes \mathbb{I}^{\otimes j} + \sum_{i+1+j=N} \mathbb{I}^{\otimes i} \otimes h\hat{z} \otimes \mathbb{I}^{\otimes j}, \tag{2.29}$$

where $\hat{x} = \hat{\sigma_x}/2$, and $\hat{\sigma_x}/2$ is the Pauli matrix along x-axis. To pass from state **1** to **2** we now need to pass from an intermediate state **3**: where there is one $\hat{x}$ on the immediate right and left. The corresponding matrices are,

$$\hat{O}^l = \begin{bmatrix} \mathbb{I} & 0 & 0 \\ \hat{x} & 0 & 0 \\ h\hat{z} & J\hat{x} & \mathbb{I} \end{bmatrix}, \ \hat{O}^1 = \begin{bmatrix} h\hat{z} & J\hat{x} & \mathbb{I} \end{bmatrix}, \hat{O}^N = \begin{bmatrix} \mathbb{I} \\ \hat{x} \\ h\hat{z} \end{bmatrix}, \tag{2.30}$$

$\forall\, l \in \{2, \dots N\}$. Hamiltonian with longer range interaction can be constructed by further adding extra intermediate states. Figure 2.9 (c) shows the finite state automaton for Hamiltonian with both nearest and next nearest neighbor interactions,

$$J_1 \sum_{l=1}^{N-1} \hat{x}_l \hat{x}_{l+1} + J_2 \sum_{l=1}^{N-2} \hat{x}_l \hat{x}_{l+2} = \sum_{i+2+j=N} \mathbb{I}^{\otimes i} \otimes \hat{x} \otimes J_1 \hat{x} \otimes \mathbb{I}^{\otimes j} + \sum_{i+3+j=N} \mathbb{I}^{\otimes i} \otimes \hat{x} \otimes \mathbb{I} \otimes J_2 \hat{x} \otimes \mathbb{I}^{\otimes j}. \tag{2.31}$$

The corresponding matrices are,

$$\hat{O}^l = \begin{bmatrix} \mathbb{I} & 0 & 0 & 0 \\ \hat{x} & 0 & 0 & 0 \\ 0 & \mathbb{I} & 0 & 0 \\ 0 & J_1\hat{x} & J_2\hat{x} & \mathbb{I} \end{bmatrix}, \ \hat{O}^1 = \begin{bmatrix} 0 & J_1\hat{x} & J_2\hat{x} & \mathbb{I} \end{bmatrix}, \hat{O}^N = \begin{bmatrix} \mathbb{I} \\ \hat{x} \\ 0 \\ 0 \end{bmatrix}, \tag{2.32}$$

$\forall\, l \in \{2, \dots N\}$. This suggests that for longer-ranged interacting hamiltonian the size of the matrix $\hat{O}^l$ scales linearly with the strength of interaction. Hamiltonians with exponentially decaying long range interaction is a special case that has a compact finite state automaton. Such Hamiltonian can be written as,

$$J \sum_{l,r} e^{-\frac{r}{\xi}} \hat{x}_l \hat{x}_{l+r} = \sum_{i+1+r+j=N} \mathbb{I}^{\otimes i} \otimes \hat{x} \otimes [\zeta \mathbb{I}]^{\otimes r-1} \otimes J\zeta\hat{x} \otimes \mathbb{I}^{\otimes j}, \tag{2.33}$$

where $\zeta = e^{1/\xi}$. Figure 2.9 (d) shows the finite state automaton corresponding to this Hamiltonian. The corresponding matrices are,

$$\hat{O}^l = \begin{bmatrix} \mathbb{I} & 0 & 0 \\ \hat{x} & \zeta\mathbb{I} & 0 \\ 0 & J\zeta\hat{x} & \mathbb{I} \end{bmatrix}, \ \hat{O}^1 = \begin{bmatrix} 0 & J\zeta\hat{x} & \mathbb{I} \end{bmatrix}, \hat{O}^N = \begin{bmatrix} \mathbb{I} \\ \hat{x} \\ 0 \end{bmatrix}, \tag{2.34}$$

$\forall\, l \in \{2, \dots N\}$.

We finally arrive to the Hamiltonian central to this thesis, long range interacting Hamiltonian with power-law decaying interaction. Unlike exponentially decaying interaction shown in equation 2.33 there is no compact finite state automaton

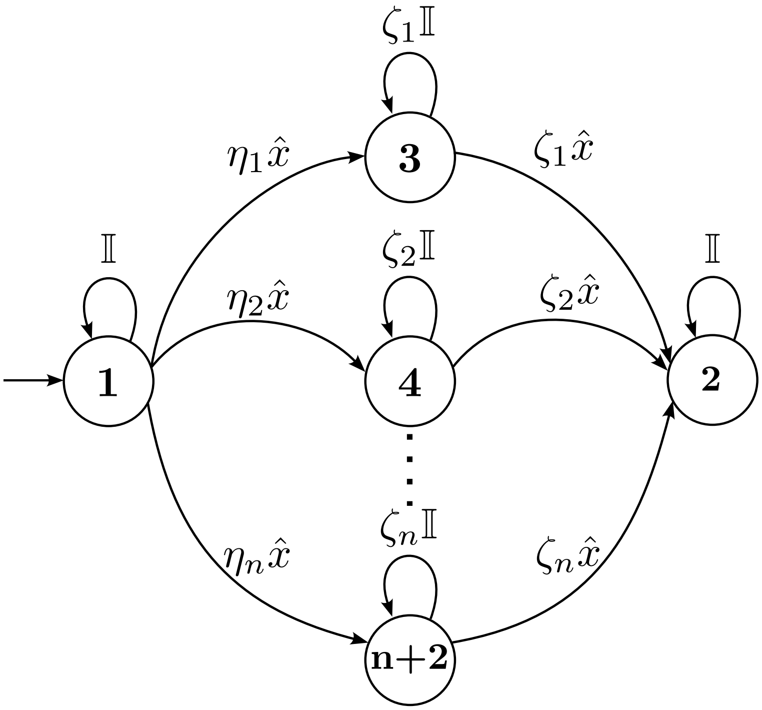

Figure 2.10: Finite state automaton representation of long range Hamiltonian with inverse power law interaction.

representation for power law decaying interaction. However, we can get a good approximation of the inverse power law with the sum of limited number of exponentials [118, 123, 120],

$$\frac{J}{r^{\alpha}} \approx \sum_{k=1}^{n} \eta_k \zeta_k^r, \tag{2.35}$$

where $n \ll N$. The long range Hamiltonian can now be approximated as

$$J \sum_{l,r} \frac{\hat{x}_l \hat{x}_{l+r}}{r^{\alpha}} = \sum_{i+1+r+j=N} \sum_{k=1}^{n} \eta_k \zeta_k^r \ \mathbb{I}^{\otimes i} \otimes \hat{x} \otimes \mathbb{I}^{\otimes r-1} \otimes \hat{x} \otimes \mathbb{I}^{\otimes j}. \tag{2.36}$$

The finite state automaton representation for this Hamiltonian is shown in figure 2.10 which is similar to the one for exponentially decaying Hamiltonian but with n independent paths going from $\mathbf{1} \to \mathbf{2}$. The corresponding matrices are,

$$\hat{O}^l = \begin{bmatrix} \mathbb{I} & 0 & \dots & 0 & 0 \\ \eta_1\hat{x} & \zeta_1\mathbb{I} & \dots & 0 & 0 \\ \eta_2\hat{x} & 0 & \zeta_2\mathbb{I} & \dots & 0 \\ \vdots & \vdots & \vdots & \vdots & \\ \eta_n\hat{x} & 0 & \dots & \zeta_n\mathbb{I} & 0 \\ 0 & \zeta_1\hat{x} & \dots & \zeta_n\hat{x} & \mathbb{I} \end{bmatrix} \hat{O}^1 = \begin{bmatrix} 0 & \zeta_1\hat{x} & \dots & \zeta_n\hat{x} & \mathbb{I} \end{bmatrix}, \hat{O}^N = \begin{bmatrix} \mathbb{I} \\ \eta_1\mathbb{I} \\ \eta_2\mathbb{I} \\ \vdots \\ \eta_n\mathbb{I} \\ 0 \end{bmatrix}, \quad (2.37)$$

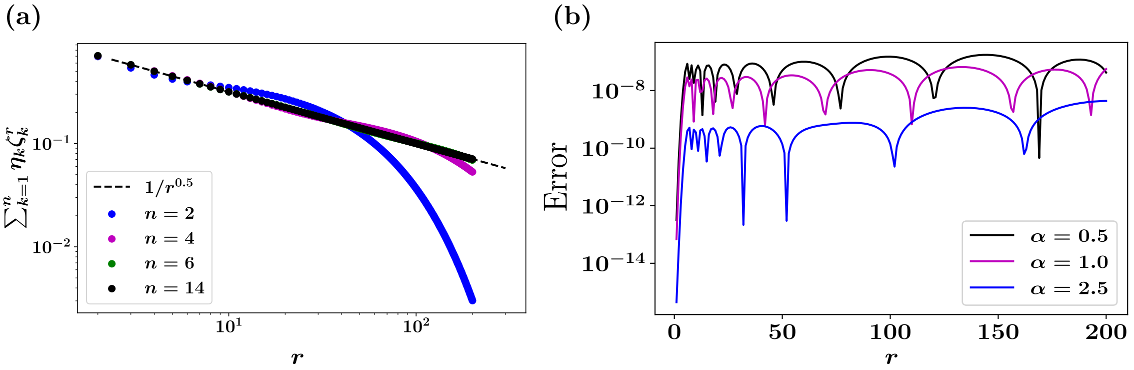

Figure 2.11: (a) Fitting power-law with the sum of exponentials with three increasing number of exponentials. There is no visible difference in the data for $n = 6$ (green scatter plot)and $n = 14$ (black scatter plot). (b) Error in fitting power-law with sum of exponentials in equation 2.35 for different α , $n = 14$, and $0 \le r \le 200$.

The accuracy of this representation depends on how precisely do we represent the power law decaying function as the sum of exponentials in equation 2.35. This is quantified by calculating the absolute error of approximation,

$$\text{Error} = \left| \frac{J}{r^\alpha} - \sum_{k=1}^{n} \eta_k \zeta_k^r \right| \quad (2.38)$$

where the number of exponentials in the sum n determines the precision of fitting. We observe that for system size $N = 200$ the relative error is 10^{-7} or smaller [*cf.* Fig. 2.11] (b) with $n = 14$. We have used $n = 14$ throughout this thesis.

2.5 Matrix product density operator

The matrix product state (MPS) framework can be extended to encompass matrix product density operators (MPDO) [116, 117] to represent mixed states that are

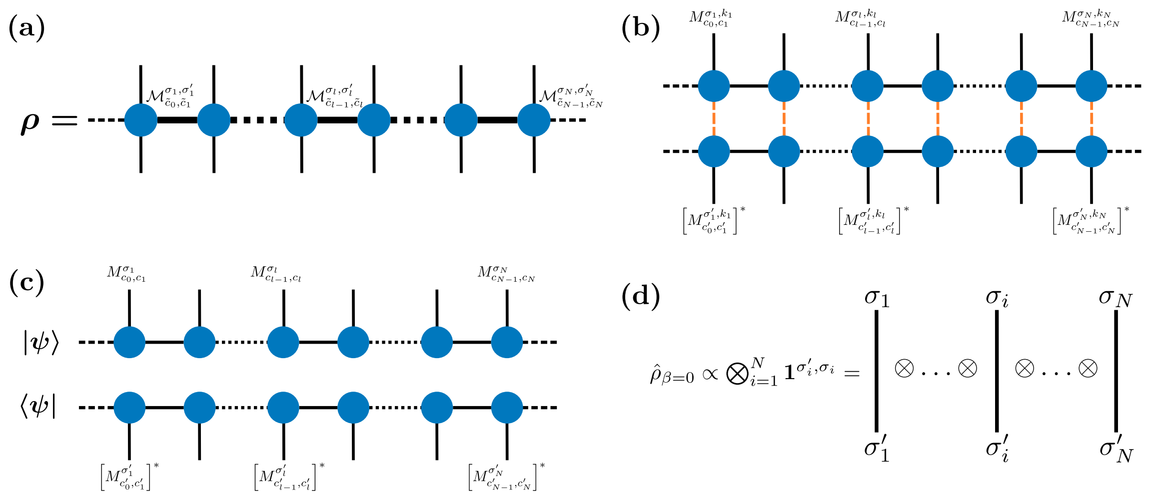

Figure 2.12: Tensor network diagram for: (a) MPDO as MPO, (b) MPDO in locally purified form, (c) projector corresponding to a pure state $|\psi\rangle$, (d) MPDO corresponding to the maximally mixed state.

central to the simulation of dissipative and thermal states. The MPDO ρ of a N particles is defined as;

$$\rho = \sum_{\boldsymbol{\sigma},\boldsymbol{\sigma'}} \mathcal{M}^{\sigma_1',\sigma_1} \ldots \mathcal{M}^{\sigma_l',\sigma_l} \ldots \mathcal{M}^{\sigma_N',\sigma_N} \left|\boldsymbol{\sigma}\right\rangle \left\langle\boldsymbol{\sigma'}\right| . \tag{2.39}$$

where $\mathcal{M}^{\sigma_l',\sigma_l}$ is compact form of rank-4 tensor $\mathcal{M}^{\sigma_l',\sigma_l}_{\tilde{c}_{l-1},\tilde{c}_l}$ has a dimension $d^2 \times \chi_{l-1}^2 \times \chi_l^2$. Figure 2.12 panel (a) shows the tensor network representation of ρ. Each $\mathcal{M}$ can be decomposed as,

$$\mathcal{M}^{\sigma_l',\sigma_l}_{\tilde{c}_{l-1},\tilde{c}_l} = \sum_{k=1}^{d^l} M^{\sigma_l,k_l}_{c_{l-1},c_l} \otimes \left[M^{\sigma_l',k_l}_{c_{l-1}',c_l'}\right]^*, \tag{2.40}$$

where k is called Krauss index and $d^l \leq d\chi_{l-1}\chi_l$ [116]. This representation of MPDO is called locally purified form and is positive by construction [116, 117]. The tensor network representation of ρ in locally purified form is shown in Figure 2.12 panel (b). For pure states $d^l = 1$ and $\mathcal{M}^{\sigma_l',\sigma_l}_{\tilde{c}_{l-1},\tilde{c}_l} = M^{\sigma_l}_{c_{l-1},c_l} \otimes [M^{\sigma_l'}_{c_{l-1}',c_l'}]^*$. In this limit ρ becomes a simple projector $|\psi\rangle\langle\psi|$. The tensor network representation is shown in Figure 2.12 panel (c). In the other extreme the MPDO corresponding to a maximally mixed state is $\mathcal{M}^{\sigma_l',\sigma_l}_{\tilde{c}_{l-1},\tilde{c}_l} = \mathbf{1}^{\sigma_l',\sigma_l}$, where $\mathbf{1}^{\sigma_l',\sigma_l}$ is a $d \times d$ identity matrix.

2.6 Density Matrix Renormalization Group

The Density Matrix Renormalization Group (DMRG) was initially introduced in 1992 [73, 74] as an advancement of existing real-space renormalization group methods. Currently, DMRG is the most precise technique for investigating one dimensional quantum systems with limited computational resources [124, 125, 121]. Although originally formulated in terms of reduced block states, it became evident early on that MPS is the the natural language for DMRG [75, 126]. This framework, in addition to its original purpose of studying the low-energy states of one dimensional quantum systems, enables the exploration of dynamical and dissipative properties. In this thesis, our discussion of DMRG is limited to the iterative ground-state search.

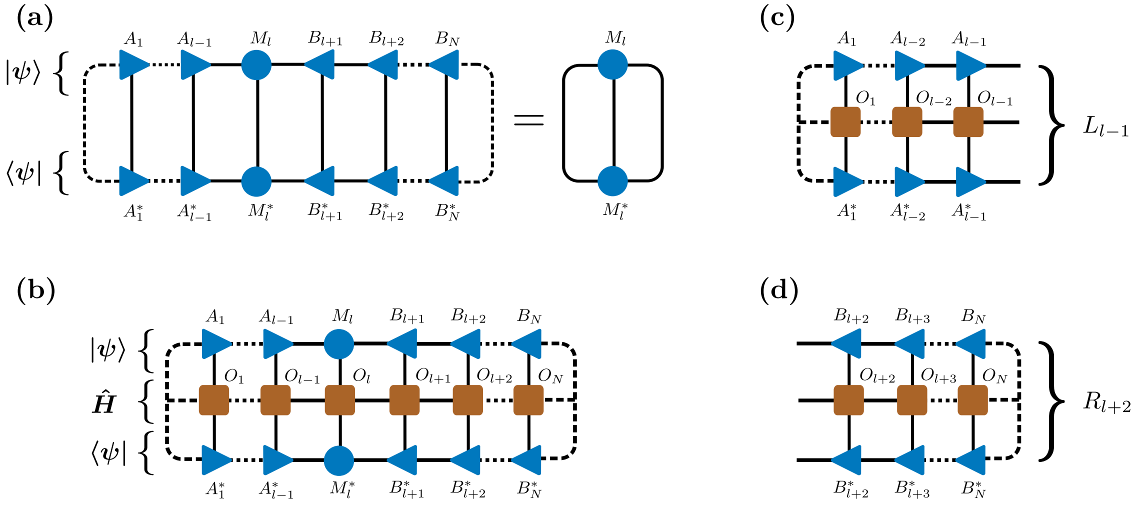

Figure 2.13: tensor network diagram of (a) $\langle\psi|\psi\rangle$, (b) $\langle\psi|\hat{H}|\psi\rangle$, (c) L_{l-1}, and (d) R_{l+1}
.

The primary idea behind DMRG is iterative ground state search by variational minimization of the energy function,

$$E = \frac{\langle\psi|\hat{H}|\psi\rangle}{\langle\psi|\psi\rangle} \tag{2.41}$$

We introduce a Lagrangian function $\mathcal{L} = \langle\psi|\hat{H}|\psi\rangle - \epsilon\langle\psi|\psi\rangle$ and find its extremum by differentiating with a variational parameter that eventually leads to the ground state. We proceed by calculating the parts of Lagrangian $\mathcal{L}$ in tensor representation with $|\psi\rangle$ as MPS and $\hat{H}$ as MPO. The expectation of Hamiltonian $\langle\psi|\hat{H}|\psi\rangle$ can be written as,

$$\begin{aligned}\langle\psi|\hat{H}|\psi\rangle &= L^{n_{l-1}}_{c_{l-1},c'_{l-1}}[M^{\sigma'_l}_{c'_{l-1},c'_l}]^*[B^{\sigma'_{l+1}}_{c'_l,c'_{l+1}}]^* O^{\sigma'_l,\sigma_l}_{n_{l-1},n_l} O^{\sigma'_{l+1},\sigma_{l+1}}_{n_l,n_{l+1}} M^{\sigma_l}_{c_{l-1},c_l} B^{\sigma_{l+1}}_{c_l,c_{l+1}} R^{n_{l+1}}_{c_{l+1},c'_{l+1}} \qquad (2.42a)\\ &= L^{n_{l-1}}_{c_{l-1},c'_{l-1}}[T^{\sigma'_l,\sigma'_{l+1}}_{c'_{l-1},c'_{l+1}}]^* O^{\sigma'_l,\sigma_l}_{n_{l-1},n_l} O^{\sigma'_{l+1},\sigma_{l+1}}_{n_l,n_{l+1}} T^{\sigma_l,\sigma_{l+1}}_{c_{l-1},c_{l+1}} R^{n_{l+1}}_{c_{l+1},c'_{l+1}}. \qquad (2.42b)\end{aligned}$$

We have employed Einsteins summation convention in the equation 2.42. The MPS is assumed to be in a mixed canonical form. Figure 2.13 (b) illustrates the tensor network diagram of $\langle\psi|\hat{H}|\psi\rangle$ and the L and R tensors are shown in figure 2.13 (c) and (d) respectively. In equation 2.42 the second line is derived from first by contracting the M and B tensors along the auxiliary index ; $\sum_{c_l} M^{\sigma_l}_{c_{l-1},c_l} B^{\sigma_{l+1}}_{c_l,c_{l+1}} \to T^{\sigma_l,\sigma_{l+1}}_{c_{l-1},c_{l+1}}$. The overlap term $\langle\psi|\psi\rangle$ can be similarly calculated,

$$\begin{aligned}\langle\psi|\psi\rangle &= \Psi^A_{c_{l-1},c'_{l-1}}[M^{\sigma'_l}_{c'_{l-1},c'_l}]^*[B^{\sigma'_{l+1}}_{c'_l,c'_{l+1}}]^* M^{\sigma_l}_{c_{l-1},c_l} B^{\sigma_{l+1}}_{c_l,c_{l+1}} \Psi^B_{c_{l+1},c'_{l+1}} \qquad (2.43a)\\ &= \Psi^A_{c_{l-1},c'_{l-1}}[T^{\sigma'_l,\sigma'_{l+1}}_{c'_{l-1},c'_{l+1}}]^* T^{\sigma_l,\sigma_{l+1}}_{c_{l-1},c_{l+1}} \Psi^B_{c_{l+1},c'_{l+1}} \qquad (2.43b)\\ &= \delta_{c_{l-1},c'_{l-1}}[T^{\sigma'_l,\sigma'_{l+1}}_{c'_{l-1},c'_{l+1}}]^* T^{\sigma_l,\sigma_{l+1}}_{c_{l-1},c_{l+1}} \delta_{c_{l+1},c'_{l+1}}. \qquad (2.43c)\end{aligned}$$

Figure 2.13 (a) illustrates the tensor network diagram of $\langle\psi|\psi\rangle$. If MPS is in mixed canonical form with orthogonality center at site l then $\Psi^A_{c_{l-1},c'_{l-1}} = \delta_{c_{l-1},c'_{l-1}}$ and $\Psi^B_{c_{l+1},c'_{l+1}} = \delta_{c_{l+1},c'_{l+1}}$ by construction. The tensor network representation of the Lagrangian function enables us to perform an iterative variational ground state. Specifically, we extremize $\mathcal{L}$ with respect to the local two site tensor $[T^{\sigma'_l,\sigma'_{l+1}}]^*$,

$$\frac{\partial\mathcal{L}}{\partial[T^{\sigma'_l,\sigma'_{l+1}}]^*} = 0 \to L^{n_{l-1}}_{c_{l-1},c'_{l-1}} O^{\sigma'_l,\sigma_l}_{n_{l-1},n_l} O^{\sigma'_{l+1},\sigma_{l+1}}_{n_l,n_{l+1}} T^{\sigma_l,\sigma_{l+1}}_{c_{l-1},c_{l+1}} R^{n_{l+1}}_{c_{l+1},c'_{l+1}} - \epsilon\, T^{\sigma_l,\sigma_{l+1}}_{c_{l-1},c_{l+1}} = 0. \qquad (2.44)$$

Equation 2.44 is a generalized eigenvalue problem. This becomes clear by reshaping $L^{n_{l-1}}_{c_{l-1},c'_{l-1}} O^{\sigma'_l,\sigma_l}_{n_{l-1},n_l} O^{\sigma'_{l+1},\sigma_{l+1}}_{n_l,n_{l+1}} R^{n_{l+1}}_{c_{l+1},c'_{l+1}} \to H^{\text{eff}}_{(\sigma_l,\sigma_{l+1},c_{l-1},c_{l+1}),(\sigma'_l,\sigma'_{l+1},c'_{l-1},c'_{l+1})}$ and $T^{\sigma_l,\sigma_{l+1}}_{c_{l-1},c_{l+1}} \to T_{\sigma_l,\sigma_{l+1},c_{l-1},c_{l+1}}$. Equation 2.44 can now be rewritten as,

$$H^{\text{eff}}_{l,l+1} T_{l,l+1} = \epsilon\, T_{l,l+1}. \qquad (2.45)$$

$H^{\text{eff}}_{l,l+1}$ is a $\chi^2 d^2 \times \chi^2 d^2$ dimension Hermitian matrix and $v_{l,l+1}$ is a $\chi^2 d^2$ dimension vector. This local eigenvalue problem can be solved for the ground state T_0 and the corresponding energy ϵ_0. Full diagonalization of equation 2.45 is still an expensive task therefore a cheaper iterative Lanczos-based eigensolver [127, 128] can be used to solve just for the ground state.

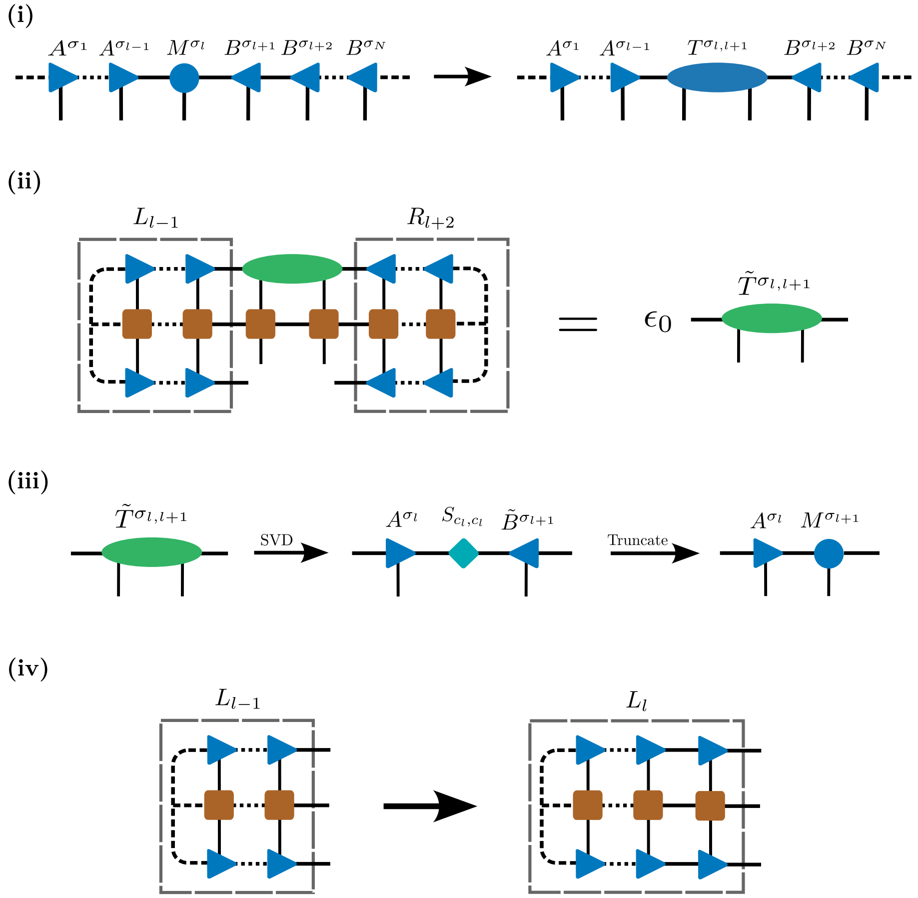

Figure 2.14: Diagrammatic representation of the left to right sweep of the two site DMRG algorithm. (i) initial state in mixed canonical form, (ii) local eigen optimization, (iii) singular value decomposition of the optimized local tensor.

The generalized eigenvalue problem defined in equation 2.44 defined on lattice sites l and $l+1$ allows for an iterative variational ground state search that forms the basis of an optimal DMRG algorithm as follows;

1. Start with a guess state $|\psi\rangle$ in right canonical form. In most cases the guess state can be chosen as a random MPS. Prepare the set of R tensors, $\{R_N, R_{N-1}, \ldots, R_3\}$.
2. Loop l over the list $[1, 2, \ldots, N-1]$,
   (a) Build two-site tensor, $M^{\sigma_l} B^{\sigma_{l+1}} \to T^{\sigma_l,\sigma_{l+1}}$.
   (b) Solve the local eigenvalue problem , $L_{l-1} R_{l+2} \tilde{T}^{\sigma_l,\sigma_{l+1}} = \epsilon_0\, \tilde{T}^{\sigma_l,\sigma_{l+1}}$.

   (c) Decompose $\tilde{T}^{\sigma_l,\sigma_{l+1}} \rightarrow A^{\sigma_l} S \tilde{B}^{\sigma_{l+1}}$. Truncate and renormalize the singular value matrix $S \rightarrow \tilde{S}$ and build $\tilde{S}\tilde{B}^{\sigma_{l+1}} \rightarrow M^{\sigma_{l+1}}$.
   (d) Build $L_{l-1}[A^{\sigma_l'}]^* O^{\sigma_l',\sigma_l} A^{\sigma_l} \rightarrow L_l$. Delete R_{l+2}.

   This iterative procedure is called the left to right DMRG sweep. Figure 2.14 illustrates the corresponding tensor network diagrams. At the end the MPS is in left canonical form.

3. Loop l over the list $[N, N-1, \ldots, 2]$,
   (a) Build two-site tensor, $A^{\sigma_{l-1}} M^{\sigma_l} \rightarrow T^{\sigma_{l-1},\sigma_l}$.
   (b) Solve the local eigenvalue problem , $L_{l-2} R_{l+1} \tilde{T}^{\sigma_{l-1},\sigma_l} = \epsilon_0 \, \tilde{T}^{\sigma_{l-1},\sigma_l}$.
   (c) Decompose $\tilde{T}^{\sigma_{l-1},\sigma_l} \rightarrow \tilde{A}^{\sigma_{l-1}} S B^{\sigma_l}$. Truncate and renormalize the singular value matrix $S \rightarrow \tilde{S}$ and build $\tilde{A}^{\sigma_{l-1}} \tilde{S} \rightarrow M^{\sigma_{l-1}}$.
   (d) Build $[B^{\sigma_l'}]^* O^{\sigma_l',\sigma_l} B^{\sigma_l} R_{l+1} \rightarrow R_l$. Delete L_{l-2}.

   This iterative procedure is called the right to left DMRG sweep. At the end the MPS is in right canonical form.

4. Repeat the left and right sweep alternatively until desired convergence in ground-state energy is achieved.

The algorithm described above is called a two-site DMRG because it entails the optimization of a local eigenvalue problem spanning two adjacent sites. A cheaper but less robust algorithm [129] performs optimization at a single site and is called one-site DMRG [121]. It is important to highlight that the global convergence in DMRG technique is achieved by iteratively optimizing a sequence of local eigenvalue problems. This allows for a relaxation of the convergence criteria for individual local eigenvalue problem while still achieving global convergence.

2.7 Time Dependent Variational Principle

Another significant issue in quantum many-body physics is the real-time evolution of quantum states. One of the earliest algorithms for this purpose is the time-evolving block decimation (TEBD) [77, 78, 130], which is based on the Lie-Trotter-Suzuki splitting of the Hamiltonian in the Schrödinger equation. Although this method is suitable for short-range systems, a version has been proposed for simulating long-range systems [131]. A more recent algorithm that is independent of the range of interaction of the system Hamiltonian is the time-dependent variational principle (TDVP) algorithm [79, 80] which is based on projecting the time-dependent Schrödinger equation into a variational manifold of MPS, followed by numerical integration of the local differential equations.

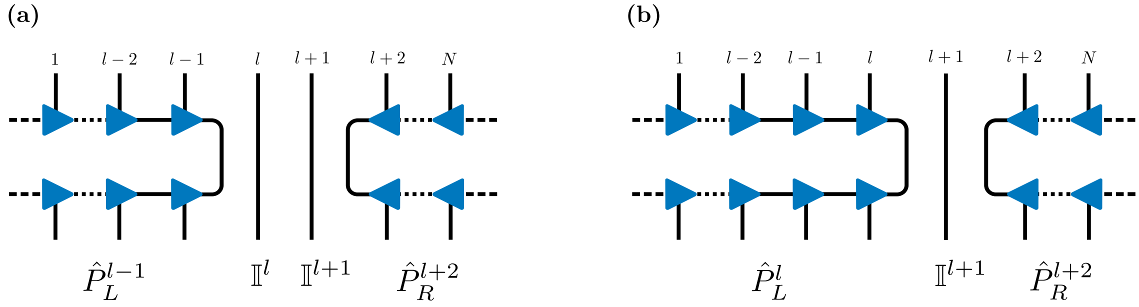

Figure 2.15: tensor network diagram of the tangent space projection operators $\hat{P}_L^{l-1} \otimes \mathbb{I}^l \otimes \mathbb{I}^{l+1} \otimes \hat{P}_R^{l+2}$ (a) and $\hat{P}_L^{l} \otimes \mathbb{I}^{l+1} \otimes \hat{P}_R^{l+2}$ (b).

Consider the real time evolution of a quantum many body state as an MPS described by the Schrödinger equation,

$$\frac{\partial}{\partial t} |\psi(M(t))\rangle = -i\hat{H} |\psi(M(t))\rangle \,. \tag{2.46}$$

MPS $|\psi(M)\rangle$ resides within a manifold denoted by $\mathbb{M}_{\text{MPS}}$ which is a subset of the complete MPS Hilbert space. This manifold is defined by imposing specific constraints on the MPS within it. An example of such a manifold is an MPS space with a fixed auxiliary index dimension. Note that other manifolds with smaller auxiliary index dimensions are singularly embedded within this manifold. During real-time evolution, the right-hand side of Equation 2.47 leads the initial MPS $|\psi(M)\rangle$ outside of the manifold, rendering the evolution computationally impractical. To facilitate the evolution of the initial MPS within the manifold, an optimal approximation is achieved by projecting the right-hand side of equation 2.46 onto the tangent space of the manifold defined at the current state,

$$\frac{\partial}{\partial t} |\psi(M(t))\rangle = -i\hat{P}_{\mathrm{T}^{[2]}_{|\psi(M(t))\rangle},\mathbb{M}_{\text{MPS}}} \hat{H} |\psi(M(t))\rangle \,, \tag{2.47}$$

where the projection operator $\hat{P}_{\mathrm{T}^{[2]}_{|\psi(M(t))\rangle},\mathbb{M}_{\text{MPS}}}$ projects the MPS $|\psi(M(t))\rangle$ onto the tangent space $\mathrm{T}^{[2]}_{|\psi(M(t))\rangle}$ corresponding to the manifold $\mathbb{M}_{\text{MPS}}$. It is defined as,

$$\hat{P}_{\mathrm{T}^{[2]}_{|\psi(M(t))\rangle},\mathbb{M}_{\text{MPS}}} = \sum_{l=1}^{N-1} \hat{P}_L^{l-1} \otimes \mathbb{I}^l \otimes \mathbb{I}^{l+1} \otimes \hat{P}_R^{l+2} - \sum_{l=1}^{N-2} \hat{P}_L^{l} \otimes \mathbb{I}^{l+1} \otimes \hat{P}_R^{l+2} \tag{2.48}$$

The superscript [2] denotes the projection operator is for a two-site TDVP algorithm [80, 132]. The equation 2.47 then becomes,

$$\frac{\partial}{\partial t}\left|\psi\right\rangle = -i\sum_{l=1}^{N-1}\hat{P}_L^{l-1}\otimes\mathbb{I}^l\otimes\mathbb{I}^{l+1}\otimes\hat{P}_R^{l+2}\hat{H}\left|\psi\right\rangle + i\sum_{l=1}^{N-2}\hat{P}_L^{l}\otimes\mathbb{I}^{l+1}\otimes\hat{P}_R^{l+2}\hat{H}\left|\psi\right\rangle . \qquad (2.49)$$

The exact solution of equation 2.49 is not tractable, however, the individual terms are integrable. This kind of problem can be solved by operator splitting method [133] by solving a pair of forward and backward differential equations,

$$\frac{\partial}{\partial t}\left|\psi\right\rangle = -i\hat{P}_L^{l-1}\otimes\mathbb{I}^l\otimes\mathbb{I}^{l+1}\otimes\hat{P}_R^{l+2}\hat{H}\left|\psi\right\rangle , \qquad (2.50)$$

$$\frac{\partial}{\partial t}\left|\psi\right\rangle = i\hat{P}_L^{l}\otimes\mathbb{I}^{l+1}\otimes\hat{P}_R^{l+2}\hat{H}\left|\psi\right\rangle . \qquad (2.51)$$

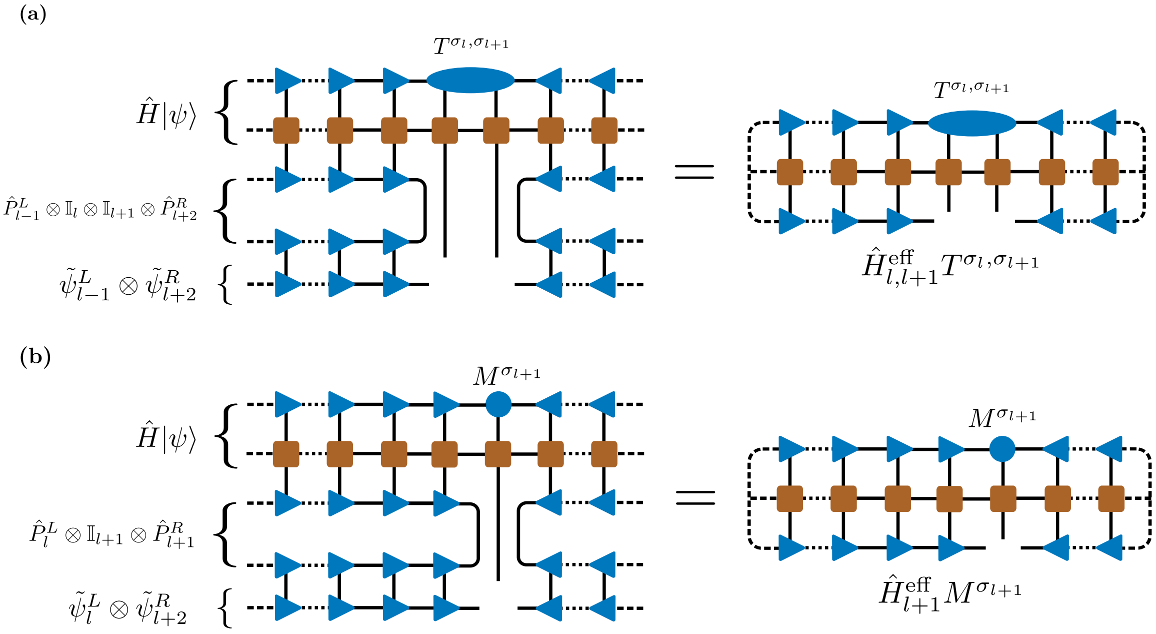

Figure 2.16: tensor network diagram corresponding to the right hand side of the local forward

Multiplying the equations 2.50 and 2.51 by $\tilde{\psi}^L_{l-1}\otimes\tilde{\psi}^R_{l+2}$ and $\tilde{\psi}^L_{l}\otimes\tilde{\psi}^R_{l+2}$ respectively simplifies these equations into local differential equations,

$$\frac{\partial}{\partial t}T^{\sigma_l,\sigma_{l+1}} = -i\,\tilde{\psi}^L_{l-1}\hat{P}_L^{l-1}\otimes\mathbb{I}^l\otimes\mathbb{I}^{l+1}\otimes\tilde{\psi}^R_{l+2}\hat{P}_R^{l+2}\hat{H}\left|\psi\right\rangle = -i\,\hat{H}^{\text{eff}}_{l,l+1}T^{\sigma_l,\sigma_{l+1}} \tag{2.52}$$

$$\frac{\partial}{\partial t}M^{\sigma_{l+1}} = i\,\tilde{\psi}^L_{l}\hat{P}_L^{l}\otimes\mathbb{I}^{l+1}\otimes\tilde{\psi}^R_{l+2}\hat{P}_R^{l+2}\hat{H}\left|\psi\right\rangle = i\,\hat{H}^{\text{eff}}_{l+1}M^{\sigma_{l+1}}, \tag{2.53}$$

The tensor network diagram corresponding to the right hand side of these equations is illustrated in 2.16 where we observe that the effective hamiltonians $\hat{H}^{\text{eff}}_{l,l+1}$ and $\hat{H}^{\text{eff}}_{l}$ are similar to that appeared in equation 2.45 for DMRG algorithm. Like DMRG each of these local differential equations can be solved with Lanczos based exponential solver [127, 128]. The error incurred during this procedure can be made arbitrarily small by increasing the Krylov space accordingly.

Solving the local equations 2.52 and 2.53 facilitates an iterative approach to solving the full Schrödinger equation. We can proceed in a manner similar to the DMRG algorithm by starting from the left edge and moving towards the right by solving a set of forward and backward discrete time differential equations in place of a local eigen value equation, followed by a right to left sweep. Ultimately, the state is evolved to time $t + 2\delta t$ with an error at $O(\delta t^3)$. By halving the time step ($\delta t \rightarrow \delta t/2$), a complete left-to-right and right-to-left sweep is defined as a unit time step. The TDVP algorithm is as follows;

1. Start with a initial state $\left|\psi_i\right\rangle|_{t=0}$ in right canonical form. Prepare the set of R tensors, $\{R_N, R_{N-1}, \ldots, R_3\}_{t=0}$.
2. Loop l over the list $[1, 2, \ldots, N-1]$,
   (a) Build two-site tensor, $M^{\sigma_l}B^{\sigma_{l+1}} \rightarrow T^{\sigma_l,\sigma_{l+1}}$.
   (b) Solve the local forward differential equation, $\frac{\partial}{\partial t}T^{\sigma_l,\sigma_{l+1}}(t) = -i\,\hat{H}^{\text{eff}}_{l,l+1}T^{\sigma_l,\sigma_{l+1}}(t)$.
   (c) Decompose $T^{\sigma_l,\sigma_{l+1}}(t+\delta t/2) \rightarrow A^{\sigma_l}S\tilde{B}^{\sigma_{l+1}}$. Truncate and renormalize the singular value matrix $S \rightarrow \tilde{S}$ and build $\tilde{S}\tilde{B}^{\sigma_{l+1}} \rightarrow M^{\sigma_{l+1}}$.
   (d) Build $L_{l-1}[A^{\sigma_l'}]^*O^{\sigma_l',\sigma_l}A^{\sigma_l} \rightarrow L_l$. Delete R_{l+2}.
   (e) Solve the local backward differential equation, $\frac{\partial}{\partial t}M^{\sigma_{l+1}}(t) = i\,\hat{H}^{\text{eff}}_{l+1}M^{\sigma_{l+1}}(t)$.

   This iterative procedure is called the left to right TDVP sweep. Figure 2.17 illustrates the corresponding tensor network diagrams. At the end the MPS is in left canonical form.
3. Loop l over the list $[N, N-1, \ldots, 2]$,
   (a) Build two-site tensor, $A^{\sigma_{l-1}}M^{\sigma_l} \rightarrow T^{\sigma_{l-1},\sigma_l}$.

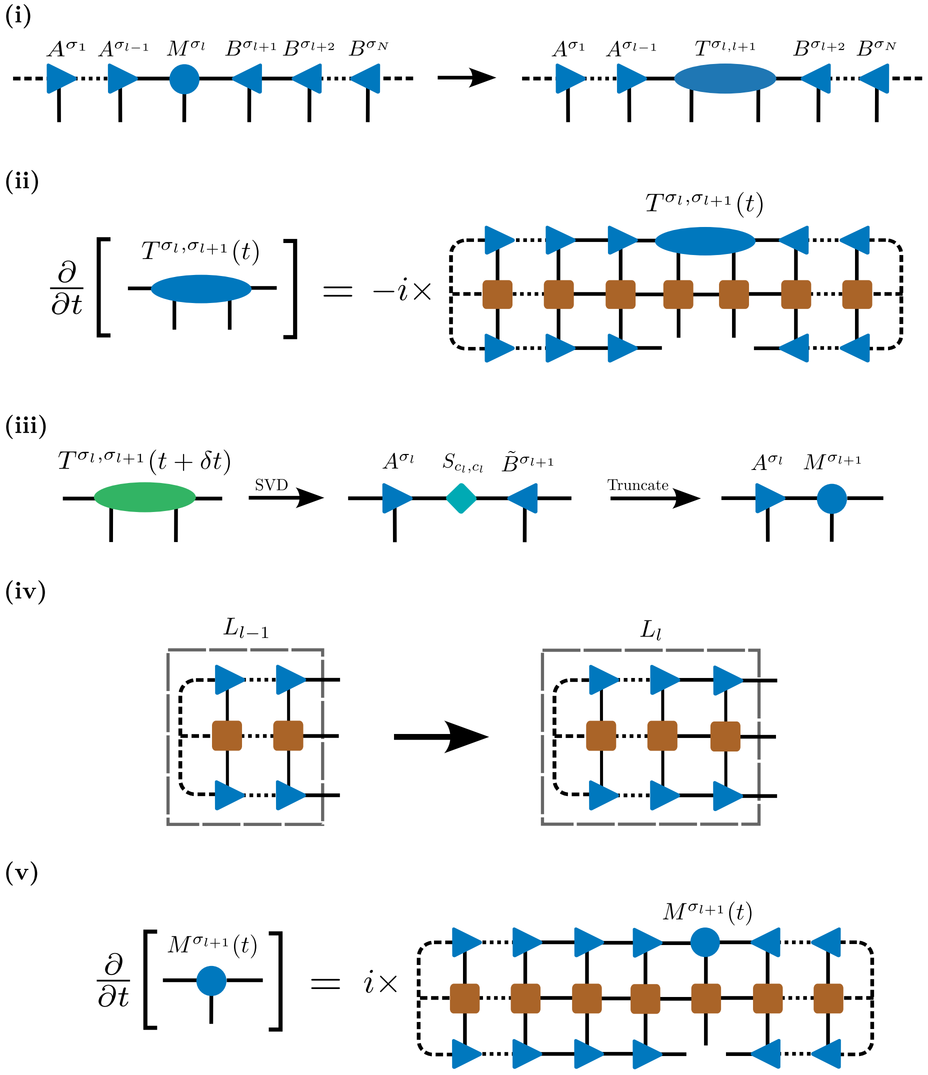

Figure 2.17: Diagrammatic representation of the left to right sweep of the two site TDVP algorithm. (i) initial state in mixed canonical form, (ii) solve the forward differential equation, (iii) singular value decomposition of the evolved local tensor, (iv) build $L_{l-1} \to L_l$, (v) solve the backward differential equation.

(b) Solve the local forward differential equation, $\frac{\partial}{\partial t}T^{\sigma_{l-1},\sigma_l}(t) = -i\,\hat{H}^{\text{eff}}_{l-1,l}T^{\sigma_{l-1},\sigma_l}(t)$.

(c) Decompose $T^{\sigma_{l-1},\sigma_l}(t+\delta t/2) \to \tilde{A}^{\sigma_{l-1}}SB^{\sigma_l}$. Truncate and renormalize the singular value matrix $S \to \tilde{S}$ and build $\tilde{A}^{\sigma_{l-1}}\tilde{S} \to M^{\sigma_{l-1}}$.

(d) Build $[B^{\sigma_l'}]^*O^{\sigma_l',\sigma_l}B^{\sigma_l}R_{l+1} \to R_l$. Delete L_{l-2}.

(e) Solve the local backward differential equation, $\frac{\partial}{\partial t}M^{\sigma_{l-1}}(t) = i\,\hat{H}^{\text{eff}}_{l-1}M^{\sigma_{l-1}}(t)$.

This iterative procedure is called the right to left DMRG sweep. At the end the MPS is in right canonical form.

4. Steps 2. and 3. evolves the state by a unit step δt, $|\psi(t)\rangle \rightarrow |\psi(t+\delta t)\rangle$. Repeating these steps will evolve the state further.

The TDVP algorithm exhibits four primary sources of error. The first arises as projection error during the transformation of the exact Schrödinger equation into 2.47. This error is a consequence of the limited bond dimensions of the auxiliary index in MPS tensors. A practical assessment of this error involves monitoring the convergence of TDVP data with several increasing bond dimensions. The second source of error is the finite time step error incurred while approximating differential equation 2.49 with a sequence of integrable local differential equations. In the context of the second-order integrator scheme detailed above, this error amounts to $O(\delta t^3)$ per time-step. The third error originates from insufficient Krylov vectors when solving the local differential equations 2.52 and 2.53. Employing a larger number of Krylov vectors in the Lanczos exponential solver allows the reduction of this error to arbitrarily small magnitudes. The final error is the truncation error incurred during the truncation of the singular values of the local MPS tensors.

2.8 Lanczos solvers

Eigen and exponential solvers are crucial to the efficiency of DMRG and TDVP algorithms. In DMRG, the eigensolution stands out as the bottleneck, whereas in TDVP, it is the exponentiation of the local effective Hamiltonian. Consequently, optimizing these steps is imperative for achieving an optimal algorithm. When dealing with Hermitian Hamiltonians, Lanczos-based iterative eigen and exponential solvers have been proven to be superior to alternative methods [127, 134, 128, 135].

The Lanczos algorithm was originally devised for the tridiagonalization of a Hermitian matrix. In essence, the Lanczos process transforms an $n \times n$ Hermitian matrix M into an $n \times n$ tridiagonal matrix in n steps. The significance of the Lanczos process lies in the fact that the extreme eigenvalues and eigenvectors of a $k \times k$ tridiagonal matrix after $k \ll n$ iteration are a good approximation of the extreme eigenvalues and eigenvectors of the Hermitian matrix M. The Lanczos algorithm takes a Hermitian matrix $M_{n\times n}$ and an initial guess vector v_{input} as inputs. After k iterations, it yields a tridiagonal matrix $T_{k\times k}$ and a set of orthogonal column vectors $V_{n\times k}$. The algorithm can be succinctly described as follows,

```
$v_1 = v_{\text{input}}/|v_{\text{input}}|$                    ▷ input vector
for $i \in [2, k+1]$ do
```

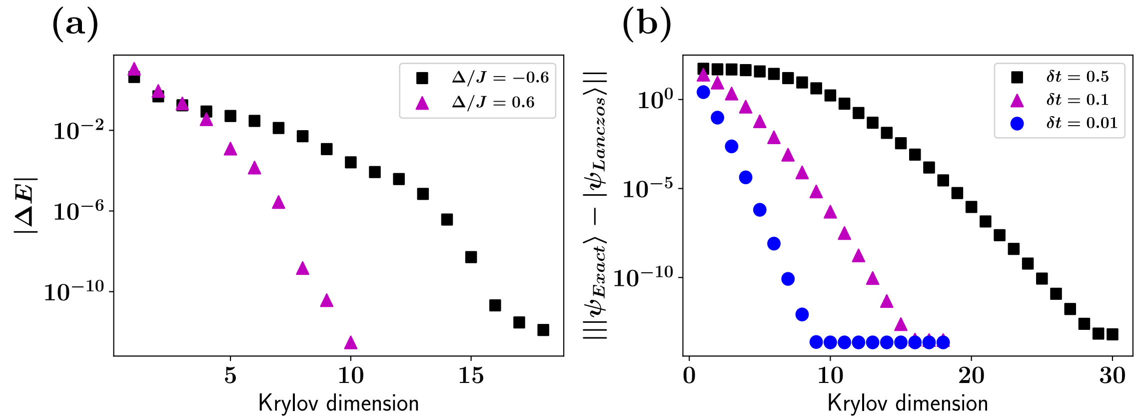

Figure 2.18: (a) Convergence of the lowest eigenvalue for a Lanczos eigen solver of a 14-site spin-1/2 XXZ Heisenberg model starting from a random input state. (b) Convergence of the operation $e^{-i\delta t\hat{H}}|\psi_{\text{rand}}\rangle$ for a Lanczos exponential solver. $\hat{H}$ is a 14-site spin-1/2 XXZ Heisenberg Hamiltonian and $|\psi_{\text{rand}}\rangle$ is a random normalized vector.

```
    $v_i = M \times v_{i-1}$
    for $j \in [i-2, i-1]$ do                          ▷ Building tridiagonal matrix
        if $j \geq 1$ then
            $T_{i-1,j} = \text{dot}(v_i, v_j)$
            $T_{j,i-1} = T^*_{i-1,j}$
    for $f \in [1, i-1]$ do                            ▷ Full reorthonormalization
        $v_i = v_f - \text{dot}(v_i, v_f) \times v_f$
        $v_i = v_i/|v_i|$
return $T$, $[v_1, v_2, \ldots, v_k]$
```

The set of orthonormal vectors $V_{n\times k} = [v_1, v_2, \ldots, v_k]$ are known as Krylov vectors that forms the basis of Krylov subspace [127, 135]. The number k is known as the Krylov dimension.

Eigen-solver : The tridiagonal matrix T is diagonalized to obtain the eigenvalues $\epsilon_1^T < \epsilon_2^T < \ldots < \epsilon_k^T$ and corresponding eigenvectors $v_1^T, v_2^T, \ldots, v_k^T$. The lowest eigenvalue of matrix M is approximated by ϵ_1^T and the corresponding eigenvector is approximated by $V_{n\times k} \times v_1^T$. The error of this approximation can be made arbitrarily small by increasing the Krylov dimensions. Figure 2.18 (a) shows the absolute difference between the exact ground state energy and the Lanczos approximation as a function of Krylov dimension for a 14−site spin−1/2 XXZ Heisenberg model (Hilbert space size is 16383) for two different anisotropy parameter[1]. In both cases we observe a rapid convergence to value less than $O(10^{-12})$ with less than 18 iterations.

Exponential-solver : Similarly, matrix exponential applied to a vector can be approximated by the tridiagonal matrix as,

$$e^{M} \times v_{\text{input}} \approx V_{n\times k} \times e^{T_{k\times k}} \times \mathbb{I}_{k\times k}[:,1], \tag{2.55}$$

where, $\mathbb{I}_{k\times k}[:,1]$ is the first column of the $k \times k$ identity matrix [136]. Accordingly, the error of this approximation can be made arbitrarily small by increasing the Krylov dimensions. Figure 2.18 (b) shows the absolute difference between the exact and Lanczos approximations of operation $e^{-i\delta t\hat{H}}\,|\psi_{\text{rand}}\rangle$ as a function of the Krylov dimension for three different values of δt. $\hat{H}$ is a 14−site spin−1/2 XXZ Heisenberg Hamiltonian with $\Delta/J = -0.6$ and $|\psi_{\text{rand}}\rangle$ is a random normalized vector. In all cases, we observe a rapid convergence to values less than $O(10^{-14})$ with less than 30 iterations. For a smaller δt this convergence is achieved much faster.

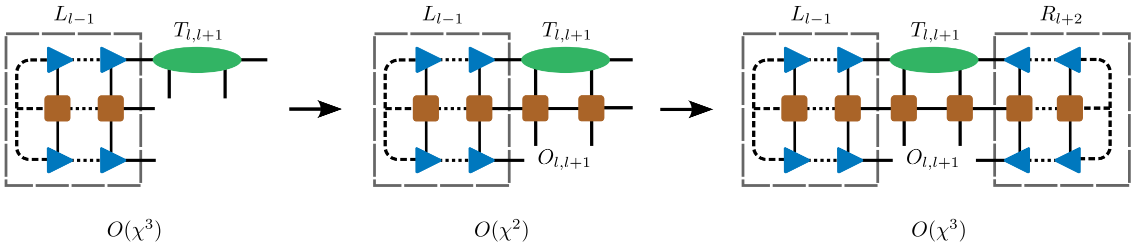

Figure 2.19: Optimal tensor operations corresponding o the matrix vector multiplication $\hat{H}^{\text{eff}} \times T$. χ is the dimension of auxiliary indices.

The algorithm's computational bottleneck arises from the matrix-vector multiplication in the third line, which operates in $O(n)$ time—a notably more cost-effective process than full diagonalization, which demands $O(n^3)$ time. Additionally, in Lanczos algorithm there is no requirement to explicitly construct matrix M, a resource-intensive task, especially when matrix sparsity is not guaranteed. For DMRG and TDVP algorithms, the effective Hamiltonian $\hat{H}^{\text{eff}}$, defined in equations 2.45 and 2.52,

---

[1] The XXZ Heisenberg model is defined as,

$$\hat{H}_{\text{XXZ}} = -J\sum_{j=1}^{N-1} \hat{\sigma}^x_j\hat{\sigma}^x_{j+1} + \hat{\sigma}^y_j\hat{\sigma}^y_{j+1} + \Delta\hat{\sigma}^z_j\hat{\sigma}^z_{j+1} \tag{2.54}$$

where $\hat{\sigma}^x, \hat{\sigma}^y, \hat{\sigma}^z$ are the Pauli matrices and Δ is the anisotropy parameter.

is the equivalent of matrix M. In tensor representation, the equivalent matrix-vector multiplication can be performed while retaining $\hat{H}^{\text{eff}}$ as its constituent tensors, without the need to explicitly construct the matrix, as illustrated in Figure 2.19. The overall computational complexity of this operation is $O(\chi^3)$, where χ represents the auxiliary index dimension. In contrast, the explicit construction of $\hat{H}^{\text{eff}}$ matrix followed by a matrix-vector multiplication incurs a cost of $O(\chi^4)$.

2.9 Codes availability

A substantial portion of my doctoral research was dedicated to writing and optimizing the tensor network and exact diagonalization codes for the simulation of the static and dynamic properties of low-dimensional quantum systems. These codes are primarily written in the Julia programming language [89]. For convenient accessibility, the codes are made available through the following links:

- Tensor Network codes: `https://github.com/NishanRanabhat/TenMB`
- ED codes: `https://github.com/NishanRanabhat/ExactDiagonalization`

Chapter 3

Dynamics of order parameter statistics

Dynamical phase transition (DPT) is one of the most interesting phenomena that highlight the nonequilibrium behavior of manybody quantum systems. In Section 1.2, we discussed how long range interactions allows $1\mathcal{D}$ LRIM to host long range ferromagnetic order at finite temperature that leads to the emergence of dynamical ferromagnetic and paramagnetic phases. Extensive investigations of DPT in LRIM have been conducted [17, 137, 138], with experimental evidence observed in systems involving trapped ions [18, 19]. Traditionally, DPT is characterized by the long time behavior of the system following a sudden quench of the order parameter and is quantified by the long-time Cesaro's average of the order parameter,

$$\bar{O} = \lim_{t\to\infty} \frac{1}{t} \int_0^t \langle \hat{O}(\tilde{t}) \rangle d\tilde{t}. \tag{3.1}$$

In LRIM, the relevant order parameter is magnetization, and the time averaged magnetization equilibrates to zero in the dynamical paramagnetic phase and remains finite in the dynamical ferromagnetic phase. However, this approach to characterize dynamical phases relies on the equilibration of the order parameter. Consequently, the dynamical phases remain inconclusive in the regime in which equilibration is not observed[17, 137]. Some studies employed higher-order moments to detect dynamical phases [18]. In this chapter, we employ full counting statistics (FCS) to study the DPT in LRIM based on the shape of the probability distribution function (PDF) of the order parameter defined in the subsystem. We highlight that it is a robust alternative approach to characterize dynamical phases because it can provide qualitative signatures of transition at transient times.

The rest of this chapter is organized as follows. In Section 3.1 we introduce FCS of the order parameter. Section 3.2 start with explanation of the quench protocol and simulation details followed by the results of quenching the transverse field in Subsection 3.2.1 and interaction range in Subsection 3.2.2. Finally, in Section 3.3

we provide the conclusion and outlook of the work. The Appendix sections are as follows. Appendix 3.A outlines the methodology to calculate PDF in MPS formalism. Appendix 3.B compares the TDVP results with two exact results at two extremes of LRIM. Appendix 3.C details the errors in the TDVP data.

3.1 Full counting statistics

Full counting statistics (FCS) was first introduced as the full probability distribution of electron fluctuations in mesoscopic transport[139]. Subsequently, FCS has been extensively applied in the study of mesoscopic systems [140, 141, 142, 143, 144, 145], where the various cumulants of the electron distribution yield measurable physical parameters such as current, noise, and the Fano factor. With significant advancements in the experimental realization of many-body interacting systems and the development of numerical algorithms for their simulation, FCS have garnered increasing attention in the realm of many-body dynamics. In particular, FCS has been employed to investigate the dynamics of ultra-cold atomic systems [146, 147, 148, 149, 150, 151, 152], entanglement dynamics [153, 154], dynamical phase transitions [155, 156, 23, 12], and many-body localization [157, 158]. These applications underscore the versatility and significance of FCS for probing a wide range of phenomena in the dynamic landscape of quantum systems.

Complete information regarding the quantum fluctuation of a system is inscribed in the probability distribution function (PDF), denoted as $P(\hat{O}, |\psi\rangle)$, where $\hat{O}$ is the order parameter of interest and $|\psi\rangle$ is the wavefunction characterizing the quantum state. Owing to its inclusion of cumulants of all orders, $P(\hat{O}, |\psi\rangle)$ provides comprehensive statistical information pertaining to order parameter $\hat{O}$ within state $|\psi\rangle$. Consequently, it is a superior entity for characterizing both the static and dynamic aspects of quantum systems [159]. Although the concept of FCS is intuitively clear, obtaining exact results for the FCS of interacting many-body systems poses significant challenges [159, 160, 161, 162, 163, 164, 165]. In this context, we aim to provide a comprehensive review of FCS, focusing on its application to many-body interacting systems and methods to calculate it in the matrix product state (MPS) formalism.

For a system comprising N site spins, our order parameter is the subsystem magnetization defined over a subsystem with size $l < N$, positioned at the center to mitigate the boundary effects,

$$\hat{M}_l = \sum_{j=1}^{l} \hat{s}_j^x. \tag{3.2}$$

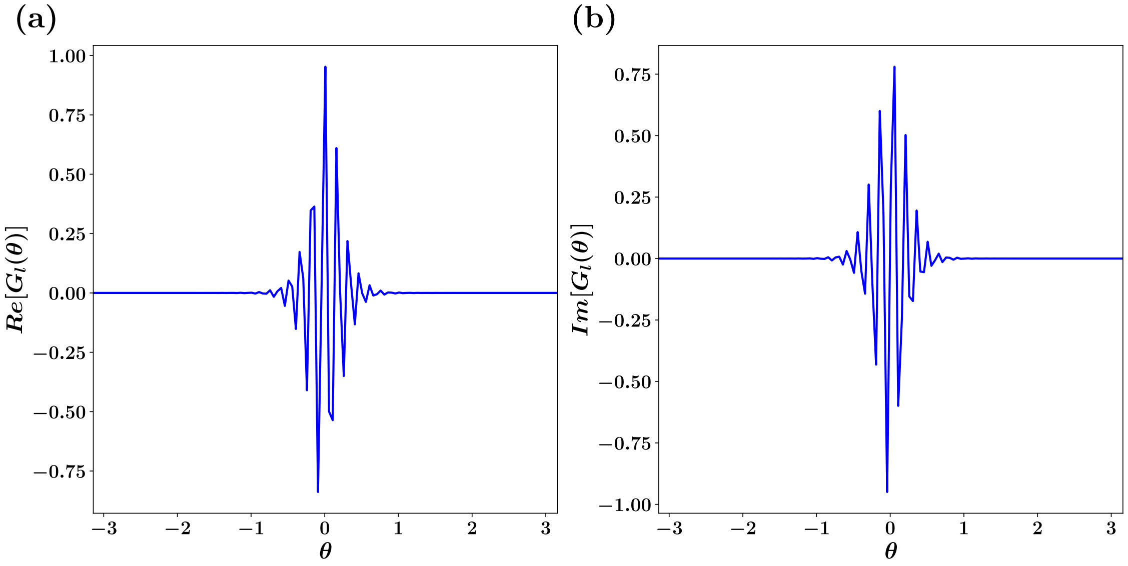

Figure 3.1: Real (a) and imaginary (b) part of the moment generating function of the ground state of the transverse field Ising model at transverse field value $h = 0.48$.

The observable $\hat{M}_l$ is local and therefore typically relaxes to a stationary state (see Section 1.1.1) and l is chosen to be sufficiently large to have a well-defined statistical distribution. The probability that a generic measurement of operator $\hat{M}_l$ in a state defined by density matrix $\hat{\rho}$ (whether pure or mixed) will yield a value m is given by the following distribution function,

$$P_l(m) = \mathrm{Tr}[\hat{\rho}\delta(\hat{M}_l - m)]. \tag{3.3}$$

Inserting the Fourier expansion of the delta function $\delta(\hat{M}_l - m) = \int_{-\infty}^{\infty} \frac{d\theta}{2\pi} e^{i\theta[\hat{M}-m]}$ in equation 3.3 we get,

$$P_l(m) = \int_{-\infty}^{\infty} \frac{d\theta}{2\pi} e^{-i\theta m} \mathrm{Tr}[\hat{\rho} e^{i\theta \hat{M}_l}], \tag{3.4}$$

where $G_l(\theta) = \mathrm{Tr}[\hat{\rho} e^{i\theta \hat{M}_l}]$ is the moment-generating function and is central to the calculation of the full PDF. Moments of any order can be derived from the moment-generating function by a straightforward differential,

$$\mathrm{Tr}[\hat{\rho}\hat{M}^n] = \left.\frac{\partial G_l(\theta)}{\partial \theta^n}\right|_{n=0}. \tag{3.5}$$

Furthermore, $G_l(\theta)$ satisfies three important properties: $G_l(0) = 1$, $G_l(-\theta) = G_l(\theta)^*$, $G_l(\theta + 2\pi) = (-1)^l G_l(\theta)$. The first two properties are trivial by construction. The last one can be proved by expanding and rearranging the exponential,

$$\begin{aligned} e^{i\theta\hat{M}_l} &= \prod_{j=1}^{l} e^{i\theta\hat{s}_j^x} && \text{(3.6a)} \\ &= \prod_{j=1}^{l} \Big[1 + i\theta\frac{\hat{s}_j^x}{1!} - \theta^2\frac{\hat{s}_j^{x2}}{2!} - i\theta^3\frac{\hat{s}_j^{x3}}{3!} + \theta^4\frac{\hat{s}_j^{x4}}{4!} + \dots\Big] && \text{(3.6b)} \\ &= \prod_{j=1}^{l} \Big[\Big[1 - \frac{(\theta/2)^2}{2!} + \frac{(\theta/2)^4}{4!} + \dots\Big] + i\Big[\frac{(\theta/2)^2}{1!}\hat{\sigma}_j^x - \frac{(\theta/2)^3}{3!}\hat{\sigma}_j^x + \dots\Big]\Big] && \text{(3.6c)} \\ &= \prod_{j=1}^{l} \Big[\cos\left(\frac{\theta}{2}\right) + i\sin\left(\frac{\theta}{2}\right)\hat{\sigma}_j^x\Big] && \text{(3.6d)} \end{aligned}$$

thus implying

$$e^{i(\theta+2\pi)\hat{M}(l)} = \prod_{j=1}^{l} \Big[-\cos\left(\frac{\theta}{2}\right) - i\sin\left(\frac{\theta}{2}\right)\hat{\sigma}_j^x\Big] = (-1)^l e^{i\theta\hat{M}(l)}. \tag{3.7}$$

we can now restrict the range of θ in equation (3.4) in the interval $-\pi \le \theta < \pi$. Figure 3.1 shows the real and imaginary part of $G_l(\theta)$ corresponding to the ground state of transverse field Ising model at $h = 0.48$. For spin one-half systems the order parameter m take either integer or half-integer discrete values in the range $m \in \{-\frac{l}{2}, -\frac{l}{2}+1, \dots, \frac{l}{2}-1, \frac{l}{2}\}$ depending upon whether l is even or odd, we can redefine the PDF as

$$P_l(m) = \begin{cases} \sum_{r\in\mathbb{Z}} \tilde{G}_l(r)\delta(m-r) & \text{if } l \text{ is even,} \\ \sum_{r\in\mathbb{Z}} \tilde{G}_l(r+\frac{1}{2})\delta(m-r-\frac{1}{2}) & \text{if } l \text{ is odd,} \end{cases} \tag{3.8}$$

where $\tilde{G}_l(r) = \int_{-\pi}^{\pi} \frac{d\theta}{2\pi} e^{-ir\theta} G_l(\theta)$. The calculation of $G_l(\theta)$ is straightforward in MPS formalism and is discussed in detail in Appendix 3.A. The integral of $\tilde{G}_l(r)$ over the range $\theta \in [-\pi, \pi]$ is calculated by discrete sum with $\Delta\theta = 0.005$.

3.2 Quench dynamics

we consider two different classes of quantum quenches to investigate the post quench dynamics of the subsystem magnetization PDF;

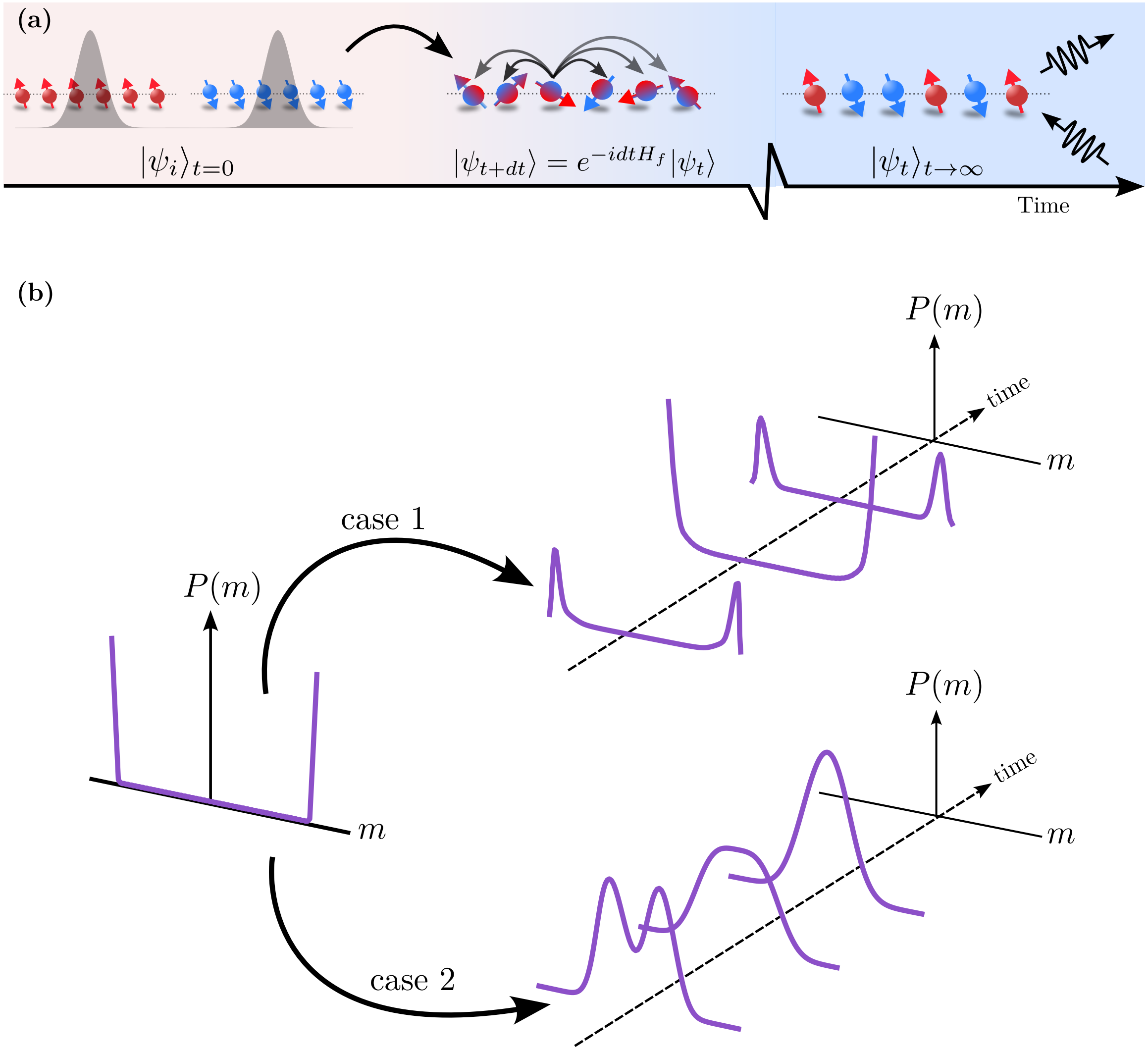

Figure 3.2: (a) Quench protocol: At time $t = 0$ initial state $|\psi_i\rangle_{t=0}$ (here Greenberger–Horne–Zeilinger state) is quenched and evolved unitarily with a post quench Hamiltonian $\hat{H}_f$. The evolution is monitored at each time step by calculating the full probability distribution of the order parameter. (b) Two possible cases for relaxation following a global quantum quench, case 1: The initial ferromagnetic order is strongly retained and the full probability distribution remains strictly bimodal, case 2: The initial ferromagnetic order quickly melts with the full probability distribution exhibiting a Gaussian shape.

1. Initialize the system at $h_i = 0$ and quench the transverse field to finite h_f for a given value of interaction range.
2. Initialize the system at $\alpha = 0$ (fully connected) and quench the interaction range to $\alpha = 10$ (short range Ising) at finite value of transverse field and vice-versa.

For finite system the ground state of ferromagnetic LRIM in the limit $h \to 0$ is the $\mathbb{Z}_2$ symmetric Greenberger–Horne–Zeilinger (GHZ) state for all values of α,

$$|\psi_i\rangle = \frac{1}{\sqrt{2}}\left[\bigotimes_{j=1}^{N} |{\rightarrow}\rangle_j^x + \bigotimes_{j=1}^{N} |{\leftarrow}\rangle_j^x\right] \tag{3.9}$$

where, $|{\rightarrow}\rangle^x = \begin{pmatrix} 1/\sqrt{2} \\ 1/\sqrt{2} \end{pmatrix}$ and $|{\leftarrow}\rangle^x = \begin{pmatrix} 1/\sqrt{2} \\ -1/\sqrt{2} \end{pmatrix}$ are the eigenkets of $\hat{s}^x$ operator. This state is characterised by a subsystem magnetization PDF, $P_l(m) = \frac{1}{2}[\delta_{m,l/2} + \delta_{m,-l/2}]$, exhibiting long range ferromagnetic order. Unlike the fully polarized state the GHZ state exhibits multi-partite entanglement and inherent long range correlation [166]. This state admits a an exact MPS representation with $\chi = 2$ following a trivial decomposition,

$$|\psi_i\rangle = \frac{1}{\sqrt{2}} M_1 M_2 \dots M_{N-1} M_N \tag{3.10}$$

where, $M_1 = \begin{pmatrix} |{\rightarrow}\rangle^x & |{\leftarrow}\rangle^x \end{pmatrix}$, $M_N = \begin{pmatrix} |{\rightarrow}\rangle^x \\ |{\leftarrow}\rangle^x \end{pmatrix}$, and $M_j = \begin{pmatrix} |{\rightarrow}\rangle^x & 0 \\ 0 & |{\leftarrow}\rangle^x \end{pmatrix}$, $\forall j \in \{2, 3, \dots, N-1\}$. Each of these matrices can be appropriately reshaped to three legged tensors to bring down to the useful MPS form.

At time $t = 0$ the system is suddenly quenched to a final Hamiltonian $\hat{H}(\alpha, h_f)$ with $0 < h_f < h_c(\alpha)$, where $h_c(\alpha)$ is the equilibrium ferromagnetic to paramagnetic transition point at a given α. For non-zero h the ground state is non-trivial, and therefore, the initial state is numerically initialized using the DMRG algorithm (see Section 2.6). The post quench unitary evolution $|\psi\rangle_{t+dt} = e^{-idt\hat{H}} |\psi\rangle_t$ is achieved using the TDVP algorithm (see Section 2.7) with a second-order integration scheme and Trotter time-step of 0.05. The details of the convergence of the data and the numerical accuracy are thoroughly explained in Appendix 3.C. Throughout this thesis, we have taken the total system size of $N = 200$ and the subsystem of $l = 100$ unless explicitly stated otherwise. Figure 3.2 (a) illustrates the general global quench protocol.

The two extremes of ferromagnetic LRIM at $\alpha = \infty$ and $\alpha = 0$ are exactly solvable, offering an excellent basis for benchmarking our methodology. In Appendix 3.B.1 we compare our numerical results with the exact analytical results for the short range transverse field Ising model. In Appendix 3.B.2 we outline a recipe for exactly calculating the time-dependent PDF for the fully connected Ising model with exact diagonalization, and compare the TDVP results with the exact results.

3.2.1 Quench of the transverse field

The post quench behaviour of the PDF strongly depend on the post quench parameters and subsystem size l. Figure 3.3 illustrates various representative quenches. In the first row, we observe a consistent qualitative behavior for $\alpha \in 0.0, 1.0$ and $h_f = 0.30$. In both cases, the system robustly maintains its initial long-range ferromagnetic order throughout temporal evolution, represented as case 1 in figure 3.2 (b). Additionally, a distinctive oscillation in the PDF is evident, characterized by a return frequency along the time axis. In the limit $N \to \infty$ and $\alpha \to 0$ mean field provides an accurate description of the dynamical behavior. The observed oscillatory behavior can be understood in large N limit with semiclassical techniques formulated as the classical trajectory of a collective spin that allows to calculate not just the expectations but also the PDF of the order parameter [52, 43]. This behavior undergoes a notable transformation when $\alpha = 2.5$, where the initial ferromagnetic order begins to dissipate at later times, indicating a fundamentally different dynamical

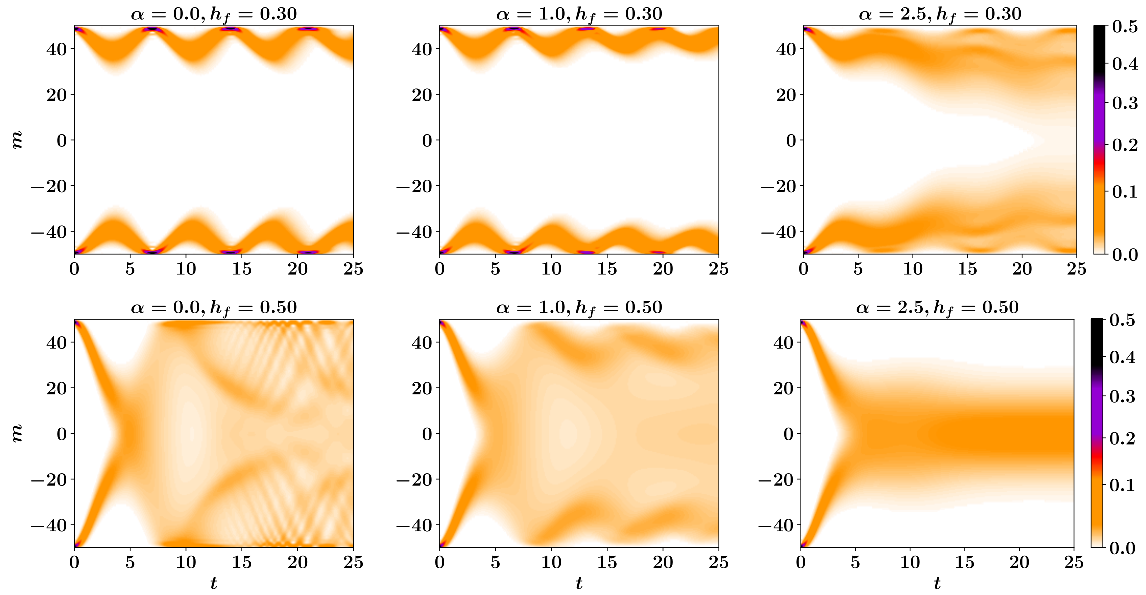

Figure 3.3: PDF dynamics of subsystem magnetization after a quantum quench for $l = 100$, $\alpha \in \{0.0, 1.0, 2.5\}$ and $h_f \in \{0.30, 0.50\}$ (in first and second rows respectively).

regime. In the second row, we observe distinct quench dynamics for the same values of α but with a higher post quench transverse field ($h_f = 0.50$). In this scenario, a larger transverse field facilitates rapid dissolution of the initial ferromagnetic order. However, the evolution of the PDF experiences a qualitative shift in its late-time dynamics contingent upon the interaction range. For $\alpha = 0.0, 1.0$, the PDF dynamics are characterized by periodic rebouncing of the probability streams, resulting in a broad and flat distribution. Consequently, the PDF does not equilibrate withing simulation time. Conversely, for $\alpha = 2.5$, this pattern transforms, with the PDF smoothly melting and eventually adopting a Gaussian shape centered around zero, represented as case 2 in figure 3.2 (b).

Gaussification of PDF is significant because it indicates a transition from the initial long-range ferromagnetic order to a paramagnetic phase. This transition is anticipated when the linear dimension of the subsystem surpasses the steady-state correlation length [167, 168]. In essence, the degree to which the PDF aligns with the Gaussian approximation suggests the extent of the departure of the system from its initial ferromagnetic order, serving as a valuable metric for characterizing the dynamical transition of the system. Gaussification of PDF is accessed by comparing the PDF with the Gaussian approximation obtained with the first two moments,

$$P_G(\mu, t) = \frac{1}{\sqrt{2\pi\sigma^2(t)}} \exp\left[-\frac{(\mu - \bar{m}(t))^2}{2\sigma^2(t)}\right] \tag{3.11}$$

where $\bar{m}(t) = \langle\psi_t| \hat{M}_l |\psi_t\rangle$ and $\sigma(t) = \langle\psi_t| [\hat{M}_l - \bar{m}(t)]^2 |\psi_t\rangle$ are the first two moments of subsystem magnetization. Quantitatively the goodness of Gaussification can be measured by defining a metric Distance to Gaussian (DG) as

$$\mathrm{DG} = \sqrt{\sum_m [P(m) - P_G(m)]^2} \tag{3.12}$$

where $P(m)$ is the numerically calculated PDF and $P_G(m)$ is the corresponding Gaussian PDF obtained using Equation 3.11. DG quantifies the proximity (or divergence) of the PDF from a Gaussian shape, where $\mathrm{DG} = 0$ indicates a perfect Gaussian form. DG is not be suitable for instances where the system fails to reach a steady state within the specified time frame and exhibits oscillations. In such scenarios, we introduce the time-averaged DG,

$$\mathrm{DG}_{\text{avg}} = \frac{1}{T - T_o} \int_{T_o}^{T} \mathrm{DG}(dt)\, dt \tag{3.13}$$

where T_o is chosen to avoid the initial sharp drop in DG [*cf.* Fig. 3.6].

Dynamical phases across $\alpha = 2$

In Figure 3.4, we present the late-time PDF of the order parameter as a function of subsystem size l for two distinct values of the interaction range, situated above and below $\alpha = 2.0$ and $h_f = 0.40$. Notably, we observe contrasting behaviors in the PDF for these two regimes. For $\alpha = 1.5$, the PDF maintains a robust double-peaked shape across all l values. Moreover, the divergence of the two branches of the PDF intensifies with increasing l, indicating a strong retention of the initial memory of

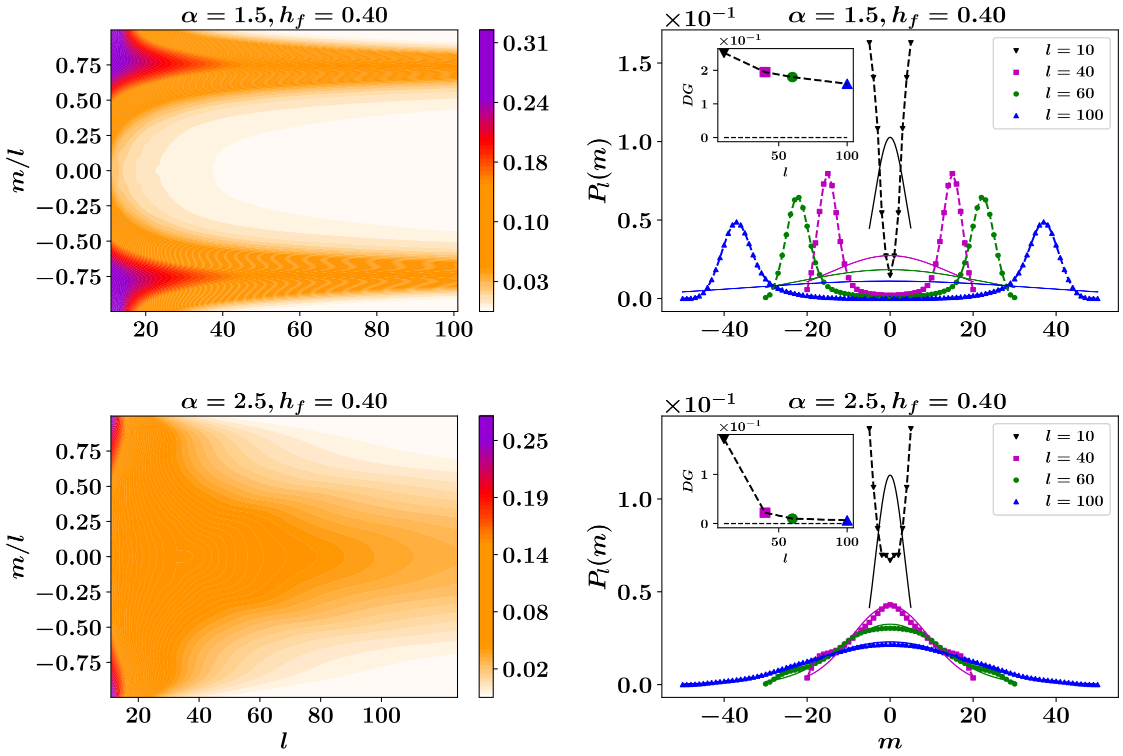

Figure 3.4: Contour plot of the late time PDF of subsystem magnetization after a quantum quench as a function of subsystem size, for $\alpha \in \{1.5, 2.5\}$, $h_f = 0.40$, and time $t = 25$. The subsystem magnetization m has been rescaled to the range $m/l \in [-1.0, 1.0]$, due to this rescaling the intensity of the contour plot decreases with increasing l and the colorbar readings doesn't signify the actual value of PDF. The second column shows PDF at four representative values of l. The symbols are TDVP results and the lines are the Gaussian approximation. The inset shows the dependence of DG on l.

the long-range order in the thermodynamic limit. Conversely, for $\alpha = 2.5$, the PDF exhibits a double-peaked profile for smaller l, becomes flat for intermediate l, and eventually transforms into a Gaussian shape for larger l. This progression suggests the complete melting of the initial memory of the long-range order in the thermodynamic limit. These distinct behaviors above and below $\alpha = 2.0$ serve as the basis for the dynamical phase transition (DPT) [17, 137, 138]. Accordingly, $\alpha = 2.0$ delineates the transition line between a dynamical ferromagnet and dynamical paramagnet.

Alternatively, it has been suggested that the ferromagnetic order persists well beyond persists well beyond $\alpha = 2.0$ and depends on both the initial and final quench parameters, based on the long-lived prethermal value of magnetization [137]. In Figure 3.5, we performed quenches similar to figure 3.4 at a smaller value of final transverse field, $h_f = 0.25$ and for a longer timescale $t = 50$. For $\alpha = 1.5$, we observe qualitatively similar behaviors across all timescales and subsystem sizes. The initial ferromagnetic order persists throughout the time evolution, and the PDF consistently maintains a distinctive double peak. Conversely, at $\alpha = 2.5$ we observe a completely different behavior, while the long-range ferromagnetic order persists at shorter timescales, it begins to melt at longer times. This trend is particularly evi-

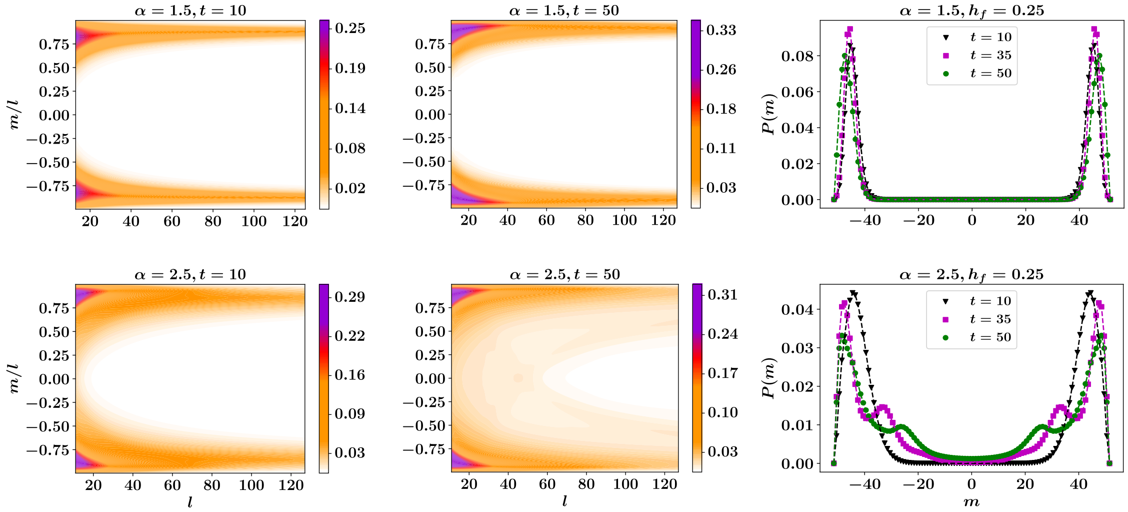

Figure 3.5: PDF of subsystem magnetization for $\alpha \in \{1.5, 2.5\}$, $h_f = 0.25$ (in first and second rows respectively) at different time scales after the quantum quench. The first two columns shows the contour plot of the rescaled PDF as a function of subsystem size at times $t \in \{10, 50\}$. The last column shows the PDF at times $t \in \{10, 35, 50\}$ and subsystem size $l = 100$.

dent in the rightmost panel of the second row of Figure 3.5, where the PDF at $t = 10$ displays a clear double peak that diminishes over time, accompanied by a stream of probability density converging toward $m = 0$. These observations suggest that the prethermal state is not robust for larger system sizes and longer timescales. Consequently, the initial long-range ferromagnetic order melts beyond $\alpha = 2$ with the expectation of Gaussification in the thermodynamic limit.

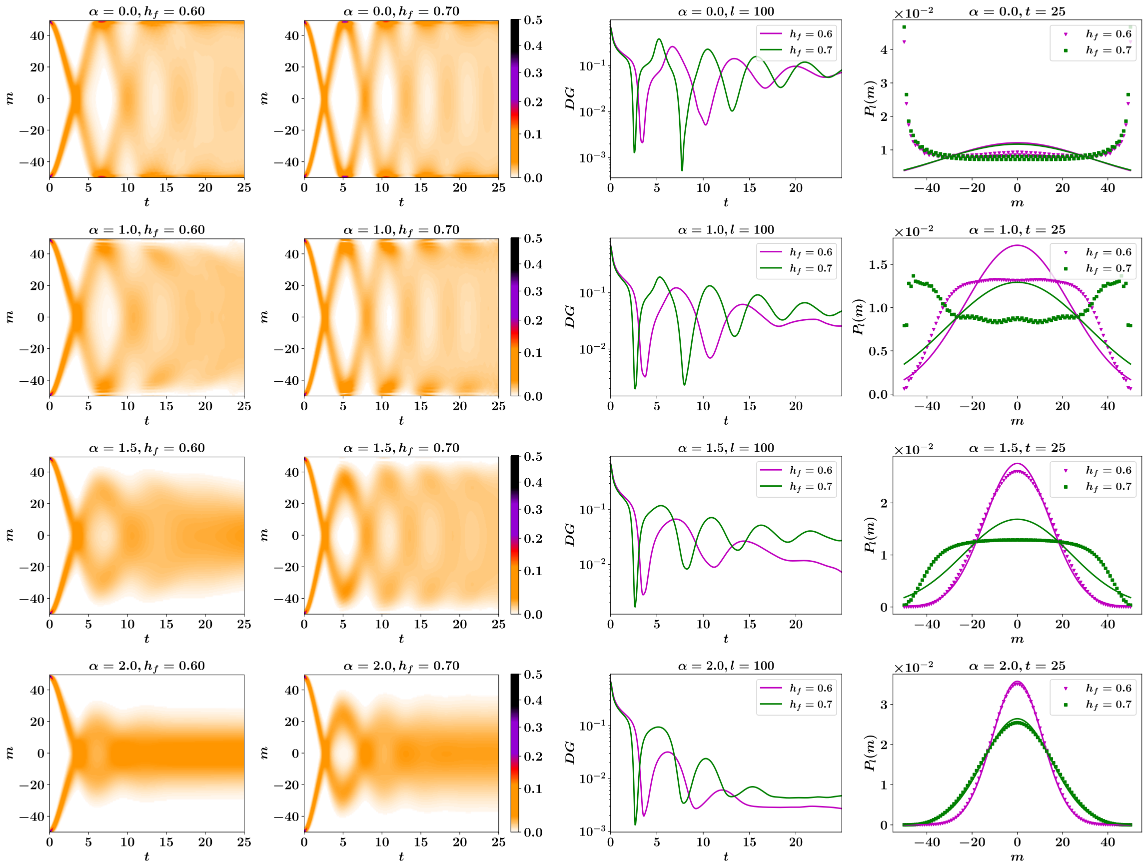

Figure 3.6: PDF of subsystem magnetization after a quantum quench for $l = 100$, $\alpha \in \{0.0, 1.0, 1.5, 2.0\}$ and $h_f \in \{0.60, 0.70\}$. The first two columns shows the evolution of the PDF as a function of time $t \in [0, 25]$. The third column shows the time evolution of DG (y-axis in log scale) and the last column shows the late time PDF at time $t = 25$ for the mentioned parameters. The symbols are the TDVP results whereas the corresponding full lines are the Gaussian approximation.

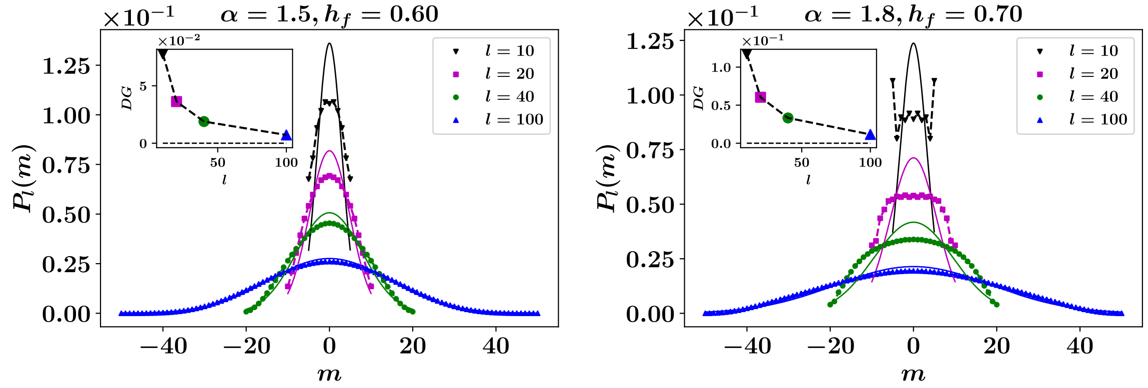

Figure 3.7: The PDF of subsystem magnetization after a quantum quench at time $t = 25$ for subsystem sizes $l \in \{10, 20, 40, 100\}$ for two representative values of post quench parameters $\alpha = 1.5, h_f = 0.60$, and $\alpha = 1.8, hf = 0.70$. The symbols are the TDVP results whereas the corresponding full lines are the Gaussian approximation. In the inset we show the dependence of DG on the subsystem size.

Quenches in $\alpha \leq 2$ and $h_f > 0.5$ regime

In Figure 3.6, we investigate the quench dynamics of the subsystem magnetization PDF for $h_f > 0.50$ for four representative values of α. For the fully connected case with $\alpha = 0.0$, the initial ferromagnetic order melts, and after a few oscillations (dependent on h_f), the PDF broadens. DG follows a similar pattern, oscillating at late times and consistently remaining above zero, indicating a lack of Gaussification. However, the system retains some memory of the initial ferromagnetic order, as evidenced by the PDF at $t = 25$, which shows two peaks at the edges for both values of h_f. At $\alpha = 1.0$, we observe two markedly different behavior of PDF at at $h_f = 0.60$ and 0.70. For $h_f = 0.60$, the late-time PDF is flat and far from Gaussian with no remnants of the initial ferromagnetic order. In contrast, at $h_f = 0.70$, remnants of the initial ferromagnetic order persist, as manifested by peaks at the edges of the late-time PDF. These differences underscore the strong dependence of PDF dynamics on the depth of the quench. A larger quench depth injects more energy into the system, delaying relaxation to a steady state and resulting in more oscillations in the PDF evolution. At $\alpha = 1.5$, Gaussification of the PDF is observed at late times for $h_f = 0.60$. However, increasing the quench depth to $h_f = 0.70$ results in a flat PDF for the same simulation time. The evolution of the DG metric provides clarity as DG starts to relax to zero for $h_f = 0.60$ but oscillates and remains well above zero for $h_f = 0.70$. By further increasing the interaction range to $\alpha = 2.0$, clear Gaussification is observed at both values of h_f. The time evolution of DG also reveals that the system relaxes to a stationary state faster and admits a smaller value for $h_f = 0.60$ than for $h_f = 0.70$.

In Figure 3.6, Gaussification is predominantly observed only for higher values of α. These observations alone do not allow us to conclusively claim the Gaussification of the subsystem magnetization. A finite-size study with several subsystem sizes provides a much stronger insight into the potential Gaussification of the PDF in the thermodynamic limit. Figure 3.7 illustrates the late-time PDF for the two representative quenches at different subsystem sizes. For $l = 100$, Gaussification is evident for both quenches. By contrast, smaller subsystem sizes predominantly exhibit flat distributions far from the Gaussian distribution. The inset, depicting the variation of DG with system size, illustrates the trend towards Gaussian behavior with increasing system size. These flat distributions resemble those observed in Figure 3.6 for a smaller α but with $l = 100$. Notably, for $\alpha = 1.8, h_f = 0.70, l = 10$, a strong remnant of the initial ferromagnetic long-range order is observed, manifested by sharp peaks at the edges. This suggests that the flat distribution may be an intermediate state between double-peaked and Gaussian distributions. This observation provides a strong signature for the Gaussification of subsystem magnetization in thermodynamic limits. This observation aligns with the DPT proposed in [17], which suggests that the dynamical critical point is approximately $h_f \approx 0.50$. Although experimental observations with trapped ions support the existence of this phenomenon [18, 19], the exact values of the dynamical critical points and critical exponents remain open for investigation.

In Figure 3.8, we investigate the dependence of Gaussification on the post quench transverse field h_f at three representative values of the interaction range. For $\alpha = 1.5$, the system tends towards a Gaussian behavior with increasing h_f up to a certain point, marked by a dip in the color plot of the PDF versus h_f in the first panel of the first row. Beyond this point, as h_f increases further, the PDF moves away from the Gaussian and broadens in shape. The second panel of the first row highlights Gaussification only for the intermediate values of h_f. This is counter-intuitive because larger transverse fields tend to disrupt the long-range ferromagnetic order. However, a larger value of h_f is associated with a higher effective temperature [53]. Consequently, the system requires a longer time and larger subsystem size to eventually relax to a Gaussian distribution. The third panel demonstrates that for sufficiently large system sizes and longer simulation times, the PDF converges towards a Gaussian shape for all values of h_f. For $\alpha \geq 2.0$, the PDF is Gaussian within the considered range of h_f and simulation parameters. However, the dip in the color plot still persists. This dip becomes less prominent with increasing α, as illustrated in the plots for $\alpha = 2.5$ in the third row.

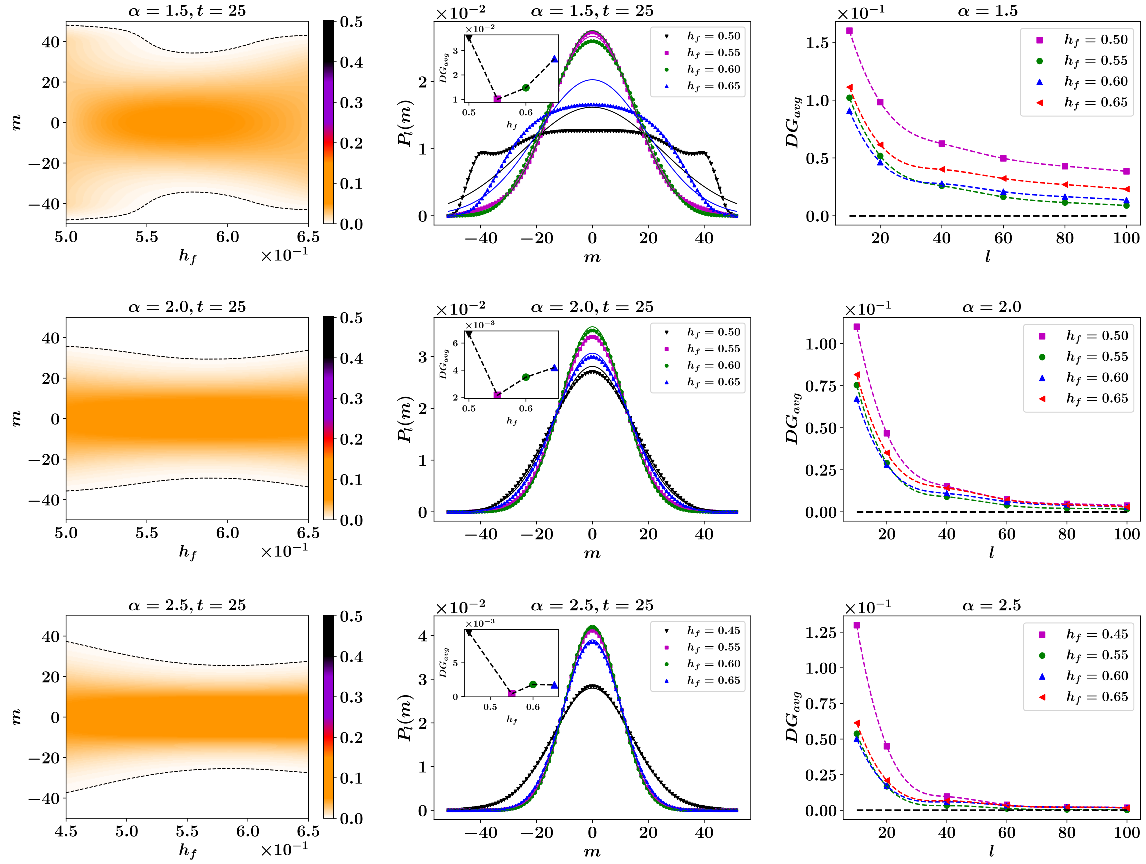

Figure 3.8: PDF dynamics of subsystem magnetization after a quantum quench as a function of post quench transverse field h_f at three representative values of interaction range $\alpha = \{1.5, 2.0, 2.5\}$. The dotted lines are the lines of constant probability at $P(m) = 0.002$, these lines don't have any quantitative significance and is plotted for better visualization of PDF. The first column shows the color plot of PDF at time $t = 25$ at different values of h_f and $l = 100$. The second column shows the PDF at $t = 25$ at different h_f, the symbols are the TDVP calculations whereas the lines are the Gaussian approximation. The inset shows DG_{avg} at corresponding values of h_f. The last column shows the finite size dependence of DG_{avg} for four different values of h_f. DG_{avg} is calculated by averaging over the final $\left(\frac{3}{5}\right)^{th}$ of the total simulation time.

3.2.2 Quench of the interaction range

Here, we investigate the relaxation of the subsystem magnetization PDF following a quantum quench in the direction of the interaction range α. Specifically, we quench the system from one extreme to the other, initializing at $\alpha = 0.0$, representing the fully connected model, and quenching to $\alpha = 10.0$, almost resembling the Ising model with nearest neighbor interactions, and vice versa. The transverse field h remains constant throughout the evolution. In addition to examining how the initial order dissipates, we are interested in understanding whether quenching in opposite directions yields qualitatively equivalent outcomes. Figure 3.9 illustrates these quenches for four representative values of the transverse field $h = \{0.30, 0.40, 0.48, 0.60\}$. Notably, the two peaks of the initial PDF are broader than those in the cases where the system is initialized with $h = 0$.

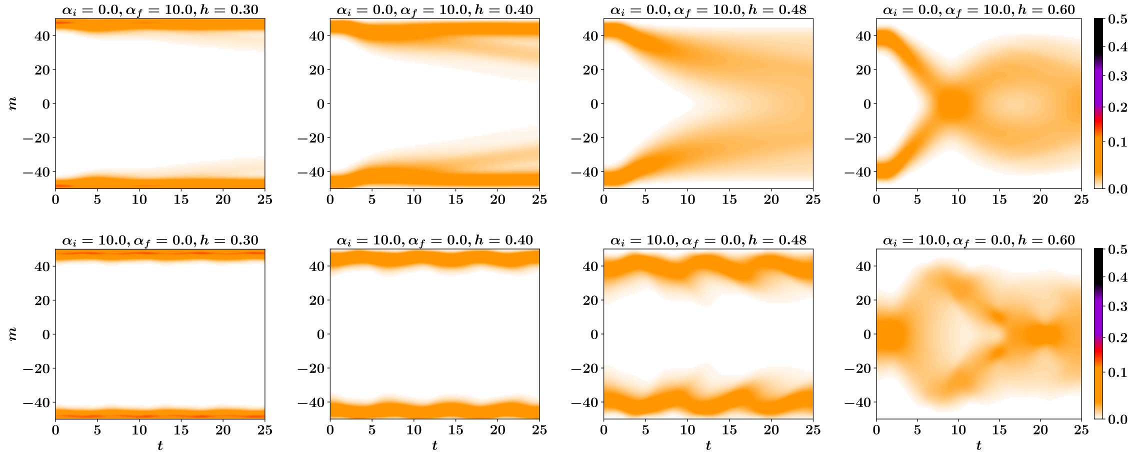

Figure 3.9: PDF dynamics of subsystem magnetization after a quantum quench along the direction of interaction range, α. The first row shows the results for quenches where the system is initialized at $\alpha_i = 0.0$ and quenched to a final $\alpha_f = 10.0$, the second row shows the results for opposite condition. The quenches are performed for three representative values transverse field $h \in \{0.30, 0.40, 0.48, 0.60\}$.

We observe distinct behaviors for the two classes of quenches undertaken. When initiating quenches from the fully connected state and evolving with the short-range Hamiltonian, we witness the dissolution of the initial ferromagnetic order for sufficiently large values of the transverse field. For $h = 0.30, 0.40$, the two branches of the PDF exhibit progressive dissolution over time, as evidenced by the emergence of probability density streams branching from the main PDF peak. However, the initial ferromagnetic order persists throughout the simulation. At $h = 0.48$, we observe a complete breakdown of the initial ferromagnetic order, with subtle indications of Gaussification at later times. Conversely, for quenches starting from the ground state of the short-range Hamiltonian and evolving with the fully connected Hamiltonian, robust remnants of the initial ferromagnetic order endure throughout the evolution, displaying no signs of breakdown. Although the PDF exhibits oscillations with increasing h, there is no discernible change in the intensity of the PDF branches over time. The results in the last column pertain to similar quenches but at $h = 0.6$. For the quench from $\alpha = 0.0$ to $\alpha = 10.0$ we observe that the initial ferromagnetic order melts faster than before, and the system is quenched to a point in the paramagnetic regime in the equilibrium phase diagram. The quench in the opposite direction is initialized at a paramagnetic point such that the PDF begins with a Gaussian shape but relaxes quickly. Interestingly, at intermediate times, we observe a double peak PDF, signifying long range ferromagnetic order. This long range order is short lived and melts quickly. However, the fate of PDF over a long time limit remains unclear.

The two cases of α represent the extremes of the long-range Ising model. When $\alpha = 10.0$, the system closely resembles the well-known transverse-field Ising model. This model does not support long-range order at finite temperatures, which aligns with our observation of melting of the initial ferromagnetic order. The protocol introduces an extensive amount of energy into the system, effectively simulating a finite-temperature environment. Consequently, although quench occurs within the ferromagnetic region in the zero-temperature equilibrium phase diagram, the system relaxes to a paramagnetic point in a finite-temperature phase diagram. In contrast, the fully connected Ising model supports long-range ferromagnetic order, even at finite temperatures [169, 49, 170]. This characteristic likely explains the robust remnants of the initial ferromagnetic order observed later in our study.

3.3 Conclusion

In this Chapter we explored the dynamical phases of LRIM through the dynamics of the PDF of the subsystem magnetization following quantum quenches. We highlighted that because the FCS includes moments of all orders, it is a more robust approach to characterize the dynamical phases. Our observations indicated that, for $\alpha > 2.0$, the initial long-range ferromagnetic order is not robust in the thermodynamic limit, where previous studies proposed conflicting conclusions [17, 137]. This was manifested by the transformation of the double-peak PDF into a Gaussian distribution. Even for cases where Gaussification was not observed for the considered system size and simulation time, a qualitative signature of the melting of the ferromagnetic order was observed in the transient time. In another work [171] it was demonstrated that for $\alpha > 2$ the order parameter decays slowly but with a finite rate for variable range of interaction. It will be interesting to see how the decay rate of the FCS observed in Figure 3.5 compares to the results reported in this article.

In the case of $\alpha \leq 2.0$, a robust remnant of the initial long-range order persisted, as highlighted by the strictly bimodal PDF throughout the post quench evolution, particularly when $h_f \lesssim 0.50$. Beyond $h_f = 0.50$, we observed Gaussification of the order parameter PDF, which is dependent on the subsystem size and total simulation time, necessitating finite-size analysis for conclusive results. Nevertheless, preliminary findings suggest that for sufficiently large system sizes and extended simulation times, Gaussification of the order parameter PDF is expected for all α values, following a quantum quench along the transverse field with $h_f \geq 0.50$. This contrasting behavior based on the shape of the post quench PDF suggests the line $h_c \approx 0.5$ as the dynamical ferromagnetic to paramagnetic transition point for $\alpha < 2$ in line with a previous study [17]. For finite systems without an explicitly symmetry breaking term in the Hamiltonian the true ground state of LRIM in the equilibrium ferromagnetic phase has bimodal PDF. We therefore initialized the state as a $\mathbb{Z}_2$ symmetric GHZ state which is the ground state of finite LRIM with zero transverse field. This symmetry remains protected through out the post quench evolution for both phases as revealed by oscillating bimodal PDF in dynamical ferromagnetic phase and Gaussian PDF in dynamical paramagnetic phase. Quenches along the interaction range revealed qualitatively distinct dynamics of the order parameter PDF depending on the quench direction. Quenches starting from the fully connected state and evolving with short-range Hamiltonians exhibit the effective melting of the initial ferromagnetic order. Conversely, quenches in the opposite direction displayed complete persistence of the initial order. The success of FCS in characterizing the dynamical phases in LRIM motivated us to employ this approach to study thermalization of LRIM or lack thereof which forms the central topic of the next chapter.

3.A Calculating full counting statistics with MPS

The computational bottleneck in calculating the PDF of an order parameter is the moment-generating function $G_l(\theta) = \mathrm{Tr}[\rho e^{i\theta\hat{M}_l}]$. For a pure state, the density matrix can be written as $\rho = |\phi\rangle\langle\phi|$ such that $G_l(\theta) = \langle\phi|e^{i\theta\hat{M}_l}|\phi\rangle = \langle\phi|\prod_{j=i}^{i+l-1} e^{i\theta\hat{s}^x_j}|\phi\rangle$. We redefine the single-site operator $e^{i\theta\hat{s}^x_j}$ as $O^{\sigma'_j,\sigma_j}$ and represent state $|\phi\rangle$ as an MPS. $G_l(\theta)$ can now be written in MPS formalism as,

$$\langle\phi|\prod_{i=j}^{j+l-1} O^{\sigma'_i,\sigma_i}|\phi\rangle = \Phi^{\mathrm{L}}_{c_{j-1},c'_{j-1}}\Big[\prod_{i=j}^{j+l-1}[M^{\sigma'_i}]^* O^{\sigma'_i,\sigma_i} M^{\sigma_i}\Big]\Phi^{\mathrm{R}}_{c_{j+l-1},c'_{j+l-1}}, \tag{3.14}$$

where $\Phi^{\mathrm{L}}_{c_{j-1},c'_{j-1}} = [M^{\sigma_1}_{c'_0,c'_1}]^* M^{\sigma_1}_{c_0,c_1} \dots [M^{\sigma_{j-1}}_{c'_{j-2},c'_{j-1}}]^* M^{\sigma_{j-1}}_{c_{j-2},c_{j-1}}$ is the trace over physical indices left of j and $\Phi^{\mathrm{R}}_{c_{j+l-1},c'_{j+l-1}} = [M^{\sigma_{j+l}}_{c'_{j+l-1},c'_{j+l}}]^* M^{\sigma_{j+l}}_{c_{j+l-1},c_{j+l}} \dots [M^{\sigma_N}_{c'_{N-1},c'_N}]^* M^{\sigma_N}_{c_{N-1},c_N}$ is the trace over physical indices right of $j + l - 1$. Figure 3.10 shows the tensor network diagram corresponding to Equation 3.14. After calculating $G_l(\theta)$, the full probability distribution $P_l(m)$ can be computed numerically using discrete Fourier transformation. For all results in the main text, we have taken $d\theta = 0.01$.

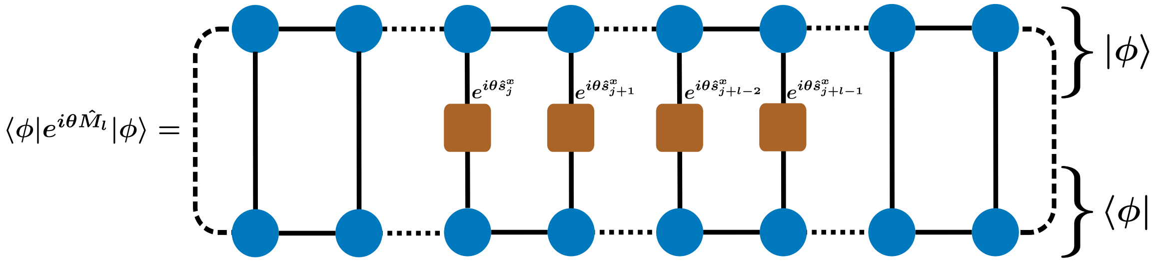

Figure 3.10: Computing the generating function $G_l(\theta)$ in matrix product state representation. The site j is chosen such that the subsystem of size l is in the center of the full system.

3.B Integrable limits

The two extremes of the LRIM at $\alpha = \infty$ and $\alpha = 0.0$ are exactly solvable. Here, we will compare the the PDF of subsystem magnetization obtained by TDVP simulations and exact analytical and numerical results in these two extremes.

3.B.1 Nearest neighbor limit

The LRIM is exactly solvable at $\alpha = \infty$; it reduces to nearest neighbor transverse field Ising model. The dynamic and stationary PDF for nearest neighbor Ising model has been analytically computed for quenches to both ferromagnetic and paramagnetic regimes by means of a relation to a 3-state classical model [168]. Here, we compare the PDF after a quantum quench in long range model with increasing values of α obtained by TDVP with the stationary PDF of the nearest neighbor transverse field Ising model computed analytically. We also compare the corresponding evolution of the formation probabilities $P_l(m = \frac{\mp l}{2})$ and $P_l(m = 0)$ for quenches to ferromagnetic and paramagnetic regimes with the analytical results.

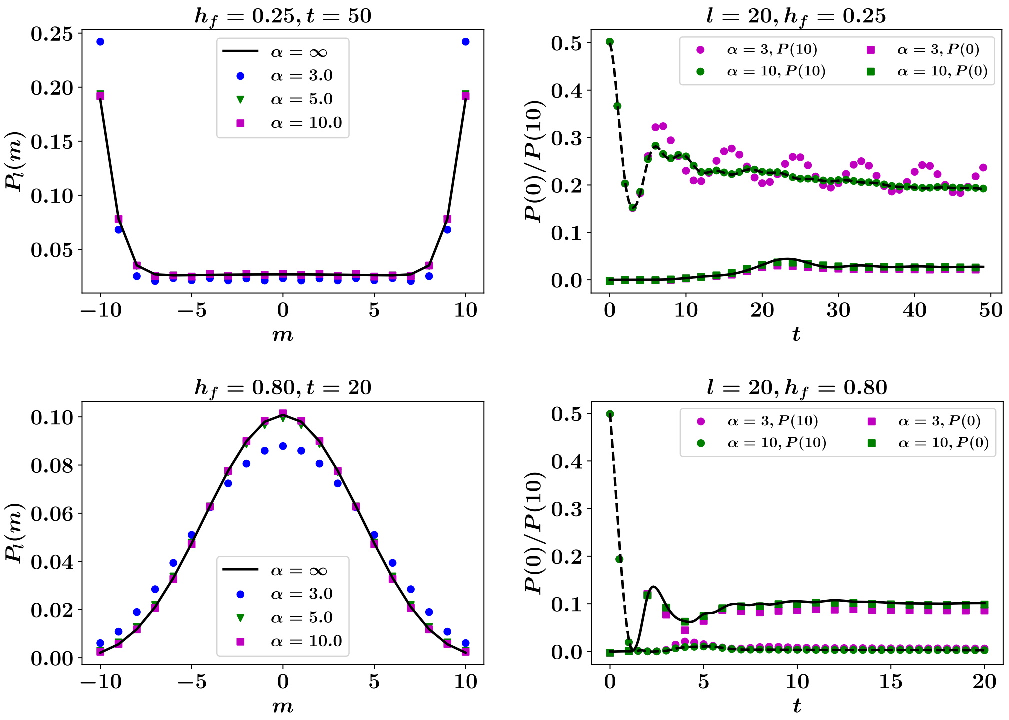

Figure 3.11: PDF of subsystem magnetization of nearest neighbor transverse field Ising model after quantum quench. The first panels on the left column are the PDF after quench to two representative final transverse field and at three increasing values of α. The panels on the right are the time evolution of formation probabilities, $P_l(m = \frac{\pm l}{2}), P_l(m = 0)$, for the corresponding final transverse fields. The lines are analytical results [168] whereas the symbols are TDVP results.

In figure 3.11 we see that the TDVP results perfectly overlaps with the analytical results for sufficiently large α. In fact we don't observe much difference between the $\alpha = 5$ and $\alpha = 10$ results.

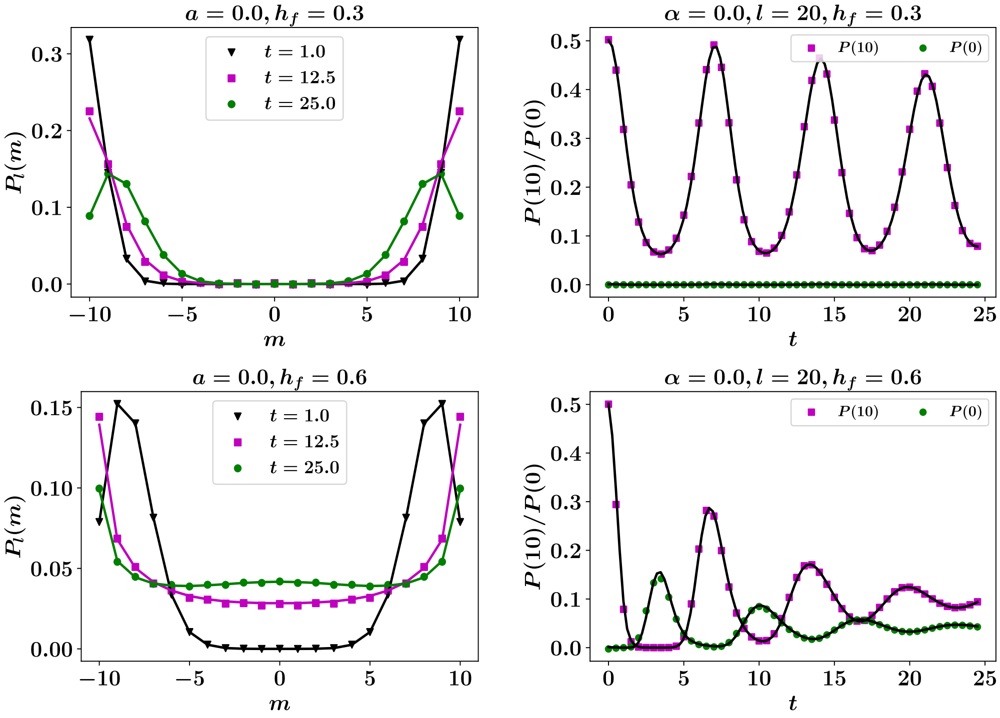

Figure 3.12: PDF of subsystem magnetization of fully connected Ising model after quantum quench. The first panels on the left column are PDF at three representative time slices at two values of final transverse field. The panels on the right are the time evolution of formation probabilities, $P_l(m = \frac{\pm l}{2}), P_l(m = 0)$, for the respective final transverse fields. The full lines are exact results calculated from equation 3.28 whereas the symbols are TDVP results.

3.B.2 Fully connected limit

The other extreme of LRIM at $\alpha = 0$ gives us the fully connected Ising Hamiltonian

$$H(h) = -\frac{1}{N}\sum_{i,j}^{N} \hat{s}_i^x \hat{s}_j^x - h\sum_{i=1}^{N} \hat{s}_i^z \tag{3.15a}$$

$$= -\frac{1}{N}(\hat{S}^x)^2 - h\hat{S}^z \tag{3.15b}$$

where $\hat{S}^a = \sum_i^N \hat{s}_i^a$, $a = x, y, z$, are the collective spin operators and has commutation relations like normal spin operators. In this regime the model behaves as a single collective spin and we can exactly solve the dynamics of our initial state with this Hamiltonian. Our initial state is the $\mathbb{Z}_2$ symmetric GHZ state

$$|\psi_i\rangle = \frac{1}{\sqrt{2}}(|\rightarrow, ... \rightarrow, \rightarrow, \rightarrow ..., \rightarrow\rangle^x + |\leftarrow, ... \leftarrow, \leftarrow, \leftarrow ..., \leftarrow\rangle^x). \tag{3.16}$$

This state evolves unitarily as $|\psi_t\rangle = e^{-i\hat{H}t}|\psi_i\rangle$, so we need to represent $|\psi_0\rangle$ as the superposition of the eigenkets of the Hamiltonian 3.15. This Hamiltonian is diagonalized with the basis $\{ \left|\frac{N}{2}, n\right\rangle \}$ that are the simultaneous eigenkets of collective spin operators $(\hat{S}^2, \hat{S}^x)$ in the maximal total spin sector. We strictly remain in this sector because our initial state $|\psi_0\rangle$ is in this sector and the unitary operation $e^{-i\hat{H}t}$ preserves the total spin quantum number. The total spin quantum number is fixed through out the time evolution and is thus redundant, so we will from hereon use the notation $\{|n\rangle\}$ where n is the number of down spins such that

$$|n\rangle = \frac{1}{\sqrt{\binom{N}{n}}} \sum_{j_1<j_2<...j_n} |...j_1..j_2...j_n...\rangle\,, \quad \hat{S}^x|n\rangle = \left(\frac{N}{2} - n\right)|n\rangle \tag{3.17}$$

where $j_1, j_2, ...j_n$ are the positions of the down spins and the sum runs over all $\binom{N}{n}$ configurations. We can represent our initial state 3.16 as the linear combination of the eigenkets $\{|E_j\rangle\}$ of the Hamiltonian 3.15

$$|\psi_i\rangle = \sum_{j=0}^{N} k_j |E_j\rangle \tag{3.18}$$

where, $\{ |E_j\rangle \}$ can be represented as the linear combination of the basis states, $|E_j\rangle = \sum_{n=0}^{N} c_n^j |n\rangle$. The coefficients $\{k_j\}$ can be extracted as

$$k_j = \langle E_j|\psi_0\rangle = \sum_{n=0}^{N} (c_n^j)^* \frac{\delta_{0,n} + \delta_{N,n}}{\sqrt{2}} = \frac{(c_0^j)^* + (c_N^j)^*}{\sqrt{2}}. \tag{3.19}$$

The evolved state is

$$|\psi_t\rangle = e^{-i\hat{H}(h)t} \sum_{j=0}^{N} k_j |E_j\rangle = \sum_{j=0}^{N} k_j e^{-iE_jt} |E_j\rangle = \sum_{n=0}^{N} X_n(t) |n\rangle \tag{3.20}$$

where the time dependent coefficient is introduced as

$$X_n(t) = \sum_{j=0}^{N} k_j c_n^j e^{-iE_jt}. \tag{3.21}$$

The generating function of the PDF can then be calculated as

$$G_l(\theta,t) = \langle\psi_t| e^{i\theta\hat{M}(l)} |\psi_t\rangle = \sum_{n,\tilde{n}} X_{\tilde{n}}(t)^* X_n(t) \langle\tilde{n}| e^{i\theta\hat{M}(l)} |n\rangle\,. \tag{3.22}$$

Since $|n\rangle$ is not an eigenket of the subsystem magnetization we have to decompose it as

$$|n\rangle = \frac{1}{\sqrt{\binom{N}{n}}} \sum_{\sigma=\max(0,n-N+l)}^{\min(l,n)} |\sigma\rangle_l \otimes |n-\sigma\rangle_{N-l} \tag{3.23}$$

where σ is the number of down spins in the subsystem of size l such that

$$|\sigma\rangle_l \otimes |n-\sigma\rangle_{N-l} = \sum_{\substack{j_1<j_2<...j_\sigma \\ \tilde{j}_1<\tilde{j}_2<...\tilde{j}_{n-\sigma}}} |...j_1..j_2...j_\sigma...\rangle_l \otimes \left|...\tilde{j}_1..\tilde{j}_2...\tilde{j}_{n-\sigma}...\right\rangle_{N-l} \tag{3.24}$$

where $j_1, j_2, ...j_\sigma$ are the positions of down spins in the subsystem l and $\tilde{j}_1, \tilde{j}_2, ...\tilde{j}_{n-\sigma}$ are the positions of down spins in rest of the system. The sum runs through all $\binom{l}{\sigma} \times \binom{N-l}{n-\sigma}$ configurations. The state in equation 3.23 is properly normalized as can be seen from the following identity,

$$\sum_{\sigma=\max(0,n-N+l)}^{\min(l,n)} \binom{l}{\sigma} \times \binom{N-l}{n-\sigma} = \binom{N}{n}. \tag{3.25}$$

It goes by the name Chu-Vandermonde identity [172]. The representation in 3.23 is particularly useful because $|\sigma\rangle_l \otimes |n-\sigma\rangle_{N-l}$ is an eigenket of the of the subsystem magnetization operator

$$\hat{M}(l)\, |\sigma\rangle_l \otimes |n-\sigma\rangle_{N-l} = \left(\frac{l}{2} - \sigma\right) |\sigma\rangle_l \otimes |n-\sigma\rangle_{N-l}\,. \tag{3.26}$$

We can now proceed to calculate the generating function

$$\langle\tilde{n}| e^{i\theta\hat{M}(l)} |n\rangle = \frac{1}{\sqrt{\binom{N}{\tilde{n}}\binom{N}{n}}} \sum_{\sigma,\tilde{\sigma}} e^{i\theta\left(\frac{l}{2}-\sigma\right)} \binom{l}{\sigma} \delta_{\tilde{\sigma},\sigma} \binom{N-l}{n-\sigma} \delta_{\tilde{n}-\tilde{\sigma},n-\sigma} \tag{3.27}$$

replacing equation 3.27 in equation 3.22 we get the final expression for generating function of the PDF

$$G_l(\theta,t) = \sum_{n=0}^{N} \sum_{\sigma=\max(0,n-N+l)}^{\min(l,n)} \frac{1}{\binom{N}{n}} |X_n(t)|^2 e^{i\theta(\frac{l}{2}-\sigma)} \binom{l}{\sigma}\binom{N-l}{n-\sigma}. \tag{3.28}$$

The PDF can be calculated from this expression of generating function by a Fourier transformation (see Section 3.1),

$$P_l(m) = \sum_{n=0}^{N} \sum_{\sigma=\max(0,n-N+l)}^{\min(l,n)} \frac{1}{\binom{N}{n}} |X_n(t)|^2 \left[\int_{-\pi}^{\pi} e^{i\theta(\frac{l}{2}-\sigma-m)} \frac{d\theta}{2\pi}\right] \binom{l}{\sigma}\binom{N-l}{n-\sigma} \tag{3.29}$$

$$= \sum_{n=0}^{N} \sum_{\sigma=\max(0,n-N+l)}^{\min(l,n)} \frac{1}{\binom{N}{n}} |X_n(t)|^2 \frac{\mathrm{Sin}[\pi(\frac{l}{2}-\sigma-m)]}{\pi(\frac{l}{2}-\sigma-m)} \binom{l}{\sigma}\binom{N-l}{n-\sigma} \tag{3.30}$$

In figure 3.12 we plot the PDF after quantum quench to two different final transverse field at three different time slices and the evolution of formation probabilities. The results show an excellent match between the exact diagonalization results and TDVP for both quenches.

3.C Convergence with bond dimension

To ensure the data generated by the simulations are correct we need to check the convergence of the errors with increasing bond dimension. In TDVP the bond dimension is responsible for projection error [132], which is a primary source of error. To check that the errors converge with increasing bond dimension we compare the time evolution of subsystem magnetization and relative errors for some representative cases of quantum quenches for $\chi = \{40, 60, 100\}$ in figure 3.13. Quenches along the transverse field show qualitatively similar behavior, the relative error converges and becomes flat in a long time limit for all values of post quench parameter. Furthermore, for times up to 25, which is the maximum time reached for most of the results in the main text, the relative error remains smaller than $O(10^{-3})$. For quenches of the interaction range with $h = 0.40$ we observe a similar behavior. For $h = 0.48$, the quench from $\alpha_i = 10.0$ to $\alpha_f = 0.0$ shows a markedly different behavior. The magnetizations at different χ maintains a constant shift from one another right from $t = 0$ throughout the evolution. This is because the point $\alpha = 10.0$ and $h = 0.48$ is close to the critical point of the equilibrium phase diagram where we see a logarithmic divergence of the entanglement entropy [107] and DMRG generate a considerable relative error while initializing the system in the ground state. This initial error simply gets propagated throughout the time evolution. The relative errors in opposite direction behaves normally attaining a flat region after oscillations.

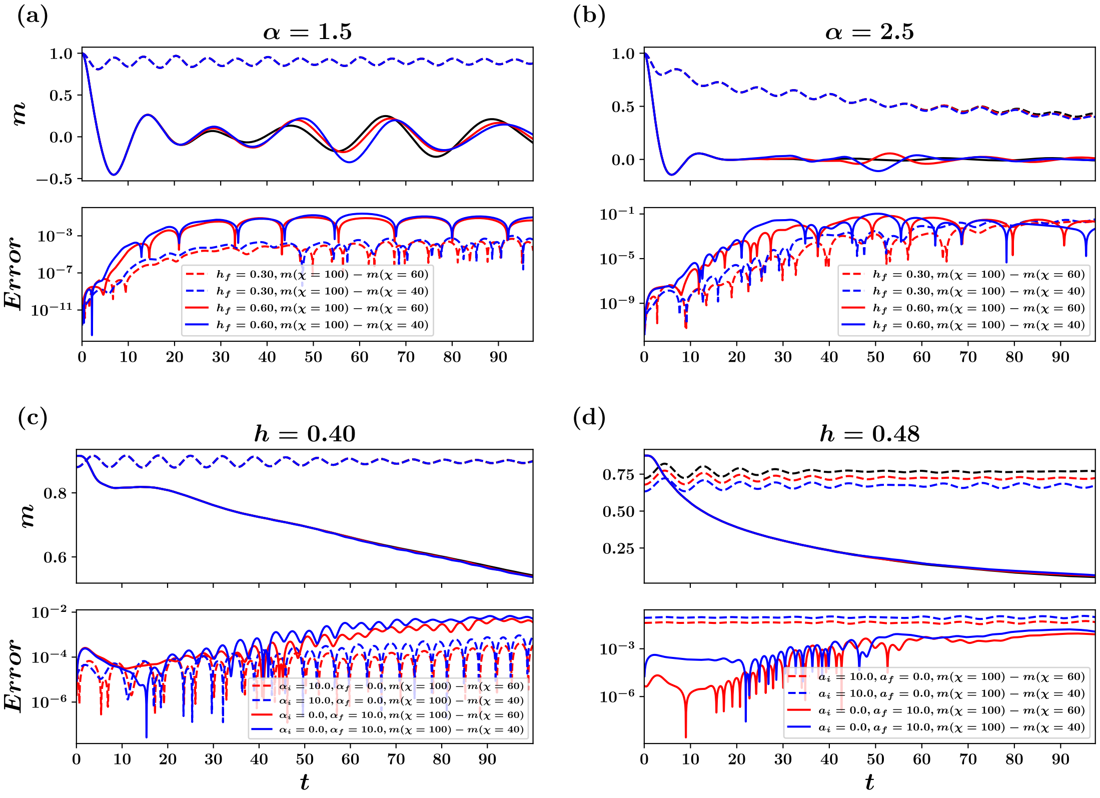

Figure 3.13: Convergence of subsystem magnetization and relative errors with increasing bond dimension, $\chi = 40$ (blue), $\chi = 60$ (red), and $\chi = 100$ (black). The top row is for $\alpha = \{1.5, 2.5\}$ and $h_f = 0.30$(colored dotted) , and $h_f = 0.60$(colored bold). The bottom row is for $h = \{0.40, 0.48\}$ and quench from $\alpha = 10.0$ to $\alpha = 0.0$ (colored dotted) $\alpha = 0.0$ to $\alpha = 10.0$ (colored bold)

In figure 3.14 we also plot the error in emptiness formation probability with respect to the exact analytical and numerical results at the two solvable extremes of the model. We observe that these errors are smaller than the order of $O(10^{-2})$ for the overall time evolution.

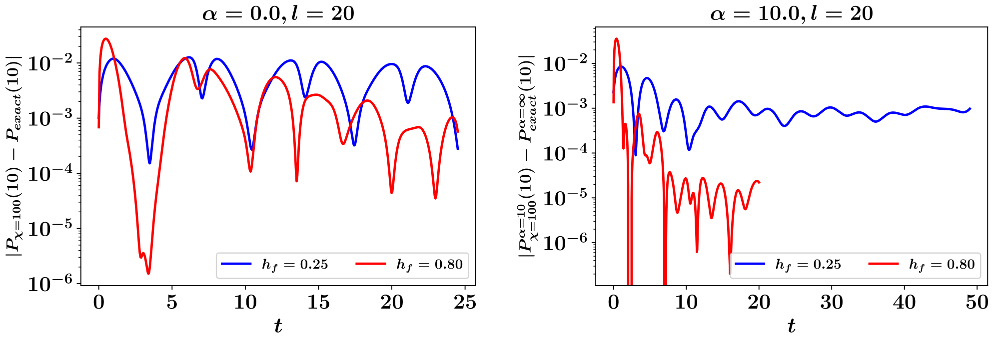

Figure 3.14: Errors in emptiness formation probability computed with bond dimension $\chi = 100$ with respect to the exact analytical and numerical results at two extremes of the LRIM for quenches to two values of final transverse fields. On the left panel the error is computed by subtracting the exact diagonalization results with the TDVP results, refer to figure 3.12. On the right panel the error is computed by subtracting the exact analytical results with the TDVP results computed for sufficiently large interaction range, $\alpha = 10$, refer to figure 3.11.

Chapter 4

Thermalization : a full counting statistics approach

The Isolated nonintegrable manybody systems are expected to thermalize, that is, the late time expectation value of a local observable equilibrate to the thermal value predicted by statistical mechanics [29, 31, 173, 30] (see Section 1.1 for a rigorous definition). However, the approach to thermalization is severely affected by different dynamical phenomena, such as many-body localization [39, 20, 21, 22] and confinement [174, 64, 23]. LRIM is non-integrable therefore, it is expected to thermalize. However, it also hosts strong confinement, which makes it a paradigmatic model for investigating the thermalization behavior. A previous study showed that LRIM exhibits prethermalization in the mean-field regime $\alpha < 1$ because of the emergence of two competing time scales with large separations [175, 52]. Furthermore, a strong prethermal regime was observed for LRIM in a system of trapped ions for $\alpha = 0.55$. However, in the previous chapter we observed a quick relaxation of the initial ferromagnetic order parameter in the dynamical paramagnetic regime with the emergence of Gaussian PDF of subsystem magnetization for larger α. Gaussification does not imply thermalization in general; however, the existence of a single timescale for equilibration is definitely a strong indication of thermalization. In contrast, in the dynamical ferromagnetic regime, the memory of the initial state was strongly retained owing to the confinement. A natural inquiry following these observations is whether the system exhibits thermalization in these different dynamical regimes. As detailed in Section 1.1.2 thermalization of a closed quantum system following a global quantum quench can be quantified with two equivalent conditions,

$$\lim_{t\to\infty} \mathrm{Tr}[\hat{\rho}(t)\hat{O}_{\mathrm{loc}}] \to \mathrm{Tr}[\hat{\rho}^{\mathrm{SS}}\hat{O}_{\mathrm{loc}}] = \frac{1}{N_{E_0,\Delta}} \sum_{|E_m - E_0| < \Delta} \langle m|\hat{O}_{\mathrm{loc}}|m\rangle. \tag{4.1}$$

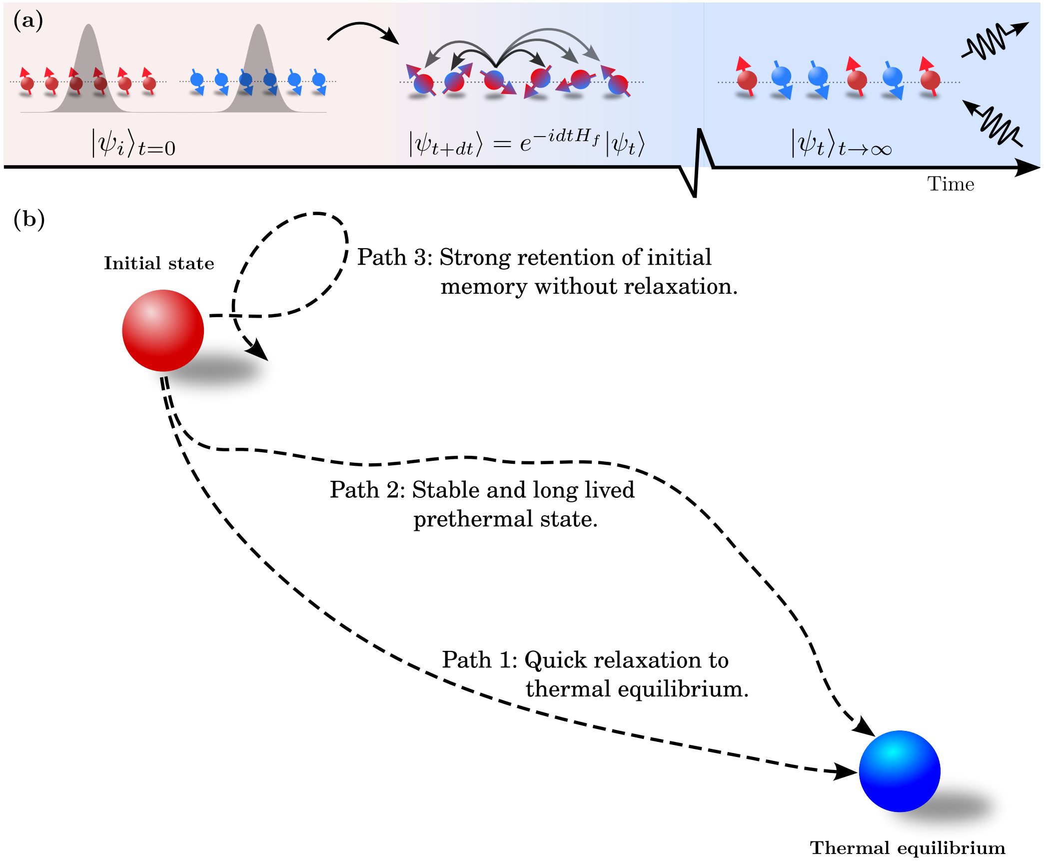

Figure 4.1: (a) Global Quench protocol: System is initialized as GHZ state, at time $t = 0$ the system is suddenly quenched to a final Hamiltonian $\hat{H}_f$ and the initial state is unitarily evolved with the final Hamiltonian. (b) The nonequilibrium state following a global quantum quench can exhibit different relaxation behavior; Path 1: a direct relaxation to thermal equilibrium with a single time scale, Path 2: a quick relaxation to a long lived prethermal state eventually followed a relaxation to thermal equilibrium, Path 3: a strong retention of initial memory and suppression of relaxation to thermal equilibrium.

$$\lim_{t\to\infty} \mathrm{Tr}[\hat{\rho}(t)\hat{O}_{\mathrm{loc}}] \to \mathrm{Tr}[\hat{\rho}^{\mathrm{SS}}\hat{O}_{\mathrm{loc}}] = \frac{\mathrm{Tr}[e^{-\beta_{\mathrm{eff}}\hat{H}}\hat{O}_{\mathrm{loc}}]}{\mathrm{Tr}[e^{-\beta_{\mathrm{eff}}\hat{H}}]}, \tag{4.2}$$

Equation (4.1) represents thermalization within the microcanonical ensemble (MCE). The summation includes all the eigenstates of the Hamiltonian within a narrow energy range Δ centered around the initial energy E_0. The normalization factor $N_{E_0,\Delta}$

counts the energy eigenstates within this range. By contrast, equation (4.2) implies thermalization within the canonical Gibbs ensemble (CGE). The parameter β_{eff} represents the inverse effective temperature, that is fixed by the initial energy of the system $E_0 = \frac{\text{Tr}[\hat{\rho}_{\beta_{\text{eff}}}\hat{H}]}{\text{Tr}[\hat{\rho}_{\beta_{\text{eff}}}]}$ (in a closed system, the energy remains constant). Constructing a microcanonical ensemble corresponding to a global quench is computationally demanding because it requires knowledge of all energy eigenstates of the post-quench Hamiltonian within the energy window Δ centered around E_0. This task is nontrivial and can scale exponentially with the system size depending on the location of E_0 in the spectrum of the post-quench Hamiltonian. By contrast, building a canonical Gibbs ensemble requires only modest numerical resources. The process of extracting β_{eff} corresponding to a global quench is detailed in Section 4.1.

Following the success of FCS in characterizing dynamical phases of LRIM, in this study we employ the PDF of the order parameter to access thermalization. PDF includes moments of all order and therefore its relaxation to the expected thermal PDF requires the collective relaxation of all the moments. Therefore this approach to study thermalization is more rigorous compared to the equilibration of the local expectations of order parameter. To evaluate thermalization, we introduce a metric termed "Distance to Thermalization," denoted as DT, similar to the metric "Distance to Gaussification" introduced in Section 3.2.1. This metric measures the Euclidean distance between the time-evolving PDF of the order parameter, denoted as $P_l(m,t)$, and the corresponding thermal PDF, represented as $P_l^{\text{TH}}(m)$. Mathematically, it is defined as

$$\text{DT}(t) = \sqrt{\sum_m [P_l(m,t) - P_l^{\text{TH}}(m)]^2}. \tag{4.3}$$

In instances where the system undergoes thermalization, DT(t) is expected to converge to zero. The real-time quench dynamics and TDVP parameters used are analogous to those explained in Section 3.2. The only difference is in the maximum bond dimension, which is set to $\chi_{\text{max}} = 128$. The accuracy of the data is tested in Appendix 4.B.2.

The rest of this chapter is organized as follows. In Section 4.1 we outline the extraction of effective temperature corresponding to a quantum quench. In Section 4.2 we present the results for quench to dynamical ferromagnetic phase (in Subsection 4.2.1) and dynamical paramagnetic phase (in Subsection 4.2.2). In Section 4.3 we present the post quench dynamics of domain wall kinks that provides addition support for our observation. In the final section we provide conclusion and outlook. The Appendix sections are as follows. In Appendix 4.A we outline the method to calculate time evolution of order parameter with exact diagonalization. In Appendix 4.B we provide details about the simulation. In Appendix 4.B.2 we outline the errors analysis for data in the main text. In Appendices 4.C and 4.D we briefly discuss the thermal phase transition in LRIM and the dynamics of correlation spreading respectively.

4.1 Numerical extraction of effective temperature

A global quantum quench, $\hat{H}_i(\alpha,0) \to \hat{H}_f(\alpha,h)$, in an isolated system adds an extensive amount of energy to the system. Consequently, the system relaxes to a state at a higher energy level than the ground state of the post-quench Hamiltonian [53].,

$$\lim_{N\to\infty} \frac{1}{N} \frac{\langle \psi_t | \hat{H}_f | \psi_t \rangle}{\langle \psi_t | \psi_t \rangle} > \lim_{N\to\infty} \frac{1}{N} \frac{\left\langle \psi_f^{\mathrm{GS}} \middle| \hat{H}_f \middle| \psi_f^{\mathrm{GS}} \right\rangle}{\left\langle \psi_f^{\mathrm{GS}} \middle| \psi_f^{\mathrm{GS}} \right\rangle} \tag{4.4}$$

where $\left| \psi_f^{\mathrm{GS}} \right\rangle$ is the ground state of the post-quench Hamiltonian $\hat{H}_f(\alpha,h)$. The left-hand side of Equation (4.4) is a conserved quantity because of the unitary real-time evolution of $|\psi_t\rangle$. For each global quantum quench, we can associate an effective temperature β_{eff}, which is the temperature at which the thermal energy density above the ground state of the post-quench Hamiltonian aligns with the conserved energy density of the system.

$$\frac{\langle \psi_t | \hat{H}_f | \psi_t \rangle}{\langle \psi_t | \psi_t \rangle} = \frac{\mathrm{Tr}(\hat{\rho}_\beta \hat{H}_f)}{\mathrm{Tr}(\hat{\rho}_\beta)}. \tag{4.5}$$

The effective temperature is determined by solving Equation (4.5). The left-hand side of the equation is calculated as $\langle \psi_t | \hat{H}_f | \psi_t \rangle = \langle \psi_i | e^{it\hat{H}_f} \hat{H}_f e^{-it\hat{H}_f} | \psi_i \rangle = \langle \psi_i | \hat{H}_f | \psi_i \rangle$. On the other hand, the right-hand side can be computed for a range of β values by numerically solving Equation (4.18) and calculating the energy density at each instance. The precision of β_{eff} depends on the trotter steps $d\beta$ in the solution of Equation (4.18). In Fig. 4.2, we present the numerical solution of Equation (4.5). The energy density attributed to quench, represented by the black dashed line, is independent of the post-quench parameters because the spin-spin interaction term in the Hamiltonian (1.15) is normalized with Kac normalization (1.16), whereas the expectation value $h \langle \psi_i | \sum_j \hat{s}_j^z | \psi_i \rangle$ taken over the transverse field term is trivially zero. If we extend the simulation to a larger β (i.e., lower temperature), all curves will converge to the ground-state energy density of $\hat{H}_f$ at the corresponding post-quench parameters. Once βeff is extracted, we can calculate the corresponding thermal PDF $P^{\mathrm{TH}}(m) = P_{\beta_{\text{eff}}}(m)$. The accuracy of the thermal states is tested by comparing with the exact results for 14 site system in Appendix 4.B.2 figure 4.12.

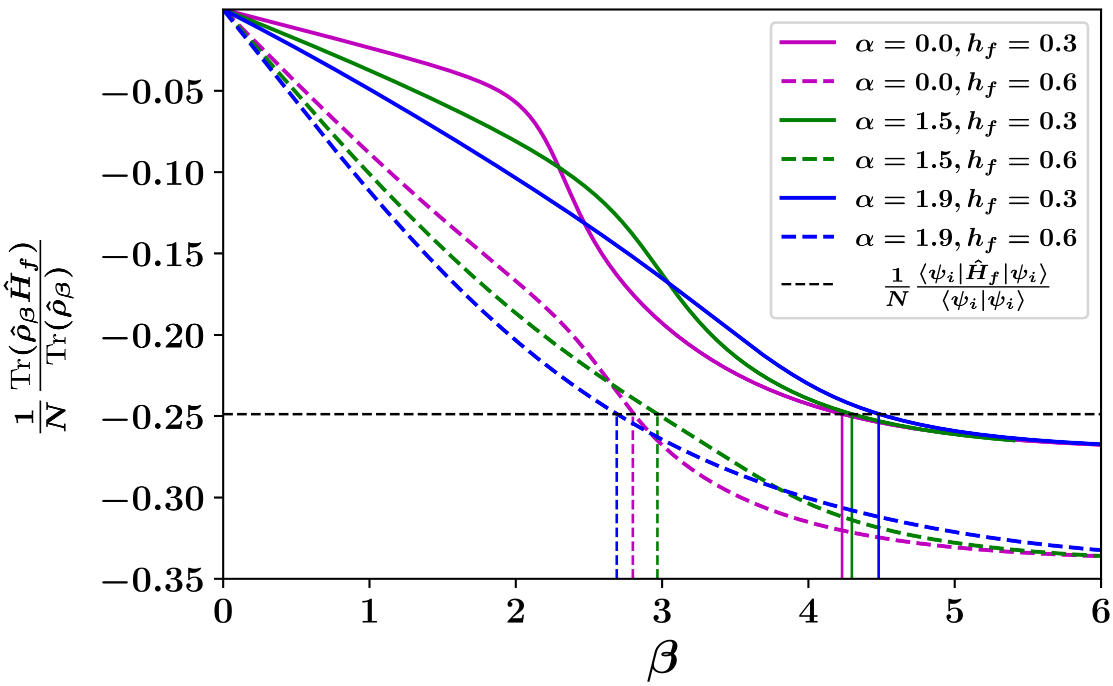

Figure 4.2: Numerical extraction of β_{eff} corresponding to a global quantum quench. The horizontal black dashed line represent the energy density attributed to the quench. The colored lines represents the energy density as the function of inverse temperature β for the corresponding post-quench parameter (in legend). The point at which the colored lines intersects the black dashed lines represents β_{eff} for the corresponding post-quench parameters (represented by vertical colored lines).

4.2 Results

We investigate quantum quenches starting from a GHZ state to two representative post-quench transverse field points: one located in the dynamical ferromagnetic regime at $h_f = 0.3$ and the other in the dynamical paramagnetic regime at $h_f = 0.6$ [17, 12]. We consider three distinct values for the interaction strength: $\alpha \in \{0.0, 1.5, 1.9\}$. At $\alpha = 0.0$, the system exhibits integrability owing to its full connectivity and complete permutation symmetry, leading to a lack of thermalization. Conversely, the choices of $\alpha = 1.5$ and $\alpha = 1.9$ are motivated by the relatively faster equilibration and Gaussification of the PDF following a quench in the dynamical paramagnetic phase, as observed previously [12].

4.2.1 Quench to dynamical ferromagnetic regime

Figure 4.3 shows the temporal evolution of DT(t) following a global quantum quench of the transverse field to $h_f = 0.3$ with $\alpha = 0.0, 1.5, 1.9$ for three subsystem sizes $l = 20, 60, 100$. Notably, all of these points fall within the dynamical ferromagnetic phase, as established in previous studies [17, 12]. For all three quenches, we observe a persistent oscillation in DT(t), indicating a robust retention of the initial ferromagnetic order and delayed thermalization. This behavior aligns with the relaxation mode represented by Path 3 in figure. 4.1(b). Specifically, for $\alpha = 0.0$, which is an integrable point, the absence of thermalization is anticipated [29, 31], whereas quenches with $\alpha = 1.5$ and $\alpha = 1.9$ are expected to thermalize. This behavior is attributed to the confinement induced by the long range interaction of the model, which effectively bounds low-energy domain wall kinks into heavier quasiparticles that typically travel slower than free quasiparticles, thereby suppressing the

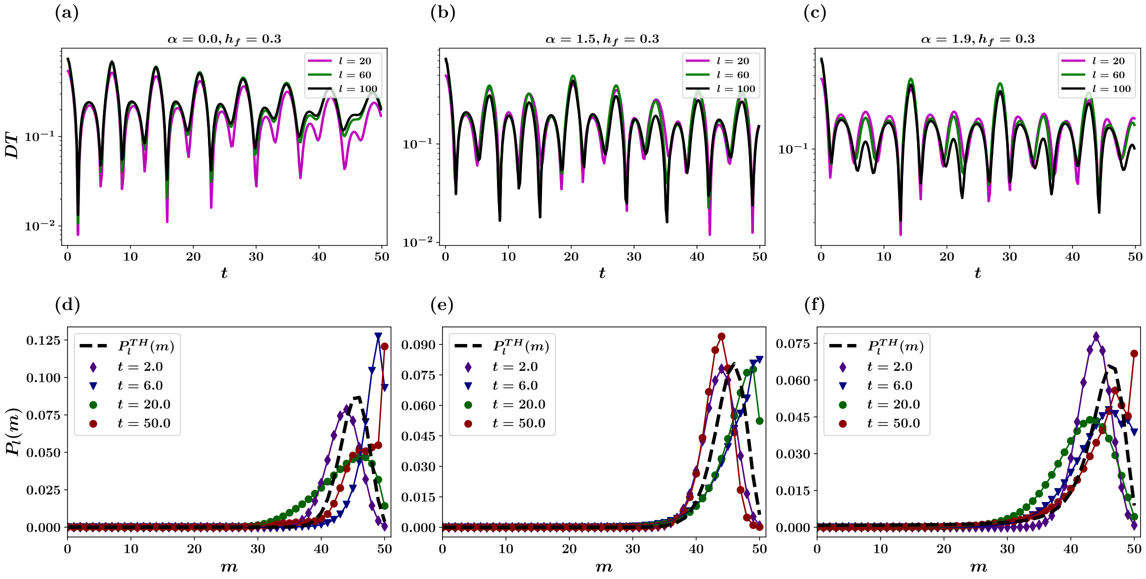

Figure 4.3: First row: Time evolution of the metric DT(t) following a global quantum quench to three interaction strength values $\alpha \in \{0.0, 1.5, 1.9\}$ and transverse field $h_f = 0.3$ at three different subsystem sizes $l = \{20, 60, 100\}$. All three points are in dynamical ferromagnetic phases[17, 12]. Second row: $P_l(m)$ versus m for $m \in [0, l/2]$ with $l = 100$ at four time different slices $t = \{2, 6, 20, 50\}$. $P_l(m)$ versus m for $m \in [-l/2, 0)$ is its mirror image. The black dashed curve represents the thermal PDF, $P^{\mathrm{TH}}(m)$ attributed to the corresponding global quantum quenches.

spread of correlations in the system [60, 61]. Consequently, although thermalization is still expected, it occurs at significantly longer time scales [23]. Appendix 4.D provides more insights into the confinement behavior in LRIM, demonstrating a strong temporal suppression in the spreading of connected correlation function $\left\langle \hat{s}^x_k \hat{s}^x_{k+\Delta} \right\rangle_c$ for $\alpha = 1.9$ and $h_f = 0.3$. The confinement behavior of the LRIM is explained in detail in Section 5.2. In panels (d), (e), and (f), the colored scattered plots depict $P_l(m)$ as a function of m at four distinct time intervals post-quench. The black dashed curve represents the PDF of the expected thermal state, $P_l^{\mathrm{TH}}(m)$. Notably, the time-evolving $P_l(m)$ persistently oscillates around $P_l^{\mathrm{TH}}(m)$ in all the three cases. Of particular importance is the observation that in all cases, the thermal PDFs are bimodal, indicating the presence of long-range ferromagnetic order, which suggests that if the system eventually thermalizes at extended time scales, it would still exhibit a long-range ferromagnetic order. This finding further strengthens the argument that this is indeed a dynamical ferromagnetic phase.

4.2.2 Quench to dynamical paramagnetic regime

Figure 4.4 depicts the temporal evolution of $\mathrm{DT}(t)$ following a global quantum quench of the transverse field to $h_f = 0.6$, with $\alpha = 0.0, 1.5, 1.9$ for subsystem sizes $l = 20, 60, 100$. Notably, these quenches are situated within the dynamical paramagnetic phase [17, 12]. We observe a distinctive relaxation behavior of $\mathrm{DT}(t)$ compared to the previous cases. In panel (a), rapid equilibration is evident for all the values of l. However, it is crucial to note that $\mathrm{DT}(t)$ remains at or above the order of $O(10^{-1})$ after equilibration, suggesting a lack of thermalization. This behavior is expected because $\alpha = 0$ is an integrable point. For $\alpha = 1.5$, $\mathrm{DT}(t)$ does not exhibit stable equilibration, as shown in panel (b). In the case of $\alpha = 1.9$, $\mathrm{DT}(t)$ equilibrates for $l = 60, 100$ and exhibits stable oscillation around a constant value of approximately $O(10^{-3})$ as depicted in panel (c). A more comprehensive picture is shown in panel (f), where the late-time PDF perfectly overlaps with the corresponding thermal PDF, represented by a black dashed curve. This is indicative of thermalization; however, the system still exhibits traces of confinement [63, 14]. In Appendix 4.D, the connected correlation function $\left\langle \hat{s}^x_k \hat{s}^x_{k+\Delta} \right\rangle_c$ for $\alpha = 1.9$ and $h_f = 0.6$ still exhibits a weaker temporal suppression. A recent study observed a de-confinement transition for a system with up to 31 spins only at a much higher value of the transverse field [63]. This suggests that while strong confinement severely hinders the approach to thermalization, the signatures of thermalization can still be detected in the presence of weak confinement.

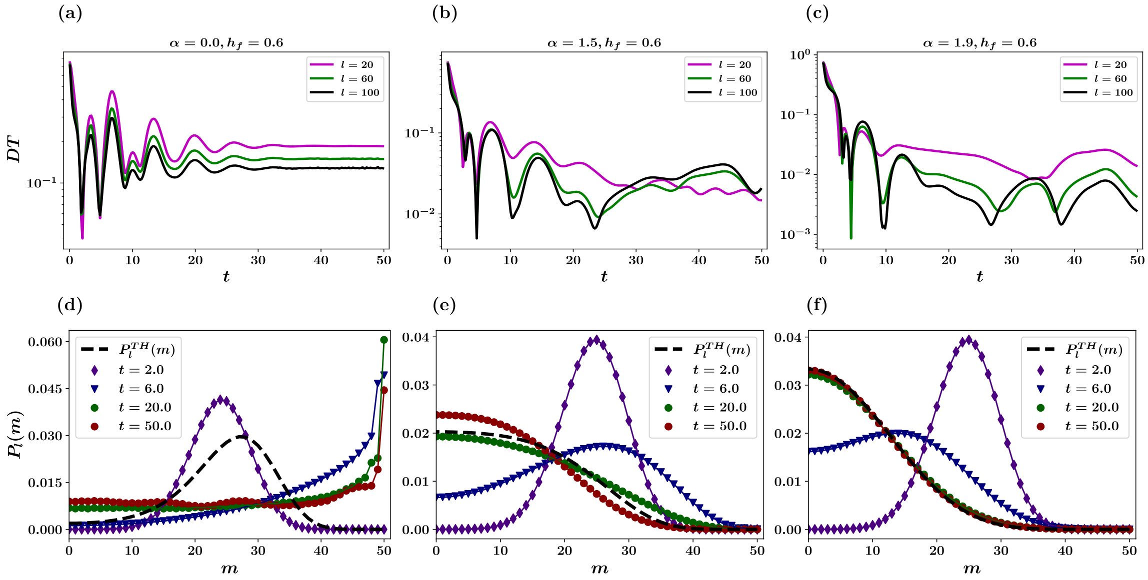

Figure 4.4: First row: Time evolution of the metric DT(t) following a global quantum quench to three interaction strength values $\alpha \in \{0.0, 1.5, 1.9\}$ and transverse field $h_f = 0.6$ at three different subsystem sizes $l = \{20, 60, 100\}$. All three points are in dynamical paramagnetic phases[17, 12]. Second row: $P_l(m)$ versus m for $m \in [0, l/2]$ with $l = 100$ at four time different slices $t = \{2, 6, 20, 50\}$. $P_l(m)$ versus m for $m \in [-l/2, 0)$ is its mirror image. The black dashed curve represents the thermal PDF, $P^{\mathrm{TH}}(m)$ attributed to the corresponding global quantum quenches.

4.3 Signatures in domain wall kink

To further support our observations, we investigate the post-quench evolution of domain wall kinks defined as

$$\hat{K} = \sum_{j=1}^{l-1} \frac{1 - \hat{s}_i^x \hat{s}_{i+1}^x}{2}. \tag{4.6}$$

Here, $\hat{K}$ quantifies the number of nearest neighbor domain wall kinks within the subsystem l. Domain wall kinks are elementary excitations that are bound into heavier quasiparticles due to confinement; therefore, this is a relevant order parameter [174, 64, 63]. In Figure 4.5, we present the temporal evolution of the average domain wall kinks following a global quantum quench. As expected, quenches to the dynamical ferromagnetic phase with $h_f = 0.3$ exhibit persistent oscillations around

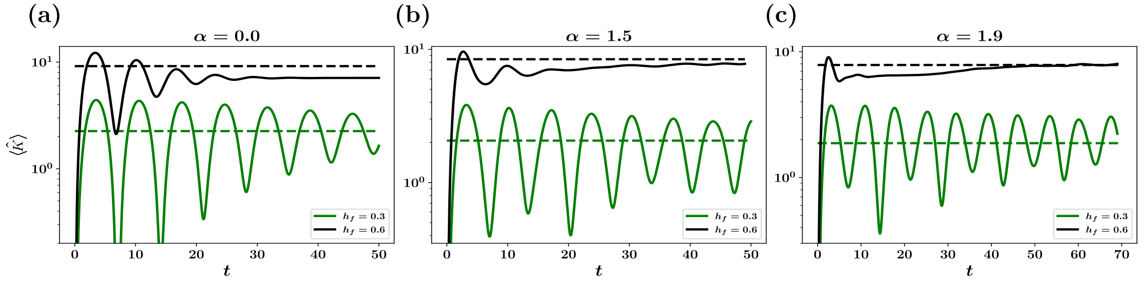

Figure 4.5: Time evolution of domain wall kinks, $\langle \hat{K} \rangle$, following a global quantum quench to three interaction strength values $\alpha \in \{0.0, 1.5, 1.9\}$ (Panels (a), (b), and (c) respectively) and $h_f = 0.3$ and $h_f = 0.6$. The dashed horizontal lines represent the expected thermal value of domain wall kinks, $\langle \hat{K} \rangle^{\text{TH}}$ corresponding to the quenches.

the expected thermal value, indicating a lack of thermalization. By contrast, for quenches to the dynamical paramagnetic phase with $h_f = 0.6$, distinct post-quench behavior is observed. For $\alpha = 0$, the domain-wall kinks equilibrate to a stable value that differs from the expected thermal value, which is consistent with its integrable nature. This observation complements the post-quench behavior of DT, as shown in Figure 4.4(a). Although $\alpha = 1.5$ is a non-integrable point, thermalization is not observed within the simulation time. At later times, a stable prethermal plateau, close but distinct from the expected thermal value, becomes apparent. Conversely, for a quench corresponding to $\alpha = 1.9$, the average domain wall kinks converge to the expected thermal value. Notably, before reaching the thermal value, the kink density exhibits a relatively stable prethermal plateau until time $t \simeq 35$. This relaxation mode, which is characterized by two time scales, is represented by Path 2 in figure 4.1 panel (b). This discovery provides another robust indicator of thermalization in weakly confined regimes.

4.4 Conclusions

We explored the relaxation dynamics of the LRIM following a global quantum quench of the transverse field and assessed thermalization on a computationally viable timescale within the canonical Gibbs ensemble (CGE). The model is non-integrable and is therefore expected to thermalize. However, the presence of confinement in the long-range Ising model strongly suppresses correlation spreading. Starting from the GHZ state, the system was subjected to two distinct dynamical regimes. As anticipated, robust confinement hindered thermalization in the dynamical ferromagnetic region. In this region, metric DT exhibits persistent oscillation characteristics of the masses of bound mesons. Conversely, for quenches to the dynamical paramagnetic region, a notably distinct behavior emerges. The persistent oscillation melts and DT relaxes more rapidly. While conclusive evidence of thermalization for $\alpha = 1.5$ is not observed within the simulation time, there are compelling indications of the thermalization surface for $\alpha = 1.9$. This observation received additional support from the convergence of the domain-wall kinks to the expected thermal value. In the dynamical ferromagnetic phase confinement strongly hinders the approach to thermalization. In the next section, we study the robustness of confinement against the thermally tuned density of excitations and investigate whether it can destroy confinement such that thermalization can be observed.

In this Chapter, we highlighted the convergence of the PDF of the local order parameter as a rigorous condition for thermalization because it involves the convergence of all underlying moments. In an interesting new experimental study [152] it was observed that the fluctuation of observables in the subsystem thermalizes at different timescales compared to the local observables. It will be interesting to study the relaxation dynamics of the full PDF in such models and compare the relaxation timescale of the PDF with relaxation timescales of different moments.

4.A Exact time evolution

For smaller system sizes we can calculate the time evolution of FCS and other relevant order parameters by exact diagonalization of the post-quench Hamiltonian. We begin from our initial state, $\mathbb{Z}_2$ symmetric GHZ state,

$$|\psi_i\rangle = \frac{1}{\sqrt{2}}(|\rightarrow, \ldots \rightarrow, \rightarrow, \rightarrow \ldots, \rightarrow\rangle^x + |\leftarrow, \ldots \leftarrow, \leftarrow, \leftarrow \ldots, \leftarrow\rangle^x). \tag{4.7}$$

The time evolved state is given by $|\psi_t\rangle = e^{-it\hat{H}} |\psi_i\rangle$, where $\hat{H}$ is the post-quench Hamiltonian. We proceed by expanding $|\psi_0\rangle$ in the eigenbasis, $\{\, |E_j\rangle \,\}$,of the post-quench Hamiltonian,

$$|\psi_i\rangle = \sum_{j=0}^{2^N-1} k_j \, |E_j\rangle \,, \tag{4.8}$$

where $k_j = \langle E_j|\psi_i\rangle$. Expanding $|E_j\rangle$ in the computational basis, $|E_j\rangle = \sum_n c_n^j \, |n\rangle$, we can derive the expression for k_j as,

$$k_j = \langle E_j|\psi_i\rangle = \frac{\left(c^j_{|\rightarrow,\ldots,\rightarrow\rangle}\right)^* + \left(c^j_{|\leftarrow,\ldots,\leftarrow\rangle}\right)^*}{\sqrt{2}}. \tag{4.9}$$

The post-quench state is

$$|\psi_t\rangle = \sum_n X_n(t)\,|n\rangle \tag{4.10}$$

where $X_n(t) = \sum_{j=0}^{N} k_j c^j_n e^{-iE_j t}$. The generating function of subsystem magnetization is then calculated as,

$$G_l(\theta,t) = \langle\psi_t|\, e^{i\theta\hat{M}(l)}\,|\psi_t\rangle = \sum_{n,\tilde{n}} X^\dagger_{\tilde{n}}(t) X_n(t)\,\langle\tilde{n}|\, e^{i\theta\hat{M}(l)}\,|n\rangle \tag{4.11}$$

$$= \sum_n |X_n(t)|^2 e^{i\theta m_n}. \tag{4.12}$$

The computational basis ket $|n\rangle$ is a simultaneous eigenket of the subsystem magnetization, $\hat{M}_l\,|n\rangle = m_n\,|n\rangle$, where m_n is the magnetization of the subsystem l. We can also access the time evolution of the expectation value of a generic parameter $\hat{O}$ as,

$$O(t) = \langle\psi_t|\,\hat{O}\,|\psi_t\rangle = \sum_{n,\tilde{n}} X^\dagger_{\tilde{n}}(t) X_n(t)\,\langle\tilde{n}|\,\hat{O}\,|n\rangle\,. \tag{4.13}$$

If $|n\rangle$ is the eigenket of the order parameter $\hat{O}$ then 4.13 becomes,

$$O(t) = \sum_n |X_n(t)|^2 O_n. \tag{4.14}$$

Finally, with the full eigenvalues of hamiltonian at hand we can also calculate the energy density corresponding to a thermal density matrix $\hat{\rho}_\beta$,

$$\epsilon_\beta = \frac{\sum_j E_j e^{-\beta E_j}}{\sum_j e^{-\beta E_j}}. \tag{4.15}$$

4.B Simulations details

In this Section we present the details of numerical simulation complementary to the results in the main text.

4.B.1 Simulation of finite temperature density operator

The finite temperature states can be simulated by casting the density operator as locally purified tensors [116, 117, 176]. The thermal density operator is defined by Gibbs distribution $\hat{\rho}_\beta = \frac{e^{-\beta\hat{H}}}{\mathrm{Tr}[e^{-\beta\hat{H}}]}$ where $\beta = \frac{1}{T}$ is the inverse temperature. At $\beta = 0$ (infinite temperature) the state is maximally mixed and is given as the tensor product of local identities $\hat{\rho}_0 = \bigotimes_{i=1}^{N} \mathbf{1}^{\sigma'_i,\sigma_i} = \mathbb{I}$, where each $\mathbf{1}^{\sigma'_i,\sigma_i}$ is a unit matrix of size (d, d), i.e. $\mathbf{1}^{\sigma'_i,\sigma_i} = [\delta_{\sigma'_i,\sigma_i}]_{d\times d}$ and d is the dimension of the physical space (for spin $\frac{1}{2}$, $d = 2$). The density operator for any finite temperature (non-zero β) is

$$\hat{\rho}_\beta \propto e^{-\beta\hat{H}} = e^{-\frac{\beta}{2}\hat{H}}\mathbb{I}e^{-\frac{\beta}{2}\hat{H}} \tag{4.16a}$$

$$\propto e^{-\frac{\beta}{2}\hat{H}}\hat{\rho}_0 e^{-\frac{\beta}{2}\hat{H}} \tag{4.16b}$$

We keep the density operator operator in locally purified form $\hat{\rho} = \mathbb{X}\mathbb{X}^\dagger$ at each stage where $\mathbb{X}$ is represented as tensor

$$\mathbb{X}^{\sigma_1,\sigma_2,\ldots\sigma_i,\ldots,\sigma_N}_{k_1,k_2,\ldots,k_i,\ldots,k_N} = \mathbf{X}^{\sigma_1,k_1}_{c_0,c_1}\mathbf{X}^{\sigma_2,k_2}_{c_1,c_2}\ldots\mathbf{X}^{\sigma_i,k_i}_{c_{i-1},c_i}\ldots\mathbf{X}^{\sigma_N,k_N}_{c_{N-1},c_N} \tag{4.17}$$

where $\sigma_i = d$, $k_i = d$ are the physical index and the Kraus index are are fixed through out and $1 \leq c_i \leq \chi_{max}$ is the bond index and χ_{max} is the maximum value of bond dimension. The density operator initialized at infinite temperature can now be purified to a finite temperature in trotterized steps

$$\hat{\rho}_{\beta+d\beta} = e^{-\frac{d\beta}{2}\hat{H}}\hat{\rho}_\beta e^{-\frac{d\beta}{2}\hat{H}} \tag{4.18a}$$

$$= e^{-\frac{d\beta}{2}\hat{H}}\mathbb{X}_\beta\mathbb{X}^\dagger_\beta e^{-\frac{d\beta}{2}\hat{H}} \tag{4.18b}$$

$$= e^{-\frac{d\beta}{2}\hat{H}}\mathbb{X}_\beta[e^{-\frac{d\beta}{2}\hat{H}}\mathbb{X}_\beta]^\dagger \tag{4.18c}$$

Equation (4.18) can be simulated using imaginary time TDVP ($-idt \to -d\beta$) in only the half Section of the density operator operator and never contracting the $\mathbb{X}$ and $\mathbb{X}^\dagger$ layer during the evolution, thus strictly preserving the locally purified form.

At infinite temperature ($\beta = 0$) the state is maximally mixed. Figure 4.6 shows the tensor notation of the maximally mixed density operator $\hat{\rho}_{\beta=0}$ which is a tensor product of identity matrices of size (d, d), where d is the physical dimension. Rather than working with the density operator as an MPO we represent the density operator in the locally purified form [176, 177] which is positive semi-definite by construction and keep it in locally purified form at every stage of the thermal purification process.

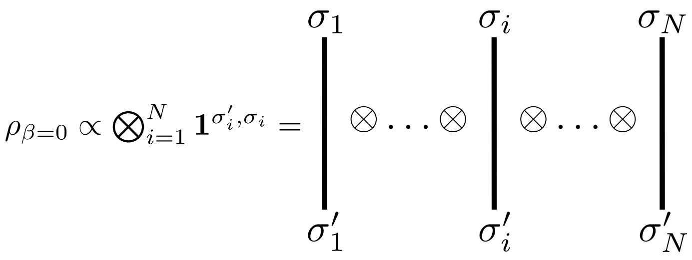

Figure 4.6: Maximally mixed density operator at $\beta = 0$ as the tensor product of local identities.

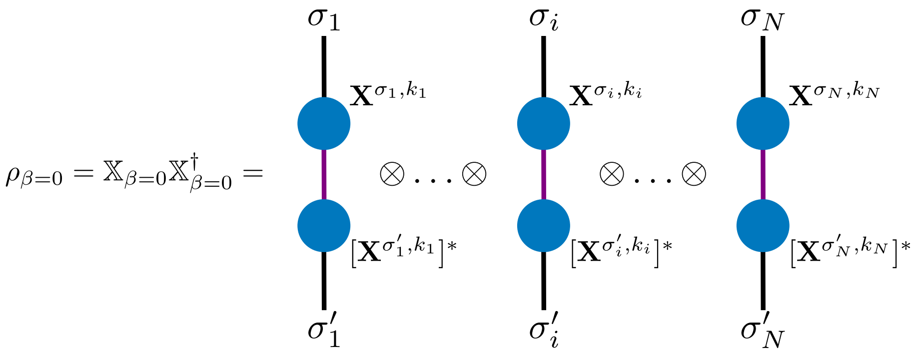

Figure 4.7: Representing $\hat{\rho}_{\beta=0}$ in the locally purified form.

In Fig. 4.7 we represent $\hat{\rho}_{\beta=0}$ in the locally purified form $\mathbb{X}_{\beta=0}\mathbb{X}^{\dagger}_{\beta=0}$, where the index in purple is an auxiliary index called the Krauss index.

we can now evolve one of the halves ($\mathbb{X}$ or $\mathbb{X}^{\dagger}$) as shown in equation (4.18) and the evolution on the other half is its trivial conjugate. This approach is computationally efficient as we can work with cheaper MPS instead of more expensive MPDO. In Fig. 4.8 one half of the $\hat{\rho}_{\beta=0}$ in locally purified form is shown, form here on we will only work with this half.

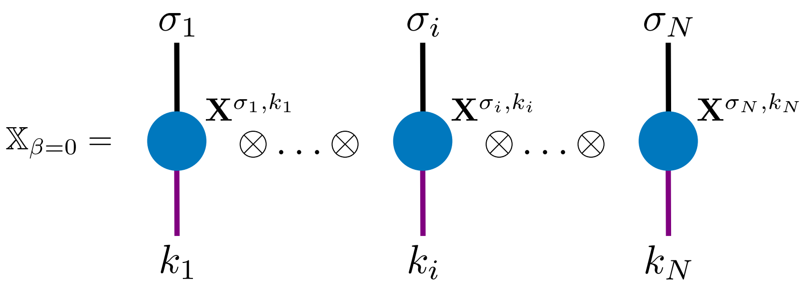

Figure 4.8: One half of the $\hat{\rho}_{\beta=0}$ in the locally purified form.

Algebraically, $\mathbb{X}_{\beta=0}$ can be written as

$$\mathbb{X}^{\sigma_1,k_1,\ldots\sigma_i,k_i,\ldots,\sigma_N,k_N} = \mathbf{X}^{\sigma_1,k_1} \otimes \ldots \mathbf{X}^{\sigma_i,k_i} \ldots \otimes \mathbf{X}^{\sigma_N,k_N} \tag{4.19}$$

For the system of spin one-half particles we choose A as

$$\mathbf{X}^{\sigma_i,k_i} = \frac{1}{\sqrt{2}} \begin{pmatrix} 1 & 0 \\ 0 & 1 \end{pmatrix} \qquad \forall\, i \in \{1, 2, \ldots, N\} \tag{4.20}$$

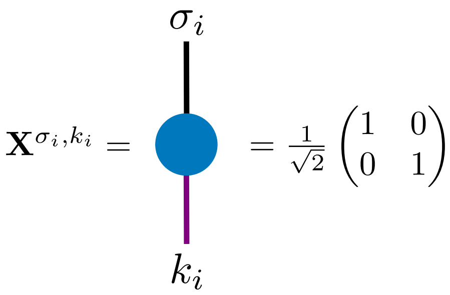

Figure 4.9: Choice of $\mathbf{X}^{\sigma_i,k_i}$ to preserve the trace of $\hat{\rho}$.

as shown in Fig. 4.9. This particular choice is taken to preserve the trace of the density operator,

$$\sum_k \mathbf{X}^{\sigma,k}[\mathbf{X}^{\sigma',k}]^* = \frac{1}{2} \begin{pmatrix} 1 & 0 \\ 0 & 1 \end{pmatrix}. \tag{4.21}$$

Finally, we reshape $\mathbb{X}_{\beta=0}$ from a string of 2×2 matrices to a string of four legged tensors of shape $(1, 2, 2, 1)$ as shown in Fig. 4.10, which is an MPS of unit bond dimension.

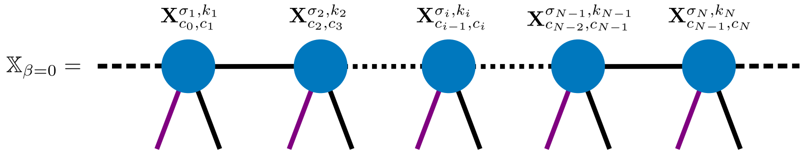

Figure 4.10: $\mathbb{X}_{\beta=0}$ in MPS form.

Now that we have our initial state as an MPS, we can simulate a finite temperature density operator by solving the equation (4.18),

Numerically, equation (4.18) can be solved for long-range spin systems through imaginary time evolution, (where $idt \to d\beta$) using the Time-Dependent Variational

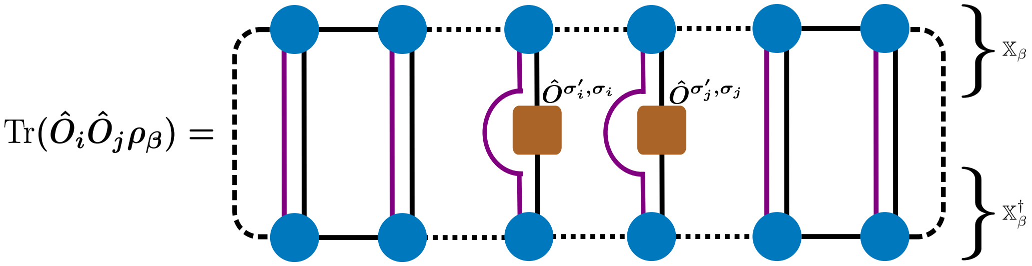

Figure 4.11: Expectation of the local operator $\hat{O}_i$ in thermal density operator $\hat{\rho}_\beta$

Principle (TDVP). The TDVP algorithm employed for simulating the thermal state remains fundamentally identical to that used for the real-time evolution of the pure state, with the distinction of an additional auxiliary Krauss index. However, in the thermal purification of a closed system, the Krauss index is obsolete because all physical operators act solely on the physical index. The Krauss indices are therefore traced over [176]. Figure 4.11 illustrates the tensor network diagram for computing the expectation value of a two point operator $\hat{O}_i\hat{O}_j$ acting on site i and j within the thermal state $\hat{\rho}_\beta$.

4.B.2 Errors and data convergence

We conducted two types of error analysis to assess the accuracy of the numerical results. In figure 4.12, we assess the absolute error of the TDVP algorithm in comparison with the numerically exact full diagonalization results for a system with size $N = 14$ and various post-quench parameters. Figure 4.12, panel (a), shows the absolute error in the energy density of the thermal states, defined as $|\epsilon_\beta^{\mathrm{ED}} - \epsilon_\beta^{\mathrm{TDVP}}|$. The absolute error remains of the order $O(10^{-5})$ or smaller across the entire temperature range under consideration. Figures 4.12, (b), (c), and (d) show the absolute error in domain wall kinks, defined as $|\langle\hat{K}\rangle^{\mathrm{ED}} - \langle\hat{K}\rangle^{\mathrm{TDVP}}|$, following a quantum quench to various post-quench parameters. $\langle\hat{K}\rangle$ is defined in equation 4.6. Notably, the error rapidly converge and is of order $O(10^{-6})$ or smaller for all the cases studied.

In Figure 4.13, we investigate the convergence of the TDVP data for $\mathrm{DT}(t)$ by computing the relative errors $|\mathrm{DT}^{\chi_1}(t) - \mathrm{DT}^{\chi_2}(t)|$ for three increasing bond dimensions. Our observations reveal that the relative error eventually converges and consistently remains in the order $O(10^{-3})$ or smaller for all cases. It is noteworthy that the error for $\alpha = 0.0$ is several orders of magnitude smaller than that for the other values of α. This is attributed to $\alpha = 0.0$ being an integrable point with an extensive number of conserved quantities, and therefore has a smaller Hilbert space to be explored compared to non-integrable points. Furthermore, for $\alpha = \{1.5, 1.9\}$, the

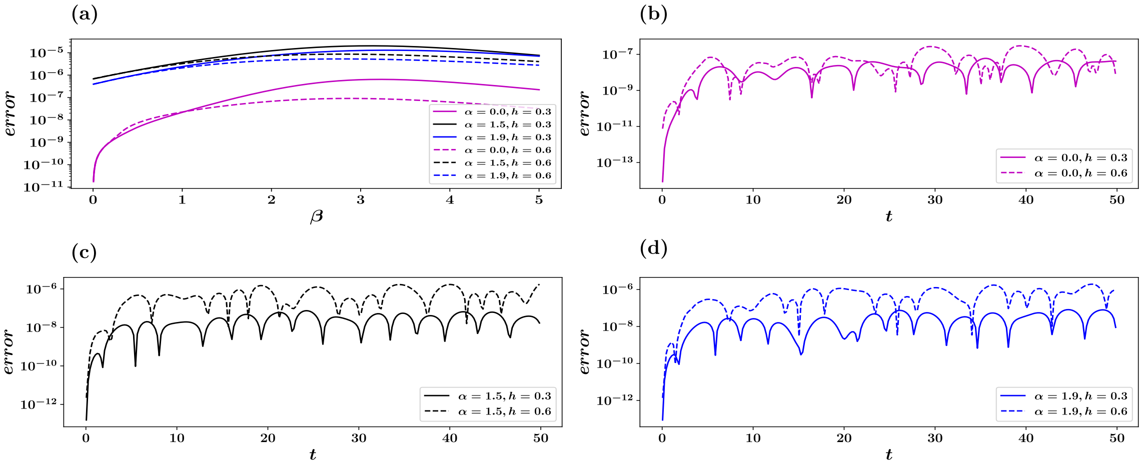

Figure 4.12: Absolute error in the energy density,$|\epsilon_\beta^{\text{ED}} - \epsilon_\beta^{\text{TDVP}}|$, of thermal states - (a). Absolute errors in the evolution domain wall kinks $|\langle \hat{K} \rangle^{\text{ED}} - \langle \hat{K} \rangle^{\text{TDVP}}|$ following a quantum quench - (b),(c),(d). The numerically exact results are calculated using equations 4.14 and 4.15 as detailed in 4.A. TDVP results are obtained with bond dimension $\chi = 128$. The system size considered is N=14.

error for $h_f = 0.3$ is approximately two orders of magnitude smaller than that for $h_f = 0.6$. This discrepancy arises because the former case exhibits dynamical confinement, which effectively suppresses the spread of correlations and constrains the total Hilbert space that can be explored during time evolution.

4.C Thermal phase transition in long range Ising model

For values of $\alpha > 2$, the long-range Ising model falls within the regime of short-range interactions and does not exhibit any finite-temperature phase transitions [178]. Extensive investigations into the critical properties of the thermal phase transition in the quantum long-range Ising model have been conducted using numerically exact path integral Monte Carlo methods [179]. The thermal phase transition is qualitatively depicted in Figures 4.14 for specific parameter values: $\alpha = 1.5, 1.9$ and $h = 0.3, 0.6$. As described in Section 4.B.1, the simulation begins with a maximally mixed state at $\beta = 0$. This initial state is characterized by a sharply peaked Gaussian distribution of $P(m)$ centered around $m = 0$, which signifies a strongly paramagnetic

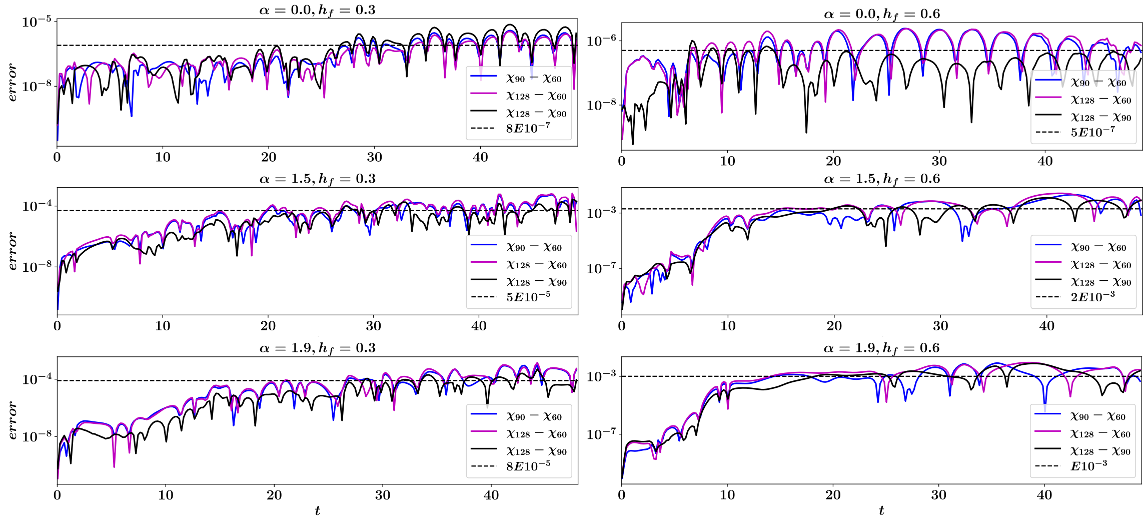

Figure 4.13: Convergence of the TDVP data for DT(t) with increasing bond dimensions, $\chi = 60, 90, 128$, for six different post-quench parameters considered in the main text. The black dashed line is for visual guidance.

phase. As the system is gradually cooled by increasing β, the distribution gradually widens, eventually becoming nearly flat around the critical temperature. A further reduction in temperature leads to the emergence of a bimodal distribution of $P(m)$, which is indicative of the ferromagnetic phase. Notably, this transition from a unimodal Gaussian distribution to a bimodal distribution highlights the $\mathbb{Z}_2$ symmetry that is inherent in the long-range Ising Hamiltonian.

4.D Confinement dynamics in different regimes

Confinement phenomena in the long-range Ising model result from ferromagnetic interactions extending over long distances between the interacting spins. However, the strength of confinement varies within different regions of the phase space [60, 61]. In this Section, we present comprehensive numerical results pertaining to the temporal spreading of correlations in the long-range Ising chain following a sudden quench to various post-quench Hamiltonians starting from a fully polarized initial state denoted as $|\psi_i\rangle = |\leftarrow, \leftarrow, \ldots, \leftarrow, \ldots, \leftarrow, \leftarrow\rangle^x$.

Figure 4.14 illustrates the time evolution of the half chain connected correlation function $\left\langle \hat{s}^x_k \hat{s}^x_{k+\Delta} \right\rangle_c = \left\langle \hat{s}^x_k \hat{s}^x_{k+\Delta} \right\rangle - \langle \hat{s}^x_k \rangle \left\langle \hat{s}^x_{k+\Delta} \right\rangle$ in a chain of 200 spins, where k is kept

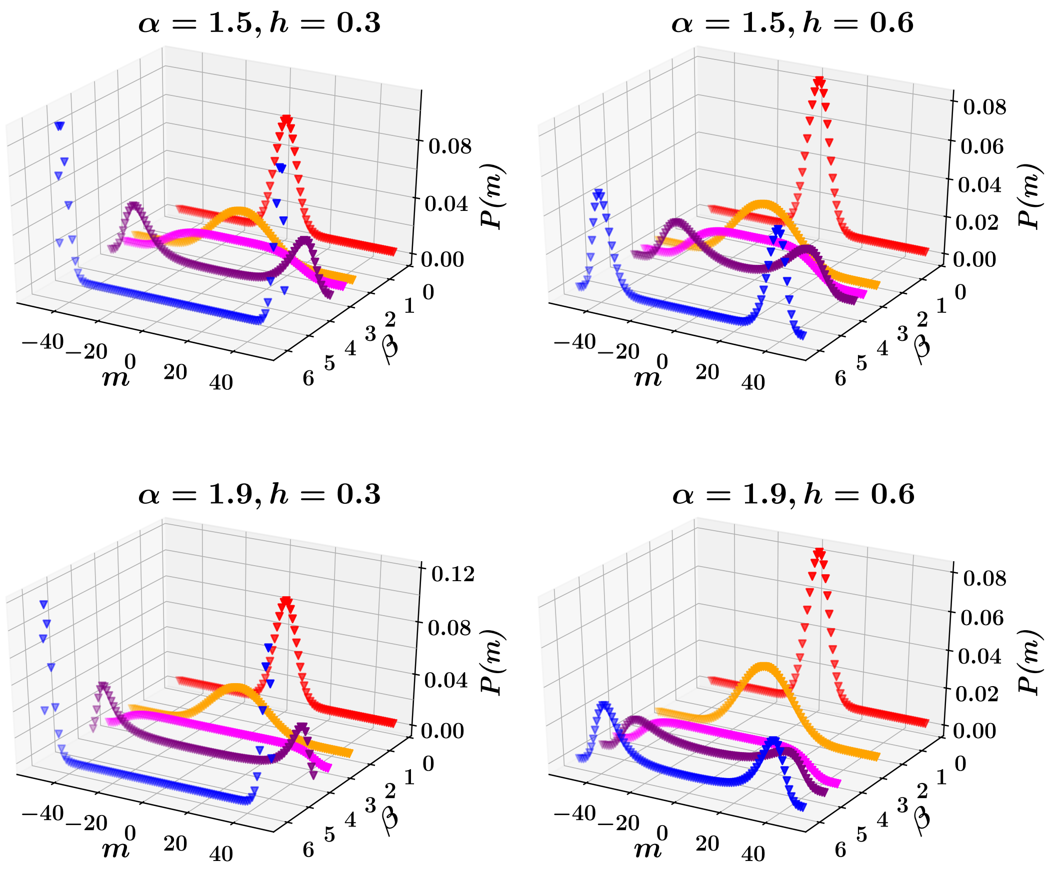

Figure 4.14: Thermal phase transition of long range Ising model at four different points in parameter space. The initial state in all cases is the maximally mixed state at infinite temperature represented by $\hat{\rho}_{\beta=0}$, refer to 4.6. The color coding from red to blue signifies decreasing temperature .

fixed at the center of the chain. In panels (a), (b), and (c), we examine a fixed value of $\alpha = 1.9$ while varying the transverse field $h = 0.3, 0.6, 0.8$. Notably, panel (a) shows a pronounced signature of confinement, which gradually diminishes as the value of h increases, as shown in panels (b) and (c). This behavior is expected because the transverse field competes with long-range interactions and weakens the confinement effect. In panel (d), we observe a linear light cone spreading of the correlation with the maximum possible velocity, $v_{\max} = 2h$ [174].

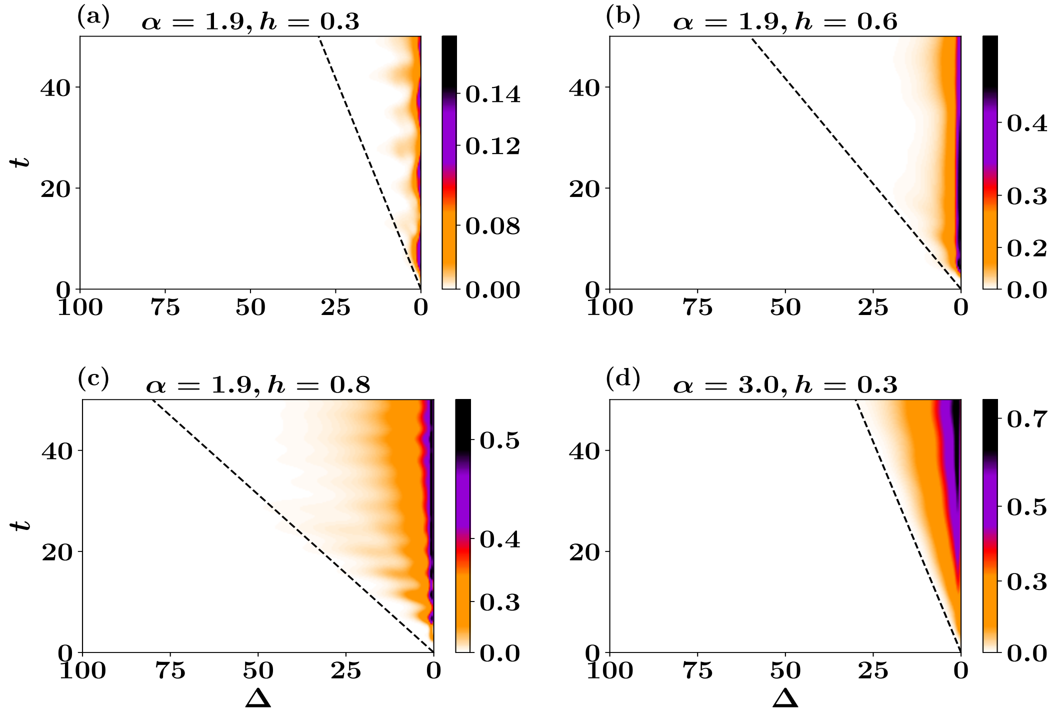

Figure 4.15: Real time dynamics of half chain connected correlation function $\left\langle \hat{s}^x_k \hat{s}^x_{k+\Delta} \right\rangle_c$after a global quantum quench of the transverse field starting from a fully polarized initial state. The dashed black lines is $v_{max} = 2h$ line for nearest neighbor transverse field Ising model[174].

Chapter 5

Dynamical deconfinement transition

5.1 Introduction

Confinement is a fundamental phenomenon that binds elementary particles such as quarks and gluons into stable and heavier hadrons such as baryons and mesons [180]. The majority of the mass of these composite particles comes from the binding energy, as the bare mass of elementary quarks contributes only approximately 0.2% of the total mass. This binding occurs because of the presence of a strong confining potential, which asymptotically increases with particle separation. A widely used model for characterizing such potential is the Cornell potential, also known as the funnel potential [181, 182]: $V_{\mathrm{Cornell}}(r) = -\frac{e}{r} + \sigma r$. Here, e represents the Coulomb strength related to the QCD strong coupling constant [183] and σ is the string tension. The Cornell potential has been successfully described in various experimental results [183, 184]. The first part of the Cornell potential resembles the Coulombic behavior and is dominant at shorter distances, typically $r < 0.1$ fm. The second part diverges linearly with the separation between the confined particles and becomes dominant at larger distances. For significantly separated quarks, it becomes energetically favorable to undergo pair production, leading to the creation of quark and anti-quark pairs, a phenomenon known as string-breaking [185].

Confinement has been explored in various condensed matter systems [62, 186, 187, 188, 189, 190, 191, 192, 193, 194, 195]. In a recent study, a global quench protocol was employed as a probe to investigate the effect of confinement on the nonequilibrium dynamics of a short-range non-integrable Ising chain [174]. This investigation revealed that confinement imposes constraints on the relaxation of the order parameter and proliferation of entanglement throughout the system. Subsequent research has extended this exploration to quantum spin chains [174, 64, 196, 197, 60, 61] and lattice gauge theories [198, 199, 200, 201, 202, 203], with a focus on understanding the consequences of confinement in nonequilibrium dynamics. Furthermore, dynamical confinement has been observed in various experimental and quantum computing platforms. These include trapped-ion experiment simulating the ferromagnetic LRIM [63], trapped-ion based quantum computer simulating the swinger model [204], and an IBM quantum computer simulating the short-range Ising model [205].

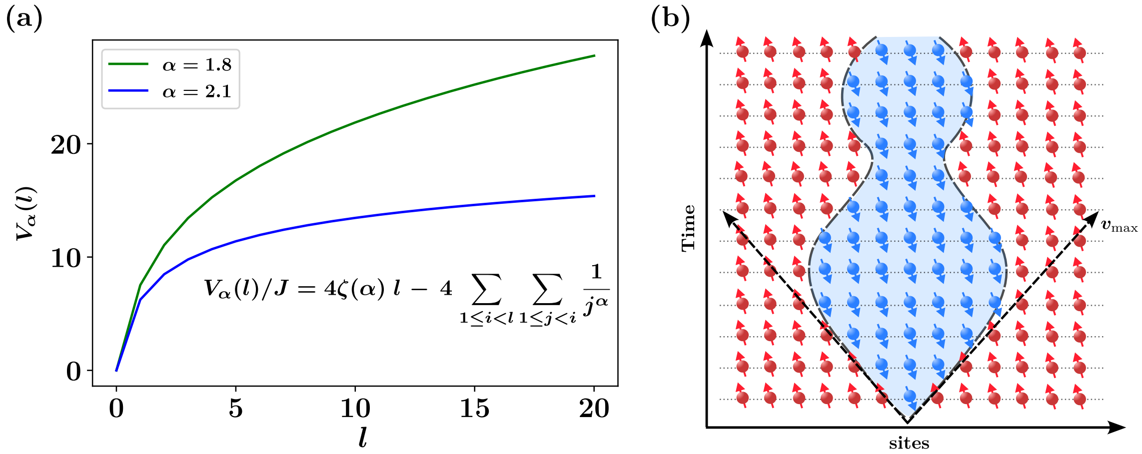

Figure 5.1: (a) Effective confining potential in LRIM in thermodynamic limit for two different values of α. For $a > 2$ it is bounded from above whereas for $\alpha < 2$ it is unbounded. (b) The confinement potential bounds the excited domains (down spins in blue in the sea of up spins in red) that suppresses correlation spreading in the system. The dashed line represents the Lieb-Robinson bound for locally interacting systems.

Confinement has dramatic effects on the nonequilibrium dynamics of many-body quantum systems. This restricts the spread of correlations in the system by constraining the proliferation of quasiparticles, fundamentally altering the light-cone spreading of the correlation. Consequently, the order parameter exhibits robust oscillations with characteristic frequencies associated with meson masses, and growth of entanglement is suppressed [174, 60, 61, 64, 12]. This alteration hinders the approach to thermalization, as evidenced in the bosonic swinger model [198], ferromagnetic LRIM [61, 13, 14], and more recently in the short-range Ising model [23]. In the latter case, rare events involving the creation of mesons in close proximity lead to an avalanche of scattering events, resulting in a long and stable prethermal regime[23]. In the short range Ising model, where confinement is due to the symmetry breaking field, it has been observed that delocalization starts to occur as the density of the excitation increases, such that the average distance between the domain wall kinks is equal to or less than the localization length [64]. This is characterized by spatial correlation and entanglement growth. Furthermore, string breaking has been studied in both short- and long-range quantum spin chains, showing that a pair of excited domain walls delocalizes over a long time limit [185]. In this chapter, we investigate the deconfinement transition in LRIM with thermally tuned excitation density. To this end, we will prepare thermal states with a nontrivial density of domain wall kinks across critical points, and study the effect of confinement on the real time dynamics of these states. We highlight that the fluctuation of domain wall kinks gives a stronger signature in characterizing the deconfinement transition than the average domain wall kinks.

The rest of this chapter is organized as follows; In Section 5.2 we introduce the mechanism of confinement in LRIM highlighting its effects in the real time dynamics. In section 5.3 we introduce the quench protocol and signatures of deconfinement transition observed in average domain wall kinks in subsection 5.3.1 and kink fluctuation in subsection 5.3.2. In the final section 5.4 we present conclusion and outlook. The Appendix sections are as follows. In Appendix 5.A we introduce the two kink model. In Appendix 5.B we introduce the single kink model and extract the effective localization length. In Appendix 5.C we outline the simulation details. Finally, in the Appendix 5.D we detail the methodology to calculate the PDF of average domain wall kinks in MPS formalism.

5.2 Confinement in LRIM

The ferromagnetic LRIM with power-law decaying interactions is a paradigmatic model for studying dynamical confinement. Inherent long-range ferromagnetic inter-

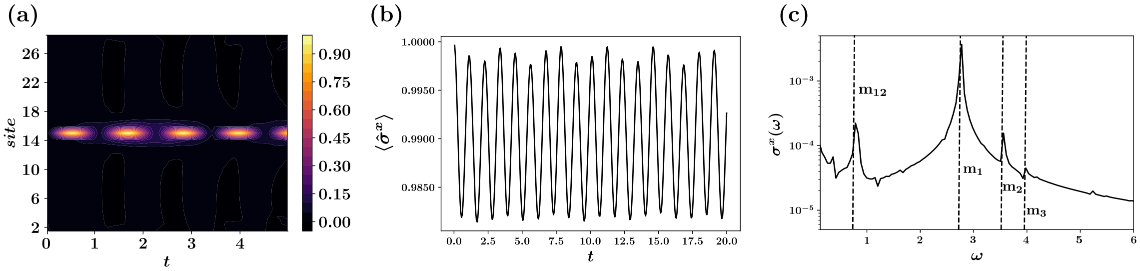

Figure 5.2: Signatures of dynamical confinement observed in LRIM at $\alpha = 2.3$ and $h_f = 0.27$: (a) time evolution of connected correlation function, (b) time evolution of magnetization, (c) Fourier spectrum of magnetization vs. time signal revealing the dominant frequencies. Vertical dashed lines are the meson masses and their difference extracted from effective two kink model.

actions intrinsically induce confinement and localize domain-wall kinks [60, 61]. To maintain consistency with existing literature, we consider the following Hamiltonian:

$$\hat{H} = -J \sum_{i<j}^{N} \frac{\hat{\sigma}_i^x \hat{\sigma}_j^x}{|i-j|^{\alpha}} - h \sum_{i=1}^{N} \hat{\sigma}_i^z, \tag{5.1}$$

where, $\hat{\sigma}_i^{\mu}$, $\mu = x, y, z$ are the Pauli matrices at site i. In contrast to the short-range Ising model, where confinement arises from the external longitudinal field [174], LRIM exhibits a distinct mechanism where the domain wall kinks, which are elementary excitations, are bound owing to the long-range interaction between spins of opposite polarity within and outside the domains (see Figure 5.1 (b)). The net energy associated with a domain of size l within an infinitely long spin chain is.

$$V_{\alpha}(l)/J = 4\zeta(\alpha)l - 4 \sum_{1\leq i<l} \sum_{1\leq j<i} \frac{1}{j^{\alpha}}, \tag{5.2}$$

where, $\zeta(\alpha) = \sum_{z=1}^{\infty} 1/z^{\alpha}$ is the Riemann zeta function. The net potential energy between two propagating domain wall kinks scales linearly with their separation, akin to the Cornell potential. Figure 5.1 (b) illustrates the effective potential energy of the propagating domain wall kinks for $\alpha = 1.8$ and $\alpha = 2.1$, showing a monotonic increase in potential with their separation. It is important to note that this potential has an upper bound for $\alpha > 2$; therefore, only low-lying excitations are bounded[60, 61] whereas it is unbounded for $\alpha < 2$. See the detailed explanation in Section 1.2. Consequently, the domain wall kinks cannot propagate indefinitely and are confined, analogous to elementary quarks confined to heavier composite particles. These bound domain wall kinks are equivalently referred to as mesons, and their binding energies are denoted as meson masses [174].

Figure 5.2 illustrates various signatures of dynamical confinement in a 30-site LRIM following the global quench of the fully polarized state with parameters $\alpha = 2.3$ and $h_f = 0.27$. Panel (a) shows the post-quench evolution of the connected correlation function $\langle \hat{\sigma}_i^x(t)\hat{\sigma}_j^x(t)\rangle_c = \langle \hat{\sigma}_i^x(t)\hat{\sigma}_j^x(t)\rangle - \langle \hat{\sigma}_i^x(t)\rangle\langle \hat{\sigma}_j^x(t)\rangle$ with $i = 15$. The correlation exhibits persistent spatial oscillations, which are distinctly different from the typical light-cone-like spreading. A similar behavior is observed in the post-quench evolution of the magnetization $\langle \hat{\sigma}^x(t)\rangle = \frac{1}{N}\sum_i \langle \hat{\sigma}_i^x(t)\rangle$. The frequency of these oscillations is characteristic of the quench and reveals the inherent energy scale associated with confined domain wall kinks. To illustrate this further, we expand the initial state based on the eigenstates of the post-quench Hamiltonian $|\psi_i\rangle = \sum_m C_m |m\rangle$. The time evolution of any order parameter $\hat{O}$ can be expressed as $\langle \hat{O}(t)\rangle = \sum_{m,n} C_m C_m^* \langle n|\hat{O}|m\rangle e^{-it(E_m - E_n)}$. Each term within the double sum oscillates in time, with frequencies corresponding to the energy differences between the

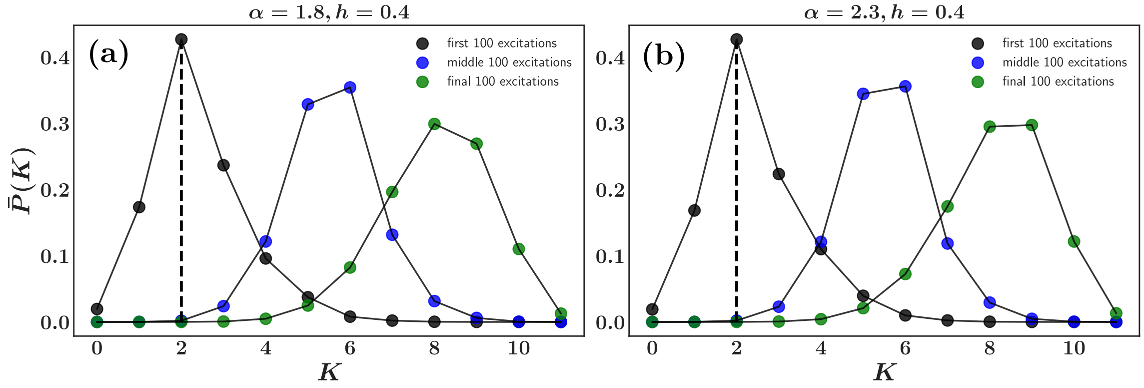

Figure 5.3: PDF of domain wall kinks averaged over 100 eigenstates in the spectrum of two different confining Hamiltonians; $\alpha = 1.8, h = 0.4$ and $\alpha = 2.3, h = 0.4$. The black dots represents data averaged over first 100 eigenstates, the blue dots represents data averaged over middle 100 eigenstates, and the green dots represents data averaged over last 100 eigenstates. The data are for $N = 12$ and are computed exactly with ED.

eigenstates of the post-quench Hamiltonian, denoted by $\Delta_{m,n} = E_m - E_n$. If the initial state has a nontrivial overlap with the eigenstates, then the oscillating terms tend to cancel out. However, if the initial state predominantly overlaps with a few specific eigenstates, a pronounced oscillation of the order parameter occurs, with frequencies corresponding to the energy differences between the eigenstates.

Additionally, the low-lying eigenstates of the confined LRIM mostly consist of two domain wall kinks [63, 61]. This has been illustrated in Figure 5.3 which shows the PDF of domain wall kinks averaged over 100 eigen states located at different points in the energy spectrum. For lower excitations (black dots) we see a distinct peak at $K = 2$ that confirms the low lying eigen states of confined LRIM is mostly composed of two kinks. It is worth mentioning that while in thermodynamic limit single kinks states are highly excited for finite system sizes the single kinks created at the edge of the chain is lowly excited therefore the probability corresponding to odd number of domain wall kinks are also considerable here. As we move higher in energy spectrum the $\bar{P}(K)$ shifts towards right signifying creation of higher number of domain wall kinks. Based on this observation we can perturbatively study the low-energy excitations of the LRIM by projecting the Hamiltonian to a restricted space consisting of only zero or two kinks. The corresponding state is defined by two quantum numbers representing the position and size of the domain (or equivalently, the separation of domain wall kinks). Details of the two-kink model are presented in Appendix 5.A.

This restricted model can be efficiently diagonalized, and, as expected, the low-lying energies corresponding to the two-kink model perfectly match the dominant frequency peaks associated with the oscillation of $\langle \hat{\sigma}^x(t) \rangle$, as shown in Figure 5.2.

5.3 Quench Dynamics

We observed that the inherent long-range interaction constrains the propagation of domain-wall kinks and suppresses correlation spreading in the system. This prompts a natural inquiry about the robustness of confinement against the density of excitations. To this end we begin with thermal states as the initial states.

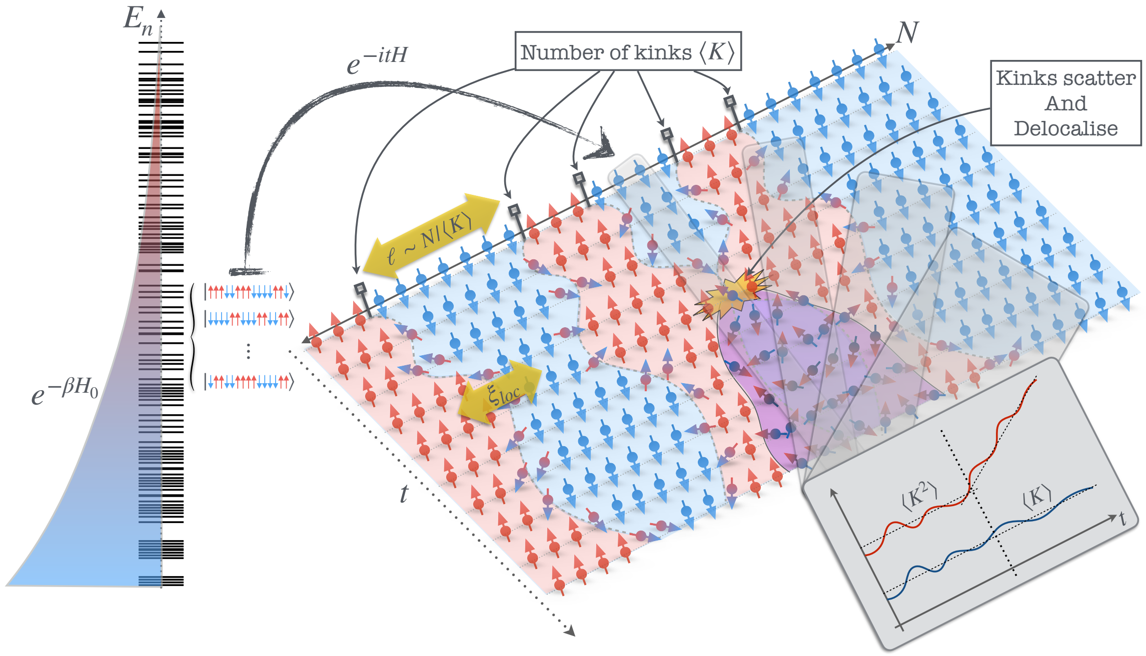

Figure 5.4: Quench protocol: (1) Initial state is prepared as thermal density matrices of the initial Hamiltonian, $\propto e^{-\beta \hat{H}_i}$ temperature ($\beta = 1/T$). (2) The initial thermal density matrix is evolved in real time with a post-quench Hamiltonian $\propto e^{-it\hat{H}}$. Here, we show the evolution of a representative state withing a thermal density matrix. $\langle K \rangle$ is the average number of domain wall kinks, l is the average distance between two kinks and ξ_{loc} is the localization length defined as the maximum distance traced by a domain wall kink with a given energy. **3)** The real time evolution is monitored by calculating the kink density and kink fluctuation at every time step.

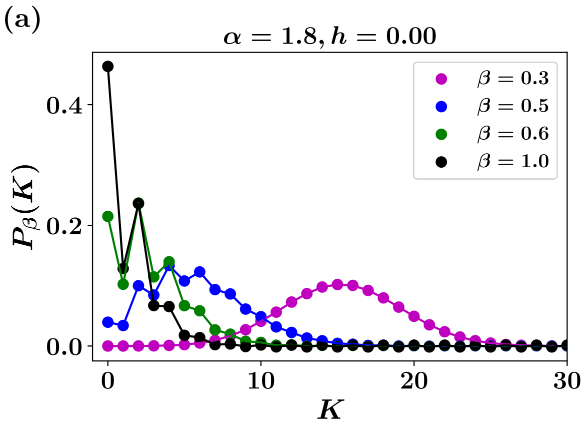

Figure 5.5: PDF of domain wall kinks in thermal states for four representative temperatures with $N = 50$.

In LRIM with $h = 0$, the density of domain wall kinks exhibits a monotonic variation from 0.5 at infinite temperature to 0 at zero temperature, independent of α. Consequently, parameter $\beta = 1/T$ serves as a tuning parameter to precisely control the initial state of the system with varying kink densities (refer to Appendix 5.C). The initial state is a thermal density matrix, denoted by $\hat{\rho}^i_\beta(t = 0) \propto e^{-\beta \hat{H}_i}$ where the Hamiltonian $\hat{H}_i$ has a zero transverse magnetic field. Figure 5.5 shows the PDF of domain wall kinks (see Equation 5.3) of the initial thermal state $P_\beta(K)$ for $N = 50$. These states are locally purified from a maximally mixed state at an infinite temperature ($\beta = 0$) as $\hat{\rho}^i_\beta = e^{-\frac{\beta}{2}\hat{H}_i}\hat{\rho}_{\beta=0}e^{-\frac{\beta}{2}\hat{H}_i}$. Further details regarding the simulation of thermal states are provided in Appendix 4.B. The initial states are quenched and evolved in real time with the post-quench Hamiltonian given by $\hat{\rho}_\beta(t) = e^{-it\hat{H}}\hat{\rho}^i_\beta(t)e^{it\hat{H}}$. This quench protocol is illustrated in figure 5.4. The parameters of the post-quench Hamiltonian are deliberately chosen to reside within the strongly confined regime [60, 61]. As domain wall kinks are elementary excitations in the system, the number of domain wall kinks emerges as a natural order parameter for investigating dynamical confinement. It is quantified by the following operator,

$$\hat{K} = \frac{1}{2}\sum_{i=1}^{N-1} 1 - \hat{\sigma}^x_i \hat{\sigma}^x_{i+1}. \tag{5.3}$$

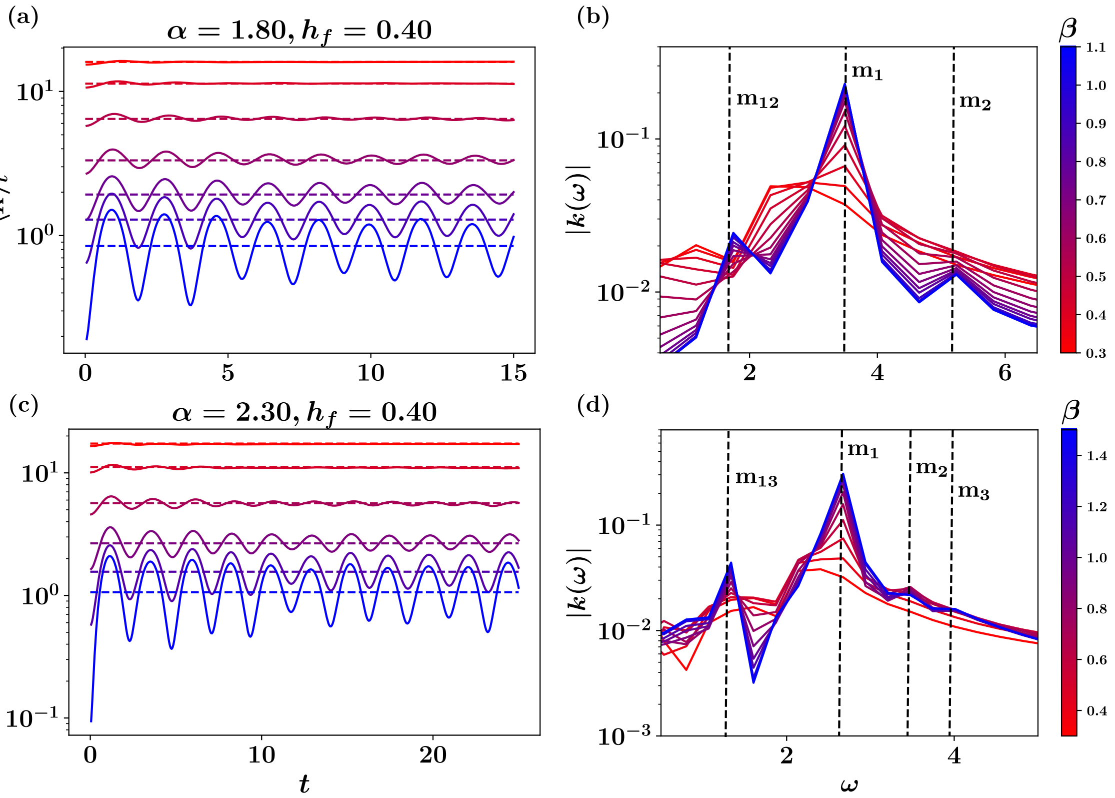

Figure 5.6: Post-quench evolution of domain wall kinks starting from different thermal states (see colorbar on the right) for $\alpha = 1.8, h_f = 0.4$ (a) and $\alpha = 2.3, h_f = 0.4$ (c). The horizontal dashed lines represent expected thermal values. The results are for system size of $N = 50$ spins. (b),(c) the corresponding Fourier spectrum. The vertical dashed lines are the meson masses and their differences extracted from the effective two kink model.

5.3.1 Signatures in average domain wall kinks

Figure 5.6 panels (a) and (c) illustrates the post-quench evolution of the average domain wall kinks initiated from various initial thermal states within a temperature range (represented by color gradient going from blue to red) for two representative post-quench parameters. The horizontal dashed lines represent the expected thermal values $\mathrm{Tr}[\hat{\rho}_{\beta_{\text{eff}}}\hat{K}]$, where $\hat{\rho}_{\beta_{\text{eff}}} \propto e^{-\beta_{\text{eff}}\hat{H}}$. The effective temperature attributed to a quench β_{eff} is extracted by solving the equation,

$$\frac{\mathrm{Tr}[\hat{\rho}^i_\beta \hat{H}_i]}{\mathrm{Tr}[\hat{\rho}^i_\beta]} = \frac{\mathrm{Tr}[\hat{\rho}_{\beta_{\mathrm{eff}}} \hat{H}]}{\mathrm{Tr}[\hat{\rho}_{\beta_{\mathrm{eff}}}]} \tag{5.4}$$

Two distinct behaviors are observed at the extremes of the investigated temperature range. At lower temperatures, the kink density oscillates persistently around the expected thermal value, without showing any signs of relaxation. This persistent oscillation indicates strong confinement, suppressing the correlation spreading within the system and leading to a delayed thermalization process. This behavior weakens as the temperature increases. At high temperatures, the kink density rapidly relaxes to the expected thermal value, suggesting robust thermalization [206]. In Figure 5.6, panels (b) and (d) depict the Fourier spectrum of $\langle \hat{K} \rangle$, revealing the dominant frequencies of oscillation. At lower temperatures, sharp frequency peaks corresponding to the dominant oscillations of $\langle \hat{K} \rangle$ are observed. These frequency peaks exhibit strong agreement with the meson masses extracted from the two-kink model, indicating the presence of strongly bound mesons. However, as the temperature increases, these frequency peaks gradually diminish and eventually melt. This indicates the dissolution of bound mesons at high temperatures [207].

As in the preceding Section, the initial state can be expanded in the basis of the eigenkets of the post-quench Hamiltonian, denoted as $\hat{\rho}^i_\beta = \sum_{m,n} C_{m,n} |m\rangle\langle n|$. The corresponding time-evolved average domain wall kinks can be expressed as $\langle \hat{K}(t) \rangle = \sum_{m,n} C_{m,n} \langle n|\hat{K}|m\rangle e^{-it(E_m - E_n)}$. At low temperatures, the initial states $\hat{\rho}^i_\beta$ consist of a few low-lying eigenkets of the post-quench Hamiltonian. Consequently, sharp frequency peaks are observed. As the temperature increases, $\hat{\rho}^i_\beta$ incorporates nontrivial contributions corresponding to high-energy excitations, and therefore we don't observe any dominant frequency peaks.

5.3.2 Signatures in kink fluctuation

The average domain wall kinks provide valuable qualitative insights into the deconfinement transition, revealing distinct behaviors at the extreme ends of the considered temperature range. However, a more pronounced signature of this transition emerges from the interaction and propagation of domain wall kinks within the system. To address this, we study the connected kink fluctuation, $\langle \hat{K}^2 \rangle_c = \langle \hat{K}^2 \rangle - \langle \hat{K} \rangle^2$. Figure 5.7 depicts the post-quench evolution of $\langle \hat{K}^2 \rangle_c$ for two sets of post-quench parameters. For both post-quench Hamiltonians, we observe two contrasting behaviors at the extremes of the temperature range. At lower temperatures, $\langle \hat{K}^2 \rangle_c$ exhibits persistent oscillations over time, similar to the behavior of $\langle \hat{K} \rangle$, indicating significant suppression in the propagation of domain wall kinks. As the temperature increases, $\langle \hat{K}^2 \rangle_c$ exhibits linear growth over time, suggesting a light-cone-like dispersion of the domain wall kinks. This observation aligns with light-cone spreading of correlation and entanglement in the deconfined phase [174, 60, 61].

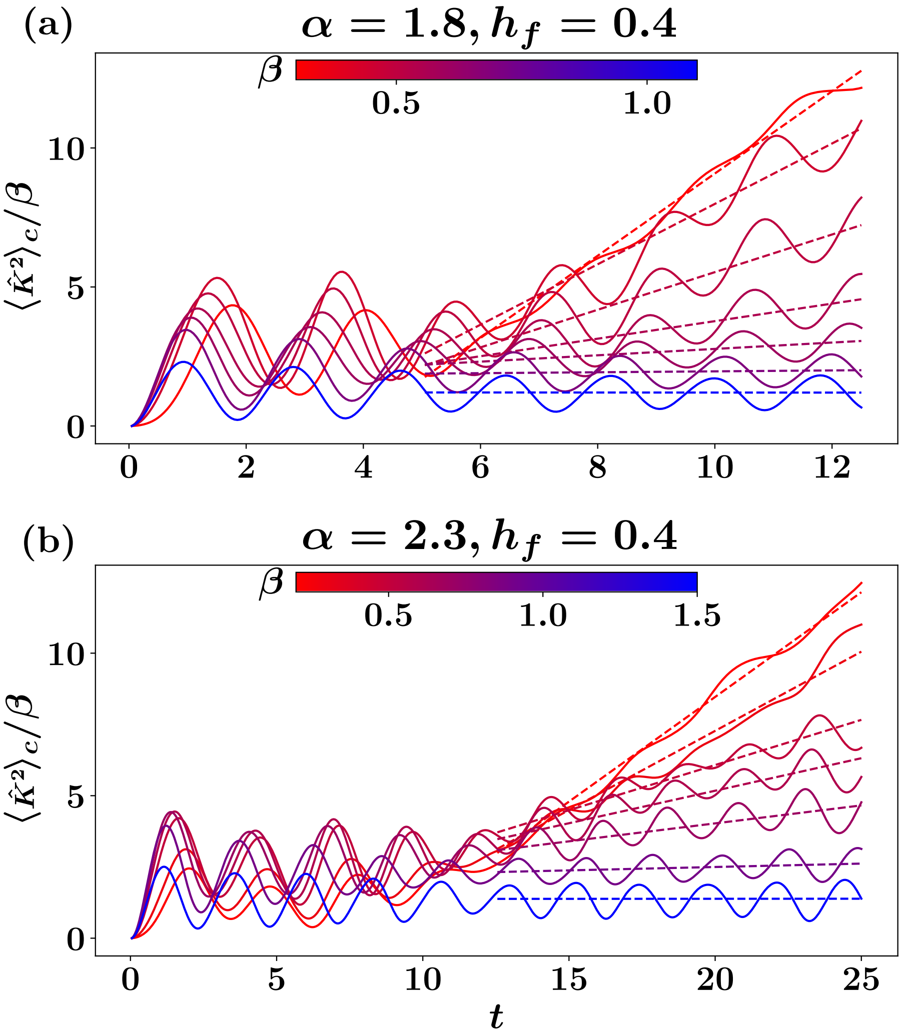

Figure 5.7: Post-quench evolution of the kink fluctuation starting from different thermal states for $\alpha = 1.8, h_f = 0.4$ (a) and $\alpha = 2.3, h_f = 0.4$ (b). The results are for system size of $N = 50$ spins. The data are rescaled by $1/\beta$ and subtracted from their initial values for better visualization. Dashed lines represent the linear fit of the data in an appropriate time window.

A more comprehensive understanding emerges when examining the full probability distribution $P(K)$ of domain-wall kinks. In Figure 5.8 panels (b) and (d), we observe that $P(K)$ monotonically broadens over time, whereas in panels (b) and (d), oscillations are observed over time. To quantitatively assess this behavior, we fit straight lines to the $\langle \hat{K}^2 \rangle_c$ data over an appropriate time window and define the slope of these lines as the velocity of kink dispersion v. In Figure 5.9, v is plotted as a function of the temperature of the initial thermal states. We observe a transition from a strongly confined regime at low temperatures, denoted by $v \approx 0$ to a de-confined regime, denoted by a monotonically increasing finite v as the temperature increases. This monotonic rise in v eventually halts owing to the finite system size.

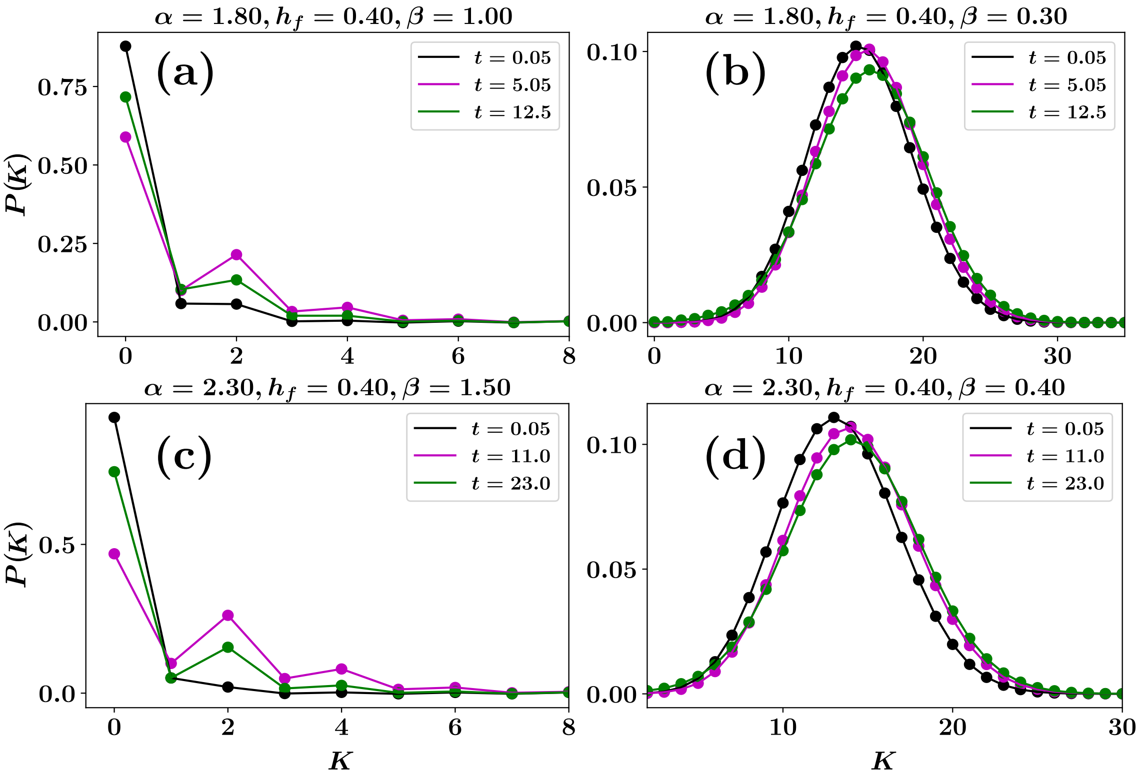

Figure 5.8: Probability distribution function (PDF) of domain wall kinks for different system parameters and temperature. Three colors represent different time slices during the real time dynamics (see label). (a) and (c) exhibits strong confinement at low temperature with persistent oscillation of PDF, (b) and (d) exhibits high temperature deconfinement where the PDF consistently gets broader with time.

The underlying mechanism of this transition can be understood by studying the dynamics of an effective single kink model [208, 60]. The semi-classical limit of the single kink model is given by the Hamiltonian,

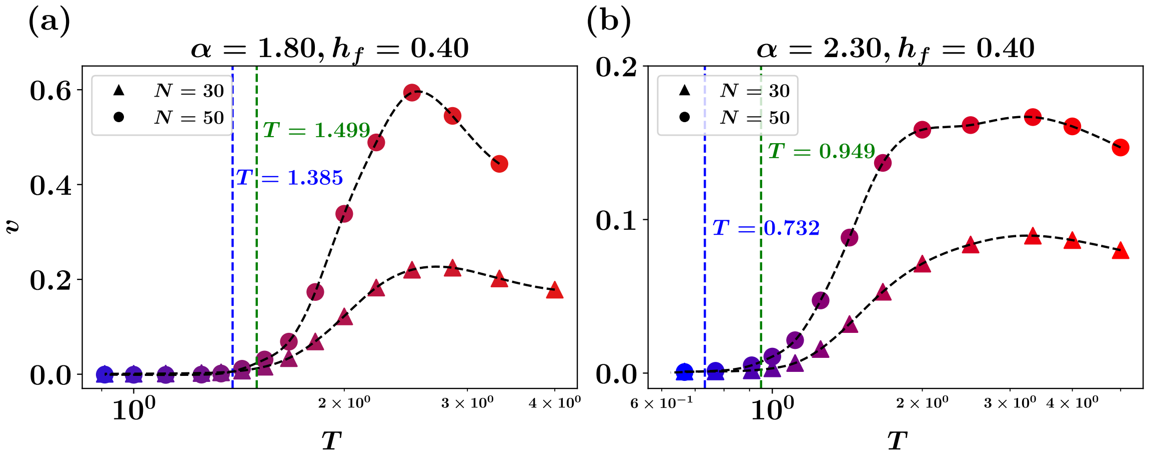

Figure 5.9: Temperature dependence of velocity of kink fluctuation extracted from 5.7 for two different quenches: $\alpha = 1.8, h_f = 0.4$ (a) and $\alpha = 2.3, h_f = 0.4$ (b) and system sizes $N = 30$ (solid triangle) and $N = 50$ (solid circle) respectively. The color gradient (from blue to red) represents varying temperature. Dashed black lines are for visual guidance. Horizontal dashed lines are the deconfinement transition temperatures predicted by the single kink model: blue for $N = 50$, green for $N = 30$.

$$H^{\text{cls}}_{\alpha,h,N}(k, q) = V_{\alpha,N}(q) - 2h\cos(k) \tag{5.5}$$

where,

$$V_{\alpha,N}(q) = \frac{2[q^{2-\alpha} + (N-q)^{2-\alpha} - (N-1)^{2-\alpha}]}{(\alpha-1)(2-\alpha)}, \tag{5.6}$$

and $(k, q) \in [0, 2\pi] \times [1, N-1]$. The detail about the single kink model is outlined in Appendix 5.B. In this framework we define the localization length ξ_{loc} as the maximum distance travelled by the kink initialized at rest with the maximum possible energy. ξ_{loc} can be extracted from single kink model by solving for maximum q in the equation,

$$H^{\text{cls}}_{\alpha,N}(0, N/2) = H^{\text{cls}}_{\alpha,N}(k, q). \tag{5.7}$$

Parameter ξ_{loc} defines a natural threshold for the deconfinement transition. If the separation between adjacent kinks exceeds the localization length, that is, $l = 1/\langle\hat{K}\rangle \gg \xi_{loc}$, then the kinks undergo uncorrelated Bloch oscillations around their origin. However, when $1/\langle\hat{K}\rangle \lessapprox \xi_{loc}$, the kinks scatter and delocalize, effectively destroying confinement. Similar delocalization has also been reported in short range

Ising model with growth of entanglement entropy observed on increasing the density of the domain wall kinks [64]. With this insight, the corresponding deconfinement transition temperature can be determined by solving the following equation for β,

$$\frac{1}{\xi_{loc}} = \overline{\langle \hat{K}_\beta(t) \rangle}. \tag{5.8}$$

$\overline{\langle \hat{K}_\beta(t) \rangle}$ denotes time-averaged $\mathrm{Tr}[\hat{\rho}_\beta(t)\hat{K}]$. As shown in Figure 5.6, it is evident that $\overline{\langle \hat{K}_\beta(t) \rangle} = \mathrm{Tr}[\hat{\rho}_{\beta_{\text{eff}}}\hat{K}]$ holds true for all values of β. By substituting this relationship into Equation 5.8, the transition temperature can be determined numerically. In Figure 5.9, dashed horizontal lines illustrate the deconfinement transition temperatures obtained using this method. Despite the simplicity of the single-kink model, it exhibits a strong predictive capacity for the transition temperature.

5.4 Conclusions

We investigated the nonequilibrium dynamics of thermal states following a global quantum quench to a confined phase of LRIM. The post-quench time evolution of domain wall kinks and their Fourier signals revealed the intricate interplay between slow-decaying long-range interactions and the emergence of confinement behavior at low temperatures. Furthermore, the time-dependent fluctuation of domain wall kinks provides compelling evidence for a dynamical deconfinement transition with increasing density of thermally tuned domain wall kinks. In future it will be inetersting to study the critical properties of the observed transition. In this thesis the system sizes studied were not big enough for a detailed finite size scaling analysis. An interesting question to be addressed is whether the transition observed on the two sides of $\alpha = 2$ line are similar.

These observations can be experimentally realized in AMO platforms, specifically in trapped-ion experiments [63, 18, 19], which can implement the global quench protocol starting from a product state. The post-quench evolution of a mixed state can be achieved by independently evolving individual pure states within a given mixed state, and then computing the weighted ensemble average over the individual pure state evolution: $\hat{\rho}\beta(0) \rightarrow \hat{\rho}\beta(t) = \sum_n P_\beta(n) \left|n(t)\right\rangle \left\langle n(t)\right|$, where $\left|n(t)\right\rangle = e^{-it\hat{H}} \left|n\right\rangle$ and $P_\beta(n) = e^{-\beta E_n}/\sum_n e^{-\beta E_n}$. Here, $\left|n\right\rangle$ represents the eigenstate of $\hat{H}_i$ (equivalently, the computational basis), and E_n corresponds to the associated eigenvalue. Notably, this procedure scales exponentially with system size. However, for practical purposes, it is feasible to consider only the dominant states, based on how $P_\beta(n)$ decays with n. This is particularly applicable to low-temperature states.

5.A Two kink model

We employ the two-kink model to investigate low-energy excitations as bound quasiparticles. The underlying concept involves projecting the Hilbert space onto a subspace in which n spins cluster together amidst a sea of up spins, thereby forming two kink domain walls that exhibit the freedom to shift, contract, or expand. The state is uniquely characterized by two quantum numbers defining the position and length of the domains,

$$|j,n\rangle = |... \uparrow\uparrow\downarrow_j\downarrow_{j+1} ... \downarrow\downarrow_{j+n-1}\uparrow\uparrow ...\rangle \tag{5.9}$$

The long-range Hamiltonian can be projected in the in the two kink subspace is $\hat{\mathcal{H}} = \hat{\mathcal{P}}^{-1}\hat{H}\hat{\mathcal{P}}$, where $\hat{\mathcal{P}}$ is the projection operator,

$$\hat{\mathcal{H}}\,|j,n\rangle = V_{\alpha,N}(j,n)\,|j,n\rangle - h[\,|j,n+1\rangle + |j,n-1\rangle + |j+1,n-1\rangle + |j-1,n+1\rangle\,] \tag{5.10}$$

where, for a finite system with N spins, $1 \le j \le N-1$ and $1 \le n \le N-j-1$. The diagonal part, $V_{\alpha,N}(j,n)$, represents the total potential energy above the ground state. For long range ferromagnetic Hamiltonians the potential energy is due to the interaction of spins with opposite polarity within and out of the domains. The off-diagonal term corresponds to the spin-flip term, which governs the shift, expansion, and contraction of domain-wall kinks. The effective Hamiltonian $\hat{\mathcal{H}}$ can be diagonalized on the $|j,n\rangle$ basis. Subsequently, the masses of the mesons can be extracted by diagonalizing the following matrix,

$$\mathcal{H}_{j,n:j',n'} = V_{\alpha,N}(j,n)\delta_{j,j'}\delta_{n,n'} - h[\delta_{j,j'}\delta_{n+1,n'} + \delta_{j,j'}\delta_{n-1,n'} + \delta_{j+1,j'}\delta_{n-1,n'} + \delta_{j-1,j'}\delta_{n+1,n'}] \tag{5.11}$$

where,

$$V_{\alpha,N}(j,n) = 2\sum_{j\le u\le j+n-1}\left[\sum_{1\le v\le j-1}\frac{1}{|v-u|^{\alpha}} + \sum_{j+n\le v\le N}\frac{1}{|v-u|^{\alpha}}\right] \tag{5.12}$$

is the potential energy of the excitation of the two kink states $|j,n\rangle$. This model effectively captures confinement in a long-range Ising chain, particularly in the limit $N\to\infty$, where the confining potential steadily increases with distance between the coupled domain walls. However, in the case of a finite spin chain, the confining potential increases with the separation of the kinks until a characteristic length is reached, beyond which it starts to decrease. This phenomenon is more pronounced for smaller values of α.

5.B Single kink model and localization length

Similar to the two kink model we can define the single kink model by projecting the Hilbert space into a subspace with just one single kink. The quantum state is defined by a single quantum number signifying the position of the single kink,

$$|j, n\rangle = |... \uparrow\uparrow\uparrow_n\downarrow_{n+1}\downarrow\downarrow ...\rangle \, . \tag{5.13}$$

The corresponding Hamiltonian matrix is defined as,

$$\mathcal{H}_{n:n'} = V_{\alpha,N}(n)\delta_{n,n'} - h[\delta_{n+1,n'} + \delta_{n-1,n'}] \tag{5.14}$$

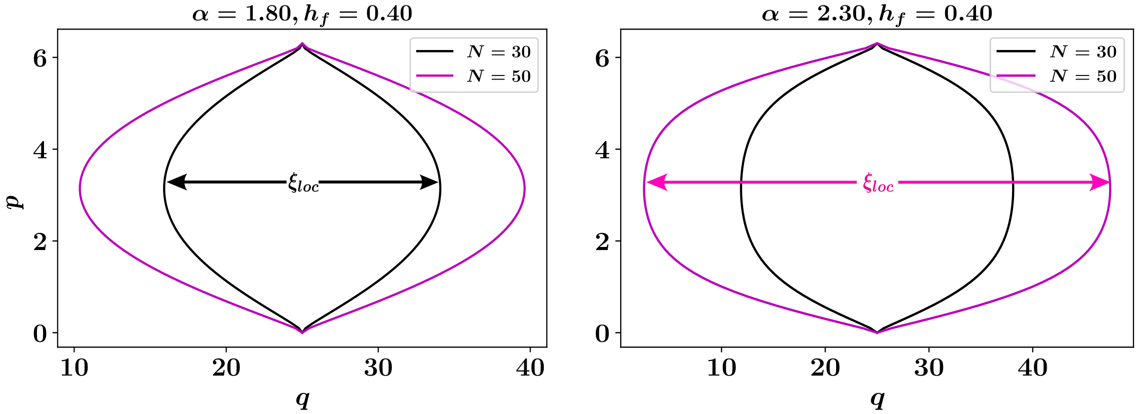

Figure 5.10: Phase space of the semi-classical Hamiltonian 5.21 over a full period of momentum for two different system parameters. ξ_{loc} is called the localization length and is defined as the maximum space traversed by the single kink originally located at the center of the system.

where the effective potential is,

$$V_{\alpha,N}(n) = 2 \sum_{1\le i\le n} \sum_{n+1\le j\le N} \frac{1}{|i-j|^{\alpha}}. \tag{5.15}$$

In thermodynamic limit the sums in the potential can be approximated with integrals,

$$V_{\alpha,N}(n) = 2\left[\sum_{r=1}^{N-n}\frac{1}{r^{\alpha}} + \sum_{r=2}^{N-n+1}\frac{1}{r^{\alpha}} + ... + \sum_{r=n}^{N-1}\frac{1}{r^{\alpha}}\right] \tag{5.16}$$

$$\approx \left[\int_{1}^{N-n}\frac{dr}{r^{\alpha}} + \int_{2}^{N-n+1}\frac{dr}{r^{\alpha}} + ... + \int_{n}^{N-1}\frac{dr}{r^{\alpha}}\right] \tag{5.17}$$

$$= \frac{1}{(\alpha-1)}\left[\sum_{r=1}^{n}\frac{1}{r^{\alpha-1}} - \sum_{n'=n}^{1}\frac{1}{(N-n')^{\alpha-1}}\right] \tag{5.18}$$

On further approximation of the sums we get,

$$V_{\alpha,N}(n) \approx \frac{2}{(\alpha-1)}\left[\int_{1}^{n}\frac{dr}{r^{\alpha-1}} - \int_{n}^{1}\frac{dn'}{(N-n')^{\alpha-1}}\right] \tag{5.19}$$

$$= \frac{2}{(\alpha-1)(2-\alpha)}\left[\frac{1}{n^{\alpha-2}} + \frac{1}{(N-n)^{\alpha-2}} - 1 - \frac{1}{(N-1)^{\alpha-2}}\right] \tag{5.20}$$

We can take the classical limit of the Hamiltonian in equation 5.14 by defining a phase space $(p, q) \in [0, 2\pi] \times [1, N-1]$ and corresponding Hamiltonian,

$$H^{cls}_{\alpha,h,N}(p,q) = V_{\alpha,N}(q) - 2h\cos(p) \tag{5.21}$$

where the function $V_{\alpha,N}(q)$ is defined in the equations 5.20. Starting from the most energetic state in a finite chain within the single kink scenario; a single static kink located at the centre of the chain, we can calculate the $p \times q$ phase space by solving;

$$H^{cls}_{\alpha,N}(0, N/2) = H^{cls}_{\alpha,N}(p,q) \tag{5.22}$$

In Figure 5.10, the classical phase space is obtained by solving 5.22 throughout the full periodicity of the momentum. Notably, the kink travels the farthest from its original position when $p = \pi$. This distance is defined as the localization length of the kink, denoted by ξ_{loc}. Localization length is a crucial parameter that distinguishes two distinct dynamical regimes. When the average separation between the kinks surpasses ξ_{loc}, the kinks exhibit uncorrelated Bloch oscillations that are strictly localized around their respective sites of origin. Conversely, as the average kink separation becomes comparable to or is smaller than ξ_{loc}, the kinks disperse and undergo delocalization. The critical temperature corresponding to this transition can be determined by numerically solving the following equation for β,

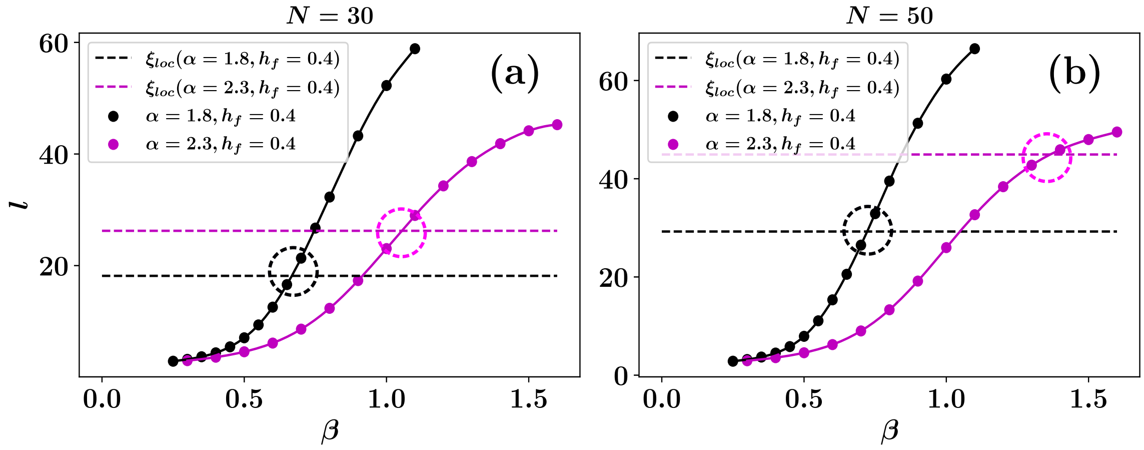

Figure 5.11: Numerical solution of the equation 5.23. The dots are the average kink separation, $l = \frac{N}{\mathrm{Tr}[\hat{\rho}_{\beta_{\mathrm{eff}}}\hat{K}]}$, as a function of β, the full lines are the cubic interpolation of the data, and the horizontal dashed lines are ξ_{loc} for the corresponding parameters. The dashed circles highlights the point of solution.

$$l = \frac{N}{\overline{\langle \hat{K}_\beta(t) \rangle}} = \xi_{loc}, \tag{5.23}$$

where $\overline{\langle \hat{K}_\beta(t) \rangle}$ is the time average of $\mathrm{Tr}[\hat{\rho}_\beta(t)\hat{K}]$. The post-quench behavior of $\langle \hat{K}_\beta(t) \rangle$ suggests that we can replace $\overline{\langle \hat{K}_\beta(t) \rangle}$ with the expected thermal average kinks $\mathrm{Tr}[\hat{\rho}_{\beta_{\mathrm{eff}}}\hat{K}]$.

5.C Simulation details

The finite temperature states are simulated by the method of purification by keeping the thermal density operator in locally purified $\hat{\rho}_\beta = \mathbb{X}_\beta \mathbb{X}_\beta^\dagger$ form throughout the procedure,

$$\hat{\rho}_{\beta+d\beta} = e^{-\frac{d\beta}{2}H}\mathbb{X}_\beta[e^{-\frac{d\beta}{2}H}\mathbb{X}_\beta]^\dagger \tag{5.24}$$

Details of the initial state preparation and subsequent imaginary time evolution are comprehensively outlined in Section 4.B.1. We employ two-site TDVP algorithm with a time step of $d\beta = 0.001$. The bond dimensions does not exhibit excessive

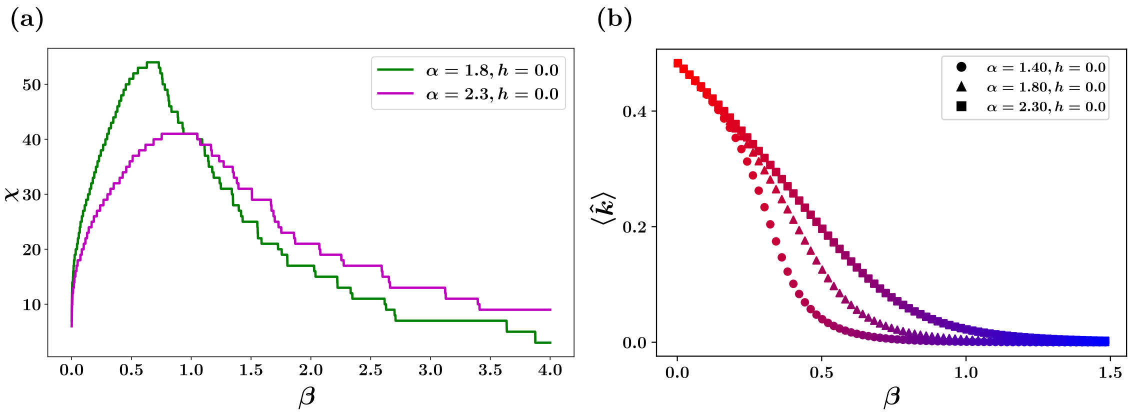

Figure 5.12: (a) Bond dimension corresponding to the central site as a function of inverse temperature during the imaginary time evolution. All singular values smaller than 10^{-8} are discarded during truncation. (b) Average kink density $\langle \hat{K} \rangle$ as a function of inverse temperature β for three different parameters and system size $N = 50$. The figure illustrates a thermal phase transition from low temperature ferromagnetic regime (in blue) to high temperature paramagnetic regime (in red) based on the kink density.

growth during the imaginary time evolution. Figure 5.12 (a) illustrates the bond dimension corresponding to the central site plotted against β, with truncation involving the discarding of all singular values smaller than 10^{-8}. The peaks in the plot indicate thermal critical regions in which the area law is invalid [101, 103, 105, 106, 107].

In Figure 5.12 (b), the average kink density $\langle \hat{k} \rangle = \langle \hat{K} \rangle / N$ is plotted against the inverse temperature β for different values of α with $h = 0.0$. At $\beta = 0$, the state is maximally mixed and $\langle \hat{k} \rangle = 0.5$ holds for all parameters (see Figure 5.5). With increasing β, there is a monotonic reduction in $\langle \hat{k} \rangle$, indicating a thermal transition to the ferromagnetic phase, where $\langle \hat{k} \rangle = 0$. Notably, the thermal phase transition observed in Figure 5.12 is robust only for $\alpha \leq 2$ in the ferromagnetic LRIM and will show singularity at critical point for $N \to \infty$. The transition observed for $\alpha = 2.3$ will crossover to $\beta = \infty$ as $N \to \infty$. This implies the thermal phase transition at $T = 0$ or equivalently absence of ferromagnetic order in LRIM for $\alpha > 2$.

Similarly, the thermal density operator can be evolved in real time while keeping the locally purified form intact,

$$\hat{\rho}_\beta(t + dt) = e^{-idt\hat{H}} \mathbf{X}_\beta(t) \left[e^{-idt\hat{H}} \mathbf{X}_\beta(t) \right]^\dagger \tag{5.25}$$

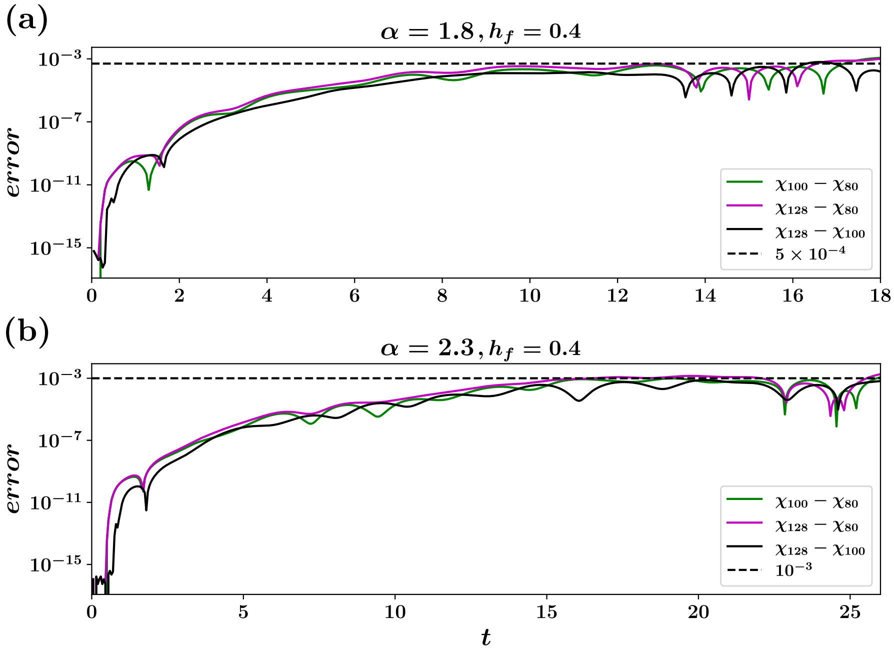

Figure 5.13: Convergence of the TDVP data for DT(t) with increasing bond dimensions, $\chi = 80, 100, 128$, for $\alpha = 1.8, h_f = 0.4$ (a) and $\alpha = 2.3, h_f = 0.4$ (b). The black dashed line is for visual guidance.

We employ a two-site Time-Dependent Variational Principle (TDVP) algorithm with a time step of $dt = 0.05$. To evaluate the convergence of the TDVP data, we examine the relative error in kink density across three increasing bond dimensions ($\chi_{\max} = 80, 100, 128$) at $\beta = 0.3$, as shown in Figure 5.13. Notably, the relative errors consistently remain below $O(10^{-3})$, indicating satisfactory convergence of the numerical results.

The reason for selecting $\beta = 0.3$ as the test case for convergence assessment of all TDVP data is straightforward. A higher temperature promotes correlation spreading throughout the system during real-time evolution, demanding a higher bond dimension to capture the dynamics effectively. Therefore, testing the convergence of errors for the worst-case scenario, where $\beta = 0.3$, is deemed sufficient for our study. The results presented in the main text are derived using a maximum bond dimension of $\chi_{\max} = 128$.

5.D Full counting statistics of domain wall kinks

The PDF of kink density operator $\hat{K}$ can be calculated over the density matrix $\hat{\rho}$ following the Equation 3.4,

$$P(K) = \int_{-\infty}^{\infty} \frac{d\theta}{2\pi} e^{-i\theta\left[K-\frac{N-1}{2}\right]} \mathrm{Tr}\left[\hat{\rho} \prod_{j=1}^{N-1} e^{-i\theta\frac{\hat{\sigma}^x_j \hat{\sigma}^x_{j+1}}{2}}\right]. \tag{5.26}$$

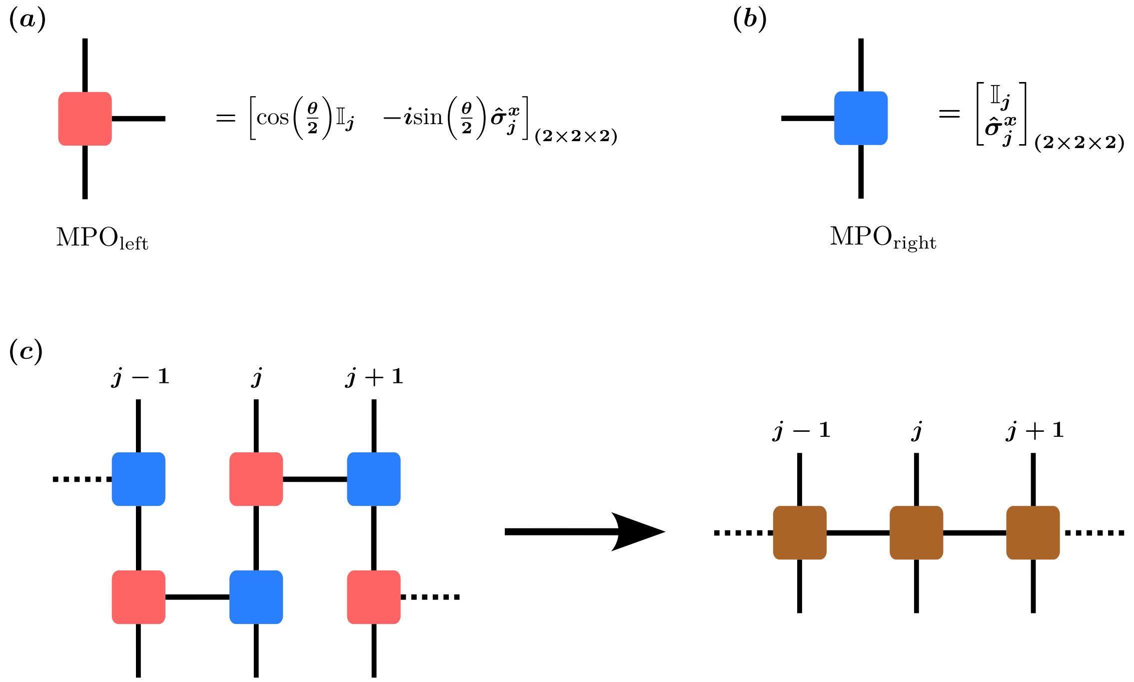

Figure 5.14: Left (red) and right (blue) MPO at site j, (a) and (b) respectively. Contracting left and right MPO at each site to build a four legged MPO (black) at each site, (c).

The moment generating function $\mathrm{Tr}\left[\hat{\rho}\prod_{j=1}^{N-1} e^{-i\theta\frac{\hat{\sigma}^x_j\hat{\sigma}^x_{j+1}}{2}}\right]$ can be calculated by directly applying the sequence of two site operators to the density matrix. Alternatively, we can expand the two site exponential operator by Taylor series and rearrange to break it down into a product of two independent single site operators acting on site j and $j+1$ respectively,

$$e^{-i\theta\frac{\hat{\sigma}^x_j\hat{\sigma}^x_{j+1}}{2}} = \cos\left(\frac{\theta}{2}\right) - i\sin\left(\frac{\theta}{2}\right)\hat{\sigma}^x_j\hat{\sigma}^x_{j+1} = \begin{bmatrix}\cos\left(\frac{\theta}{2}\right)\mathbb{I}_j & -i\sin\left(\frac{\theta}{2}\right)\hat{\sigma}^x_j\end{bmatrix}\begin{bmatrix}\mathbb{I}_{j+1}\\ \hat{\sigma}^x_{j+1}\end{bmatrix} \tag{5.27}$$

Equation 5.27 suggests that that the integral in equation 5.26 has a periodicity of 2π so the integral can be restricted to $\theta \in [-\pi, \pi]$. We reshape and redefine the operators acting on site i and $i + 1$ in equation 5.27 as $\mathrm{MPO}_{\mathrm{left}}$ and $\mathrm{MPO}_{\mathrm{right}}$ respectively (see (a) and (b) in figure 5.14). Each site now has two single site tensors that can be compressed together into a four legged MPO (see (c) in figure 5.14) which can directly act on a matrix product density operator.

Chapter 6

Summary and Outlook

In this thesis we investigate the different aspects related to the dynamics of ferromagnetic long range Ising model (LRIM) following a global quantum quench. Specifically, we study three interrelated topics: dynamics of full counting statistics, thermalization in different dynamical regimes, and dynamical deconfinement transition driven by thermally tuned density of excitations.

In Chapter 3, we explored the dynamical phases of LRIM following a global quantum quench by monitoring the late time PDF of the order parameter. The PDF, encompassing moments of all orders, has emerged as a robust alternative method for characterizing different dynamical phases, offering compelling qualitative signatures, especially in scenarios where lower moments fail to provide conclusive insights due to the absence of stable equilibration. A noteworthy example is the $\alpha > 2$ regime, in which the absence of long-range ferromagnetic order is evident. A prior investigation [137] suggested a persistent ferromagnetic order for all α values, based on the finite prethermal value of average magnetization. However, the emergence of a Gaussian-shaped PDF in the same region suggests complete meltdown of the initial ferromagnetic order. Even for smaller post quench transverse field values, where a conclusive Gaussian shape isn't observed within the simulation time, the PDF still undergoes a qualitative change of shape in transient time with the initial sharp bimodal shape melting away with a stream of probability density moving towards each other suggesting the absence of any robust ferromagnetic order. In the $\alpha \leq 2$ regime, that sustains long range magnetic order at finite temperature [209], we observe a dynamical phase transition. The dynamical ferromagnetic regime is characterized by an oscillating PDF that robustly remains bimodal, transitions to a paramagnetic regime marked by the dissolution of the initial ferromagnetic order. Notably, the dynamical transition observed here is not associated with the breaking of $\mathbb{Z}_2$ symmetry as the symmetry of the initial GHZ state remains unbroken in both phases, but rather on the shape of the shape of the post quench PDF of order parameter.

While for larger value of α we observed the emergence of Gaussian shaped PDF signifying the complete loss of initial order, for smaller α the Gaussification of PDF remains inconclusive within the simulation time and system sizes considered. The region of small α is however tractable with mean field theory, recently some promising analytical results have been developed for post quench evolution of full counting statistics for different magnetic models including LRIM at $0 < \alpha < 1$ using the self consistent time dependent mean field theory (SCTDMFT)[210]. Finally, even though the dynamical phases are qualitatively characterized the exact location of transition points and the critical properties of the transition specially in the regime $1 \leq \alpha \leq 2$ still remain as open questions [138, 17].

In Chapter 4, we investigated thermalization in LRIM across various dynamical regimes. LRIM is nonintegrable for $0 < \alpha < \infty$ and is generally expected to thermalize. However, the model hosts a phenomenon known as confinement, which suppresses correlation spreading throughout the system and tends to hinder thermalization [60, 174]. This is evident from the persistence of the initial ferromagnetic order in the dynamical ferromagnetic phase. In contrast, the dynamical paramagnetic phase witnesses the dissolution of the initial ferromagnetic order, leading to the emergence of a Gaussian-shaped PDF for the order parameter. Our study focused on the signatures of thermalization within the accessible timescales of our simulations. Building upon the success of FCS in characterizing different dynamical phases, we quantified thermalization using the parameter DT, which represents the Euclidean distance between the post-quench PDF and the expected thermal PDF. This is a stringent criterion for thermalization compared with monitoring only the expectation value of the order parameter. In the dynamical ferromagnetic regime, confinement strongly hinders thermalization, as evidenced by the persistent oscillation of the post-quench PDF around the expected thermal value. Conversely, in the dynamical paramagnetic phase for $\alpha = 1.9$, a strong signature of thermalization is observed, with the post-quench PDF equilibrating to the expected thermal value. This observation is further corroborated by the signature observed in the post-quench evolution of domain wall kinks. For $\alpha = 1.5$, the results were inconclusive, with post-quench domain wall kinks exhibiting a prethermal plateau in later times. In the $0 < \alpha < 1$ regime, where MPS-based simulations become inconclusive owing to strong finite-size effects, relaxation dynamics are tractable with the mean field approximation. A previous study [175] based on mean-field approximations and discrete truncated Wigner approximation (DTWA) indicated that in the $0 < \alpha < 1$ regime, long-range interactions give rise to two distinct time scales with significant separations, leading to prethermalization. One time scale involves the relaxation of quasi-conserved local permutation operators, scaling as a power law with the system size, whereas the other is the time of initial relaxation, scaling logarithmic with the system size.

In a recent study with a system of the Bose-Hubbard model realized with systems of ^{133}Cs atoms [152] it was observed that the fluctuation of observables in the subsystem thermalizes at different timescales compared with the local observables. The PDF includes moments of all orders therefore it would be interesting to study thermalization in such systems based on the relaxation of the PDF.

In Chapter 5 we investigated the confinement-deconfinement transition driven by the thermally tuned density of excitation. Previously, it has been observed in short-range models with confinement that increasing the density of excitation in the initial state eventually breaks down confinement, leading to faster entanglement growth [64], prethermalization [23] and meson melting [207]. In LRIM, dynamical confinement is responsible for various exotic emergent behaviors such as slow entanglement growth and dynamical phase transitions. To study the deconfinement, we quenched the initial thermal state at different temperatures across two different thermal phases. We observed a strong signature of dynamical transition in the post-quench evolution of kink fluctuation that showed a transition from a persistent horizontal oscillation at low temperature, signifying strong confinement, to a linear growth at high temperature, signifying deconfinement. This transition was correctly predicted using an effective single-kink model. This transition can be observed in AMO platforms, specifically in systems of trapped ions. The post-quench evolution of a mixed state can be mimicked by evolving pure states within a given mixed state and then computing the weighted ensemble average over each pure state evolution. The simulation time and system size in this study were greatly constrained because the initial thermal states were already highly entangled. In the future, it will would be interesting to simulate larger systems to study the critical properties of the transition and to understand whether they are the same or distinct from the underlying thermal transition.

References

[1] P. W. Anderson, "More is different," *Science*, vol. 177, no. 4047, pp. 393–396, 1972. [Online]. Available: https://www.science.org/doi/abs/10.1126/science.177.4047.393

[2] *More is Different: Fifty Years of Condensed Matter Physics.* Princeton University Press, 2001. [Online]. Available: http://www.jstor.org/stable/j.ctv16t6n15

[3] J. Eisert, M. Friesdorf, and C. Gogolin, "Quantum many-body systems out of equilibrium," *Nature Physics*, vol. 11, no. 2, p. 124–130, 02 2015. [Online]. Available: http://dx.doi.org/10.1038/nphys3215

[4] A. Polkovnikov, K. Sengupta, A. Silva, and M. Vengalattore, "Colloquium: Nonequilibrium dynamics of closed interacting quantum systems," *Reviews of Modern Physics*, vol. 83, no. 3, p. 863–883, 08 2011. [Online]. Available: http://dx.doi.org/10.1103/RevModPhys.83.863

[5] T. Kinoshita, T. Wenger, and D. S. Weiss, "A quantum newton's cradle," *Nature*, vol. 440, no. 7086, pp. 900–903, 04 2006. [Online]. Available: https://doi.org/10.1038/nature04693

[6] C. Monroe, W. C. Campbell, L.-M. Duan, Z.-X. Gong, A. V. Gorshkov, P. W. Hess, R. Islam, K. Kim, N. M. Linke, G. Pagano, P. Richerme, C. Senko, and N. Y. Yao, "Programmable quantum simulations of spin systems with trapped ions," *Rev. Mod. Phys.*, vol. 93, p. 025001, 04 2021. [Online]. Available: https://link.aps.org/doi/10.1103/RevModPhys.93.025001

[7] T. D. Farokh Mivehvar, Francesco Piazza and H. Ritsch, "Cavity qed with quantum gases: new paradigms in many-body physics," *Advances in Physics*, vol. 70, no. 1, pp. 1–153, 2021. [Online]. Available: https://doi.org/10.1080/00018732.2021.1969727

[8] C. Gross and I. Bloch, "Quantum simulations with ultracold atoms in optical lattices," *Science*, vol. 357, no. 6355, pp. 995–1001, 2017. [Online]. Available: https://www.science.org/doi/abs/10.1126/science.aal3837

[9] M. Saffman, T. G. Walker, and K. Mølmer, "Quantum information with rydberg atoms," *Rev. Mod. Phys.*, vol. 82, pp. 2313–2363, 08 2010. [Online]. Available: https://link.aps.org/doi/10.1103/RevModPhys.82.2313

[10] T. Lahaye, C. Menotti, L. Santos, M. Lewenstein, and T. Pfau, "The physics of dipolar bosonic quantum gases," *Reports on Progress in Physics*, vol. 72, no. 12, p. 126401, nov 2009. [Online]. Available: https://dx.doi.org/10.1088/0034-4885/72/12/126401

[11] L. D. Carr, D. DeMille, R. V. Krems, and J. Ye, "Cold and ultracold molecules: science, technology and applications," *New Journal of Physics*, vol. 11, no. 5, p. 055049, may 2009. [Online]. Available: https://dx.doi.org/10.1088/1367-2630/11/5/055049

[12] N. Ranabhat and M. Collura, "Dynamics of the order parameter statistics in the long range Ising model," *SciPost Phys.*, vol. 12, p. 126, 2022. [Online]. Available: https://scipost.org/10.21468/SciPostPhys.12.4.126

[13] ——, "Thermalization of long range ising model in different dynamical regimes: a full counting statistics approach," 2023.

[14] N. Ranabhat, A. Santini, E. Tirrito, and M. Collura, "Dynamical deconfinement transition driven by density of excitations," 2023.

[15] S. Sotiriadis, P. Calabrese, and J. Cardy, "Quantum quench from a thermal initial state," *EPL (Europhysics Letters)*, vol. 87, no. 2, p. 20002, Jul. 2009. [Online]. Available: http://dx.doi.org/10.1209/0295-5075/87/20002

[16] T. Barthel and U. Schollwöck, "Dephasing and the steady state in quantum many-particle systems," *Physical Review Letters*, vol. 100, no. 10, 03 2008. [Online]. Available: http://dx.doi.org/10.1103/PhysRevLett.100.100601

[17] B. Žunkovič, M. Heyl, M. Knap, and A. Silva, "Dynamical quantum phase transitions in spin chains with long-range interactions: Merging different concepts of nonequilibrium criticality," *Physical Review Letters*, vol. 120, no. 13, 03 2018. [Online]. Available: http://dx.doi.org/10.1103/PhysRevLett.120.130601

[18] J. Zhang, G. Pagano, P. W. Hess, A. Kyprianidis, P. Becker, H. Kaplan, A. V. Gorshkov, Z.-X. Gong, and C. Monroe, “Observation of a many-body dynamical phase transition with a 53-qubit quantum simulator,” *Nature*, vol. 551, no. 7682, p. 601–604, 11 2017. [Online]. Available: http://dx.doi.org/10.1038/nature24654

[19] P. Jurcevic, H. Shen, P. Hauke, C. Maier, T. Brydges, C. Hempel, B. P. Lanyon, M. Heyl, R. Blatt, and C. F. Roos, “Direct observation of dynamical quantum phase transitions in an interacting many-body system,” *Physical Review Letters*, vol. 119, no. 8, 08 2017. [Online]. Available: http://dx.doi.org/10.1103/PhysRevLett.119.080501

[20] E. Canovi, D. Rossini, R. Fazio, G. E. Santoro, and A. Silva, “Quantum quenches, thermalization, and many-body localization,” *Physical Review B*, vol. 83, no. 9, 03 2011. [Online]. Available: http://dx.doi.org/10.1103/PhysRevB.83.094431

[21] M. Serbyn, Z. Papić, and D. A. Abanin, “Quantum quenches in the many-body localized phase,” *Physical Review B*, vol. 90, no. 17, 11 2014. [Online]. Available: http://dx.doi.org/10.1103/PhysRevB.90.174302

[22] M. Schreiber, S. S. Hodgman, P. Bordia, H. P. Lüschen, M. H. Fischer, R. Vosk, E. Altman, U. Schneider, and I. Bloch, “Observation of many-body localization of interacting fermions in a quasirandom optical lattice,” *Science*, vol. 349, no. 6250, pp. 842–845, 2015. [Online]. Available: https://www.science.org/doi/abs/10.1126/science.aaa7432

[23] S. Birnkammer, A. Bastianello, and M. Knap, “Prethermalization in one-dimensional quantum many-body systems with confinement,” *Nature Communications*, vol. 13, no. 1, 12 2022. [Online]. Available: http://dx.doi.org/10.1038/s41467-022-35301-6

[24] M. Fagotti and F. H. L. Essler, “Reduced density matrix after a quantum quench,” *Phys. Rev. B*, vol. 87, p. 245107, 06 2013. [Online]. Available: https://link.aps.org/doi/10.1103/PhysRevB.87.245107

[25] P. Calabrese, F. H. L. Essler, and M. Fagotti, “Quantum quench in the transverse field ising chain: I. time evolution of order parameter correlators,” *Journal of Statistical Mechanics: Theory and Experiment*, vol. 2012, no. 07, p. P07016, 07 2012. [Online]. Available: http://dx.doi.org/10.1088/1742-5468/2012/07/P07016

[26] M. Cramer, C. M. Dawson, J. Eisert, and T. J. Osborne, "Exact relaxation in a class of nonequilibrium quantum lattice systems," *Physical Review Letters*, vol. 100, no. 3, 01 2008. [Online]. Available: http://dx.doi.org/10.1103/PhysRevLett.100.030602

[27] R. Vasseur and J. E. Moore, "Nonequilibrium quantum dynamics and transport: from integrability to many-body localization," *Journal of Statistical Mechanics: Theory and Experiment*, vol. 2016, no. 6, p. 064010, Jun. 2016. [Online]. Available: http://dx.doi.org/10.1088/1742-5468/2016/06/064010

[28] F. Jin, T. Neuhaus, K. Michielsen, S. Miyashita, M. A. Novotny, M. I. Katsnelson, and H. De Raedt, "Equilibration and thermalization of classical systems," *New Journal of Physics*, vol. 15, no. 3, p. 033009, 03 2013. [Online]. Available: http://dx.doi.org/10.1088/1367-2630/15/3/033009

[29] J. M. Deutsch, "Quantum statistical mechanics in a closed system," *Phys. Rev. A*, vol. 43, pp. 2046–2049, Feb 1991. [Online]. Available: https://link.aps.org/doi/10.1103/PhysRevA.43.2046

[30] M. Rigol, V. Dunjko, and M. Olshanii, "Thermalization and its mechanism for generic isolated quantum systems," *Nature*, vol. 452, no. 7189, p. 854–858, 04 2008. [Online]. Available: http://dx.doi.org/10.1038/nature06838

[31] M. Srednicki, "Chaos and quantum thermalization," *Phys. Rev. E*, vol. 50, pp. 888–901, Aug 1994. [Online]. Available: https://link.aps.org/doi/10.1103/PhysRevE.50.888

[32] H. Kim, T. N. Ikeda, and D. A. Huse, "Testing whether all eigenstates obey the eigenstate thermalization hypothesis," *Physical Review E*, vol. 90, no. 5, 11 2014. [Online]. Available: http://dx.doi.org/10.1103/PhysRevE.90.052105

[33] L. F. Santos and M. Rigol, "Onset of quantum chaos in one-dimensional bosonic and fermionic systems and its relation to thermalization," *Physical Review E*, vol. 81, no. 3, 03 2010. [Online]. Available: http://dx.doi.org/10.1103/PhysRevE.81.036206

[34] A. M. Kaufman, M. E. Tai, A. Lukin, M. Rispoli, R. Schittko, P. M. Preiss, and M. Greiner, "Quantum thermalization through entanglement in an isolated many-body system," *Science*, vol. 353, no. 6301, p. 794–800, 06 2016. [Online]. Available: http://dx.doi.org/10.1126/science.aaf6725

[35] M. Rigol, "Breakdown of thermalization in finite one-dimensional systems," *Physical Review Letters*, vol. 103, no. 10, 09 2009. [Online]. Available: http://dx.doi.org/10.1103/PhysRevLett.103.100403

[36] C. Neill, P. Roushan, M. Fang, Y. Chen, M. Kolodrubetz, Z. Chen, A. Megrant, R. Barends, B. Campbell, B. Chiaro, A. Dunsworth, E. Jeffrey, J. Kelly, J. Mutus, P. J. J. O'Malley, C. Quintana, D. Sank, A. Vainsencher, J. Wenner, T. C. White, A. Polkovnikov, and J. M. Martinis, "Ergodic dynamics and thermalization in an isolated quantum system," *Nature Physics*, vol. 12, no. 11, p. 1037–1041, 07 2016. [Online]. Available: http://dx.doi.org/10.1038/nphys3830

[37] S. Sugimoto, R. Hamazaki, and M. Ueda, "Test of the eigenstate thermalization hypothesis based on local random matrix theory," *Physical Review Letters*, vol. 126, no. 12, 03 2021. [Online]. Available: http://dx.doi.org/10.1103/PhysRevLett.126.120602

[38] N. Shiraishi and K. Matsumoto, "Undecidability in quantum thermalization," *Nature Communications*, vol. 12, no. 1, 08 2021. [Online]. Available: http://dx.doi.org/10.1038/s41467-021-25053-0

[39] R. Nandkishore and D. A. Huse, "Many-body localization and thermalization in quantum statistical mechanics," *Annual Review of Condensed Matter Physics*, vol. 6, no. 1, p. 15–38, 03 2015. [Online]. Available: http://dx.doi.org/10.1146/annurev-conmatphys-031214-014726

[40] N. Defenu, T. Donner, T. Macrì, G. Pagano, S. Ruffo, and A. Trombettoni, "Long-range interacting quantum systems," *Rev. Mod. Phys.*, vol. 95, p. 035002, 08 2023. [Online]. Available: https://link.aps.org/doi/10.1103/RevModPhys.95.035002

[41] N. Defenu, A. Lerose, and S. Pappalardi, "Out-of-equilibrium dynamics of quantum many-body systems with long-range interactions," 2023.

[42] N. Defenu, A. Codello, S. Ruffo, and A. Trombettoni, "Criticality of spin systems with weak long-range interactions," *Journal of Physics A: Mathematical and Theoretical*, vol. 53, no. 14, p. 143001, 03 2020. [Online]. Available: https://dx.doi.org/10.1088/1751-8121/ab6a6c

[43] M. Knap, A. Kantian, T. Giamarchi, I. Bloch, M. D. Lukin, and E. Demler, "Probing real-space and time-resolved correlation functions with many-body ramsey interferometry," *Phys. Rev. Lett.*, vol. 111, p. 147205, 10 2013. [Online]. Available: https://link.aps.org/doi/10.1103/PhysRevLett.111.147205

[44] E. Gonzalez Lazo, M. Heyl, M. Dalmonte, and A. Angelone, “Finite-temperature critical behavior of long-range quantum ising models,” *SciPost Physics*, vol. 11, no. 4, 10 2021. [Online]. Available: http://dx.doi.org/10.21468/SciPostPhys.11.4.076

[45] J. Zhang, G. Pagano, P. W. Hess, A. Kyprianidis, P. Becker, H. Kaplan, A. V. Gorshkov, Z.-X. Gong, and C. Monroe, “Observation of a many-body dynamical phase transition with a 53-qubit quantum simulator,” *Nature*, vol. 551, no. 7682, p. 601–604, 11 2017. [Online]. Available: http://dx.doi.org/10.1038/nature24654

[46] P. Pfeuty, “The one-dimensional ising model with a transverse field,” *Annals of Physics*, vol. 57, no. 1, pp. 79–90, 1970. [Online]. Available: https://www.sciencedirect.com/science/article/pii/0003491670902708

[47] E. Lieb, T. Schultz, and D. Mattis, “Two soluble models of an antiferromagnetic chain,” *Annals of Physics*, vol. 16, no. 3, pp. 407–466, 1961. [Online]. Available: https://www.sciencedirect.com/science/article/pii/0003491661901154

[48] M. Gabbrielli, L. Lepori, and L. Pezzè, “Multipartite-entanglement tomography of a quantum simulator,” *New Journal of Physics*, vol. 21, no. 3, p. 033039, 03 2019. [Online]. Available: http://dx.doi.org/10.1088/1367-2630/aafb8c

[49] A. Dutta and J. K. Bhattacharjee, “Phase transitions in the quantum ising and rotor models with a long-range interaction,” *Phys. Rev. B*, vol. 64, p. 184106, 10 2001. [Online]. Available: https://link.aps.org/doi/10.1103/PhysRevB.64.184106

[50] H. Lipkin, N. Meshkov, and A. Glick, “Validity of many-body approximation methods for a solvable model: (i). exact solutions and perturbation theory,” *Nuclear Physics*, vol. 62, no. 2, pp. 188–198, 1965. [Online]. Available: https://www.sciencedirect.com/science/article/pii/002955826590862X

[51] F. Pan and J. Draayer, “Analytical solutions for the lmg model,” *Physics Letters B*, vol. 451, no. 1, pp. 1–10, 1999. [Online]. Available: https://www.sciencedirect.com/science/article/pii/S0370269399001914

[52] A. Lerose, B. Žunkovič, J. Marino, A. Gambassi, and A. Silva, “Impact of nonequilibrium fluctuations on prethermal dynamical phase transitions in long-range interacting spin chains,” *Phys. Rev. B*, vol. 99, p. 045128, 01 2019. [Online]. Available: https://link.aps.org/doi/10.1103/PhysRevB.99.045128

[53] F. H. L. Essler and M. Fagotti, "Quench dynamics and relaxation in isolated integrable quantum spin chains," *Journal of Statistical Mechanics: Theory and Experiment*, vol. 2016, no. 6, p. 064002, 06 2016. [Online]. Available: http://dx.doi.org/10.1088/1742-5468/2016/06/064002

[54] E. H. Lieb and D. W. Robinson, "The finite group velocity of quantum spin systems," *Communications in Mathematical Physics*, vol. 28, no. 3, pp. 251–257, 09 1972. [Online]. Available: https://doi.org/10.1007/BF01645779

[55] M. Foss-Feig, Z.-X. Gong, C. W. Clark, and A. V. Gorshkov, "Nearly linear light cones in long-range interacting quantum systems," *Phys. Rev. Lett.*, vol. 114, p. 157201, 04 2015. [Online]. Available: https://link.aps.org/doi/10.1103/PhysRevLett.114.157201

[56] J. Schachenmayer, B. P. Lanyon, C. F. Roos, and A. J. Daley, "Entanglement growth in quench dynamics with variable range interactions," *Phys. Rev. X*, vol. 3, p. 031015, Sep 2013. [Online]. Available: https://link.aps.org/doi/10.1103/PhysRevX.3.031015

[57] S. Pappalardi, A. Russomanno, B. Žunkovič, F. Iemini, A. Silva, and R. Fazio, "Scrambling and entanglement spreading in long-range spin chains," *Phys. Rev. B*, vol. 98, p. 134303, 10 2018. [Online]. Available: https://link.aps.org/doi/10.1103/PhysRevB.98.134303

[58] A. Lerose and S. Pappalardi, "Origin of the slow growth of entanglement entropy in long-range interacting spin systems," *Phys. Rev. Res.*, vol. 2, p. 012041, 02 2020. [Online]. Available: https://link.aps.org/doi/10.1103/PhysRevResearch.2.012041

[59] ——, "Bridging entanglement dynamics and chaos in semiclassical systems," *Phys. Rev. A*, vol. 102, p. 032404, 09 2020. [Online]. Available: https://link.aps.org/doi/10.1103/PhysRevA.102.032404

[60] A. Lerose, B. Žunkovič, A. Silva, and A. Gambassi, "Quasilocalized excitations induced by long-range interactions in translationally invariant quantum spin chains," *Phys. Rev. B*, vol. 99, p. 121112, 03 2019. [Online]. Available: https://link.aps.org/doi/10.1103/PhysRevB.99.121112

[61] F. Liu, R. Lundgren, P. Titum, G. Pagano, J. Zhang, C. Monroe, and A. V. Gorshkov, "Confined quasiparticle dynamics in long-range interacting quantum spin chains," *Phys. Rev. Lett.*, vol. 122, p. 150601, 04 2019. [Online]. Available: https://link.aps.org/doi/10.1103/PhysRevLett.122.150601

[62] B. Lake, A. M. Tsvelik, S. Notbohm, D. Alan Tennant, T. G. Perring, M. Reehuis, C. Sekar, G. Krabbes, and B. Büchner, "Confinement of fractional quantum number particles in a condensed-matter system," *Nature Physics*, vol. 6, no. 1, pp. 50–55, 01 2010. [Online]. Available: https://doi.org/10.1038/nphys1462

[63] W. L. Tan, P. Becker, F. Liu, G. Pagano, K. S. Collins, A. De, L. Feng, H. B. Kaplan, A. Kyprianidis, R. Lundgren, W. Morong, S. Whitsitt, A. V. Gorshkov, and C. Monroe, "Domain-wall confinement and dynamics in a quantum simulator," *Nature Physics*, vol. 17, no. 6, p. 742–747, 03 2021. [Online]. Available: http://dx.doi.org/10.1038/s41567-021-01194-3

[64] A. Lerose, F. M. Surace, P. P. Mazza, G. Perfetto, M. Collura, and A. Gambassi, "Quasilocalized dynamics from confinement of quantum excitations," *Phys. Rev. B*, vol. 102, p. 041118, 07 2020. [Online]. Available: https://link.aps.org/doi/10.1103/PhysRevB.102.041118

[65] G. E. Moore, "Cramming more components onto integrated circuits, reprinted from electronics, volume 38, number 8, april 19, 1965, pp.114 ff." *IEEE Solid-State Circuits Society Newsletter*, vol. 11, no. 3, pp. 33–35, 2006.

[66] J. Koomey, S. Berard, M. Sanchez, and H. Wong, "Implications of historical trends in the electrical efficiency of computing," *IEEE Annals of the History of Computing*, vol. 33, no. 3, pp. 46–54, 2011.

[67] T. Westerhout, M. I. Katsnelson, and B. L. Chamberlain, "Large-scale and user-friendly exact diagonalization in chapel," 2022. [Online]. Available: https://api.semanticscholar.org/CorpusID:249916389

[68] A. Wietek and A. M. Läuchli, "Sublattice coding algorithm and distributed memory parallelization for large-scale exact diagonalizations of quantum many-body systems," *Phys. Rev. E*, vol. 98, p. 033309, Sep 2018. [Online]. Available: https://link.aps.org/doi/10.1103/PhysRevE.98.033309

[69] A. Georges, G. Kotliar, W. Krauth, and M. J. Rozenberg, "Dynamical mean-field theory of strongly correlated fermion systems and the limit of infinite dimensions," *Rev. Mod. Phys.*, vol. 68, pp. 13–125, Jan 1996. [Online]. Available: https://link.aps.org/doi/10.1103/RevModPhys.68.13

[70] P. H. Acioli, "Review of quantum monte carlo methods and their applications," *Journal of Molecular Structure: THEOCHEM*, vol. 394, no. 2, pp. 75–85, 1997, proceedings of the Eighth Brazilian Symposium of

Theoretical Chemistry. [Online]. Available: https://www.sciencedirect.com/science/article/pii/S016612809604821X

[71] J. Oitmaa, C. Hamer, and W. Zheng, *Series Expansion Methods for Strongly Interacting Lattice Models*, ser. Online access with purchase: Cambridge Books Online. Cambridge University Press, 2006. [Online]. Available: https://books.google.it/books?id=VCYUMPDK73IC

[72] R. Parr and Y. Weitao, *Density-Functional Theory of Atoms and Molecules*, ser. International Series of Monographs on Chemistry. Oxford University Press, 1994. [Online]. Available: https://books.google.it/books?id=mGOpScSIwU4C

[73] S. R. White, "Density matrix formulation for quantum renormalization groups," *Phys. Rev. Lett.*, vol. 69, pp. 2863–2866, 11 1992. [Online]. Available: https://link.aps.org/doi/10.1103/PhysRevLett.69.2863

[74] ——, "Density-matrix algorithms for quantum renormalization groups," *Phys. Rev. B*, vol. 48, pp. 10 345–10 356, 10 1993. [Online]. Available: https://link.aps.org/doi/10.1103/PhysRevB.48.10345

[75] S. Östlund and S. Rommer, "Thermodynamic limit of density matrix renormalization," *Phys. Rev. Lett.*, vol. 75, pp. 3537–3540, Nov 1995. [Online]. Available: https://link.aps.org/doi/10.1103/PhysRevLett.75.3537

[76] J. Dukelsky, M. A. Martín-Delgado, T. Nishino, and G. Sierra, "Equivalence of the variational matrix product method and the density matrix renormalization group applied to spin chains," *Europhysics Letters (EPL)*, vol. 43, no. 4, pp. 457–462, aug 1998. [Online]. Available: https://doi.org/10.1209%2Fepl%2Fi1998-00381-x

[77] G. Vidal, "Efficient simulation of one-dimensional quantum many-body systems," *Phys. Rev. Lett.*, vol. 93, p. 040502, 07 2004. [Online]. Available: https://link.aps.org/doi/10.1103/PhysRevLett.93.040502

[78] S. R. White and A. E. Feiguin, "Real-time evolution using the density matrix renormalization group," *Phys. Rev. Lett.*, vol. 93, p. 076401, 08 2004. [Online]. Available: https://link.aps.org/doi/10.1103/PhysRevLett.93.076401

[79] J. Haegeman, J. I. Cirac, T. J. Osborne, I. Pižorn, H. Verschelde, and F. Verstraete, "Time-dependent variational principle for quantum lattices," *Phys. Rev. Lett.*, vol. 107, p. 070601, 08 2011. [Online]. Available: https://link.aps.org/doi/10.1103/PhysRevLett.107.070601

[80] J. Haegeman, C. Lubich, I. Oseledets, B. Vandereycken, and F. Verstraete, "Unifying time evolution and optimization with matrix product states," *Phys. Rev. B*, vol. 94, p. 165116, 10 2016. [Online]. Available: https://link.aps.org/doi/10.1103/PhysRevB.94.165116

[81] J. Jordan, R. Orús, G. Vidal, F. Verstraete, and J. I. Cirac, "Classical simulation of infinite-size quantum lattice systems in two spatial dimensions," *Phys. Rev. Lett.*, vol. 101, p. 250602, 12 2008. [Online]. Available: https://link.aps.org/doi/10.1103/PhysRevLett.101.250602

[82] G. Vidal, "Class of quantum many-body states that can be efficiently simulated," *Phys. Rev. Lett.*, vol. 101, p. 110501, 09 2008. [Online]. Available: https://link.aps.org/doi/10.1103/PhysRevLett.101.110501

[83] M. Levin and C. P. Nave, "Tensor renormalization group approach to two-dimensional classical lattice models," *Phys. Rev. Lett.*, vol. 99, p. 120601, 09 2007. [Online]. Available: https://link.aps.org/doi/10.1103/PhysRevLett.99.120601

[84] G. Evenbly, "A practical guide to the numerical implementation of tensor networks i: Contractions, decompositions, and gauge freedom," *Frontiers in Applied Mathematics and Statistics*, vol. 8, 2022. [Online]. Available: https://www.frontiersin.org/articles/10.3389/fams.2022.806549

[85] R. Orús, "A practical introduction to tensor networks: Matrix product states and projected entangled pair states," *Annals of Physics*, vol. 349, pp. 117–158, oct 2014. [Online]. Available: https://doi.org/10.1016%2Fj.aop.2014.06.013

[86] P. Silvi, F. Tschirsich, M. Gerster, J. Jünemann, D. Jaschke, M. Rizzi, and S. Montangero, "The tensor networks anthology: Simulation techniques for many-body quantum lattice systems," *SciPost Physics Lecture Notes*, mar 2019. [Online]. Available: https://doi.org/10.21468%2Fscipostphyslectnotes.8

[87] S.-J. Ran, E. Tirrito, C. Peng, X. Chen, L. Tagliacozzo, G. Su, and M. Lewenstein, *Tensor Network Contractions.* Springer International Publishing, 2020. [Online]. Available: https://doi.org/10.1007%2F978-3-030-34489-4

[88] L. Devos, M. V. Damme, J. Haegeman, and contributors, "Tensoroperations.jl," oct 2023. [Online]. Available: https://github.com/Jutho/TensorOperations.jl

[89] J. Bezanson, A. Edelman, S. Karpinski, and V. B. Shah, "Julia: A fresh approach to numerical computing," *SIAM Review*, vol. 59, no. 1, pp. 65–98, 2017. [Online]. Available: https://epubs.siam.org/doi/10.1137/141000671

[90] R. N. C. Pfeifer, J. Haegeman, and F. Verstraete, "Faster identification of optimal contraction sequences for tensor networks," *Physical Review E*, vol. 90, no. 3, sep 2014. [Online]. Available: https://doi.org/10.1103%2Fphysreve.90.033315

[91] G. Evenbly and R. N. C. Pfeifer, "Improving the efficiency of variational tensor network algorithms," *Phys. Rev. B*, vol. 89, p. 245118, jun 2014. [Online]. Available: https://link.aps.org/doi/10.1103/PhysRevB.89.245118

[92] J. Gray and S. Kourtis, "Hyper-optimized tensor network contraction," *Quantum*, vol. 5, p. 410, mar 2021. [Online]. Available: https://doi.org/10.22331%2Fq-2021-03-15-410

[93] J. M. Dudek, L. Dueñas-Osorio, and M. Y. Vardi, "Efficient contraction of large tensor networks for weighted model counting through graph decompositions," 2020. [Online]. Available: https://arxiv.org/abs/1908.04381

[94] L. Trefethen and D. Bau, *Numerical Linear Algebra.* Society for Industrial and Applied Mathematics, 1997. [Online]. Available: https://books.google.it/books?id=5Y1TPgAACAAJ

[95] G. Golub and C. Van Loan, *Matrix Computations*, ser. Johns Hopkins Studies in the Mathematical Sciences. Johns Hopkins University Press, 1996. [Online]. Available: https://books.google.it/books?id=mlOa7wPX6OYC

[96] M. M. Vopson, "Estimation of the information contained in the visible matter of the universe," *AIP Advances*, vol. 11, no. 10, p. 105317, 10 2021. [Online]. Available: https://doi.org/10.1063/5.0064475

[97] J. S. Bell, "On the einstein podolsky rosen paradox," *Physics Physique Fizika*, vol. 1, pp. 195–200, Nov 1964. [Online]. Available: https://link.aps.org/doi/10.1103/PhysicsPhysiqueFizika.1.195

[98] A. Aspect, J. Dalibard, and G. Roger, "Experimental test of bell's inequalities using time-varying analyzers," *Phys. Rev. Lett.*, vol. 49, pp. 1804–1807, Dec 1982. [Online]. Available: https://link.aps.org/doi/10.1103/PhysRevLett.49.1804

[99] D. M. Greenberger, M. A. Horne, and A. Zeilinger, "Going beyond bell's theorem," 2007.

[100] W. K. Wootters and W. S. Leng, "Quantum entanglement as a quantifiable resource [and discussion]," *Philosophical Transactions: Mathematical, Physical*

and Engineering Sciences, vol. 356, no. 1743, pp. 1717–1731, 1998. [Online]. Available: http://www.jstor.org/stable/55007

[101] J. Eisert, M. Cramer, and M. B. Plenio, "Colloquium: Area laws for the entanglement entropy," *Rev. Mod. Phys.*, vol. 82, pp. 277–306, Feb 2010. [Online]. Available: https://link.aps.org/doi/10.1103/RevModPhys.82.277

[102] J. D. Bekenstein, "Black holes and entropy," *Phys. Rev. D*, vol. 7, pp. 2333–2346, Apr 1973. [Online]. Available: https://link.aps.org/doi/10.1103/PhysRevD.7.2333

[103] M. Srednicki, "Entropy and area," *Phys. Rev. Lett.*, vol. 71, pp. 666–669, Aug 1993. [Online]. Available: https://link.aps.org/doi/10.1103/PhysRevLett.71.666

[104] C. Callan and F. Wilczek, "On geometric entropy," *Physics Letters B*, vol. 333, no. 1-2, pp. 55–61, jul 1994. [Online]. Available: https://doi.org/10.1016%2F0370-2693%2894%2991007-3

[105] M. B. Plenio, J. Eisert, J. Dreißig, and M. Cramer, "Entropy, entanglement, and area: Analytical results for harmonic lattice systems," *Phys. Rev. Lett.*, vol. 94, p. 060503, Feb 2005. [Online]. Available: https://link.aps.org/doi/10.1103/PhysRevLett.94.060503

[106] P. Calabrese and J. Cardy, "Entanglement entropy and quantum field theory," *Journal of Statistical Mechanics: Theory and Experiment*, vol. 2004, no. 06, p. P06002, jun 2004. [Online]. Available: https://doi.org/10.1088%2F1742-5468%2F2004%2F06%2Fp06002

[107] G. Vidal, J. I. Latorre, E. Rico, and A. Kitaev, "Entanglement in quantum critical phenomena," *Phys. Rev. Lett.*, vol. 90, p. 227902, Jun 2003. [Online]. Available: https://link.aps.org/doi/10.1103/PhysRevLett.90.227902

[108] O. Legeza and J. Sólyom, "Quantum data compression, quantum information generation, and the density-matrix renormalization-group method," *Phys. Rev. B*, vol. 70, p. 205118, Nov 2004. [Online]. Available: https://link.aps.org/doi/10.1103/PhysRevB.70.205118

[109] M. B. Hastings, "Solving gapped hamiltonians locally," *Phys. Rev. B*, vol. 73, p. 085115, Feb 2006. [Online]. Available: https://link.aps.org/doi/10.1103/PhysRevB.73.085115

[110] M. Nielsen and I. Chuang, *Quantum Computation and Quantum Information: 10th Anniversary Edition.* Cambridge University Press, 2010. [Online]. Available: https://books.google.it/books?id=-s4DEy7o-a0C

[111] C. Eckart and G. Young, "The approximation of one matrix by another of lower rank," *Psychometrika*, vol. 1, pp. 211–218, sep 1936. [Online]. Available: https://doi.org/10.1007/BF02288367

[112] M. Fannes, B. Nachtergaele, and R. F. Werner, "Finitely correlated states on quantum spin chains," *Communications in Mathematical Physics*, vol. 144, no. 3, pp. 443–490, Mar 1992. [Online]. Available: https://doi.org/10.1007/BF02099178

[113] S. Rommer and S. Östlund, "Class of ansatz wave functions for one-dimensional spin systems and their relation to the density matrix renormalization group," *Phys. Rev. B*, vol. 55, pp. 2164–2181, Jan 1997. [Online]. Available: https://link.aps.org/doi/10.1103/PhysRevB.55.2164

[114] F. Verstraete and J. I. Cirac, "Matrix product states represent ground states faithfully," *Phys. Rev. B*, vol. 73, p. 094423, Mar 2006. [Online]. Available: https://link.aps.org/doi/10.1103/PhysRevB.73.094423

[115] T. Kuwahara and K. Saito, "Area law of noncritical ground states in 1d long-range interacting systems," *Nature Communications*, vol. 11, no. 1, p. 4478, Sep 2020. [Online]. Available: https://doi.org/10.1038/s41467-020-18055-x

[116] F. Verstraete, J. J. García-Ripoll, and J. I. Cirac, "Matrix product density operators: Simulation of finite-temperature and dissipative systems," *Phys. Rev. Lett.*, vol. 93, p. 207204, 11 2004. [Online]. Available: https://link.aps.org/doi/10.1103/PhysRevLett.93.207204

[117] M. Zwolak and G. Vidal, "Mixed-state dynamics in one-dimensional quantum lattice systems: A time-dependent superoperator renormalization algorithm," *Phys. Rev. Lett.*, vol. 93, p. 207205, 11 2004. [Online]. Available: https://link.aps.org/doi/10.1103/PhysRevLett.93.207205

[118] B. Pirvu, V. Murg, J. I. Cirac, and F. Verstraete, "Matrix product operator representations," *New Journal of Physics*, vol. 12, no. 2, p. 025012, 02 2010. [Online]. Available: https://dx.doi.org/10.1088/1367-2630/12/2/025012

[119] G. M. Crosswhite and D. Bacon, "Finite automata for caching in matrix product algorithms," *Physical Review A*, vol. 78, no. 1, 07 2008. [Online]. Available: https://doi.org/10.1103%2Fphysreva.78.012356

[120] G. M. Crosswhite, A. C. Doherty, and G. Vidal, "Applying matrix product operators to model systems with long-range interactions," *Physical Review B*, vol. 78, no. 3, 07 2008. [Online]. Available: https://doi.org/10.1103%2Fphysrevb.78.035116

[121] U. Schollwöck, "The density-matrix renormalization group in the age of matrix product states," *Annals of Physics*, vol. 326, no. 1, pp. 96–192, 01 2011. [Online]. Available: https://doi.org/10.1016%2Fj.aop.2010.09.012

[122] I. P. McCulloch, "From density-matrix renormalization group to matrix product states," *Journal of Statistical Mechanics: Theory and Experiment*, vol. 2007, no. 10, p. P10014, 10 2007. [Online]. Available: https://dx.doi.org/10.1088/1742-5468/2007/10/P10014

[123] T. Bochud and D. Challet, "Optimal approximations of power-laws with exponentials," 2006.

[124] U. Schollwöck, "The density-matrix renormalization group," *Rev. Mod. Phys.*, vol. 77, pp. 259–315, 04 2005. [Online]. Available: https://link.aps.org/doi/10.1103/RevModPhys.77.259

[125] K. A. Hallberg, "New trends in density matrix renormalization," *Advances in Physics*, vol. 55, no. 5-6, pp. 477–526, 07 2006. [Online]. Available: https://doi.org/10.1080%2F00018730600766432

[126] J. Dukelsky, M. A. Martín-Delgado, T. Nishino, and G. Sierra, "Equivalence of the variational matrix product method and the density matrix renormalization group applied to spin chains," *Europhysics Letters (EPL)*, vol. 43, no. 4, pp. 457–462, 08 1998. [Online]. Available: https://doi.org/10.1209%2Fepl%2Fi1998-00381-x

[127] C. Lanczos, "An iteration method for the solution of the eigenvalue i problem. of linear differential and integral operators," *Journal of Research of the National Bureau of Standards*, vol. 45, pp. 255–282, 1950. [Online]. Available: https://nvlpubs.nist.gov/nistpubs/jres/045/jresv45n4p255_a1b.pdf

[128] H. D. Simon, "Analysis of the symmetric lanczos algorithm with reorthogonalization methods," *Linear Algebra and its Applications*, vol. 61, pp. 101–131, 1984. [Online]. Available: https://www.sciencedirect.com/science/article/pii/0024379584900259

[129] S. R. White, "Density matrix renormalization group algorithms with a single center site," *Phys. Rev. B*, vol. 72, p. 180403, 11 2005. [Online]. Available: https://link.aps.org/doi/10.1103/PhysRevB.72.180403

[130] R. Orús and G. Vidal, "Infinite time-evolving block decimation algorithm beyond unitary evolution," *Phys. Rev. B*, vol. 78, p. 155117, 10 2008. [Online]. Available: https://link.aps.org/doi/10.1103/PhysRevB.78.155117

[131] M. P. Zaletel, R. S. K. Mong, C. Karrasch, J. E. Moore, and F. Pollmann, "Time-evolving a matrix product state with long-ranged interactions," *Phys. Rev. B*, vol. 91, p. 165112, 04 2015. [Online]. Available: https://link.aps.org/doi/10.1103/PhysRevB.91.165112

[132] S. Paeckel, T. Köhler, A. Swoboda, S. R. Manmana, U. Schollwöck, and C. Hubig, "Time-evolution methods for matrix-product states," *Annals of Physics*, vol. 411, p. 167998, 2019. [Online]. Available: https://www.sciencedirect.com/science/article/pii/S0003491619302532

[133] H. Holden, K. Karlsen, K.-A. Lie, and H. Risebro, *Splitting Methods for Partial Differential Equations with Rough Solutions: Analysis and MATLAB programs*, 04 2010.

[134] *Lanczos Algorithms for Large Symmetric Eigenvalue Computations Vol. I Theory*, ser. Lanczos Algorithms for Large Symmetric Eigenvalue Computations. Birkhäuser Boston, 1985. [Online]. Available: https://books.google.it/books?id=GeVQAAAAMAAJ

[135] C. C. Paige, "The computation of eigenvalues and eigenvectors of very large sparse matrices," 1971. [Online]. Available: https://api.semanticscholar.org/CorpusID:19735646

[136] C. Moler and C. Loan, "Nineteen dubious ways to compute the exponential of a matrix, twenty-five years later," *Society for Industrial and Applied Mathematics*, vol. 45, pp. 3–49, 03 2003.

[137] J. C. Halimeh, V. Zauner-Stauber, I. P. McCulloch, I. de Vega, U. Schollwöck, and M. Kastner, "Prethermalization and persistent order in the absence of a thermal phase transition," *Phys. Rev. B*, vol. 95, p. 024302, 01 2017. [Online]. Available: https://link.aps.org/doi/10.1103/PhysRevB.95.024302

[138] J. C. Halimeh and V. Zauner-Stauber, "Dynamical phase diagram of quantum spin chains with long-range interactions," *Phys. Rev. B*, vol. 96, p. 134427,

10 2017. [Online]. Available: https://link.aps.org/doi/10.1103/PhysRevB.96.134427

[139] L. S. Levitov, H. Lee, and G. B. Lesovik, "Electron counting statistics and coherent states of electric current," *Journal of Mathematical Physics*, vol. 37, no. 10, p. 4845–4866, 10 1996. [Online]. Available: http://dx.doi.org/10.1063/1.531672

[140] C. W. J. Beenakker and H. Schomerus, "Counting statistics of photons produced by electronic shot noise," *Phys. Rev. Lett.*, vol. 86, pp. 700–703, 01 2001. [Online]. Available: https://link.aps.org/doi/10.1103/PhysRevLett.86.700

[141] D. A. Bagrets and Y. V. Nazarov, "Full counting statistics of charge transfer in coulomb blockade systems," *Phys. Rev. B*, vol. 67, p. 085316, 02 2003. [Online]. Available: https://link.aps.org/doi/10.1103/PhysRevB.67.085316

[142] W. Belzig, "Full counting statistics of super-poissonian shot noise in multilevel quantum dots," *Phys. Rev. B*, vol. 71, p. 161301, 04 2005. [Online]. Available: https://link.aps.org/doi/10.1103/PhysRevB.71.161301

[143] S. Gustavsson, R. Leturcq, B. Simovič, R. Schleser, T. Ihn, P. Studerus, K. Ensslin, D. C. Driscoll, and A. C. Gossard, "Counting statistics of single electron transport in a quantum dot," *Phys. Rev. Lett.*, vol. 96, p. 076605, 02 2006. [Online]. Available: https://link.aps.org/doi/10.1103/PhysRevLett.96.076605

[144] C. Matthiesen, M. J. Stanley, M. Hugues, E. Clarke, and M. Atatüre, "Full counting statistics of quantum dot resonance fluorescence," *Scientific Reports*, vol. 4, no. 1, p. 4911, 05 2014. [Online]. Available: https://doi.org/10.1038/srep04911

[145] Z. Yu, G.-M. Tang, and J. Wang, "Full-counting statistics of transient energy current in mesoscopic systems," *Phys. Rev. B*, vol. 93, p. 195419, 05 2016. [Online]. Available: https://link.aps.org/doi/10.1103/PhysRevB.93.195419

[146] A. Nunnenkamp, D. Meiser, and P. Meystre, "Full counting statistics of heteronuclear molecules from feshbach-assisted photoassociation," *New Journal of Physics*, vol. 8, no. 6, p. 88, 06 2006. [Online]. Available: https://dx.doi.org/10.1088/1367-2630/8/6/088

[147] S. P. Rath and W. Zwerger, "Full counting statistics of the interference contrast from independent bose-einstein condensates," *Phys. Rev. A*, vol. 82,

p. 053622, 11 2010. [Online]. Available: https://link.aps.org/doi/10.1103/PhysRevA.82.053622

[148] I. Lovas, B. Dóra, E. Demler, and G. Zaránd, "Full counting statistics of time-of-flight images," *Phys. Rev. A*, vol. 95, p. 053621, 05 2017. [Online]. Available: https://link.aps.org/doi/10.1103/PhysRevA.95.053621

[149] M. Gring, M. Kuhnert, T. Langen, T. Kitagawa, B. Rauer, M. Schreitl, I. Mazets, D. A. Smith, E. Demler, and J. Schmiedmayer, "Relaxation and prethermalization in an isolated quantum system," *Science*, vol. 337, no. 6100, p. 1318–1322, Sep. 2012. [Online]. Available: http://dx.doi.org/10.1126/science.1224953

[150] N. Malossi, M. M. Valado, S. Scotto, P. Huillery, P. Pillet, D. Ciampini, E. Arimondo, and O. Morsch, "Full counting statistics and phase diagram of a dissipative rydberg gas," *Phys. Rev. Lett.*, vol. 113, p. 023006, 07 2014. [Online]. Available: https://link.aps.org/doi/10.1103/PhysRevLett.113.023006

[151] P. Devillard, D. Chevallier, P. Vignolo, and M. Albert, "Full counting statistics of the momentum occupation numbers of the tonks-girardeau gas," *Phys. Rev. A*, vol. 101, p. 063604, 06 2020. [Online]. Available: https://link.aps.org/doi/10.1103/PhysRevA.101.063604

[152] J. F. Wienand, S. Karch, A. Impertro, C. Schweizer, E. McCulloch, R. Vasseur, S. Gopalakrishnan, M. Aidelsburger, and I. Bloch, "Emergence of fluctuating hydrodynamics in chaotic quantum systems," 2023.

[153] I. Klich and L. Levitov, "Quantum noise as an entanglement meter," *Phys. Rev. Lett.*, vol. 102, p. 100502, 03 2009. [Online]. Available: https://link.aps.org/doi/10.1103/PhysRevLett.102.100502

[154] H. F. Song, S. Rachel, C. Flindt, I. Klich, N. Laflorencie, and K. Le Hur, "Bipartite fluctuations as a probe of many-body entanglement," *Phys. Rev. B*, vol. 85, p. 035409, 01 2012. [Online]. Available: https://link.aps.org/doi/10.1103/PhysRevB.85.035409

[155] A. del Campo, "Universal statistics of topological defects formed in a quantum phase transition," *Phys. Rev. Lett.*, vol. 121, p. 200601, 11 2018. [Online]. Available: https://link.aps.org/doi/10.1103/PhysRevLett.121.200601

[156] J.-M. Cui, F. J. Gómez-Ruiz, Y.-F. Huang, C.-F. Li, G.-C. Guo, and A. del Campo, "Experimentally testing quantum critical dynamics beyond the

kibble–zurek mechanism," *Communications Physics*, vol. 3, no. 1, p. 44, 03 2020. [Online]. Available: https://doi.org/10.1038/s42005-020-0306-6

[157] D. J. Luitz, N. Laflorencie, and F. Alet, "Many-body localization edge in the random-field heisenberg chain," *Phys. Rev. B*, vol. 91, p. 081103, Feb 2015.

[158] R. Singh, J. H. Bardarson, and F. Pollmann, "Signatures of the many-body localization transition in the dynamics of entanglement and bipartite fluctuations," *New Journal of Physics*, vol. 18, no. 2, p. 023046, feb 2016.

[159] S. Groha, F. Essler, and P. Calabrese, "Full counting statistics in the transverse field ising chain," *SciPost Physics*, vol. 4, no. 6, Jun. 2018. [Online]. Available: http://dx.doi.org/10.21468/SciPostPhys.4.6.043

[160] P. Calabrese, M. Collura, G. D. Giulio, and S. Murciano, "Full counting statistics in the gapped xxz spin chain," *Europhysics Letters*, vol. 129, no. 6, p. 60007, 04 2020. [Online]. Available: https://dx.doi.org/10.1209/0295-5075/129/60007

[161] N. R. Smith, P. L. Doussal, S. N. Majumdar, and G. Schehr, "Full counting statistics for interacting trapped fermions," *SciPost Phys.*, vol. 11, p. 110, 2021. [Online]. Available: https://scipost.org/10.21468/SciPostPhys.11.6.110

[162] A. Bastianello and L. Piroli, "From the sinh-gordon field theory to the one-dimensional bose gas: exact local correlations and full counting statistics," *Journal of Statistical Mechanics: Theory and Experiment*, vol. 2018, no. 11, p. 113104, 11 2018. [Online]. Available: https://dx.doi.org/10.1088/1742-5468/aaeb48

[163] L. Capizzi, S. Murciano, and P. Calabrese, "Full counting statistics and symmetry resolved entanglement for free conformal theories with interface defects," *Journal of Statistical Mechanics: Theory and Experiment*, vol. 2023, no. 7, p. 073102, Jul. 2023. [Online]. Available: http://dx.doi.org/10.1088/1742-5468/ace3b8

[164] F. Ares, M. A. Rajabpour, and J. Viti, "Exact full counting statistics for the staggered magnetization and the domain walls in the *xy* spin chain," *Phys. Rev. E*, vol. 103, p. 042107, 04 2021. [Online]. Available: https://link.aps.org/doi/10.1103/PhysRevE.103.042107

[165] M. N. Najafi and M. A. Rajabpour, "Formation probabilities and statistics of observables as defect problems in free fermions and quantum spin

chains," *Phys. Rev. B*, vol. 101, p. 165415, Apr 2020. [Online]. Available: https://link.aps.org/doi/10.1103/PhysRevB.101.165415

[166] S. Campbell and M. Paternostro, "Multipartite nonlocality in a thermalized ising spin chain," *Phys. Rev. A*, vol. 82, p. 042324, 10 2010. [Online]. Available: https://link.aps.org/doi/10.1103/PhysRevA.82.042324

[167] M. Collura and F. H. L. Essler, "How order melts after quantum quenches," *Phys. Rev. B*, vol. 101, p. 041110, Jan 2020. [Online]. Available: https://link.aps.org/doi/10.1103/PhysRevB.101.041110

[168] M. Collura, "Relaxation of the order-parameter statistics in the Ising quantum chain," *SciPost Phys.*, vol. 7, p. 072, 2019. [Online]. Available: https://scipost.org/10.21468/SciPostPhys.7.6.072

[169] F. J. Dyson, "Existence of a phase-transition in a one-dimensional ising ferromagnet," *Communications in Mathematical Physics*, vol. 12, no. 2, pp. 91–107, 06 1969. [Online]. Available: https://doi.org/10.1007/BF01645907

[170] E. G. Lazo, M. Heyl, M. Dalmonte, and A. Angelone, "Finite-temperature critical behavior of long-range quantum Ising models," *SciPost Phys.*, vol. 11, p. 076, 2021. [Online]. Available: https://scipost.org/10.21468/SciPostPhys.11.4.076

[171] M. Collura, A. De Luca, D. Rossini, and A. Lerose, "Discrete time-crystalline response stabilized by domain-wall confinement," *Phys. Rev. X*, vol. 12, p. 031037, 09 2022. [Online]. Available: https://link.aps.org/doi/10.1103/PhysRevX.12.031037

[172] R. Askey, *Connection Coefficients.* SIAM, 1975, ch. 7, pp. 57–69. [Online]. Available: https://epubs.siam.org/doi/epdf/10.1137/1.9781611970470.ch7

[173] H. Tasaki, "From quantum dynamics to the canonical distribution: General picture and a rigorous example," *Phys. Rev. Lett.*, vol. 80, pp. 1373–1376, 02 1998. [Online]. Available: https://link.aps.org/doi/10.1103/PhysRevLett.80.1373

[174] M. Kormos, M. Collura, G. Takács, and P. Calabrese, "Real-time confinement following a quantum quench to a non-integrable model," *Nature Physics*, vol. 13, no. 3, pp. 246–249, 03 2017. [Online]. Available: https://doi.org/10.1038/nphys3934

[175] T. Mori, "Prethermalization in the transverse-field ising chain with long-range interactions," *Journal of Physics A: Mathematical and Theoretical*, vol. 52, no. 5, p. 054001, 01 2019. [Online]. Available: https://dx.doi.org/10.1088/1751-8121/aaf9db

[176] A. H. Werner, D. Jaschke, P. Silvi, M. Kliesch, T. Calarco, J. Eisert, and S. Montangero, "Positive tensor network approach for simulating open quantum many-body systems," *Phys. Rev. Lett.*, vol. 116, p. 237201, 6 2016. [Online]. Available: https://link.aps.org/doi/10.1103/PhysRevLett.116.237201

[177] D. Jaschke, S. Montangero, and L. D. Carr, "One-dimensional many-body entangled open quantum systems with tensor network methods," *Quantum Science and Technology*, vol. 4, no. 1, p. 013001, nov 2018. [Online]. Available: https://dx.doi.org/10.1088/2058-9565/aae724

[178] E. G. Lazo, M. Heyl, M. Dalmonte, and A. Angelone, "Finite-temperature critical behavior of long-range quantum Ising models," *SciPost Phys.*, vol. 11, p. 076, 2021. [Online]. Available: https://scipost.org/10.21468/SciPostPhys.11.4.076

[179] A. Dutta and J. K. Bhattacharjee, "Phase transitions in the quantum ising and rotor models with a long-range interaction," *Phys. Rev. B*, vol. 64, p. 184106, Oct 2001. [Online]. Available: https://link.aps.org/doi/10.1103/PhysRevB.64.184106

[180] K. G. Wilson, "Confinement of quarks," *Phys. Rev. D*, vol. 10, pp. 2445–2459, 10 1974. [Online]. Available: https://link.aps.org/doi/10.1103/PhysRevD.10.2445

[181] E. Eichten, K. Gottfried, T. Kinoshita, K. D. Lane, and T. M. Yan, "Charmonium: The model," *Phys. Rev. D*, vol. 17, pp. 3090–3117, 06 1978. [Online]. Available: https://link.aps.org/doi/10.1103/PhysRevD.17.3090

[182] E. Eichten, K. Gottfried, T. Kinoshita, J. Kogut, K. D. Lane, and T. M. Yan, "Spectrum of charmed quark-antiquark bound states," *Phys. Rev. Lett.*, vol. 34, pp. 369–372, 02 1975. [Online]. Available: https://link.aps.org/doi/10.1103/PhysRevLett.34.369

[183] V. Mateu, P. G. Ortega, D. R. Entem, and F. Fernández, "Calibrating the naïve cornell model with nrqcd," *The European Physical Journal C*, vol. 79, no. 4, p. 323, 04 2019. [Online]. Available: https://doi.org/10.1140/epjc/s10052-019-6808-2

[184] E. J. Eichten, K. Lane, and C. Quigg, "New states above charm threshold," *Phys. Rev. D*, vol. 73, p. 014014, 01 2006. [Online]. Available: https://link.aps.org/doi/10.1103/PhysRevD.73.014014

[185] J. Bulava, B. Hörz, F. Knechtli, V. Koch, G. Moir, C. Morningstar, and M. Peardon, "String breaking by light and strange quarks in qcd," *Physics Letters B*, vol. 793, pp. 493–498, 2019. [Online]. Available: https://www.sciencedirect.com/science/article/pii/S0370269319303284

[186] F. B. Ramos, M. Lencsés, J. C. Xavier, and R. G. Pereira, "Confinement and bound states of bound states in a transverse-field two-leg ising ladder," *Phys. Rev. B*, vol. 102, p. 014426, Jul 2020. [Online]. Available: https://link.aps.org/doi/10.1103/PhysRevB.102.014426

[187] L. Vanderstraeten, E. Wybo, N. Chepiga, F. Verstraete, and F. Mila, "Spinon confinement and deconfinement in spin-1 chains," *Phys. Rev. B*, vol. 101, p. 115138, Mar 2020. [Online]. Available: https://link.aps.org/doi/10.1103/PhysRevB.101.115138

[188] C. M. Morris, R. Valdés Aguilar, A. Ghosh, S. M. Koohpayeh, J. Krizan, R. J. Cava, O. Tchernyshyov, T. M. McQueen, and N. P. Armitage, "Hierarchy of bound states in the one-dimensional ferromagnetic ising chain $\mathrm{conb_2o_6}$ investigated by high-resolution time-domain terahertz spectroscopy," *Phys. Rev. Lett.*, vol. 112, p. 137403, 04 2014. [Online]. Available: https://link.aps.org/doi/10.1103/PhysRevLett.112.137403

[189] Z. Wang, M. Schmidt, A. K. Bera, A. T. M. N. Islam, B. Lake, A. Loidl, and J. Deisenhofer, "Spinon confinement in the one-dimensional ising-like antiferromagnet $\mathrm{srco_2v_2o_8}$," *Phys. Rev. B*, vol. 91, p. 140404, Apr 2015. [Online]. Available: https://link.aps.org/doi/10.1103/PhysRevB.91.140404

[190] Z. Wang, J. Wu, S. Xu, W. Yang, C. Wu, A. K. Bera, A. T. M. N. Islam, B. Lake, D. Kamenskyi, P. Gogoi, H. Engelkamp, N. Wang, J. Deisenhofer, and A. Loidl, "From confined spinons to emergent fermions: Observation of elementary magnetic excitations in a transverse-field ising chain," *Phys. Rev. B*, vol. 94, p. 125130, Sep 2016. [Online]. Available: https://link.aps.org/doi/10.1103/PhysRevB.94.125130

[191] B. M. McCoy and T. T. Wu, "Two-dimensional ising field theory in a magnetic field: Breakup of the cut in the two-point function," *Phys. Rev. D*, vol. 18, pp. 1259–1267, Aug 1978. [Online]. Available: https://link.aps.org/doi/10.1103/PhysRevD.18.1259

[192] S. B. Rutkevich, “On the weak confinement of kinks in the one-dimensional quantum ferromagnet conb2o6,” *Journal of Statistical Mechanics: Theory and Experiment*, vol. 2010, no. 07, p. P07015, 07 2010. [Online]. Available: https://dx.doi.org/10.1088/1742-5468/2010/07/P07015

[193] G. Lagnese, F. M. Surace, M. Kormos, and P. Calabrese, “Confinement in the spectrum of a heisenberg–ising spin ladder,” *Journal of Statistical Mechanics: Theory and Experiment*, vol. 2020, no. 9, p. 093106, 09 2020. [Online]. Available: https://dx.doi.org/10.1088/1742-5468/abb368

[194] Z. Wang, J. Wu, W. Yang, A. K. Bera, D. Kamenskyi, A. T. M. N. Islam, S. Xu, J. M. Law, B. Lake, C. Wu, and A. Loidl, “Experimental observation of bethe strings,” *Nature*, vol. 554, no. 7691, pp. 219–223, 02 2018. [Online]. Available: https://doi.org/10.1038/nature25466

[195] Z. Wang, M. Schmidt, A. Loidl, J. Wu, H. Zou, W. Yang, C. Dong, Y. Kohama, K. Kindo, D. I. Gorbunov, S. Niesen, O. Breunig, J. Engelmayer, and T. Lorenz, “Quantum critical dynamics of a heisenberg-ising chain in a longitudinal field: Many-body strings versus fractional excitations,” *Phys. Rev. Lett.*, vol. 123, p. 067202, Aug 2019. [Online]. Available: https://link.aps.org/doi/10.1103/PhysRevLett.123.067202

[196] G. Lagnese, F. M. Surace, M. Kormos, and P. Calabrese, “False vacuum decay in quantum spin chains,” *Phys. Rev. B*, vol. 104, p. L201106, 11 2021. [Online]. Available: https://link.aps.org/doi/10.1103/PhysRevB.104.L201106

[197] ——, “Quenches and confinement in a heisenberg–ising spin ladder,” *Journal of Physics A: Mathematical and Theoretical*, vol. 55, no. 12, p. 124003, 03 2022. [Online]. Available: http://dx.doi.org/10.1088/1751-8121/ac5215

[198] T. Chanda, J. Zakrzewski, M. Lewenstein, and L. Tagliacozzo, “Confinement and lack of thermalization after quenches in the bosonic schwinger model,” *Phys. Rev. Lett.*, vol. 124, p. 180602, 05 2020. [Online]. Available: https://link.aps.org/doi/10.1103/PhysRevLett.124.180602

[199] R. D. Sedgewick, D. J. Scalapino, and R. L. Sugar, “Fractionalized phase in an $\mathrm{XY}--Z_2$ gauge model,” *Phys. Rev. B*, vol. 65, p. 054508, 01 2002. [Online]. Available: https://link.aps.org/doi/10.1103/PhysRevB.65.054508

[200] T. Pichler, M. Dalmonte, E. Rico, P. Zoller, and S. Montangero, “Real-time dynamics in u(1) lattice gauge theories with tensor networks,” *Phys. Rev. X*, vol. 6, p. 011023, 03 2016. [Online]. Available: https://link.aps.org/doi/10.1103/PhysRevX.6.011023

[201] E. Zohar, J. I. Cirac, and B. Reznik, "Simulating compact quantum electrodynamics with ultracold atoms: Probing confinement and nonperturbative effects," *Phys. Rev. Lett.*, vol. 109, p. 125302, 09 2012. [Online]. Available: https://link.aps.org/doi/10.1103/PhysRevLett.109.125302

[202] J. C. P. Barros, M. Dalmonte, and A. Trombettoni, "String tension and robustness of confinement properties in the schwinger-thirring model," *Phys. Rev. D*, vol. 100, p. 036009, 08 2019. [Online]. Available: https://link.aps.org/doi/10.1103/PhysRevD.100.036009

[203] J. C. Halimeh, I. P. McCulloch, B. Yang, and P. Hauke, "Tuning the topological θ-angle in cold-atom quantum simulators of gauge theories," *PRX Quantum*, vol. 3, p. 040316, 11 2022. [Online]. Available: https://link.aps.org/doi/10.1103/PRXQuantum.3.040316

[204] E. A. Martinez, C. A. Muschik, P. Schindler, D. Nigg, A. Erhard, M. Heyl, P. Hauke, M. Dalmonte, T. Monz, P. Zoller, and R. Blatt, "Real-time dynamics of lattice gauge theories with a few-qubit quantum computer," *Nature*, vol. 534, no. 7608, pp. 516–519, 06 2016. [Online]. Available: https://doi.org/10.1038/nature18318

[205] J. Vovrosh and J. Knolle, "Confinement and entanglement dynamics on a digital quantum computer," *Scientific Reports*, vol. 11, no. 1, 06 2021. [Online]. Available: http://dx.doi.org/10.1038/s41598-021-90849-5

[206] M. C. Bañuls, J. I. Cirac, and M. B. Hastings, "Strong and weak thermalization of infinite nonintegrable quantum systems," *Phys. Rev. Lett.*, vol. 106, p. 050405, 02 2011. [Online]. Available: https://link.aps.org/doi/10.1103/PhysRevLett.106.050405

[207] M. C. Bañuls, M. P. Heller, K. Jansen, J. Knaute, and V. Svensson, "Quantum information perspective on meson melting," *Physical Review D*, vol. 108, no. 7, 10 2023. [Online]. Available: http://dx.doi.org/10.1103/PhysRevD.108.076016

[208] P. P. Mazza, G. Perfetto, A. Lerose, M. Collura, and A. Gambassi, "Suppression of transport in nondisordered quantum spin chains due to confined excitations," *Phys. Rev. B*, vol. 99, p. 180302, 05 2019. [Online]. Available: https://link.aps.org/doi/10.1103/PhysRevB.99.180302

[209] A. Dutta and J. K. Bhattacharjee, "Phase transitions in the quantum ising and rotor models with a long-range interaction," *Phys. Rev. B*, vol. 64, p. 184106, 10 2001. [Online]. Available: https://link.aps.org/doi/10.1103/PhysRevB.64.184106

[210] R. Senese, J. H. Robertson, and F. H. L. Essler, “Out-of-equilibrium full-counting statistics in gaussian theories of quantum magnets,” 2023.